LA-11300-P
Proposal

UC-410
Issued: April 1988

LA--11300-P

DE88 008516

A Proposal for a Precision Test of the Standard Model by Neutrino-Electron Scattering

(Large Čerenkov Detector Project)

R. C. Allen, X-Q. Lu, K. Gollwitzer
University of California, Irvine

G. J. Igo, E. Gulmez, C. Whitten
University of California, Los Angeles

G. VanDalen, J. Layter, Sun Yui Fung, B. C. Shen
University of California, Riverside

R. Ristinen, R. Smythe
University of Colorado

R. C. Carlini
CEBAF/William and Mary

K. Black, R. Burman, J. Donahue, D. Fitzgerald, W. Foreman, M. Hoehn, T. Kozlowski, D. M. Lee, W. C. Louis, R. Macek, J. McGill, E. C. Milner, M. Oothoudt, V. Sandberg, G. Sanders, M. Schillaci, R. Werbeck, R. Westervelt, D. H. White
Los Alamos National Laboratory

B. B. Dieterle, C. P. Leavitt, J. Kang
University of New Mexico

W. Frati, A. K. Mann, M. Newcomer, R. van Berg
University of Pennsylvania

L. A. Auerbach, V. L. Highland, W. K. McFarlane
Temple University

R. T. Seigel
College of William and Mary

Los Alamos National Laboratory
Los Alamos, New Mexico 87545

Herb Chen died on November 7, 1987, after a long illness. He made seminal contributions to this proposal, and we shall miss him. His contributions to neutrino physics at LAMPF have been considerable, and we expect his influence to continue through the people at Irvine and through this group as a whole.

Contents

Large Čerenkov Detector

Facility

Beam Characteristics

Detector

Abstract

A precision measurement of neutrino-electron elastic scattering from a beam stop neutrino source at LAMPF is proposed. The total error in $\sin^2\theta_W$ *is estimated to be* $\pm 0.89\%$. *The experiment also will be sensitive to neutrino oscillations and supernova-neutrino bursts, and should set improved limits on the neutrino-charge radius and magnetic-dipole moment. The detector consists of a 2.5-million-gallon tank of water with approximately 14,000 photomultiplier tubes lining the surfaces of the tank. Neutrino-electron scattering events will be observed from the Čerenkov radiation emitted by the electrons in the water.*

1 INTRODUCTION

A precision measurement of neutrino-electron elastic scattering from a beam stop neutrino source at LAMPF is proposed. The total error in $\sin^2\theta_W$ is estimated to be $\pm 0.89\%$. The detector also will be sensitive to neutrino oscillations and supernova neutrino bursts, and should set improved limits on the neutrino-charge radius and magnetic-dipole moment.

We propose a precision measurement of neutrino-electron scattering from a beam stop neutrino source at LAMPF. Neutrino-electron scattering can be described in detail by the Standard Model without complications from effects of strong or electromagnetic interactions. Reactions involving neutrinos and charged leptons are unique in this respect. Neutrinos are produced copiously at LAMPF from 800-MeV protons producing pions in a beam stop. The pions travel a short distance in the heavy material in which they are produced and then come to rest in almost all cases. Not only are π^- produced less frequently than π^+, but π^- are almost completely absorbed by heavy nuclei before they can decay. After π^+ decays to $\mu^+\nu_\mu$, the μ^+ decays in turn to e^+, ν_e, and $\bar{\nu}_\mu$. The flux of ν_μ and the fluxes of ν_e and $\bar{\nu}_\mu$ are very nearly equal; small deviations from equality are well understood and can be calculated.

Figures 1.1 and 1.2 are schematics of the LAMPF accelerator and the proton storage ring (PSR), and the Large Water Čerenkov Detector (LCD). The detector consists of a 2.5 million gallon cylindrical tank of water with over 10,000 phototubes lining the walls of the tank. The experimental fiducial volume is larger than the Kamioka water Čerenkov detector and smaller than the IMB detector. The PSR accepts beam from LAMPF over a macropulse of about a millisecond, and after the proton beam is accumulated, it is extracted in a single turn, giving a spill of about 270 ns. The time distribution of the neutrino flux is such as to allow separation of events from pion decay (ν_μ) and muon decay (ν_e and $\bar{\nu}_\mu$). The experiment is a measurement of the ratio of the neutrino-electron cross sections from these two groups of neutrinos. Neutrino interactions are observed using the recoil electrons which produce Čerenkov radiation in the water. This radiation is detected by the phototubes lining the tank, giving signals at the one photoelectron level in the tubes. Both pulse height in each of the tubes and time with respect to the proton pulse will be recorded, allowing reconstruction of the Čerenkov ring as the light impinges on the phototubes at the walls. From this information it is possible to deduce the time and spatial position of the neutrino electron event and the direction of the recoiling electron track to sufficient precision for the experiment. A ratio measurement has

the advantage that systematic effects largely cancel, because in the final state of all reactions, the single electron has an energy of about 20 MeV.

The Standard Model of electroweak interactions (SM) leads to the predictions of W and Z^0 intermediate vector bosons close to the mass values that have been observed at CERN. These bosons, along with the photon, mediate the electroweak force. At the next level of precision the boson masses and the strength of specific interactions are modified by radiative corrections, which involve the constituent particles of the model. The single most important parameter of the theory is $\sin^2\theta_W$, where θ_W is the Weinberg angle. Measurement of the intermediate vector boson masses produces a value of $\sin^2\theta_W$ that will be different by approximately 7% from the value measured in neutrino-electron scattering if radiative corrections are not included. This experiment is, therefore, complementary to those performed at the highest available energies. We propose to measure $\sin^2\theta_W$ from neutrino-electron scattering with a total error of 1%. This measurement, in conjunction with a determination of $\sin^2\theta_W$ at a precision better than 1% from measurements of the W and Z masses, will provide one of the most precise tests of the SM (at the level of one-loop diagrams in the radiative corrections) while at the same time serving as a sensitive probe of new physics manifested at high energy.[1]

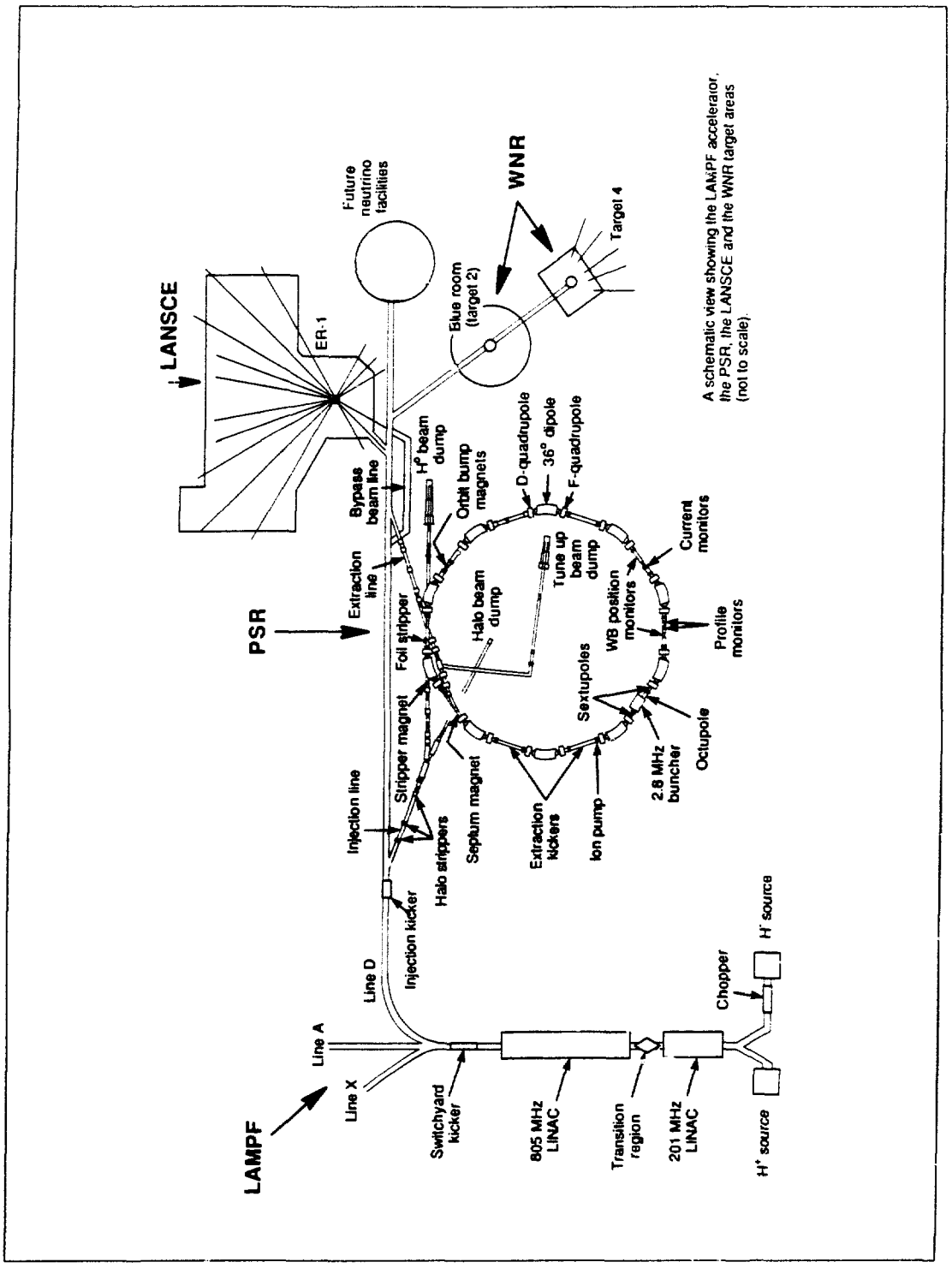

Fig. 1.1. Layout of the Proton Storage Ring, showing the injection and extraction lines, and the LAMPF accelerator.

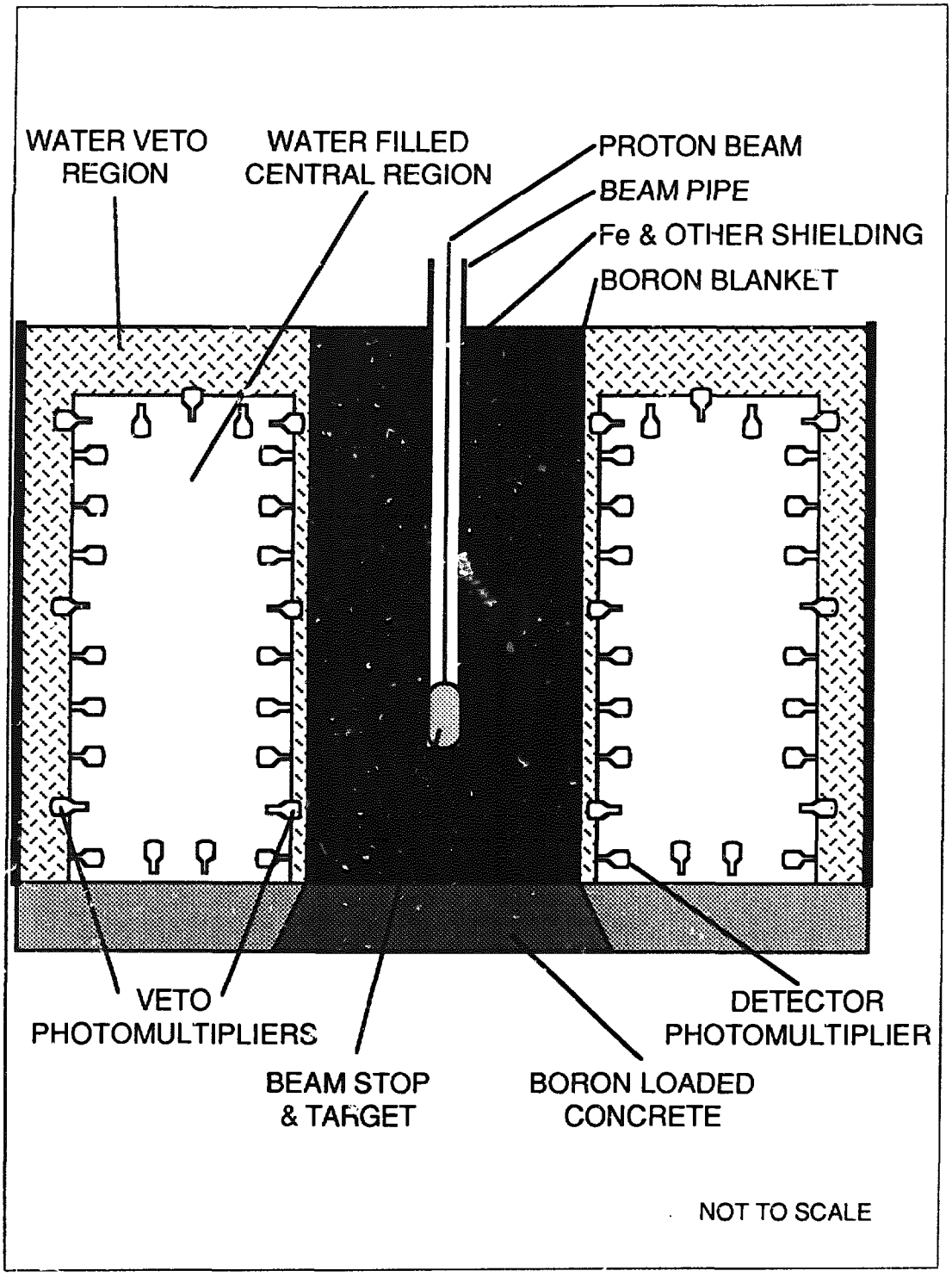

Fig. 1.2. Elevation view of the Large Čerenkov Detector.

1.1 The Standard Model

The major accomplishment in elementary particle physics in the last fifteen years has been the success of the electroweak model of Glashow, Weinberg, and Salam in describing the unification of the electromagnetic and weak forces. The SM describes experimental data to within the measured precision, apart from masses and mixing angles, in terms of a single phenomenological parameter $\sin^2\theta_W$. The success of the theory is epitomized by a fit to a large body of data described by Amaldi et al[1] with a value of $\sin^2\theta_W = 0.230 \pm 0.005$. Reference 1 exhibits the relative precision of various weak neutral-current experiments, demonstrates that a consistent description of all data is possible now only if one-loop radiative corrections are applied to the data, and shows that the details of such corrections are sensitive to the underlying structure in the elementary particle mass spectrum.

1.2 Proposed Experiment

Measurements of the masses of the vector bosons that are likely to be made in the next few years are expected to provide the most accurate determination of the parameter $\sin^2\theta_W$. The prediction of the Standard Model that $\sin^2\theta_W$ is a universal parameter must, however, be rigorously tested in neutral-current scattering processes. Deep inelastic scattering on nucleons has proved to be the most accurate method so far but has the problem common to hadronic processes that calculation of the result involves theoretical uncertainty at the level of a few percent. Neutrino-electron scattering experiments have been limited in the past by shortage of events, subtraction of background and difficulties in the neutrino normalization. The most precise neutrino-electron measurements have been of the ratio of neutrino to antineutrino scattering. A substantial contribution to the systematic error in these experiments has arisen from the uncertainty in the characteristics of the two beams. We propose to measure the ratio,

$$R = \frac{\sigma(\nu_\mu e)}{\sigma(\nu_e e) + \sigma(\bar{\nu}_\mu e)}.$$

The cross section for ν_μ - e scattering is

$$\frac{d\sigma(\nu_\mu e \rightarrow \nu_\mu e)}{dy} = \frac{G_\mu^2 m_e E_\nu}{2\pi}\left[(2s^2 - 1)^2 + (2s^2)^2(1 - y)^2 - 2s^2(2s^2 - 1)\frac{m_e}{E_\nu}\, y\right]$$

where $y = (E_e - m_e)/E_\nu$, $s^2 = \sin^2\theta_W$. For ν_ee scattering, replace $2s^2 - 1$ by $2s^2 + 1$, while for $\bar{\nu}_\mu$e scattering interchange $2s^2 - 1$ with $2s^2$.

If we ignore the term linear in y, since m_e/E_ν is small, and integrate over y, the SM expression for the ratio of the cross sections may be written

$$R = \frac{3}{4} \quad \frac{1 - 4s^2 + 16/3\, s^4}{1 + 2s^2 + 8s^4}$$

($R \sim 0.13$ for $\sin^2\theta_W = 0.23$). When $\sin^2\theta_W$ increases by a given relative amount, the ratio R increases by a larger fraction (2.08 with a 10 MeV electron energy cut, 1.66 with no energy cut). We discuss below in more detail the effect of measuring the ratio when the linear terms are included, and exact neutrino spectra and threshold functions are used.

In summary, we propose to make a precision measurement of the ratio of neutrino electron scattering with neutrinos from pion decay and muon decay simultaneously: measurement of the ratio (R above) with an accuracy of 2% will yield $\sin^2\theta_W$ with a total error less than 1%.

1.3 Experimental Error

Statistical

We have evaluated errors on the basis of 625 days of running at 100μA (1.5 A-Hr or 3.38×10^{22} protons on target). Under these conditions, the event rates will be 12/day for the prompt component (ν_μe) and 101/day for the delayed component ($\bar{\nu}_\mu$e + ν_ee), giving a sample of about 7500 ν_μe events and 63,400 ν_ee and $\bar{\nu}_\mu$e events. Fluctuations in these overall numbers and the shape of the beam spill combine to give a statistical error of 1.4%. This dominates the accuracy of the experiment. Additional statistical error results from the subtraction of background from cosmic rays (1 delayed event per day), neutrons (< 1 prompt event and < 1 delayed event per day after cuts), and ν_e-oxygen scattering (22 delayed events per day under the forward peak). Inclusion of these backgrounds raises the statistical error on the ratio R to 1.60%. Table 1.1 summarizes these event rates.

Systematic

There are several components to the systematic error, but most of these can be seen to be small (see Table 1.2). π decay in flight results in contamination of the ν source at high energy, but the corrections are small and well understood. The main instrumental error is in the photomultiplier calibration, which is taken to give $\pm$ 1 p.e. error in the energy threshold for Čerenkov detection, corresponding to a 0.4% systematic error. The most important contributions to the systematic error come from the uncertainties in the angular shape of the background spectrum. Until recently, the forward electron cross section from oxygen was not well known. Recent

calculations by Haxton[2] have reduced uncertainties in the small nuclear amplitudes that contribute to this cross section. We now believe the systematic error in the subtraction of this background is 0.5% in R.

Table 1.1. Summary of event rates.

Type of Event	*#/day*	*#/day* $\cos\theta > 0.76$	*Sect.*
All ν e scattering	112.0	106.5	12.8.1
ν_μe	12.0	11.3	12.8.1
ν_ee	87.3	82.5	12.8.1
$\bar{\nu}_\mu$e	13.6	12.8	12.8.1
Beam-induced background			
Neutron-induced gammas	4.1	0.49	7.10
Neutron-induced pions (prompt)	0.22	0.22	7.1.4
(delayed)	0.544	0.065	7.1.4
Neutrino-oxygen	331	22.2	12.8.3
Cosmic-ray-induced background (5 μs gate)			
Stopped muon decay			
Out of 5 σ "dead zone"	1.73	0.21	9.3
Decay after 30 μs	0.04	0.004	9.3
Interactions of throughgoing muons	2.5	0.25	9.4.1
Muon capture and beta decay			
^{16}N beta decay (7s, 10.4 MeV)	0.9	0.09	9.4.2
^{12}B beta decay (27μs, 14 MeV)	1.4	0.14	9.4.2
Gammas from showers	0.04	0.004	9.5.1
Neutrons from hadronic interactions	1.4	0.14	9.5.2

Table 1.2. Contribution to systematic errors in R.

Cause	*Error in %*
1. Decay in Flight	0.12
2. Cosmic Rays	0.01
3. ν_e - O	0.50
4. Prompt γ and $\pi^{\pm}$ from n interactions	0.65
5. Delayed e from n induced π^+ decay	0.01
6. Measurement of PSR Shape	0.15
7. Systematic time shift	0.08
8. Absolute threshold energy	0.40
9. Non uniform efficiency	0.10
Total Systematic error	0.94 (added in quadrature)
Total Statistical error	1.60
Total error in R	1.86 (added in quadrature)
Total error in $\sin^2\theta_W$	0.89

The other contribution to background that may have angular dependence is prompt γ's and π's from neutron interactions in the water. We have the ability to reduce this background to an arbitrarily low value by adding iron absorber. However, this costs about \$1M for each meter that we add (mainly due to extra PMT's required to maintain the same photocathode coverage). At this time, a 7.5m radius cylinder shielding the production target gives a neutron flux that we think corresponds to about 0.7 prompt neutron background events per day after cuts. This is a critical value, and we are still working to reduce the uncertainty in the required neutron shielding. Measurements will be made at LAMPF to determine the neutron-induced background more accurately. It is possible that the diameter of the iron cylinder could be changed by as much as 0.25m after these results are evaluated. With a 7.5m diameter the systematic error is about 0.65% in R from neutrons, while an extra 0.25m of steel reduces this to 0.2%. The overall effect on

systematic errors of an additional $0.25m$ of steel is to reduce the systematic error in R from 0.94% to 0.71%.

Using these estimates we conclude that the error

$$\frac{\Delta \sin^2 \theta_W}{\sin^2 \theta_W} \textit{ is } 0.84\% \textit{ to } 0.89\%.$$

1.4 Other Neutrino Experiments

1.4.1 BNL $\nu_\mu e$ Experiment

The Brookhaven neutrino-electron scattering experiment was designed to measure the ratio of neutrino to antineutrino scattering on electrons. The neutrino beams were produced from pions and kaons focused by a double horn system; the mean energy of the neutrino beam was 1.3 GeV and the antineutrino beam was 1.2 GeV. The contamination of the neutrino beam by antineutrinos was typically $\sim$3%, and the contamination of the antineutrino beam by neutrinos was $\sim$10%. The beam flux characteristics were different in energy distribution as well as in absolute flux. Data with a particular beam were normalized to quasi-elastic scattering

$$\nu_\mu + n \rightarrow \mu^- + p$$

for neutrinos, and

$$\bar{\nu}_\mu + p \rightarrow \mu^+ + n$$

for antineutrinos.

Many of the systematic errors in the measurement of a single cross section were offset in the ratio. These systematic errors are tabulated in Table 1.3.

The BNL experiment was limited by statistical precision but the systematic precision quoted was ± 0.013 on $\sin^2 \theta_W$. The statistical precision was ± 0.029 and will improve to ± 0.020 when all the data are analyzed. The present result for the ratio of the cross sections is

$$R_{BNL} = 1.38^{+0.40}_{-0.31}$$

giving

$$\sin^2 \theta_W = 0.209 \pm 0.029 \text{ (stat)} \pm 0.015 \text{ (sys)} \quad .$$

Table 1.3. Contributions to the error in $\sigma(\nu_\mu e)/\sigma(\bar{\nu}_\mu e) = R_{BNL}$ in the BNL experiment.

Component	*Uncertainty in R_{BNL}*
a) M_A	1%
b) Neutrino flux shape uncertainty	3%
c) Acceptances*	4%
d) Single pion cross section	5%
e) Multi pion cross section and acceptance	5%
f) Tracking and event selection efficiency	3%

* Includes hadron and pion scattering effects both inside and outside the target nucleus for events occurring on bound targets.

a) M_A is the axial vector mass describing the form factor of the nucleon. It is well known and contributes little to the uncertainty in the normalization.

b) The flux uncertainty is difficult to improve, although more comprehensive measurements on the individual beams could be made.

c) The interaction probability of hadrons in the dense medium of the detector dominates this uncertainty and dilution of the mass of the detector would make significant improvement.

d, e) The basic cross sections are not well known and represent an intrinsic limitation.

f) If this uncertainty were the basic limitation then improvements could be made.

1.4.2 CHARM I

The CHARM I neutrino-electron scattering measurement was very similar to the BNL experiment described above with the exception that the mean energy of the neutrino beam was about a factor-of-20 higher in energy. The mean energy of the CHARM I neutrino beam was 31 GeV and of the antineutrino beam was 24 GeV. As a consequence, the kinematic limit on the scattering angle for electron scattering was considerably smaller than the angular resolution of the experiment, and the signal to noise of the detected events was somewhat worse than the BNL experiment. Nevertheless, the systematic error on the ratio of neutrino to antineutrino scattering quoted[3] is comparable to the BNL experiment. Primary sources of systematic error come from background subtraction ($\pm 10\%$) and normalization of both beams ($\pm 7\%$). Because both experiments are limited by statistical precision to about the

same degree, the precision on $\sin^2\theta_W$ is comparable in both measurements. The result of the CHARM I experiment is

$$R_{CHARMI} = 1.27^{+0.65}_{-0.44}$$

giving

$$\sin^2\theta_W = 0.215 \pm 0.040\ (\text{stat}) \pm 0.015\ (\text{sys})\ .$$

1.4.3 CHARM II

CHARM II is a considerably larger version of the CHARM I experiment with improved angular resolution. This is expected to improve the signal to background ratio, and hence to yield an improved systematic error. The experiment is similar to CHARM I except for the mass of the detector, which translates into improved statistical precision. It is expected that the experiment will yield 2000 events of each kind, giving a statistical precision on $\sin^2\theta_W$ of ± 0.003. A corresponding improvement in the systematic uncertainty will be necessary but is not easily foreseen.

1.5 Other Physics

i) The precision of the absolute cross section from this experiment leads to an estimated limit for the charge radius of the muon and electron neutrinos of $< r^2 > \ < 10^{-33}\ cm^2$. Because of the low energy of the neutrinos compared to other experiments, an even greater improvement in the limit on the magnetic dipole moment is realized.

ii) ν - oscillations. Measurement of R to 2% is shown to probe $\nu_\mu \rightarrow \nu_e$ oscillations with $0.0002 \leq \sin^2 2\alpha$ and Δm^2_{21} as small as $0.06\ \text{eV}^2$.[4]

iii) The apparatus may be operated as a supernova detector. The experiment is sensitive to antimatter supernovae because of the enhanced cross section for $\bar{\nu}_e + p \rightarrow e^+ + n$ in the low-energy regime.

1.6 Cost

The cost is divided into:

a) Conventional construction of the neutrino source, shielding and experimental area as a facility.

b) PSR extraction and beam transport.

c) The LCD detector and auxiliary equipment.

Details of these costs, including contingency, have been evaluated and are contained in a separate document.

1.7 Summary

A realizable measurement of

$$R = \frac{\sigma(\nu_\mu e)}{\sigma(\nu_e e) + \sigma(\bar{\nu}_\mu e)}$$

with an accuracy of 2% can be carried out at LAMPF utilizing the pulsed beam available from the proton storage ring. This will yield a determination of $\sin^2\theta_W$ with a total error not exceeding 1%. This measurement, taken in conjunction with precision measurements of the W and Z^o masses, will probe the radiative corrections to the SM at the important one loop level, providing a sensitive test of the constituents of the theory.

In the case that the SM proves capable of describing physics in the presently accessible energy regime, the universality of $\sin^2\theta_W$ after one loop corrections implies constraints on neutrino osciliation parameters. These constraints are more severe by about a factor of ten over existing measurements at accelerators for $\nu_\mu \rightarrow \nu_e$, $\nu_e \rightarrow \nu_\tau$, and ν_e and ν_μ disappearance. In addition, an absolute measurement of the neutrino electron scattering cross sections in conjunction with the y dependence provides constraints on the electric and magnetic dipole moments of the neutrino which are also a factor of ten better than existing measurements.

When operational, the detector will augment the present capabilities for observing supernovae through the detection of electrons from neutrino interactions with about a factor of three greater sensitivity than either KII or IMB. Measurement of the absolute time to a precision of a microsecond will allow base line determination of the supernova position.

References

1. U. Amaldi et al., *Physical Review* **D36,** 1385 (1987).
2. W. C. Haxton, *Neutrino Reactions on Oxygen and the Proposed LAMPF Measurement of the Weinberg Angle*, (1987).
3. F. Bergsma et al., *Physics Letters* **117B,** 272 (1982), *Physics Letters* **147B,** 481 (1984).
4. W. J. Marciano, Brookhaven National Laboratory, (June 1987).

2 PHYSICS

A review of the one-loop corrections to electroweak processes is presented and the Standard Model radiative corrections for neutrino-electron scattering are given. Other high precision tests are surveyed.

2.1 Introduction

We discuss some of the theoretical foundations for the proposed experiment and compare other precision tests of the standard model. As was described in Chapter 1, this experiment will measure the cross section $\sigma(\nu_\mu e)$ and the sum of two cross sections $\sigma(\bar{\nu}_\mu e)+\sigma(\nu_e e)$ from neutrino-electron reactions in the beam spill and post-beam spill windows, respectively, to a precision of a few percent. We define R to be the ratio of these two quantities, which to the lowest order in the standard model is given by

$$R \equiv R_{LCD} \equiv \frac{\sigma(\nu_\mu e)}{\sigma(\bar{\nu}_\mu e)+\sigma(\nu_e e)}$$

$$= \frac{3}{4} \quad \frac{1-4\sin^2\theta_W+\frac{16}{3}\sin^4\theta_W}{1+2\sin^2\theta_W+8\sin^4\theta_W} \quad .$$

For $\sin^2\theta_W = 0.23$ and restricting electron energies to be greater than 10 MeV the error on R is related to the error in $\sin^2\theta_W$ by

$$\frac{\Delta R}{R} \times 0.481 = \frac{\Delta \sin^2\theta_W}{\sin^2\theta_W} \quad .$$

We propose to determine $\sin^2\theta_W$ to 1%, which will require a 2.08% measurement of R.

The present level of precision is illustrated by Fig. 2.1 ($\sin^2\theta_W$ as determined from a global fit of existing data by Amaldi et al.[1]), Fig. 2.2 (one-sigma errors in the $g_V - g_A$ plane), and Fig. 2.3 ($\sin^2\theta_W$ as determined from contemporary measurements, presented by the 1986 Particle Data Group[2]). The deep inelastic neutrino-hadron scattering experiments[1] measuring the ratio of neutral to charge current cross sections have given us the best measurement to date of $\sin^2\theta_W = 0.233 \pm 0.0058$, which has a precision of 2.5%. Using all available data, Amaldi et al. have concluded that one-loop corrections to $\sin^2\theta_W$ have been observed at the level of three standard deviations. The next generation of experiments should provide detailed tests of these corrections.

$\sin^2 \theta_W$ as Presented by the Global Fit

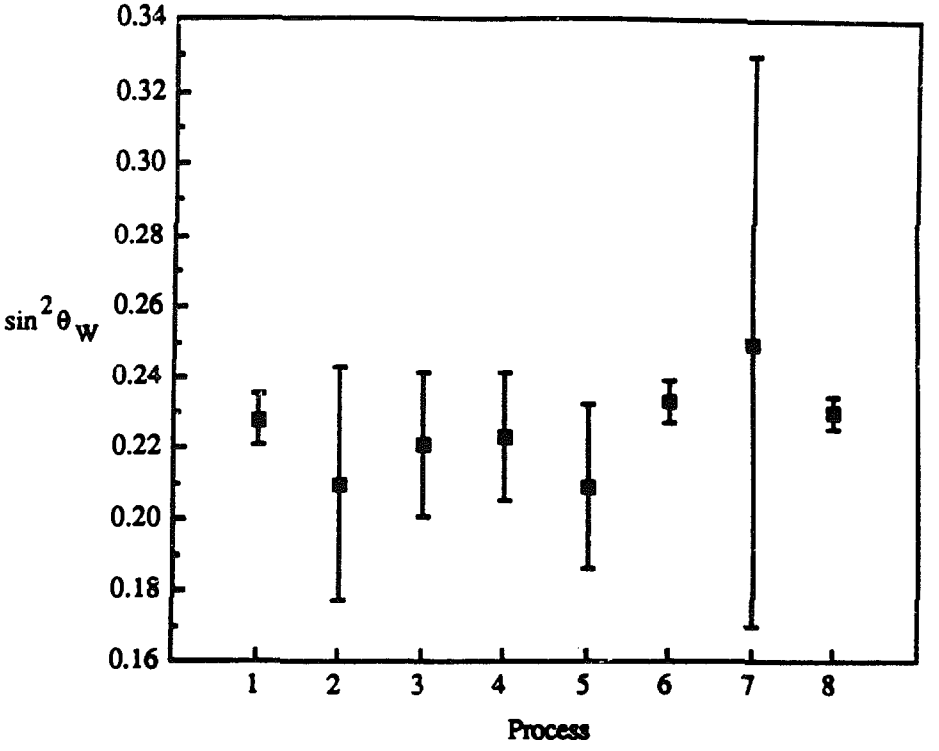

	Process	$\sin^2 \theta_W$	$\Delta\sin^2 \theta_W$
1	W, Z	0.228	0.0073
2	$\nu_\mu(\bar{\nu}_\mu)p \rightarrow \nu_\mu(\bar{\nu}_\mu)p$	0.21	0.033
3	SLAC eD asymmetry	0.221	0.02
4	$\nu_\mu(\bar{\nu}_\mu)e \rightarrow \nu_\mu(\bar{\nu}_\mu)e$	0.223	0.018
5	Atomic parity violation	0.209	0.023
6	Deep inelastic	0.233	0.0058
7	μC	0.25	0.08
8	all data	0.23	0.0048

Fig. 2.1. The measurement of $\sin^2\theta_W$ from different processes. Data compiled by Amaldi *et al.*, Phys. Rev. **D36**, 1385 (1987).

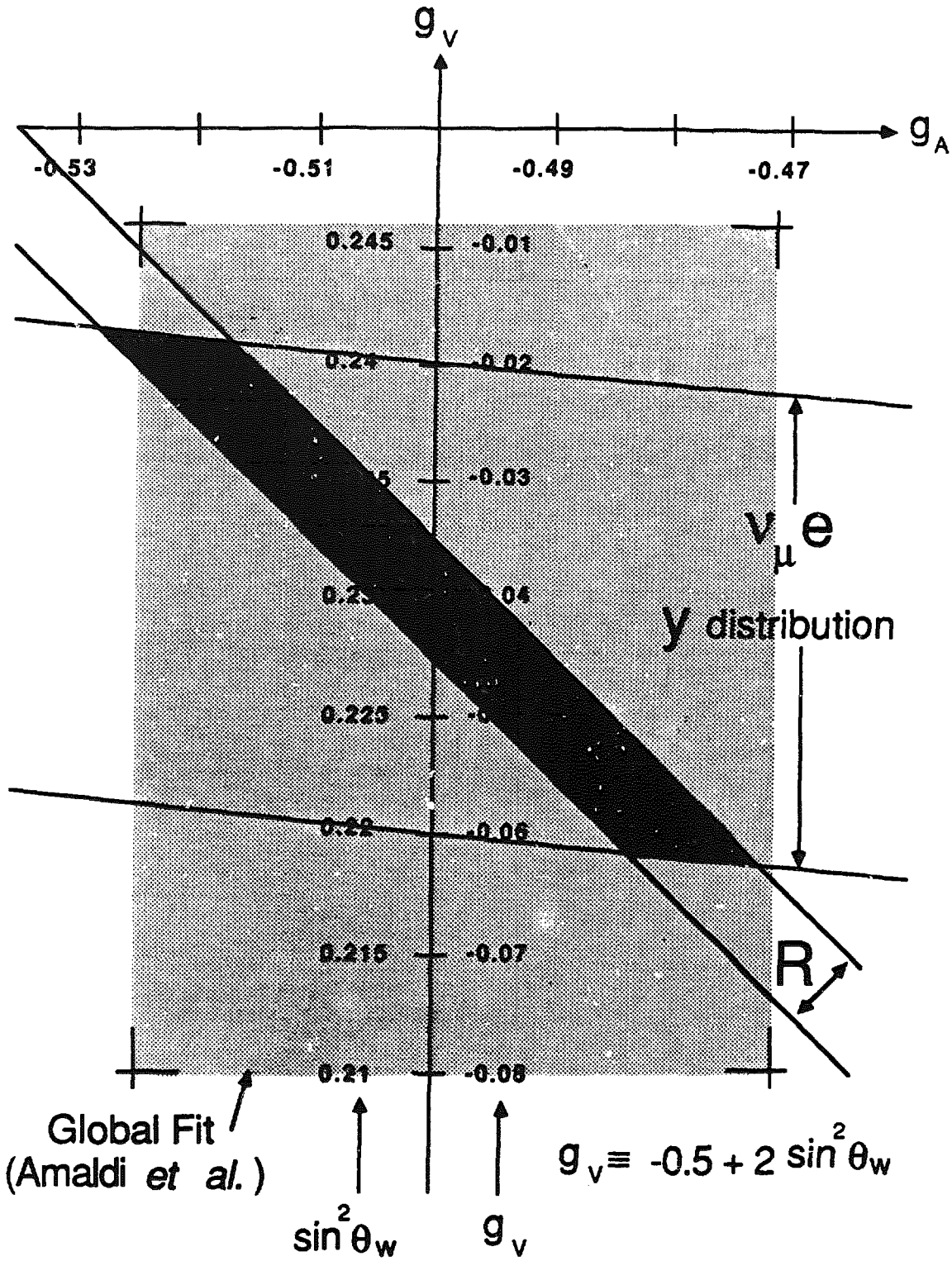

Fig. 2.2. The one-sigma LCD measurement errors in the g_V-g_A plane. The Global Fit (Amaldi *et al.*, Phys. Rev. **D36**, 1385 (1987)) errors are shown as uncorrelated.

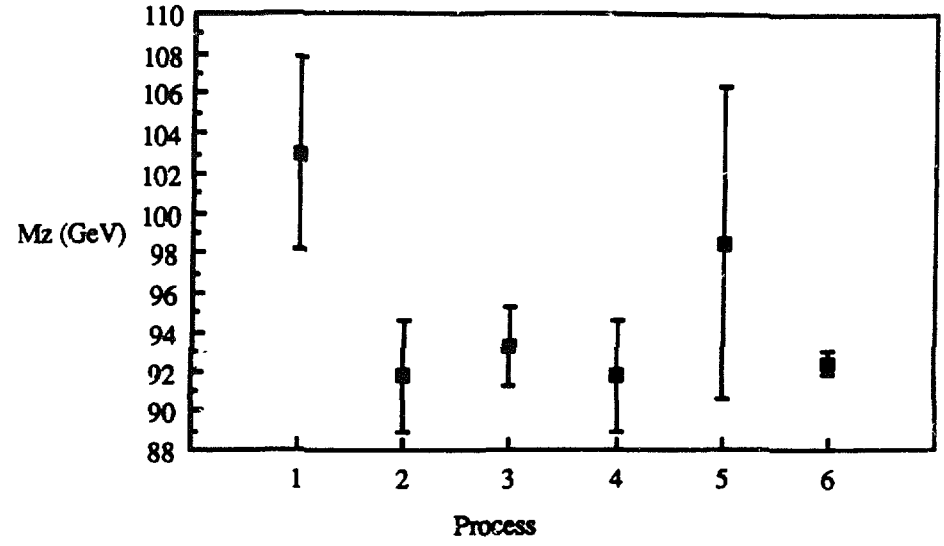

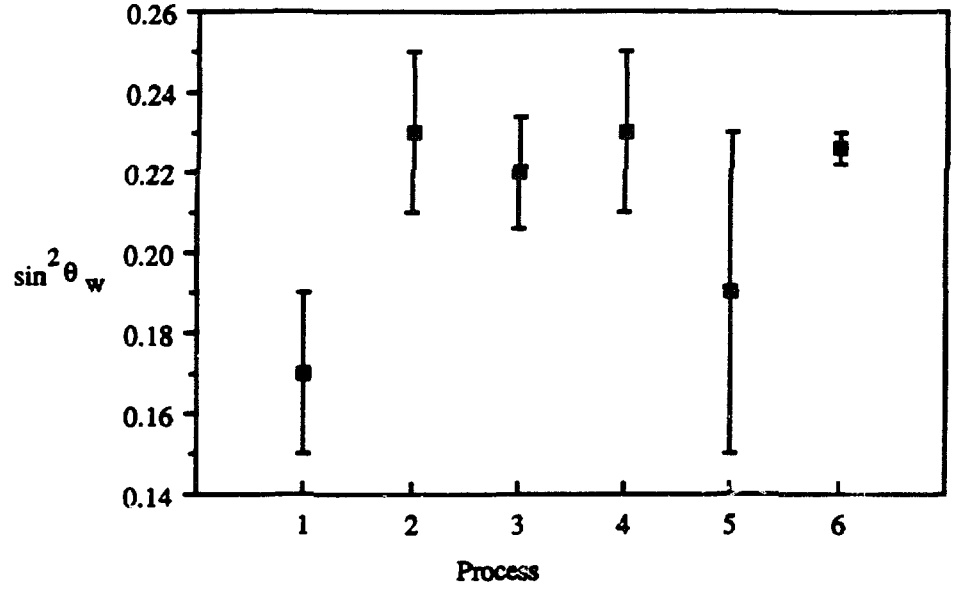

	Process	M_Z (GeV)	ΔM_Z (GeV)	$\sin^2\theta_W$	$\Delta\sin^2\theta_W$
1	$e^+e^-\rightarrow\mu^+\mu^-$	103	4.8	0.17	0.02
2	$\nu(\bar{\nu})p\rightarrow\nu(\bar{\nu})p$	91.8	2.8	0.23	0.02
3	eD asymmetry	93.3	2.1	0.22	0.014
4	$\nu_\mu e\rightarrow\nu_\mu e$	91.8	2.8	0.23	0.02
5	Atomic parity violation	98.5	7.9	0.19	0.04
6	$\nu(\bar{\nu})N\rightarrow\mu X,\nu(\bar{\nu})X$	92.4	0.6	0.226	0.004

Fig. 2.3. Standard Model Parameters as presented by the 1986 Particle Data Group.

2.2 Electroweak Theory

2.2.1 $SU(2)_L \times U(1)$ Standard Model

The minimal $SU(2)_L \times U(1)$ electroweak model has three SU(2) and one U(1) gauge bosons, one Higgs doublet, six quark flavors, and six leptons.[3,4,5] The fermions are grouped into left handed SU(2) doublets and right handed singlets. Each multiplet is assigned a U(1) hypercharge Y so as to satisfy the Gell-Mann - Nishijima relation between the third component of weak isospin $T_{(3)}$, electric charge Q, and Y; namely

$$Q = T_{(3)} + \frac{1}{2}\, Y \quad .$$

The gauge bosons $A_\lambda^{(i)}$ and B_λ appear though SU(2) and U(1) gauge-covariant derivatives acting on the various multiplets, which have the form

$$g \sum_{i=1}^{3} A_\lambda^{(i)}\, T_{(i)} \;+\; g'\, \frac{1}{2}\, Y\, B_\lambda \quad .$$

The parameters in the Lagrangian of the theory after spontaneous symmetry breaking are the coupling constants g and g', the vacuum expectation value v of the neutral Higgs boson, and the masses of the fundamental fermions. The "mass matrix" (the coefficients of the terms quadratic in just the gauge fields) is diagonalized by the linear transformation of the neutral fields given by

$$A_\lambda^{(3)} = \cos\theta_W Z_\lambda + \sin\theta_W A_\lambda$$

$$B_\lambda^{(3)} = \cos\theta_W A_\lambda - \sin\theta_W Z_\lambda$$

with the choice $\tan\theta_W = g'/g$. The charge eigenstates are given by the linear combinations

$$W_\lambda^{\pm} \;=\; -(-A_\lambda^{(1)} \;\pm\; iA_\lambda^{(2)})/\sqrt{2} \quad .$$

These fields are identified with the photon A_λ, the neutral Z boson Z_λ, and the charged W bosons $W_\lambda^{\pm}$, respectively, and have masses m_Z and m_W. (The photon remains massless, protected by the symmetry that remains after the spontaneous symmetry breaking.)

The interactions and currents associated with these vectors are (unless otherwise noted, we use the notation of Ref. 6):

1. The electromagnetic interaction

$$eA_\lambda \; J_\gamma^\lambda$$

and electromagnetic current

$$J_\gamma^\lambda \; = \sum_f \; Q_f \; \bar{\psi}_f \; \gamma^\lambda \; \psi_f$$

where the summation is over the fermions in the theory. (In what follows we will only be interested in the sum over electrons, muons, and their neutrinos.)

2. The weak neutral current interaction

$$\frac{g'}{\sin\theta_W} \; Z_\lambda J_Z^\lambda$$

and weak neutral current

$$J_Z^\lambda = \sum_f \quad \bar{\psi}_f \gamma^\lambda \; [T_{(3)} \; \frac{1}{2} \; (1-\gamma_5) - Q_f \sin^2\theta_W] \; \psi_f \quad .$$

3. The weak charged current interaction

$$\frac{g}{\sqrt{2}} \quad [W_\lambda^+ \; J_{W+}^\lambda \; + \; W^-\lambda \; J_{W-}^\lambda]$$

and weak charged currents

$$J_{W+}^\lambda = \bar{\nu}_e \gamma^\lambda \; \frac{1}{2} \; (1-\gamma_5) e + \bar{\nu}_\mu \gamma^\lambda \; \frac{1}{2} \; (1-\gamma_5) \mu$$

$$J_{W-}^\lambda = \bar{e} \gamma^\lambda \; \frac{1}{2} \; (1-\gamma_5) \nu_e + \bar{\mu} \gamma^\lambda \; \frac{1}{2} \; (1-\gamma_5) \nu_\mu$$

(restricted to electron and muon type leptons).

2.2.2 Renormalization Framework

At the tree level of approximation in perturbation theory (where all momenta are determined from the incident particles' momenta) the parameters g, g', and v

can be related to the electric charge e, masses of the gauge bosons m_W and m_Z, and the electroweak mixing angle θ_W by the relations:

$$g = \frac{e}{\sin\theta_W} \qquad g' = \frac{e}{\cos\theta_W}$$

$$m_Z = \frac{v}{2}\sqrt{g^2 + g'^2} \qquad m_W = m_Z \cos\theta_W$$

$$\frac{g^2}{8m_W^2} = \frac{1}{2v^2} \ .$$

It is well known[7,8] that these relations do not all hold when loop corrections are included. Some relations are valid as identities or definitions, others acquire finite $O(\alpha)$ corrections, and all the relations are renormalization framework dependent. The parameters are renormalized by the interactions to one-loop order and it becomes necessary to precisely define the "framework" the analysis is done in to make comparisons. We adopt Sirlin's[7] "renormalization framework" that uses the physical charge e (or $\alpha = 1/137.036$), the physical mass of the Z boson m_Z, and the muon lifetime τ_μ as the three fundamental parameters of the theory. The remaining renormalized parameters are then derived from these parameters to one-loop order [$O(G_\mu\alpha)$] and are thus gauge invariant and infrared free. Sirlin's framework is described in detail by him in Ref. 7, where he computes to this order the corrections to the gauge bosons and derives the counterterms for the theory. We refer the reader to his paper for details and briefly review here the relationships of the theory's parameters and the neutrino-electron cross sections.

In Sirlin's framework the mixing angle θ_W is chosen so that after writing the bare coupling constants in terms of their renormalized values and the corresponding counterterms, the coefficient of A_λ in the boson mass matrix is zero. The condition to satisfy this is $\tan\theta_W = g'/g$, where the renormalized values for g' and g are used. This is equivalent to the <u>definition</u>

$$\cos\theta_W \equiv \frac{m_W}{m_Z} \ ,$$

where m_Z and m_W are the <u>physical</u> masses of the W and Z bosons. The renormalized g is determined from the <u>physical</u> electric charge e by the <u>definition</u>

$$g \equiv \frac{e}{\sin\theta_W} \ .$$

To complete and close the relationships among the g, g', v, m_W, θ_W, e, m_Z, and G_μ parameters, to one-loop order, the charged-current coupling is defined in terms of the measured muon lifetime. This determines the parameter G_μ in terms

of τ_μ and defines the radiative correction Δr. The muon decay rate predicted by the charged-current interaction including pure QED corrections ("photonic V-A") but not including the W and Z bosonic corrections is given by[9,10]

$$\frac{1}{\tau_\mu} = \left(\frac{G_\mu^2 m_\mu^5}{192\,\pi^3}\right) \times \left[1 - 8\left(\frac{m_e^2}{m_\mu^2}\right)\right] \times \left[1 + \frac{3}{5}\left(\frac{m_\mu^2}{m_w^2}\right) + \frac{\alpha}{2\pi}\left(\frac{25}{4} - \pi^2\right)\right] .$$

This relation should be regarded as defining G_μ in terms of the measured τ_μ and gives the value

$$G_\mu = (1.16632 \pm 0.00002) \times 10^{-5} GeV^{-2} .$$

The one-loop corrections from W and Z exchanges modify the lowest order amplitude by a correction factor (1+Δr), which gives the relation between G_μ (as determined from τ_μ) and g to $O(G_\mu \alpha)$ as

$$\frac{G_\mu}{\sqrt{2}} = \frac{g^2}{8 m_W^2}\,(1 + \Delta r) .$$

In terms of these renormalized parameters we have the useful relations

$$\frac{(g^2 + g'^2)}{8 m_Z^2} = \frac{g^2}{8 m_W^2} = \frac{G_\mu}{\sqrt{2}}\,(1 - \Delta r) ,$$

which will be used below in the discussion of corrections to neutral current processes.

The last remaining parameter, assuming the minimal Higgs doublet, is m_W and is given by

$$m_W^2 = \frac{1}{2}\, m_Z^2 \left(1 + \left(1 - \frac{4}{m_Z^2}\,\frac{\pi\alpha}{\sqrt{2} G_\mu}\,\frac{1}{1 - \Delta r}\right)^{\frac{1}{2}}\right) .$$

The value of $\sin^2\theta_W$ is now given by

$$\sin^2\theta_W \equiv 1 - \frac{m_W^2}{m_Z^2}$$

with m_W given by the above expression.

The detailed formula for Δr is given by Sirlin in Ref. 7. The recent global fit by Amaldi et al.[1] gives the prediction from theory

$$\Delta r = 0.0713 \pm 0.0013$$

for the values $m_{Top} = 45$ GeV and $m_{Higgs} = 100$ GeV. In deriving Δr there are three components[7,11,12,13]: the leptonic term $\Delta r^{(lepton)}$, the hadronic term $\Delta r^{(quark)}$, and

the part coming from the gauge bosons, Higgs boson, and the ghost fields, which are collectively called the bosonic term $\Delta r^{(boson)}$:

$$\Delta r = \Delta r^{(lepton)} + \Delta r^{(quark)} + \Delta r^{(boson)} \quad .$$

The bosonic contributions vary from -0.002 for $m_{Higgs} = 0$ to + 0.01 for $m_{Higgs} =$ 10,000 GeV. For $m_{Higgs} \approx m_Z$, $\Delta r^{(boson)} \approx 0.0015$. The leptonic and hadronic terms arise through self-energy and vacuum-polarization diagrams. The leptonic term can be accurately predicted and is given by $\Delta r^{(lepton)} = 0.0328$. The hadronic contribution is more uncertain due to the effects of the strong interactions at low q^2.

At present the best approach is to use perturbative QCD above a cross over momentum of ≈100 GeV and use a dispersion relation below the cross over momentum.[11,12,13] The hadronic contribution is given by $\Delta r^{(quark)} = \mathrm{Re}[\Pi(0) - \Pi(m_Z^2)]$, where Π is the hadronic vacuum polarization. The imaginary part of Π is given by

$$Im\Pi(-q^2)|_{q^2 \geq 4m_\pi^2} = \frac{\alpha}{3} \; R_{e^+e^-}$$

where

$$R_{e^+e^-} = \frac{\sigma(e^+e^- \rightarrow hadrons)}{\sigma(e^+e^- \rightarrow \mu^+\mu^-)} \quad .$$

This may be related to the real part of Π by a Hilbert transform and is given by

$$\Delta r^{(quark)} = \frac{\alpha}{3} \; m_Z^2 \; Re \int_{4m_\pi^2}^{\infty} \frac{R_{e^+e^-}(x)}{x(x - m_Z^2 + i\epsilon)} \; dx$$

where $-q^2 = x + iy$. Verzegnassi (Ref. 11), Wetzel (Ref. 12), and Marciano and Sirlin (Ref. 13) have carried out this calculation and give the prediction $\Delta r^{(quark)} \approx 0.0262 \pm 0.0024$ with the conservative upper bound of $\Delta r^{(quark)} \leq 0.0311$. This is the dominant source of uncertainty in predicting Δr, but it only contributes a fractional uncertainty of 0.14% in determining the renormalized g, which is negligible for this experiment.

A very large t-quark mass would change the value of Δr by an amount

$$\delta \simeq -\frac{3\alpha}{16\pi} \frac{\cos^2\theta_W}{\sin^4\theta_W} \frac{m_t^2}{m_W^2} \qquad m_t \gg m_W \quad .$$

In fact, a global fit to all determinations of $\sin^2\theta_W$ produces a limit on the t-quark mass of about 180 GeV.[1] A fourth generation of quarks and leptons would affect the estimate of radiative corrections to the intermediate boson masses. However, the radiative corrections depend on the mass splitting between pairs in the

same doublet, which is why a high mass of the t quark implies a significant correction, given that the mass of the b quark is known. It is not possible to put limits on a fourth generation if there is freedom to make the internal splitting in a massive doublet small.

The shift in the radiative correction as a function of the Higgs mass is given by

$$\delta \simeq \frac{11\alpha}{48\pi \sin^2\theta_W} \ln\left(\frac{m_H^2}{m_W^2}\right) - \frac{0.53\alpha^2}{128\pi^2 \sin^4\theta_W} \frac{m_H^2}{m_W^2} \ ,$$

when $m_H \gg m_W$. Numerically,

$$\delta = 2.3 \times 10^{-3} \ln(m_H^2/m_W^2) - 4.2 \times 10^{-7}(m_H^2/m_W^2) \ .$$

If the Higgs mass is 1 TeV, then $\delta = 0.012$.

2.2.3 Neutrino-Electron Scattering

The lowest-order amplitude for neutral-current neutrino-electron scattering is given by[14]

$$M^{(0)} = \frac{i}{2} \frac{g^2 + g'^2}{q^2 - m_Z^2} < e_f|J_Z^\lambda|e_i > L_\lambda \ ,$$

where

$$L_\lambda = \bar{\mu}_{\nu_f} \gamma^\lambda \frac{1}{2} (1 - \gamma_5) \mu_{\nu i}$$

represents the neutrino current, $\mu_{\nu i}$ and $\mu_{\nu f}$ are the initial and final neutrino spinors, and the matrix element of the weak neutral current operator J_Z^λ between initial and final electron states is given by

$$< e_f| J_Z^\lambda|e_i > = -\frac{1}{2} \bar{\mu}_f \gamma^\lambda \frac{1}{2} (1 - \gamma_5)\mu_i + \sin^2\theta_W \bar{\mu}_f \gamma^\lambda \mu_i \ ,$$

where μ_i and μ_f are the initial and final electron spinors. For the following discussion it is convenient to define the corresponding matrix element for the electromagnetic current from the scattered electron by

$$< e_f|J_\gamma^\lambda|e_i > = \bar{\mu}_f \gamma^\lambda \mu_i \ .$$

The O($G_\mu\alpha$) diagrams are illustrated in Fig. 2.4. They may be grouped into vertex, charge radius, γ-Z mixing, boson self-energy, and box diagrams. When summed these amplitudes collect into terms proportional to $< e_f|J_\gamma^\lambda|e_i >$ and terms proportional to $< e_f|J_\gamma^\lambda|e_i >$. The terms proportional to $e_f|J_Z^\lambda|e_i >$ come from

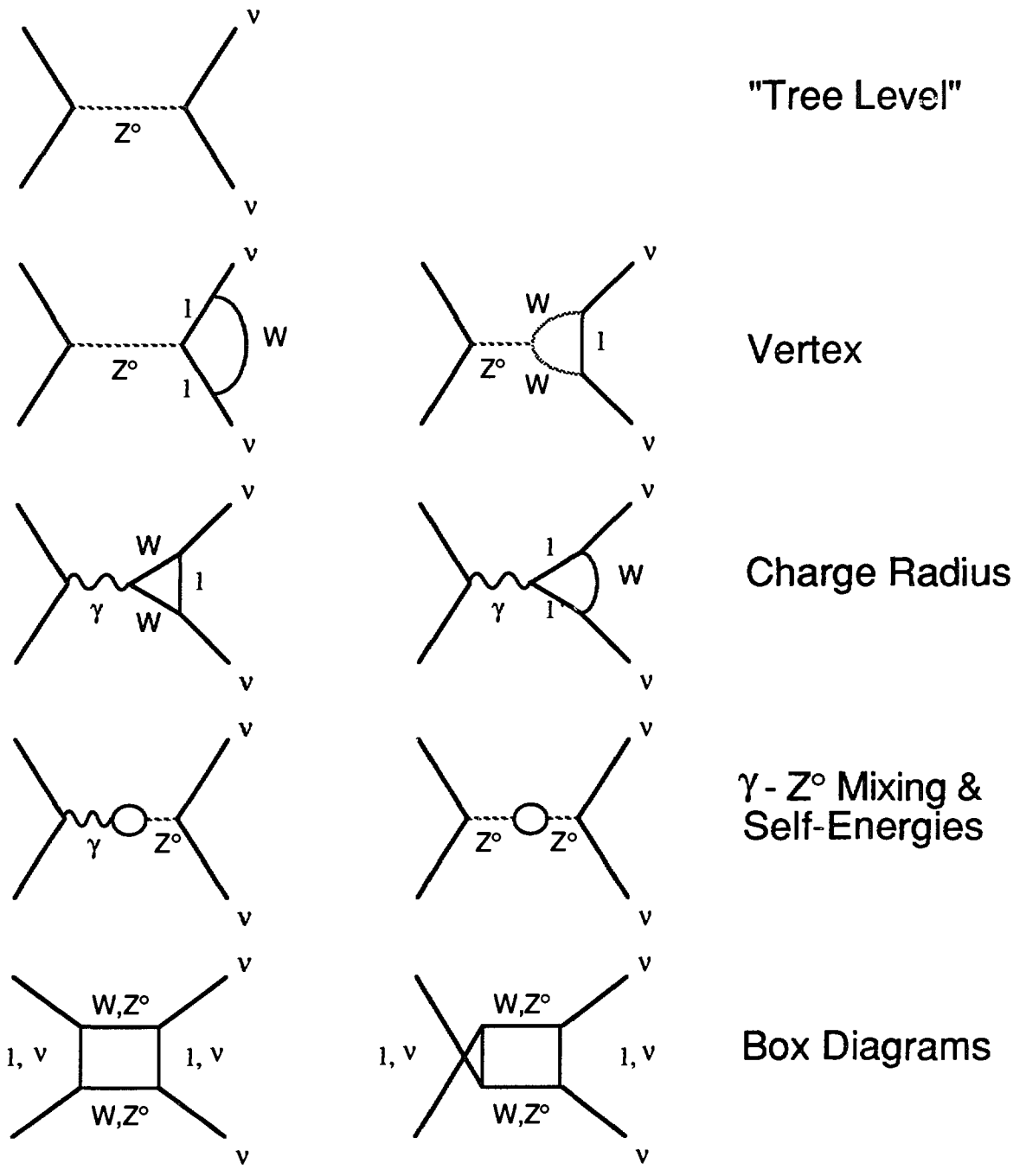

Fig. 2.4. Example diagrams.

vertex, self- energy, and box diagrams, sum to an amplitude that is proportional to $M^{(0)}$, and can be written in the form

$$M^{(0)} + M^{(1)}_{J_Z} = M^{(0)}[1 + \delta_Z(q^2)] \quad .$$

The correction to the coupling constants is shown above and can also be written as proportional to $M^{(0)}$. These corrections may be combined to define a factor $\rho^{(\nu;e)}_{N.C.}$ and the relation

$$M^{(0)} + M^{(1)}_{J_Z} = \overline{M}^{(0)}[1 + \delta_{J_Z}(q^2) - \Delta r] \equiv \rho^{(\nu;e)} J_{N.C.} \overline{M}^{(0)} \quad .$$

In the combination [$\delta_Z(q^2)$ - Δr] there are several cancellations, which we refer the reader to Marciano and Sirlin[14] for details, that render $\rho^{(\nu;e)}_{N.C.}$ less sensitive to hadronic contributions and their uncertainties. Predicted values for $\rho^{(\nu;e)}_{N.C.}$ as a function of m_{Higgs} are shown in Fig. 2.5. A representative value is $\rho^{(\nu;e)}_{N.C.} \approx 1.005$.

The terms proportional to $< e_f|J^\lambda_\gamma|e_i >$ come from vertex, charge radius, γ-Z mixing, and box diagrams. Their sum leads to an amplitude of the form

$$M^{(1)}_{J_\gamma} = \frac{i}{2} \frac{g^2 + g'^2}{q^2 - m_Z^2} < e_f|J^\lambda_\gamma|e_i > L_\lambda \Delta^{(\nu_\ell;e)}(q^2) \sin^2\theta_W \quad .$$

These corrections can be grouped into a factor $\kappa^{(\nu_\ell;e)} = 1 - \Delta^{(\nu_\ell;e)}$ multiplying $\sin^2\theta_W$. The quantity $\Delta^{(\nu_\ell;e)}$ is neutrino-type dependent, due to the charge-radius diagram, and is given by the sum of three terms: bosonic, hadronic, and leptonic

$$\Delta^{(\nu_\ell;e)} = \delta^{(b)}_\theta(q^2) + \delta^{(h)}_\theta(q^2) + \delta^{(\ell)}_\theta(q^2) \quad .$$

For ν_μ-e scattering at $q^2 = 0$: $\delta^{(b)}_\theta(q^2 = 0) = 0.027, \delta^{(h)}_\theta(q^2 = 0) = -0.0186, \delta^{(\ell)}_\theta(q^2 = 0) = -0.00052$ and $\Delta^{(\nu_\mu;e)} = 0.0079$. There is a partial cancellation between the bosonic and hadronic part that is responsible for the small size of the total correction. For ν_e-e scattering $\delta^{(b)}_\theta(q^2 = 0)$ is increased and gives $\Delta^{(\nu_e;e)} = 0.0258$. This distinction between $\Delta^{(\nu_\mu;e)}$ and $\Delta^{(\nu_e;e)}$ is a consequence of the charge-radius diagrams and holds only for $-q^2 < m_\mu^2$, but this is precisely in the kinematic range of this experiment. The variation of $\Delta^{(\nu_\mu;e)}$ with q^2 is shown in Fig. 2.6.

ρ DEPENDENCE ON HIGGS MASS

$$\rho_{N.C.}^{(\nu\mu;l)} - 1$$

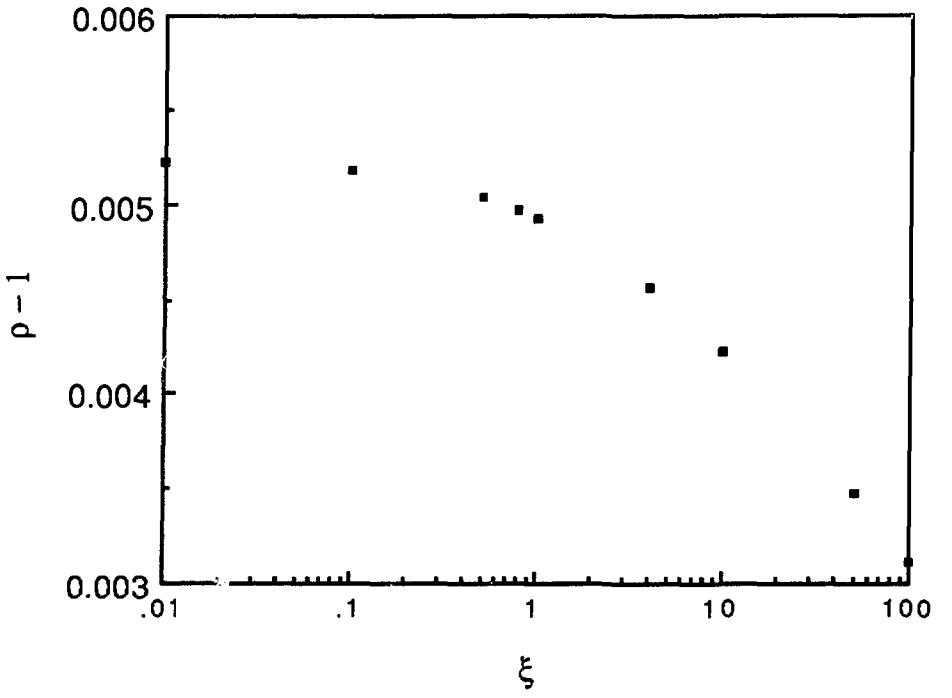

$$\xi = \frac{m_H^2}{m_Z^2}$$

Fig. 2.5. Variation of the neutral current factor ρ as a function of Higgs mass. The above values are for $\sin^2\theta_W = 0.215$ and $m_t = 20$ GeV.

VARIATION OF κ WITH y

$$\kappa_{N.C.}^{(\nu_\mu;l)} - 1$$

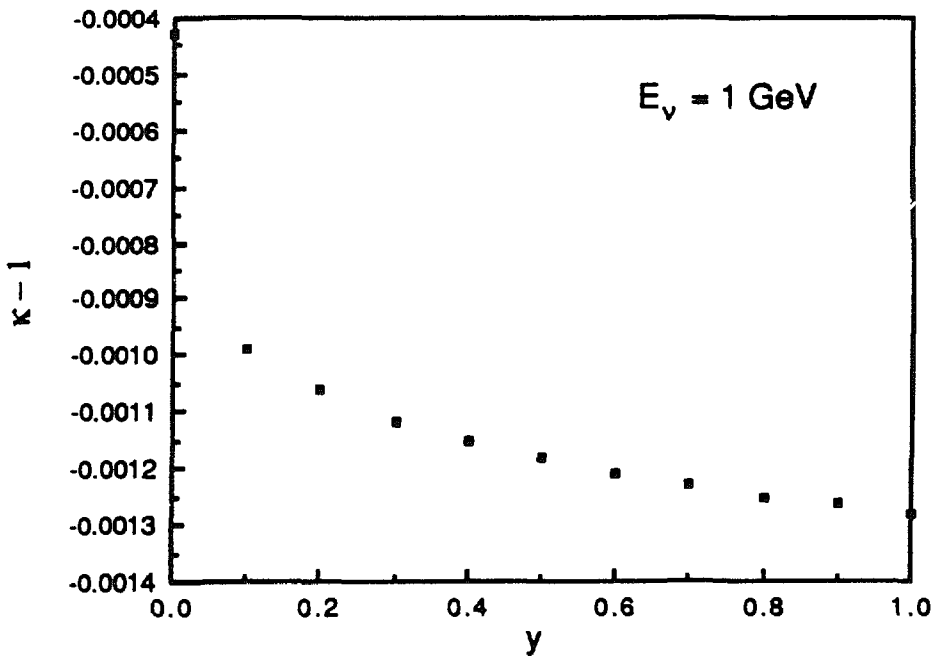

$$y \equiv \frac{E'_e - m_e}{E_\nu} \qquad E_\nu = 1 \text{ GeV}$$

Fig. 2.6. Variation of the parameter κ with fractional momentum transfer y.

The effect of the one-loop corrections on the amplitude for neutral-current neutrino-electron scattering is summarized in the effective amplitude given by:

$$M_{eff} = \rho_{N.C.}^{(\nu;e)} \frac{im_Z^2}{(q^2 - m_Z^2)} \frac{G_\mu}{\sqrt{2}}$$

$$x L_\lambda \left[-\bar{\mu}_f \gamma_\lambda \frac{1}{2} \left(1 - \gamma_5\right) \mu_i + 2\kappa^{(\nu_\ell;e)} \sin^2\theta_W \bar{\mu}_f \gamma_\lambda \mu_i \right] \quad .$$

The cross sections for neutrino-electron scattering using this amplitude have been calculated by Sarantakos, Sirlin, and Marciano[15]. The kinematic variables used to describe the neutrino-electron scattering are shown in Fig. 2.7. For the neutral-current processes of ν_μ-e and $\bar{\nu}_\mu$-e scattering they give

$$\frac{d\sigma}{dy}|_{\nu_\mu e} = \frac{2}{\pi} G_\mu^2 \, [\rho_{N.C.}^{(\nu;\ell)}]^2 \, m_e E_\nu$$

$$x \left[\epsilon_-^2(q^2)\left(1 + \frac{\alpha}{\pi} f_-(y)\right) + \epsilon_+^2(q^2)(1-y^2)\left(1 + \frac{\alpha}{\pi} f_+(y)\right) - \epsilon_-\epsilon_+ \frac{m_e}{E_\nu} y \right]$$

where

$$\epsilon^{(\nu_\mu;e)} = \frac{1}{2}\left(1 - 2\kappa^{(\nu_\mu;e)}(q^2)\sin^2\theta_W\right) \quad ,$$

$$\epsilon_+^{(\nu_\mu;e)} = -\kappa^{(\nu_\mu;e)}(q^2)\sin^2\theta_W \quad ,$$

and $f_\pm$ are the pure QED corrections that were not included in the W and Z boson corrections. The $f_\pm$ are tabulated in Ref. 15 and illustrated here in Fig. 2.8 (which is Fig. 2 from their paper[15]). The $\bar{\nu}_\mu$-e cross section is given by interchanging ϵ_+ with ϵ_- in the above formula.

For the case of ν_e-e scattering there is a charged-current contribution in addition to the neutral current. The lowest order charged-current amplitude is described by simple W_μ^- exchange. The proposed experiments take place at low q^2 so the boson propagators may be replaced by their $q^2 = 0$ values, the product of the charged currents rearranged by a Fierz transformation into charge-retaining form, and combined with the neutral current (see, for example, Itzykson and Zuber[16]). The one-loop corrections to the charged-current interaction separate into two parts: diagrams from virtual photons and inner bremsstrahlung that are identical to the pure QED corrections to a local V-A theory and are described by the $f\pm$ terms; and a class of "photonic" corrections that are identical to the $O(G_\mu\alpha)$ terms as calculated in muon decay and are accounted for by using G_μ and Δr. The cross

SCATTERING KINEMATICS

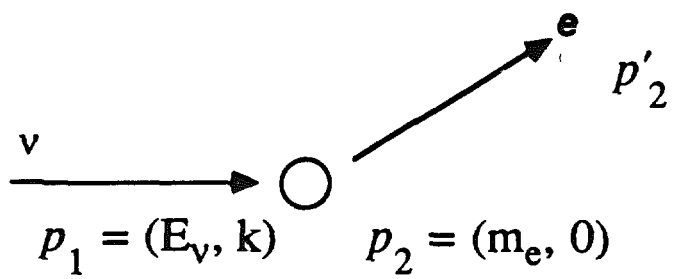

$$(p_1 \bullet p_2) = m_e E_\nu \qquad q^2 = (p_2 - p'_2)^2$$

$$y \equiv \frac{-q^2}{2(p_1 \bullet p_2)} = \frac{E'_e - m_e}{E_\nu}$$

Fig. 2.7. Neutrino-electron scattering kinematic variables.

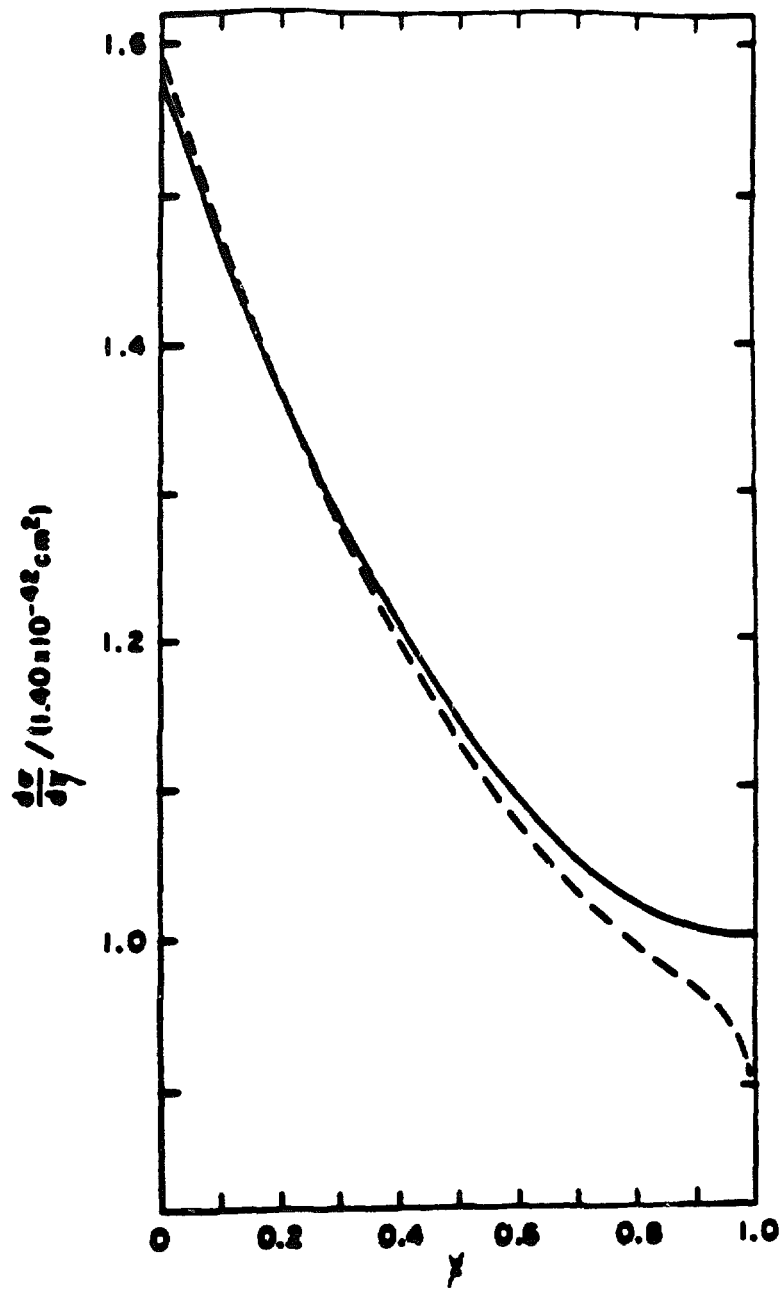

Fig. 2.8. ν_μ e scattering cross section for E_ν = 1 GeV with QED corrections. The dashed curve includes QED and electroweak corrections, the solid curve has only the electroweak corrections included so that their difference illustrates the QED correction.

section for ν_e-e scattering is then given by the replacements

$$\epsilon_-^{(\nu_\mu;e)} \rightarrow \epsilon_-^{(\nu_e;e)} = \frac{1}{2}\left(1 - 2\kappa^{(\nu_e;e)}(q^2)\sin^2\theta_W\right) - \frac{1}{\rho_{N.C.}^{(\nu;e)}}$$

$$\epsilon_+^{(\nu_e;e)} = -\kappa^{(\nu_e;e)}(q^2)\sin^2\theta_W \quad .$$

Note that the interference between the neutral and charged currents appears in the presence of the $-1/\rho_{N.C.}^{(\nu;e)}$ term. This term also prevents the cancellation of the $\rho_{N.C.}^{(\nu;e)}$ between the numerator and the denominator in R_{LCD}.

In summary, the corrections to neutrino-electron scattering are described by

$$\rho_{N.C.}^{(\nu;e)} = 1.0050$$
$$\kappa^{(\nu_\mu;e)}(0) = 0.992$$
$$\kappa^{(\nu_e;e)}(0) = 0.974$$

which can be written in the form

$$\rho = 1 + \Delta\rho \qquad \Delta\rho = 0.005$$
$$\kappa^{(\nu_\mu;e)} = 1 - \Delta\kappa \qquad \Delta\kappa = 0.008$$
$$\kappa^{(\nu_e;e)} = 1 - \Delta\kappa - \delta \qquad \delta = 0.018$$

R_{LCD} is then shifted from the tree-level value by an amount

$$R_{LCD} + \Delta R_{LCD} = \left[1. + 2.33\ \Delta\rho + 1.7\ \Delta\kappa + 0.6\ \delta\right]$$
$$= 1.036$$

which increases R_{LCD} by $\approx$3.6%. This shift should be clearly visible with the proposed 2% measurement precision.

2.3 Effect of E6 Models

Most Grand Unified Theories (GUTS) predict additional gauge bosons beyond the known W and Z bosons. Recent interest has focused on spontaneously broken E6 models due to the connection between supersymmetric E6 models and ten-dimensional superstrings.[17] These E6 models[18,19] predict one or two heavy neutral bosons (Z', Z") carrying exotic U(1) hypercharges and exotic fermions that complete the three 27's of E6 to which the standard quarks and leptons are assigned. The existence of heavy E6 exotic fermions can be detected from precise measurements of νe scattering, polarized electron scattering, atomic parity violation, and the W and Z masses. Furthermore, heavy E6 exotics give effects that are different than those

for the top quark, supersymmetry, or a fourth generation.[19] Below we describe a particular E6 model and show what constraints LCD can place on the heavy exotic bosons and fermions.

Limits on Heavy Exotic Bosons and Fermions

We shall assume a particular E6 model[19] with only one heavy boson, Z'. The Z' hypercharge is parameterized by an angle θ_1, and θ_2 represents the mixing between the Z' and the standard Z. The Z' will modify neutral currents and shift the Z mass by mixing. There also exist three generations of exotic leptons: $(EN)_L$ $(EN')_R$, where each generation has a charge -1 lepton E and two isodoublet partner neutrinos N and N'. The neutrinos may form one Dirac neutrino or two Majorana neutrinos. Also, the lepton E has purely vector neutral currents, as does the neutrino in the Dirac case. The exotic leptons can effect electroweak processes through radiative corrections, the dominant correction being vacuum polarization diagrams involving loops of exotic leptons. Effects due to exotic quarks are much smaller and will not be considered. One signature of E6 is the discrepancy of $sin^2\theta_W$ determinations from different experiments. From m_Z, m_W, and neutrino-electron scattering measurements one can define three nonequivalent definitions of $\sin^2\theta_W$:[19]

$\sin^2\theta_W{}^{(1)} = 1-m_W^2/m_Z^2$, the conventional definition.

$\sin^2\theta_W{}^{(2)} = (37.281\ \text{GeV})^2/m_W^2(1\text{-}\Delta r)$, where Δr is a Marciano-Sirlin parameter[3] for radiative corrections.

$\sin^2\theta_W{}^{(3)}$ extracted from our experimental R, involving two other Marciano-Sirlin parameters[3] for radiative corrections.

In the absence of E6, $\sin^2\theta_W$ will be corrected for the standard radiative effects and all three definitions will be equivalent; however, if E6 is present the three definitions will disagree. Fig. 2.9 shows[19] $\sin^2\theta_W$ as a function of m_E for the particular case $m_N = m'_N = 0.5$ GeV and $\sin^2\theta_W{}^{(1)} = 0.23$. In the figure, plots (1) and (2) are for $\sin^2\theta_W{}^{(2)}$ with and without the effect of a heavy degenerate top quark, and (3) and (4) are similar plots for $\sin^2\theta_W{}^{(3)}$. It is interesting to note that heavy exotics produce the signature: $\sin^2\theta_W{}^{(2)} > \sin^2\theta_W{}^{(1)} > \sin^2\theta_W{}^{(3)}$, while a fourth generation, a heavy top quark alone, or supersymmetry produces the opposite signature: $\sin^2\theta_W{}^{(3)} > \sin^2\theta_W{}^{(1)} > \sin^2\theta_W{}^{(2)}$. In this particular model, LCD should place an upper limit on the charged exotic lepton mass of $m_E < 200$ GeV. Fig. 2.10 shows the effects of a heavy Z' boson on $\sin^2\theta_W{}^{(3)}$, assuming $\sin^2\theta_W{}^{(1)} = \sin^2\theta_W{}^{(2)} = 0.23$ and $\theta_2 = 0$. In the figure, plots (1) and (2) are for $\theta_1 = 0$ and 58°, respectively. Generally, Z' effects are not as large as those due to exotic leptons discussed above, although for large values of θ_1, LCD should set

lower bounds on the Z' mass of $m_{Z'} > 600$ GeV. For other E6 models,[18] LCD may probe mass scales of order 800 GeV.

Comparison With Other Experiments

At present, low-energy experiments such as neutrino-electron scattering, polarized-electron scattering, and atomic-parity violation, can set bounds[18] on additional gauge bosons in the 100-250 GeV range. It is expected[18] that the Fermilab Collider and CHARM II will extend this range to about 400 GeV, and the SSC possibly to 10 TeV. In this context it is interesting to see that LCD should probe up to 600-800 GeV, and possibly will be more sensitive to heavy exotic leptons. A very precise measurement of m_Z does not lessen the importance of performing other electroweak measurements. As shown above, comparisons of $\sin^2\theta_W$ from different experiments help signal the presence of new physics and, once new physics has been observed, help identify the source. Therefore, several independent 1% measurements of $\sin^2\theta_W$ provide a stringent test of the Standard Model and can detect the existence of exotic E6 bosons and leptons.

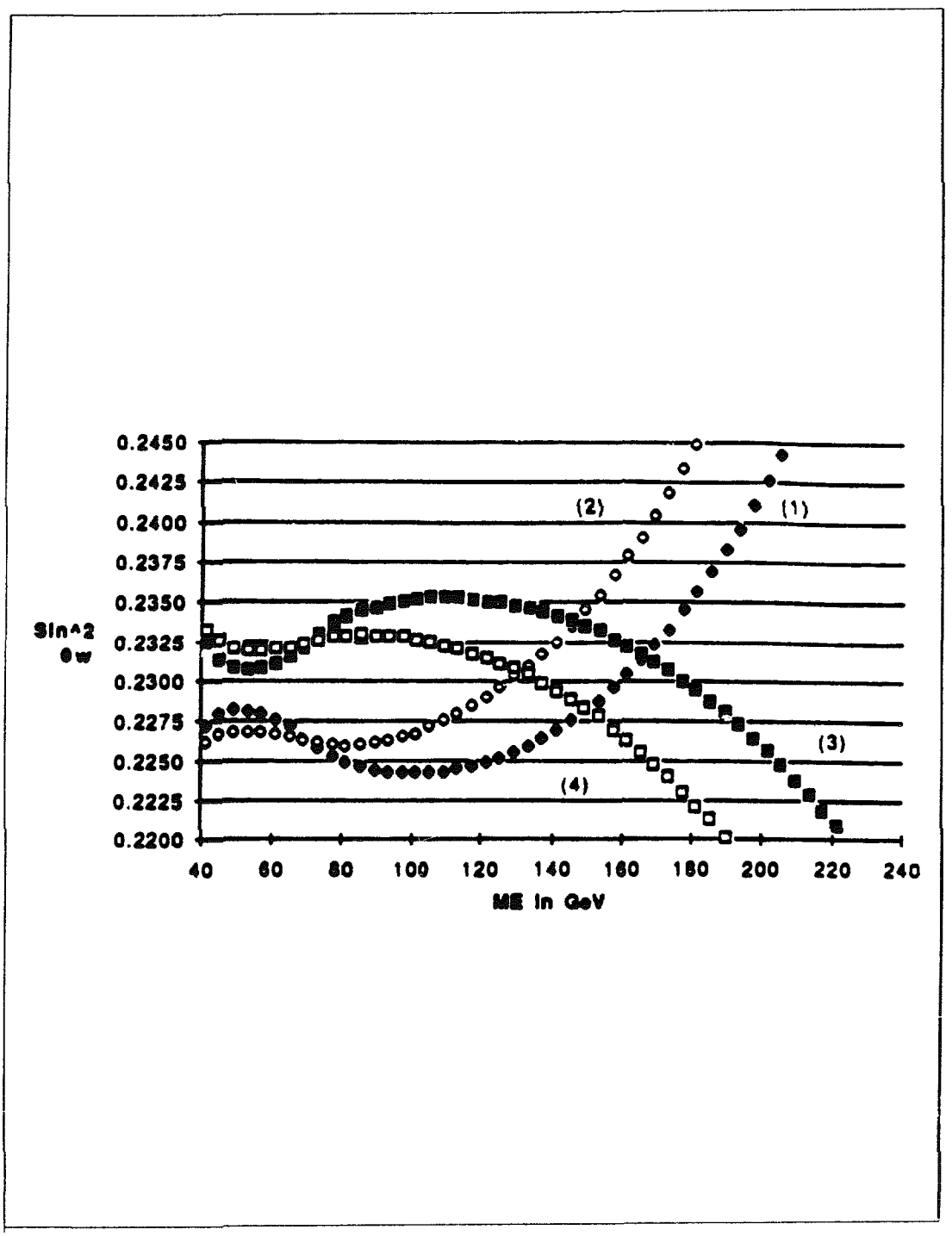

Fig. 2.9. $Sin^2\theta_W$ as a function of m_E for $m_N = m'_N = 0.5\ GeV/c^2$. Plots (1) and (2) are for $\sin^2\theta_W$ [2] with and without the effect of a heavy degenerate top quark, and (3) and (4) are similar plots for $\sin^2\theta_W$ [3] (from reference 19).

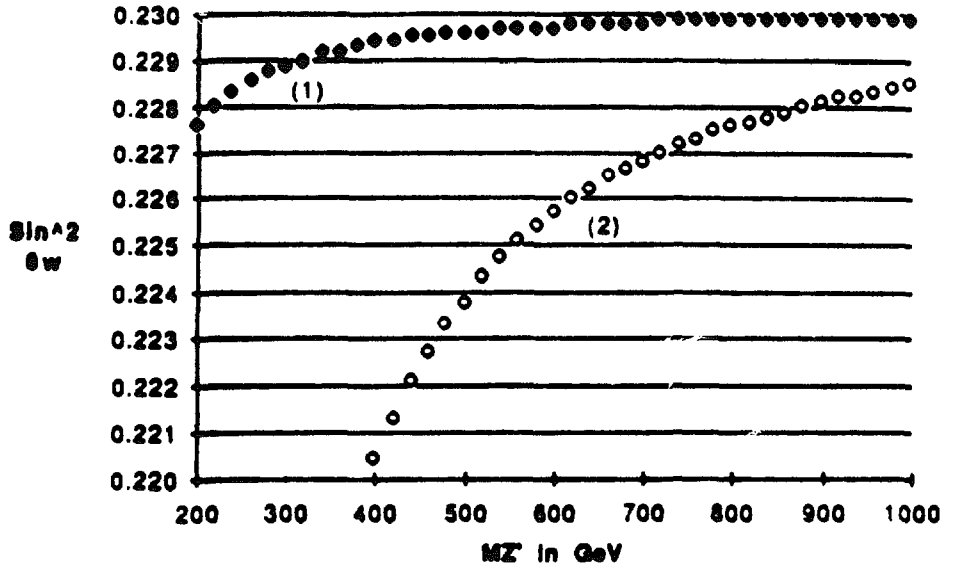

Fig. 2.10. Effects of a heavy Z' boson on $\sin^2\theta_W$ [3]. Plots (1) and (2) are for $\theta_1 = 0^\circ$ and 58°, respectively (from reference 19).

2.4 Model Independent Analysis

In general, the neutrino-electron differential cross section can be written as:

$$d\sigma/dy = G_\mu^2 m_e E_\nu / 2\pi [A + 2B(1-y) + C(1-y)^2] \ ,$$

where y= $(E_e - m_e)/E_\nu$. Scaler, pseudoscaler, tensor, or right-handed couplings will show up as a nonzero B, although B is usually expected to be very small. If we assume only vector and axial-vector couplings, g_V and g_A, then B=0, and A and C are equal to:

for $\nu_\mu e \rightarrow \nu_\mu e$

$$A = (g_V + g_A)^2, \qquad C = (g_V - g_A)^2,$$

for $\bar{\nu}_\mu e \rightarrow \bar{\nu}_\mu e$

$$A = (g_V - g_A)^2, \qquad C = (g_V + g_A)^2,$$

for $\nu_e e \rightarrow \nu_e e$

$$A = (2 + g_V + g_A)^2, \qquad C = (g_V - g_A)^2,$$

for $\bar{\nu}_e e \rightarrow \bar{\nu}_e e$

$$A = (g_V - g_A)^2, \qquad C = (2 + g_V + g_A)^2 \ .$$

Note that in the Standard Model of weak interactions, $g_V = -0.5 + 2\sin^2\theta_W$ and $g_A = -0.5$. However, since LCD is testing the Standard Model, it is interesting to see how well LCD will measure g_V and g_A independent of any other assumptions. Figure 2.2 shows a small portion of the g_V and g_A plane and the one-sigma LCD measurement errors. The constraints are mostly due to our measurement of R and the $\nu_\mu e$ y distribution, although measurements of the absolute neutrino electron elastic cross sections add redundancy. From the figure one sees that in addition to measuring g_V or $\sin^2\theta_W$ to high accuracy, we will also make a precision measurement of g_A and test whether g_A actually equals -0.5.

2.5 Physics at the Z^0

2.5.1 Z^0 Mass Measurement

The Z^0 will be produced copiously at the SLC and LEP electron colliders in the next few years. Measuring the mass of the Z^0 will be a principal concern at these colliders, and we assume a great deal of effort will be focused on reducing the

systematic errors of the determination. The statistical errors will not be important at the expected luminosities. LEP is a conventional electron collider, and we assume that the experience gained at existing colliders will offer a guide to the precision that will be achieved.

At lower energies the mass of the upsilon (Υ) has been measured at CESR and DORIS to an accuracy of 0.2 MeV and an absolute accuracy of 2×10^{-5}. The establishment of this precision depends on the depolarization technique invented at Novosibirsk. In an electron collider the beam becomes transversely polarized through emission of synchrotron radiation, and that polarization may be measured in real time. There are a series of depolarizing resonances that depend on $(g-2)$ for the electron such that if the energy of the beam is at one of these resonances the beam becomes depolarized within a few revolutions. These resonances are sharp, limited mainly by the energy spread in the accelerator, and are equally spaced at 440 MeV. The resonance position establishes the beam energy, and absolute accuracy only involves a relatively small interpolation between resonances, since $(g-2)$ is known well.

At LEP it is probable that this technique will not be applicable because the energy spread in the beam will be sufficient to prevent polarization. However, assuming that at least partial polarization will be feasible, an extrapolation of the Υ experience leads to a precision of 2 MeV. The width of the Z^0 is about 2 GeV, so that systematic problems inherent in understanding the contribution of QED radiative corrections to the line shape will probably dominate the ultimate precision.

The proponents of experiments at LEP claim that a precision of 20 MeV is achievable with depolarization measurements.[20] If the depolarization technique does not work at LEP, then the estimate of the precision is lowered to 50 MeV. Assuming that radiative corrections to the Z^0 mass are taken care of, this reflects into a precision of 0.05% for m_Z and 0.1% for $\sin^2\theta_W$.

At SLC the beam energy at the collision point is to be measured with a magnetic spectrometer.[21] The beams lose about 1 GeV in traversing the arcs from the linac to the collision point, inducing an energy spread of about 80 MeV, so that it is clearly necessary to measure the beam energy at the collision point to maintain precision. Estimates for this measurement are ± 45 MeV, leading to $\pm 0.1\%$ on $\sin^2\theta_W$. We assume that the importance of the measurements of the Z^0 mass are such that enough effort will be expended by both colliders to reach a precision better than $\pm 0.1\%$.

2.5.2 Asymmetry Tests

Another class of processes described by photon and Z^0 exchanges between leptons are the asymmetries in the distributions of $\mu^+\mu^-$ pairs and $\tau^+\tau^-$ pairs produced in e^+e^- annihilations. We take the direction of the e^- as forward and define θ as the angle between the e^- and the outgoing negative μ or τ lepton. The charge forward-backward asymmetry A_{FB} is then defined as the fractional difference between the number of negative μ or τ leptons in the forward and backward hemispheres surrounding the collision,

$$A_{FB} \equiv \frac{\left(\frac{d\sigma}{d\Omega}\right)_{\theta < 90^\circ} - \left(\frac{d\sigma}{d\Omega}\right)_{\theta > 90^\circ}}{\left(\frac{d\sigma}{d\Omega}\right)_{\theta < 90^\circ} + \left(\frac{d\sigma}{d\Omega}\right)_{\theta > 90^\circ}} \ .$$

We also define for the case of polarized electron beams the left-right asymmetry,

$$A_{LR} \equiv \frac{\sigma_L - \sigma_R}{\sigma_L + \sigma_R} \ .$$

For center-of-momentum energies in the range 14 GeV $< \sqrt{s} <$ 46 GeV the cross sections and forward-backward charge asymmetries A_{FB} have been measured by the experiments at PEP and PETRA. They confirm the existence of photon-Z^0 interference at the lowest-order electroweak level, but are limited in precision by their statistical error. The PEP and PETRA results are summarized in Figs. 2.11 and 2.12. LEP and SLC will extend these measurements to $\sqrt{s} \sim m_Z$, where the systematic errors are expected to be the limiting factors. The resonance production of the Z^0 compensates for the $1/s$ fall in the cross sections, and thus statistical errors are not expected to dominate. Also, at LEP and SLC the development of longitudinally polarized beams will allow for the measurement of the left-right asymmetry A_{LR} and will improve the sensitivity to A_{FB}. These tests are expected to provide high-statistics measurements of the electroweak parameters with precisions at the one-loop level.[22,23,24]

The production cross section for a lepton pair $l\bar{l}$ (where l is either a μ or a τ) above threshold may be written

$$\frac{d\sigma}{d\Omega} = \frac{\sigma_0}{4\pi} R_{ll} \left[\frac{3}{4}(1 + \cos^2\theta) + 2A_{ll}\cos\theta\right] \ ,$$

where

$$\sigma_0 \equiv \frac{4\pi\alpha^2}{3\ s}$$

is the "point" QED cross section, the coefficient R_{ll} is the ratio of the total cross section to the point cross section, and A_{ll} is the forward-backward asymmetry. These, to lowest order, are given by

$$R_{ll} = 1 - 2\nu_e\,\nu_l\ \mathrm{Re}\ \chi + (\nu_e^2 + a_e^2)(\nu_l^2 + a_l^2)\mid \chi \mid^2$$

and

$$A_{ll} = \frac{3}{8R_{ll}}(-4a_e\,a_l\ \mathrm{Re}\ \chi + 8\nu_e\nu_l\,a_e a_l \mid \chi \mid^2)\ ,$$

and (assuming lepton universality) the neutral-current couplings are

$$\nu_e = \nu_l = \sin^2\theta_W - \frac{1}{4} = -0.020 \qquad \text{for } \sin^2\theta_W = 0.23$$

and

$$a_e = a_l = -\frac{1}{4}\ ,$$

χ is the Z^0 propagator

$$\chi = \frac{G_\mu(1-\Delta r)}{8\sqrt{2}\,\pi\alpha}\,\frac{m_Z^2 s}{s - m_Z^2 + i m_Z\,\Gamma_Z}\ .$$

The Breit-Wigner form is used to describe the resonant behavior at $\sqrt{s} = m_Z$. For small variations of s about m_Z^2, the Breit-Wigner form is an adequate approximation to the full Z^o propagator, but for more detailed calculations the width must be replaced with the one-particle irreducible Z^o self-energy $\Pi_{ZZ}(s)$.[25] We note that $\mathrm{Re}\Pi_{ZZ}(s = m_Z^2) = 0$. The width (i.e., the imaginary part of Π_{ZZ}) may be estimated by summing the partial rates for the Z^0 to decay into neutrinos (no electric charge), charged leptons (unit electric charge), or quarks (1/3 or 2/3 fractional electric charge),[5] and is given by

$$\Gamma_Z = 3\Gamma_{\nu\bar{\nu}} + 3\Gamma_{l\bar{l}} + 9\Gamma_{u\bar{u}} + 9\Gamma_{d\bar{d}}\ ,$$

where the partial rates are

$$\Gamma_{ff} = \frac{G_\mu\,m_Z^3}{24\sqrt{2}\,\pi}(1 + a_{ff}^2)\ ,$$

as shown in Table 2.1.

Table 2.1. Z^o Partial Widths

ff	a_{ff}	$1 + a_{ff}^2$ (Using $\sin^2\theta_W = 0.23$)
$\nu\bar{\nu}$	1	2
$l\bar{l}$	$1 - 4\sin^2\theta_W$	1.0064
$u\bar{u}$	$1 - 8/3\sin^2\theta_W$	1.150
$d\bar{d}$	$1 - 4/3\sin^2\theta_W$	1.480

These rates are proportional to $(v^2 + a^2)$ and are dominated by the axial-vector coupling. (We will use the 1986 Particle Data Group's values $m_Z = 92.5$ GeV and $\Gamma_Z = 2.8$ GeV.) The cross section into a definite final state is then given by

$$\sigma(ff) = \frac{12\pi s}{m_Z^2} \frac{\Gamma_{ee}\,\Gamma_{ff}}{(s - m_Z^2)^2 + \Gamma_Z^2\, m_Z^2} \ .$$

In particular, at $s = m_Z^2$ the branching ratio for decay into μ's or τ's is 4×10^{-2}.

The Z^0 propagator shown above includes the $O(\alpha)$ radiative corrections relating muon decay, electric charge renormalization, and W and Z^0 self-energies in the form of the $(1 - \Delta r)$ factor multiplying G_μ. The Δr correction is defined by the relation

$$\sqrt{2}\, G_\mu (1 - \Delta r) = \pi\alpha \frac{m_Z^2}{m_W^2 (m_Z^2 - m_W^2)} \ ,$$

which is described in more detail in Section 2.2 and has the value $\Delta r = 0.0713 \pm 0.0013$ (as calculated in the Standard Model with $m_t = 45$ GeV and $m_H = 100$ GeV). The tree-level charge asymmetry and the cross section represented by the above equations with the Δr corrections are shown in Figs. 2.13 and 2.14, respectively.

Higher-order corrections have been calculated by several groups.[25] These include initial- and final-state radiation, vertex corrections, self-energies, and leptonic and hadronic vacuum polarization. When comparing measurements the term "radiative corrections" needs to be defined by the experiment reporting the measurement. The QED box diagrams and vertex corrections are usually included in the experiment's reported number. This is because the detector resolution and soft photon threshold to bremsstrahlung must be known to cancel the divergent QED

self energies and vertex corrections. Caution is advised in making comparisons with experimental and theoretical numbers to make sure a class of corrections has not been either over counted or left out. For the case of collisions at SLC and LEP the bremsstrahlung of a photon off of an incident electron or positron (that is, initial-state radiation) has a marked effect on the line shape of the Z^0 cross section, particularly above the Z^0 peak. There is a large probability of radiating a photon by an incident electron or positron that reduces the remaining energy. The effect on A_{LR} is to reduce the asymmetry for $\sqrt{s} > m_Z$ and to distort the line shape for $\sqrt{s} \sim m_Z$. This is illustrated in Fig. 2.15, illustrating the various one-loop corrections as calculated in Ref. 25. The detailed line shape will depend on the full detector Monte Carlo — in particular the effects of soft and hard photons.

The beam energies at SLC and LEP are expected to be known to 35–45 MeV. At SLC the beam will be measured by an external magnetic spectrometer after the interaction region. There is also the possibility of using a polarized electron beam and its spin precession in the arcs of SLC to provide an independent absolute energy calibration with a precision of a few tens of MeV. The LEP machine's orbit dynamics (the chromaticity, positional accuracy, and the precision of the magnetic field in the ring) are expected[22] to yield a similar energy resolution. LEP also expects to transversely polarize the electron and positron beams through the Sokolov-Ternov effect (the asymmetry in the spin flip from emission of photons from electrons in a magnetic field) and to use the method of spin-precession resonance. There exists some question as to the effect of machine resonances (separated by $\approx$400 MeV) on the transverse polarization in the rather broadband LEP machine. On either machine, the uncertainty in the beam energy will add a systematic uncertainty to the measurement of m_Z of $\Delta m_Z \approx \pm 35 - \pm 50$ MeV.

At PEP and PETRA energies the $|\chi|^2$ term may be neglected and the asymmetry is proportional to

$$A_{FB} \propto -a_e\, a_\ell\, s \ ,$$

which is sensitive to the axial-vector couplings only. As shown in Figs. 2.11 and 2.12, these experiments were dominated by statistical errors, which is not expected to be the case at the Z^0 resonance. It is useful to examine the sources of their systematic errors to gauge what is to be expected from the detectors at SLC and LEP. The systematic errors common to the PEP and PETRA experiments consist of the following: background contamination $\approx$1%, detector simulation (that is, Monte Carlo) and analysis uncertainty $\approx$1%, detector asymmetries $\approx$0.5%, higher-order QED-induced asymmetries $\approx$0.5%, and hadronic vacuum polarization uncertainties $\approx$0.5%.

At $\sqrt{s} = m_Z$ the forward-backward asymmetry for an unpolarized beam can be written

$$A_{FB} = \frac{3a_e\,\nu_e\,a_l\,\nu_l}{(a_e^2+\nu_e^2)(a_l^2+\nu_l^2)} \simeq 0.038 \ ,$$

which is quadratic in the vector and axial-vector couplings and rather insensitive because of the two factors of the vector coupling, note: $\Delta \sin^2\theta_W \approx 0.5\ \Delta A_{FB}$.

For polarized beams we have

$$A_{LR}(m_Z) = \frac{2a_e\,\nu_e}{a_e^2+\nu_e^2} \simeq 0.21$$

and

$$A_{FB}(P) = \frac{P}{A_{LR}}\,A_{FB}(P=0) \ ,$$

where the polarization is given by

$$P = \frac{p_e + A_{LR}}{1 + p_e\,A_{LR}}$$

(p_e is the beam polarization). These expressions are proportional to the vector coupling. For 45% electron polarization and $10^5 Z^0$'s (producing 40 000 μ-pairs), a statistical precision of $\Delta A_{LR} = 0.035$ and $\Delta A_{FB} = 0.016$ can be attained. The systematic errors for these asymmetries will be quite different. A_{FB} varies much more rapidly with s than A_{LR}, so that A_{FB} is more sensitive to uncertainties in beam energy and initial-state radiation corrections. A_{LR} will depend on the degree of polarization (initially to be $\approx$45% and expected to improve to 100%) and its resolution $\Delta p/p$ (initially $\approx$5%, but will have to be reduced to 1% to be sensitive to one-loop corrections).

In summary, these asymmetry measurements made at $\sqrt{s} = m_Z$ will test the Standard Model at the one-loop level. This is assuming all goes well with the commissioning of the machines, achieving the planned-for luminosity, and keeping the systematics under control.

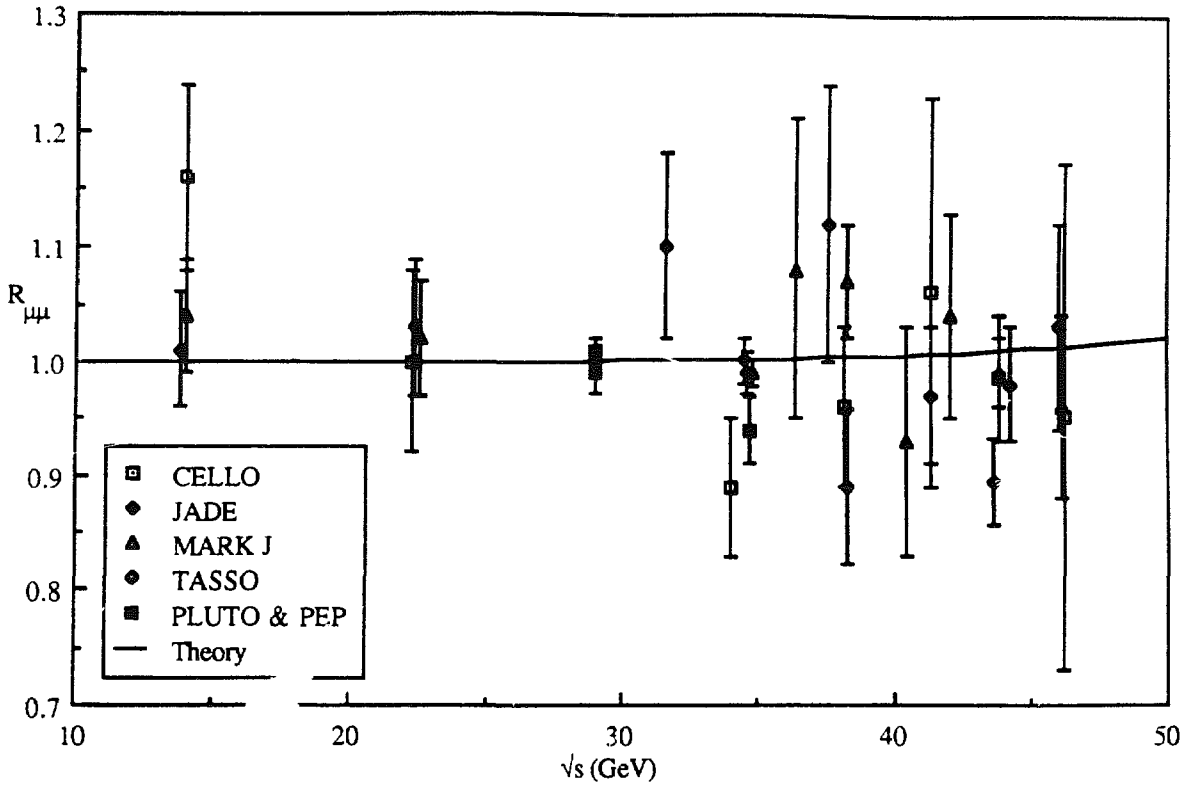

$R_{\mu\mu}$ Summary

Group	√s(GeV)	$R_{\mu\mu}$	±stat.	±syst.	$R_{\mu\mu}$(theory)
CELLO	14	0.0116	0.0008	0.0005	1
	22.2	0.01	0.0008	0.0005	1
	34	0.0089	0.0006	0.0005	1.002
	38.2	0.0096	0.0007	0.0004	1.005
	41.3	0.0106	0.0017	0.0004	1.007
	43.8	0.00985	0.00055	0.0004	1.01
	46.2	0.0095	0.0022	0.0004	1.013
JADE	13.8	0.0101	0.0005	0.0005	1
	22.3	0.0103	0.0006	0.0005	1
	31.6	0.011	0.0008	0.0005	1.002
	34.6	0.00991	0.00018	0.0005	1.003
	37.6	0.0112	0.0012	0.0005	1.004
	41.3	0.0097	0.0006	0.0005	1.007
	44.2	0.0098	0.0005	0.0005	1.01
	46	0.0103	0.0009	0.0005	1.013
MARK J	14	0.0104	0.0005	0.0004	1
	22.5	0.0102	0.0005	0.0004	1
	34.8	0.0099	0.00012	0.0003	1.003
	36.4	0.0108	0.0013	0.0003	1.004
	38.3	0.0107	0.0005	0.0003	1.005
	40.4	93	0.001	0.0003	1.006
	42	0.0104	0.0009	0.0003	1.008
	43.8	0.0099	0.0003	0.0003	1.01
	46.1	0.0096	0.0008	0.0003	1.013
PLUTO	34.7	0.0094	0.0003	0.0004	1.003
TASSO	34.5	0.01112	0.0002	0.00035	1.003
	38.3	0.00889	0.00068	0.00052	1.005
	43.6	0.00894	0.00037	0.00048	1.009
HRS	29	0.0099	0.00017	0.0003	1.001
MARK II	29	0.01002	0.00013	0.00016	1.001
MAC	29	0.0101	0.0001	0.0003	1.001

Fig. 2.11 (a). DESY and PEP summary of cross section ratios.

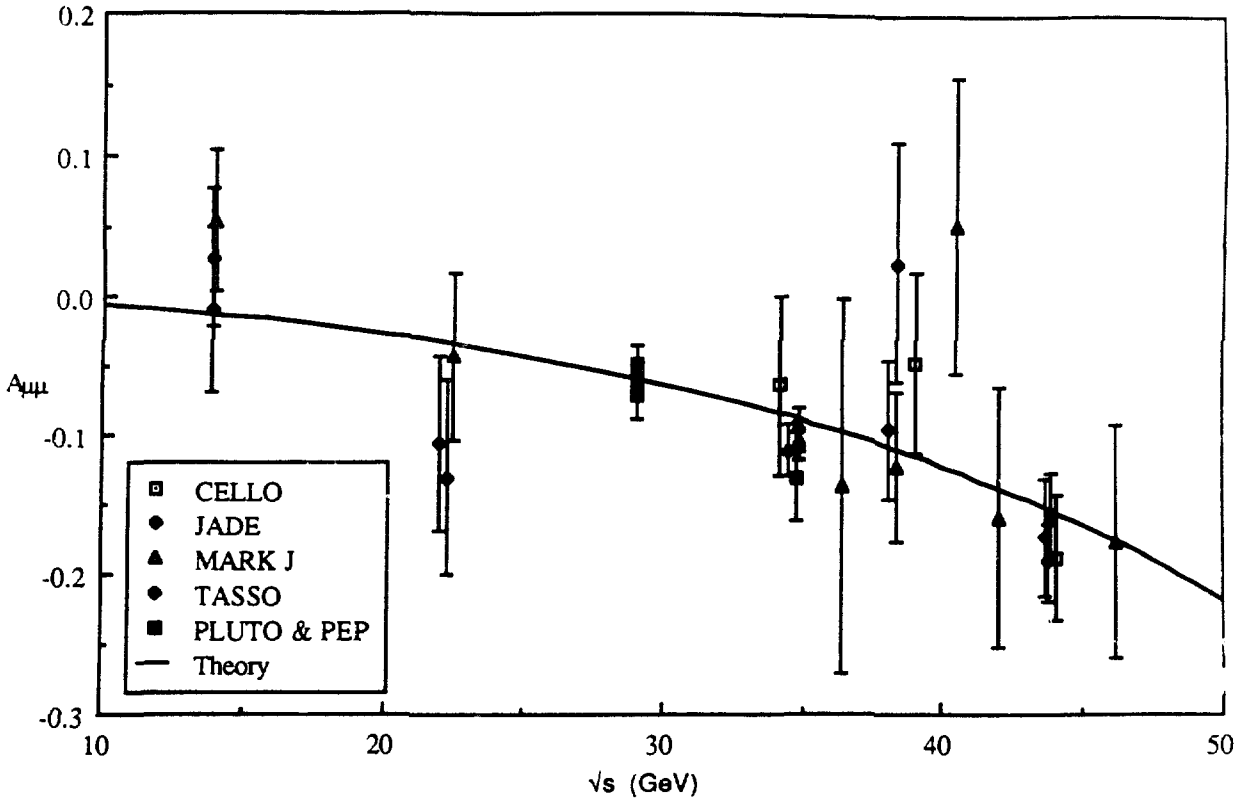

$A_{\mu\mu}$

Group	√s(GeV)	$A_{\mu\mu}$	± stat.	± syst.	$A_{\mu\mu}$(theory)
CELLO	34.2	-0.064	0.064		-0.085
	39	-0.048	0.065	0.01	-0.115
	44	-0.188	0.045	0.01	-0.155
JADE	13.9	0.027	0.049	0.01	-0.012
	22	-0.106	0.064	0.01	-0.032
	34.4	-0.111	0.018	0.01	-0.086
	38	*-0.097*	*0.05*	*0.01*	*-0.108*
	43.7	-0.191	0.028	0.01	-0.153
MARK J	14	0.053	0.05	0.005	-0.013
	22.5	-0.043	0.061	0.005	-0.034
	34.8	-0.104	0.013	0.005	-0.088
	36.4	-0.136	0.135	0.005	-0.098
	38.3	-0.123	0.053	0.005	-0.11
	40.4	0.05	0.105	0.005	-0.126
	42	-0.159	0.093	0.005	-0.138
	43.8	-0.156	0.03	0.005	-0.154
	46.1	-0.176	0.083	0.005	-0.175
PLUTO	34.7	-0.13	0.032	0.01	-0.088
TASSO	13.9	-0.01	0.06		-0.012
	22.3	-0.13	0.07		-0.033
	34.8	-0.096	0.015	0.005	-0.088
	38.3	0.024	0.086	0.005	-0.11
	43.6	-0.173	0.043	0.005	-0.152
HRS	29	-0.049	0.015	0.005	-0.058
MARK II	29	-0.071	0.017		-0.058
MAC	29	-0.057	0.008	0.002	-0.058

Fig. 2.11 (b). DESY and PEP summary of charge forward-backward asymmetry.

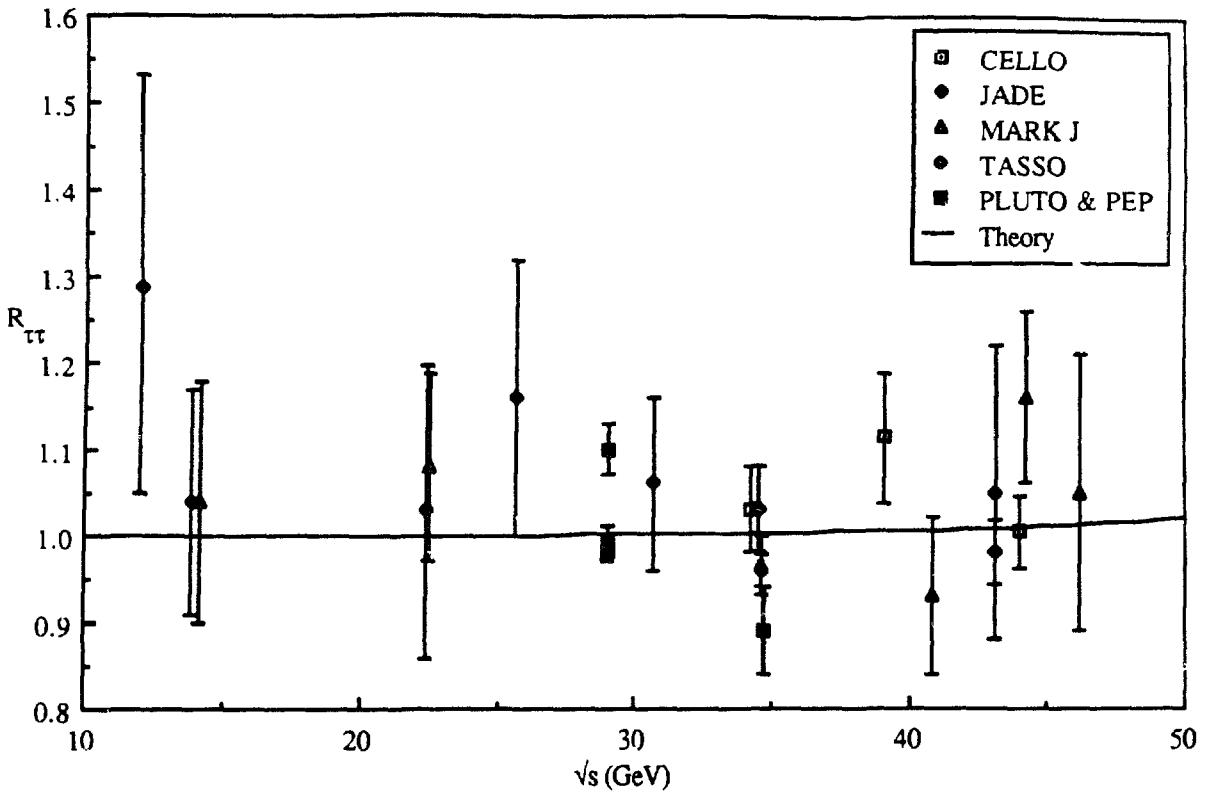

$R_{\tau\tau}$ Summary

Group	√s(GeV)	$R_{\tau\tau}$	± stat.	± syst.	$R_{\tau\tau}$(theory)
CELLO	34.2	1.03	0.05	0.07	1.003
	39	1.114	0.076	0.06	1.005
	44	1.004	0.041	0.052	1.01
JADE	12	1.29	0.24	0.2	1
	25.6	1.16	0.16	0.11	1.001
	30.6	1.06	0.1	0.08	1.001
	34.6	0.959	0.019	0.033	1.003
	43.1	0.98	0.037	0.041	1.009
MARK J	14.1	1.04	0.14	0.04	1
	22.4	1.08	0.11	0.03	1
	34.6	0.965	0.033	0.03	1.003
	40.8	0.93	0.09	0.03	1.006
	44.2	1.16	0.1	0.03	1.01
	46.1	1.05	0.16	0.03	1.013
PLUTO	34.7	0.89	0.05	0.08	1.003
TASSO	13.9	1.04	0.13		1
	22.3	1.03	0.17		1
	34.5	1.03	0.05	+.06 -.11	1.003
	43.1	1.05	0.17		1.009
HRS	29	1.1	0.03	0.04	1.001
MARK II	29	0.996	0.016	0.028	1.001
MAC	29	0.98	0.01	0.034	1.001

Fig. 2.12 (a). DESY and PEP summary of cross section ratios.

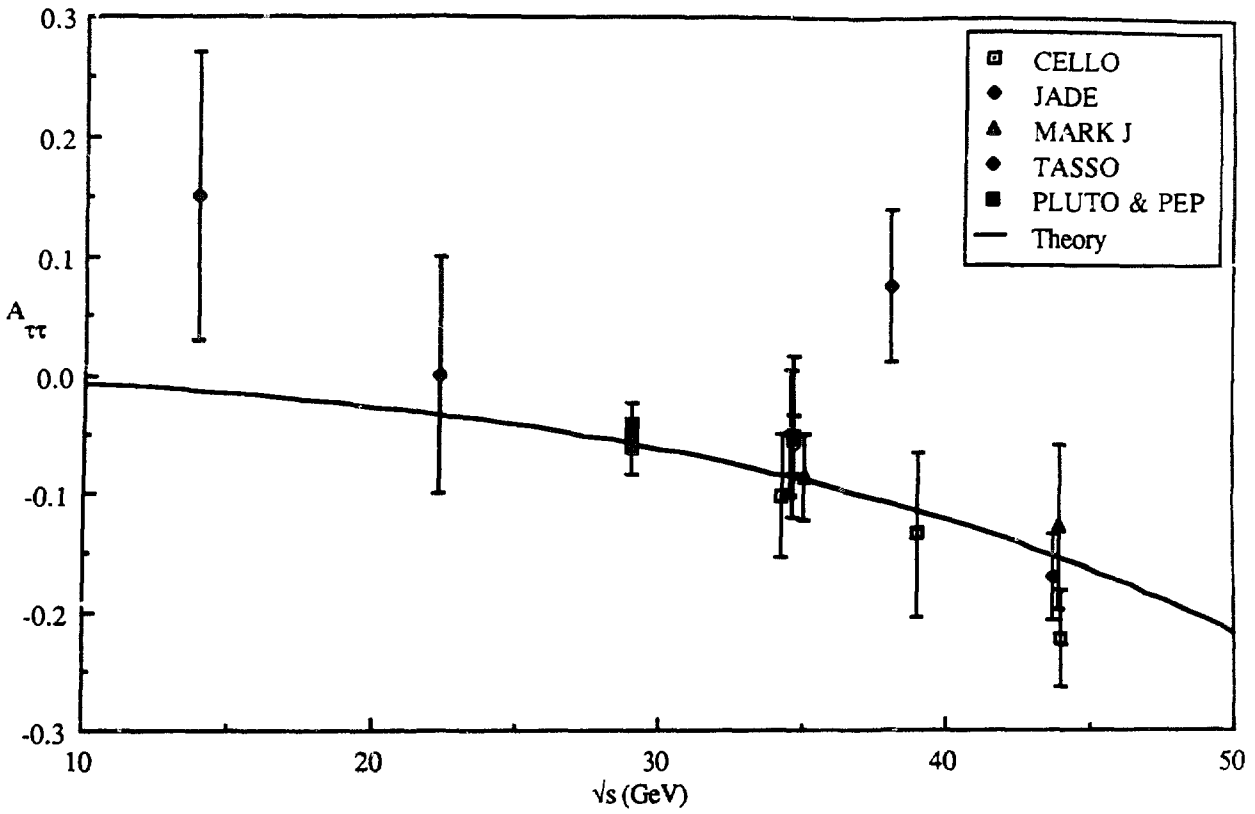

$A_{\tau\tau}$

Group	√s(GeV)	$A_{\tau\tau}$	± stat.	± syst.	$A_{\tau\tau}$(theory)
CELLO	34.2	-0.103	0.052		-0.085
	39	-0.135	0.069	0.02	-0.115
	44	-0.223	0.041	0.02	-0.155
JADE	34.6	-0.06	0.025	0.01	-0.087
	38	0.075	0.063	0.01	-0.108
	43.7	-0.17	0.036	0.01	-0.153
MARK J	35	-0.086	0.037	0.015	-0.089
	43.9	-0.128	0.07	0.015	-0.154
PLUTO	34.6	-0.052	0.068	+0, -.025	-0.087
TASSO	13.9	0.15	0.12		-0.012
	22.3	0	0.1		-0.033
	34.5	-0.049	0.053	0.012	-0.086
HRS	29	-0.061	0.023	0.005	-0.058
MARK II	29	-0.042	0.02		-0.058
MAC	29	-0.049	0.012	0.005	-0.058

Fig. 2.12 (b). DESY and PEP summary of charge forward-backward asymmetry.

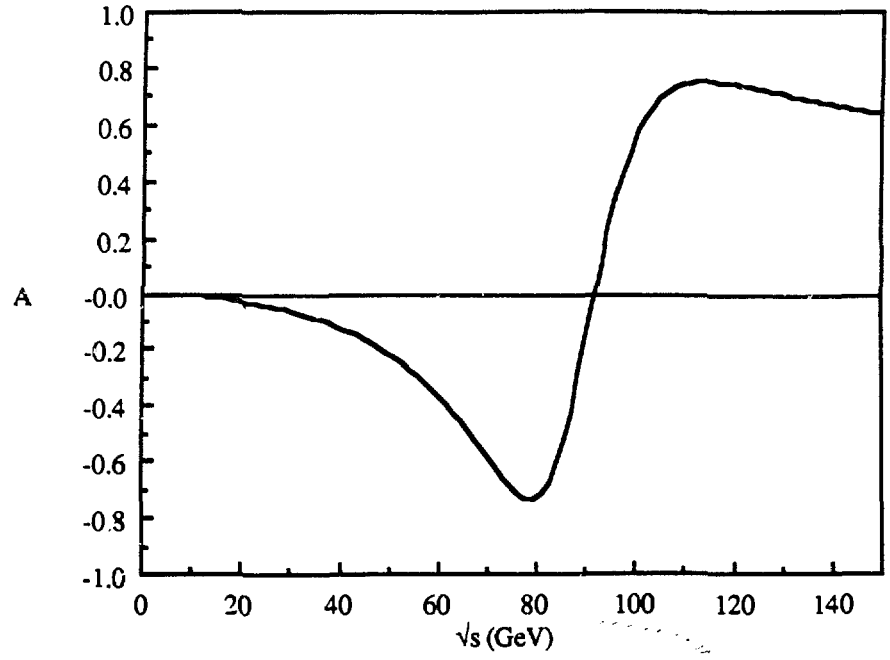

Fig. 2.13. Lepton charge asymmetry to lowest order, i.e., without radiative corrections.

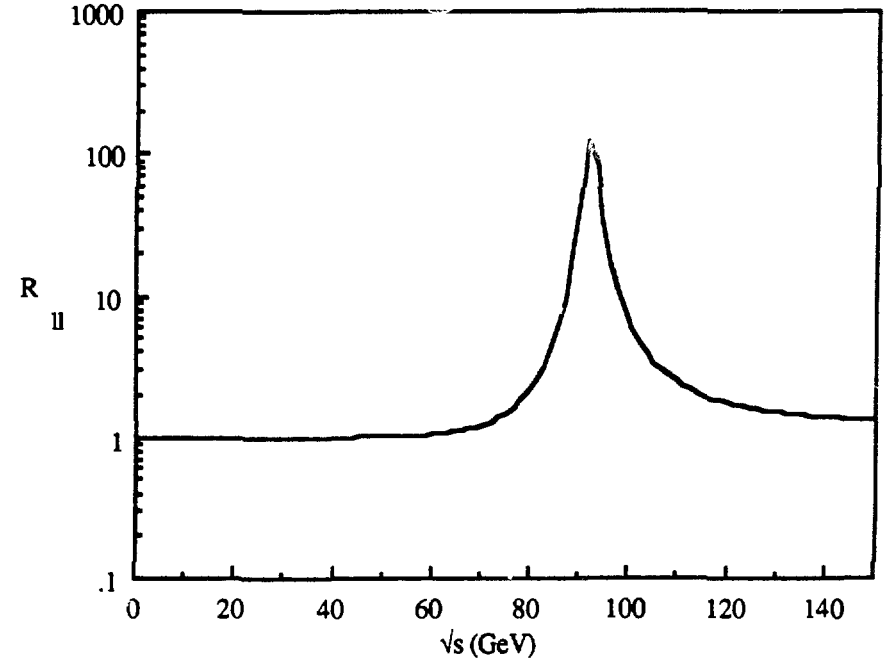

Fig. 2.14. Cross section ratio: $R = \sigma_{ll} / \sigma_{QED}$.
The values $m_Z = 91.9$ GeV and $\Gamma_Z = 2.8$ GeV were used in the two graphs shown on this page.

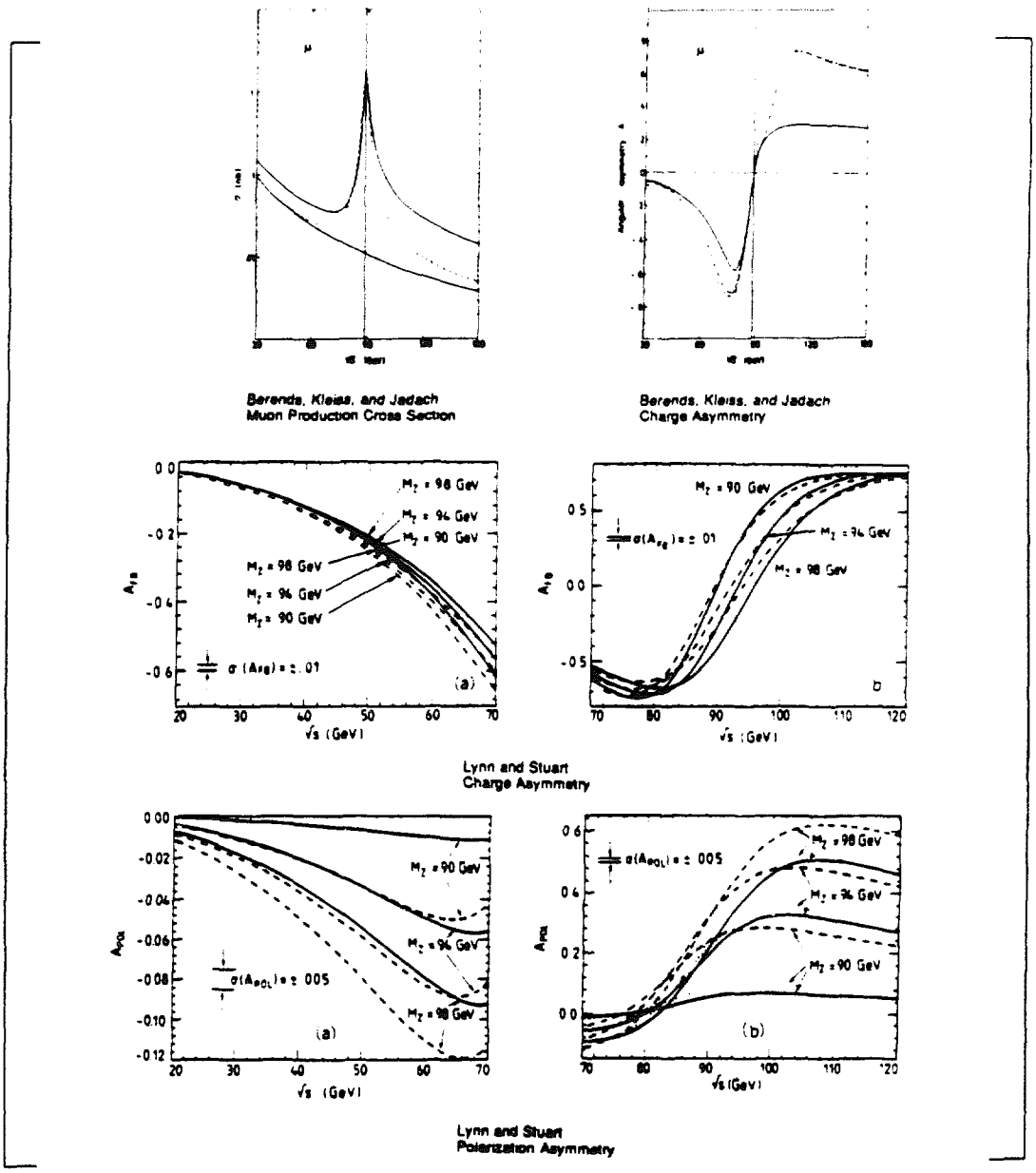

Fig. 2.15. One-loop corrections to the lepton asymmetries as calculated by B. W. Lynn and R. G. Stuart (Nucl. Phys. B253, 216 (1985)) and F. A. Berends, R. Kleiss, and S. Jadach (Nuclear Physics B202,63 (1982)). The dashed lines are the tree-level values and solid lines are the corrected values. Lynn and Stuart do not include the QED self-energies, box diagrams, and vertex corrections, as these require information from an experiment's Monte Carlo simulation. All other one-loop corrections from the Standard Model are included. Berends, Kleiss, and Jadach do include QED corrections and these are shown as a dotted line for 20% in bremsstrahlung and a solid line for 100% in bremsstrahlung of the maximum energy. Their papers should be referred to for more details.

2.6 W and Z Mass Measurement at $p - \bar{p}$ Colliders

The hadronic colliders at CERN and Fermilab are able to measure the W and Z masses with fair precision at present; this precision should improve greatly over the next several years as the luminosity of both machines increases. From these mass measurements $sin^2\theta_W$ will eventually be determined to high accuracy. Below we discuss the current situation and give estimates of future mass determinations.

Mass Measurements at CERN

At present, the world's best W and Z mass measurements are from the UA2 experiment[26] at the CERN Collider. Using data corresponding to an integrated luminosity of 142 nb^{-1} at $\sqrt{s}$=546 GeV and 768 nb^{-1} at $\sqrt{s}$=630 GeV, UA2 has collected 251 $W \rightarrow e\nu$ candidates and 39 $Z \rightarrow e^+e^-$ candidates, where there are approximately 25.5 and 1.3 background events, respectively. For the W mass the best fit to the experimental distribution is m_W=80.2$\pm$0.6(stat)$\pm$0.5(sys1)$\pm$0.3(sys2) GeV, where the first systematic error (sys1) is due mainly to possible biases in the neutrino transverse momentum and the second systematic error (sys2) reflects uncertainty in the energy calibration. For the Z-mass determination a sub-sample of 25 events is used for which both electron energies are accurately measured. The result is m_Z=91.5$\pm$.2(stat)$\pm$.7(sys) GeV, where the systematic error results mainly from uncertainty in the energy calibration. From these mass measurements, $sin^2\theta_W$ implied via the relation $sin^2\theta_W = 1 - (m_W/m_Z)^2$ is $sin^2\theta_W$ =0.232$\pm$0.025(stat)$\pm$0.010(syst), where the systematic error does not include contributions related to the energy calibration of the calorimeter, which is common to both the W and Z. A more precise measurement of $sin^2\theta_W$ is obtained from the relations m_W^2 =37.281^2/(1$-\Delta$r)$sin^2\theta_W$ and m_Z^2 =37.281^2/(1$-\Delta$r)$sin^2\theta_W cos^2\theta_W$ where Δr accounts for the effects of one-loop radiative corrections on the W and Z masses and is computed to be[10] Δr =0.0711$\pm$0.0013. UA2 is then able to measure $sin^2\theta_W$ =0.232$\pm$0.003(stat)$\pm$0.008(syst). UA2 will continue to take data for several more years, and with increasing luminosities at the CERN Collider they hope to improve these measurements by close to an order of magnitude.

Mass Measurements at Fermilab

The D0 group should obtain the best mass measurements at Fermilab because they will use a liquid argon electromagnetic calorimeter instead of the scintillator calorimeter used by the CDF group. After a few years of data collection, D0 will have[27] approximately 10,000 $W \rightarrow e\nu$ events and 1000 $Z \rightarrow e^+e^-$ events. With this data sample, D0 will measure the W,Z masses and $sin^2\theta_W$ in a similar way as UA2.

The expected statistical error of the mass measurements is 100 MeV, although the mass resolution will be dominated by the systematic error, which is not fully known. The D0 group is hoping to obtain[27] a 200 MeV systematic error or a total mass error of about 225 MeV (0.25%) for both m_W and m_Z. If the Z mass is normalized to the extremely precise LEP or SLC Z-mass measurement, thereby eliminating the 200 MeV systematic error due to the uncertainty in the energy calibration, the error in the W mass will be reduced to the 100 MeV statistical error.

From the equation $sin^2\theta_W = 1 - m_Z^2/m_Z^2$, $sin^2\theta_W$ will then be measured to approximately 2.4% accuracy, while from the equation $sin^2\theta_W = 37.281/m_W^2(1-\Delta r)$, $sin^2\theta_W$ will be measured more precisely to an accuracy of about 0.5%. These errors will be further improved to approximately 0.8% and 0.2%, respectively, if the Z mass is normalized to the LEP or SLC Z-mass measurement. It is interesting to note that the D0 group believes[27] that their W-mass measurement will be superior to the mass measurements from LEP II at CERN. The CDF and UA2 groups should obtain measurements only slightly worse than the D0 determinations.

2.7 Hadron Experiments

2.7.1 Deep Inelastic Neutrino Scattering

Llewellyn Smith[28] has shown that for isoscalar target nuclei the contribution of u and d quarks to the cross sections for deep inelastic scattering of neutrinos by the weak neutral current (NC) and charged current (CC) is given by

$$\frac{d^2}{dxdy}\left(\sigma_{NC}^{\nu(\bar{\nu})}\right) = \left(\frac{1}{2} - \sin^2\theta_W + \frac{5}{9}\sin^4\theta_W\right)\frac{d^2}{dxdy}\left(\sigma_{CC}^{\nu(\bar{\nu})}\right) + \frac{5}{9}\sin^4\theta_W\frac{d^2}{dxdy}\left(\sigma^{\nu(\bar{\nu})}\right) .$$

The validity depends on weak isospin symmetry, and so this relation can be extended to include heavier quark families subject to the symmetry assumption. Integrating the cross section over x and y, one obtains

$$R^\nu = \sigma_{NC}/\sigma_{CC} = \frac{1}{2} - \sin^2\theta_W + \frac{5}{9}\sin^4\theta_W(1 + r)$$

where

$$r = \sigma_{CC}^{\bar{\nu}}/\sigma_{CC}^{\nu} .$$

The experiments[29] measure R^ν precisely, independent of the details of the incident neutrino flux, providing that the energy is relatively high. Charged-current and

neutral-current events are separated by observing the outgoing muon. High neutrino energy is also desirable so that the assumption of deep inelastic scattering can be easily met and so that the outgoing muon is readily separable from hadronic showers. In the case of the CHARM experiment, for example, about 96% of the muons can be identified directly and the losses calculated with precision. The quantity r, the ratio of CC contributions from antineutrinos and neutrinos, appears with the coefficient $\frac{5}{9}\sin^4\theta_W = 0.029$. This limits the effect of the uncertainty in the relative neutrino fluxes, so that a measurement of r at the level of a few percent is adequate. The assumption of deep inelastic scattering cannot be verified directly for neutral-current events because of the missing neutrino, but with a narrow-band beam the energy of the hadrons is correlated with the momentum transfer Q^2, and a cut on the hadron energy, $E_h > 4$ GeV, ensures that the deep inelastic assumption is effectively met.

Some processes that contribute to deep inelastic scattering break the weak isospin symmetry assumption. The asymmetry of the strange and charm quark contributions to the sea occurs because of the difference in their masses and d and s quark mixing. These asymmetries are estimated to be $\Delta R^\nu/R^\nu \cong 2\%$ and a correction has to be made. The uncertainty in the quark structure of the nucleon contributes to the final systematic error of $\pm$ 0.005 in $\sin^2\theta_W$, with the most significant systematic problem being the lack of knowledge of the quark mass.

Some of the experimental effects for which corrections are made include:

i) Charged current/neutral current classification inefficiencies.
ii) π and K decays in the hadron shower faking a primary muon.
iii) ν_e background in the beam.
iv) Cosmic ray background.

The uncertainty in these contributions is much reduced by the fact that a ratio is being measured and compared to theory directly. After all corrections are made, the average value of $\sin^2\theta_W$ from the three most recent experiments CCFR, CDHS, CHARM is

$$0.233 \pm 0.004(exp) \pm 0.005(theor) \quad .$$

This gives a value for the radiative correction from the present best value of the W mass of

$$\Delta r = 0.077 \pm 0.025(exp) \pm 0.038(sys) \quad .$$

These experiments are perceived to be at the experimental limit that is attainable, and the likelihood that they will improve significantly in the determination of

$\sin^2\theta_W$ is remote in the near future. They are, however, the most accurate experiments at present and dominate the result that is obtained from the global fit.[1]

2.7.2 ν_μ - p at BNL

The semileptonic reactions $\nu_\mu p \rightarrow \nu_\mu p, \bar{\nu}_\mu p \rightarrow \bar{\nu}_\mu p$ are simple reactions, both theoretically and experimentally, with which to test the theory of weak neutral currents. The cross sections for these reactions are well known, within small theoretical uncertainty, and radiative corrections are small, characteristic of neutral-current neutrino scattering. Dependence on the quark structure of the nucleon is avoided by using results from electron scattering and CVC to describe the vector part of the neutral current. The axial current is parameterized in a similar way. The cross section for elastic scattering is given by

$$\frac{d\sigma}{dQ^2} = \frac{G_\mu^2 M_p^2}{8\pi E_\nu^2}\left(A \pm B\,\frac{(s-u)}{M_p^2} + C\,\frac{(s-u)^2}{M_p^4}\right) ,$$

where the plus sign is for neutrinos and the minus sign for antineutrinos, and $(s-u) = 4M_p\,E_\nu - Q^2$,

$$A = \frac{Q^2}{M_p^2}\left[G_A^2\left(1+\frac{Q^2}{4M_p^2}\right) - F_1^2\left(1-\frac{Q^2}{4M_p^2}\right) + F_2^2\left(1-\frac{Q^2}{4M_p^2}\right)\frac{Q^2}{4M_p^2} + F_1F_2\frac{Q^2}{M_p^2}\right] ,$$

$$B = \frac{Q^2}{M_p^2}\,G_A(F_1 + F_2) ,$$

$$C = \frac{1}{4}\left(G_A^2 + F_1^2 + F_2^2\,\frac{Q^2}{4M_p^2}\right) .$$

The vector form factors:

$$F_1 + F_2 = \alpha G_V^3 + \gamma G_V^0 ,$$
$$F_2 = \alpha F_V^3 + \gamma F_V^0 .$$

In the Standard Model

$$\alpha = 1 - 2\,\sin^2\theta_W \qquad \gamma = -\frac{2}{3}\,\sin^2\theta_W .$$

In the dipole representation,

$$G_V^3 = \frac{1}{2} \frac{(1+\kappa_p-\kappa_n)}{(1+Q^2/M_V^2)^2} ,$$

$$G_V^0 = \frac{3}{2} \frac{(1+\kappa_p+\kappa_n)}{(1+Q^2/M_V^2)^2} ,$$

$$F_V^3 = \frac{1}{2} \frac{(\kappa_p-\kappa_n)}{(1+\tau)(1+Q^2/M_V^2)} ,$$

$$F_V^0 = \frac{3}{2} \frac{(\kappa_p+\kappa_n)}{(1+\tau)(1+Q^2/M_V^2)} ,$$

$$\tau = \frac{Q^2}{4M_p^2} ,$$

where $\kappa_p = 1.793$ and $\kappa_n = -1.913$ are the anomalous magnetic moments of proton and neutron respectively, and $M_V = 0.84$ GeV/c^2 is the vector dipole mass.

The axial vector form factor

$$G_A(Q^2) = \beta G_A^3 + \delta G_A^0$$

is less well known. In the Standard Model, $\beta = 1$ and δ is identically zero, but the possibility exists that additional contributions might enter due to heavy quark contributions that do not exist in the vector form factors. In the dipole representation,

$$G_A^3 = \frac{1}{2} \frac{g_A(0)}{(1 + Q^2/M_A^2)^2},$$

where $g_A(0) = 1.263$ as measured by polarized neutron β decay asymmetry.[30] M_A = 1.09 GeV/c^2 as measured in charged-current quasi-elastic scattering.

The formalism with which the elastic scattering experiment is analyzed is without substantial uncertainty and the experimental signal was extracted fairly cleanly (Experiment 734, BNL).[31] The experimental signature was a recoil proton that stopped in the detector and was identified by the pattern of energy deposition. Contamination from other particles was small, as was the background level. The energy of the proton was used to determine Q^2, and an absolute cross section was determined by using quasi-elastic scattering as a normalizing reaction. The fit to both neutrino and antineutrino scattering data produced a value of $\sin^2\theta_W = 0.220 \pm 0.016(\text{stat}) \, {}^{+\,0.023}_{-\,0.031}$ (sys). The systematic error is a little disappointing. It comes in part from the fact that most of the target protons are bound in ^{12}C in the detector, and the calculation of experimental acceptance is complicated by nuclear effects. The hypothesis that $g_A(0)$ was given by the isovector term alone was tested

by allowing a possible extra contribution over the value from neutron decay. The fit value for this extra contribution was 0.12 ± 0.07. This value, although hardly significant, is in agreement with theoretical estimates.[31]

The determination of $\sin^2\theta_W$ by the BNL experiment suffers from a number of small systematic errors that combine to yield the error quoted. These errors are unlikely to be improved in a major way in the near future. Fig. 2.2 shows the BNL measurement of $\sin^2\theta_W$, together with measurements from different processes.

References

1. U. Amaldi et al., *Physical Review* **D36,** 1385 (1987).
2. M. Aguilar-Benitez et al., Review of Particle Properties, Particle Data Group, Physics Letters **170B**, 1 (1986).
3. C. Quigg, Gauge Theories of the Strong, Weak, and Electromagnetic Interactions, Benjamin/Cummings, Menlo Park, California (1983); W. J. Marciano and Z. Parsa, *Annual Review of Nuclear and Particle Science* **36,** 171 (1986).
4. E. S. Abers and B. W. Lee, Physics Report **9C**, 1 (1973).
5. E. D. Commins and P. H. Bucksbaum, Weak Interactions of Leptons and Quarks, Cambridge Univ. Press, Cambridge (1983).
6. J. D. Bjorken and S. D. Drell, Relativistic Quantum Mechanics, McGraw-Hill, New York (1965); J. D. Bjorken and S. D. Drell, Relativistic Quantum Fields, McGraw-Hill, New York (1965).
7. A. Sirlin, Physical Review **D22**, 971 (1980).
8. Workshop on Radiative Corrections in SU(2)L x U(1), Trieste, Italy, June 6-8, 1983, B. W. Lynn and J. F. Wheater, Editors, World Scientific, Singapore (1984).
9. A. Sirlin, Physical Review **D29**, 89 (1984).
10. W. J. Marciano and A. Sirlin, Physical Review **D29,** 945 (1984), erratum Physical Review **D31**, 213 (1985).
11. C. Verzegnassi, Physics Letters **147B**, 455 (1984).
12. W. Wetzel, Z. Physik C **11,** 117 (1981).
13. W. J. Marciano and A. Sirlin, Physical Review **D29**, 75 (1984).
14. W. J. Marciano and A. Sirlin, Physical Review **D22**, 2695 (1980).
15. S. Sarantakos, A. Sirlin, and W. J. Marciano, Nucl. Phys. **B217**, 84 (1983).
16. C. Itzykson and J.-B. Zuber, Quantum Field Theory, McGraw-Hill, New York (1980).
17. P. Candelas, G. T. Horowitz, A. Strominger, and E. Witten, *Nuclear Physics* **B258,** 46 (1985).

18. S. Godfrey and W. J. Marciano, *Brookhaven National Laboratory Neutrino Workshop*, (February 1987), BNL 52079.
19. Joseph D. Lykken, "Radiative Effects of E_6 Exotic Fermions on Precision Measurements of $Sin^2\Theta_W$," Los Alamos National Laboratory document LA-UR-87-1051 (submitted to Physical Review D); "The Signature of E_6 in Precision Measurements of $Sin^2\Theta_W$," Los Alamos National Laboratory document LA-UR-87-1282 (submitted to Physics Letters B).
20. A. Blondel, CERN-EP/87-174, invited talk given at the *22nd Rencontres de Moriond:Electroweak Interactions and Unified Theories*, Les Arcs, (8-15 March, 1987).
21. K. Moffeit, SLAC-PUB 4326, invited talk given at the *22nd Rencontres de Moriond:Electroweak Interactions and Unified Theories*, Les Arcs, (8-15 March, 1987).
22. Dydak, La Thiuble meeting, (March 1-8, 1987).
23. B. C. Barish and R. Stroynowski, *The Physics of the Tau Lepton*, CALT-68-1425 (April 1987).
24. D. Blockus et al., *Proposal for Polarization at the SLC*, SLAC Proposal (April 1986).
25. Berends, Kleiss, and Jadach, *Nuclear Physics* **B202,** 63 (1982); Lynn and Stuart, *Nuclear Physics* **B253,** 216 (1985); and Alexander et al., SLAC-PUB-4376 (1987).
26. R. Ansari et al., *Physics Letters* **B186,** 440 (1987).
27. R. Raja, private communication.
28. C. M. Llewellyn Smith, *Nuclear Physics* **B228,** 205 (1983).
29. P. Reutens et al., *Physics Letters* **152B,** 404 (1985); Abramowicz et al., *Zeitschrift fuer Physik* **C28,** 51 (1985); J. V. Allaby et al., CERN-EP/87-140, submitted to *Zeitschrift fuer Physik*.
30. J. Collins et al., *Physical Review*, **D18,** 242 (1981); R. Mohapatra et al., *ibid* **19,** 2165 (1979); S. Oneda et al., *Physics Letters* **88B,** 343 (1979); L. Wolfenstein, Carnegie- Mellon University Report No. COO-3066-119, unpublished (1979).
31. L.A. Ahrens et al., *Physical Review* **D35,** 785 (1987).

3 PHYSICAL PLANT

The location of the LCD facility relative to the LAMPF linear accelerator and the Proton Storage Ring is described. The construction of the detector tank and beam line is carried out by standard techniques, specified in a study done by an architect/engineer. The means of access to the tank, and the support structure for the photomultiplier tubes have been planned as part of this conceptual study.

The LAMPF and PSR accelerators provide the proton beam necessary to produce the neutrinos. Figure 4.1 shows a schematic view of these accelerators. Figures 3.1(a) and 3.1(b) show the time-separated neutrino source and Large Čerenkov Detector. The principal systems are a beam line parallel to the existing Line D, a superconducting vertical bending magnet and focusing system delivering protons to the experimental target, a target and shield assembly, and the water Čerenkov detector. The conventional design of the facility described here is the result of a study conducted by the architect/engineer firm, Black and Veatch, which specified the structural designs, construction methods and plans, and the costs.

3.1 Layout and Construction

Figure 3.2 shows an isometric view of the PSR/WNR facility. The required time-separated neutrino source is located downstream of the existing PSR magnet LDQD30. In order to place the detector between existing buildings at the LAMPF site, the beam must exit through the southeast corner of the building housing Line D. The beam runs approximately 71 meters beyond the end of the existing building, with 44 meters of beam line located within the building. The additional beam tunnel will be constructed by trenching into the tuff, inserting a 10-foot diameter corrugated metal pipe, pouring a 1-foot thick reinforced concrete floor within the pipe, and back-filling over the pipe to existing grade.

The 16.1-meter radius tank is constructed by digging a ramp down to the top level of the tank, setting 16-inch diameter auger cast piles into the tuff with a 12-inch separation, and excavating within the circle defined by the piles. This is a common and conventional construction method. The tank is approximately 18 meters deep, and the piles extend 13 meters below the tank floor. The piles are tied to the surrounding tuff and covered with mesh and gunite, yielding a smooth, water-resistant inner surface. The actual waterproof barrier will be a suspended high-density polyethylene liner. The tank floor is constructed of magnetite-loaded concrete, and will be 2 meters thick. This floor provides adequate support for the

tank, shield, and water, and reduces neutron groundshine into the sensitive detector volume.

The central target and shield assembly is a 7.5-meter radius reinforced concrete cylinder. It is filled with steel surrounding the target, magnetite loaded concrete below the target, and compacted magnetite above the target region. The total weight is 46000 tons. This assembly is the principal structural load supported by the floor mat and tuff below. The required steel is 6300 tons, of which nearly 4000 tons are currently available at LAMPF in existing inventory. It appears likely that all of the steel required will become available from excess material.

The detector and beam line join at the 90° downbend shown. In order to bend the 800-MeV proton beam with no losses and good optical transport, a conventional bending magnet is impractical. Such a magnet would require a very large iron yoke for flux return, approximately 1 megawatt of power, and the tunnel near the bend would have to curve gently downward. This would complicate the facility design and the shielding of the beam line. These considerations would raise the construction costs. A superconducting dipole can be built at an acceptable cost to meet the optical requirements. The dipole parameters would have a central field of 4T, an effective length of 2 meters, and a clear bore of 30-cm diameter. It would not be iron-dominated. Magnets similar to the required dipole have been built for synchrotron radiation facilities.

The dipole is housed in the concrete building shown. Directly below the dipole, the final focusing triplet, diagnostics, and target assembly are suspended. The building rests on spread-foot pilings supported on the magnetite, thus maintaining internal alignment during post-construction settling. The region surrounding the dipole building, and above it, is filled with recompacted tuff removed from the tank excavation. The tuff overburden provides the required 2500gm/cm^2 cosmic-ray shield.

The vertical assembly (dipole to target) follows the LAMPF design shown below, which has been maintenance free and will be constructed to avoid the need for any repair, though access will be feasible as described. Maintenance of this portion of the detector is facilitated by removing the tuff overburden, lifting off the concrete plug in the roof of the dipole building, removing the dipole, and withdrawing the vertical target string with an overhead mobile crane.

Utilities, power supplies, cryogenics support, water purification and experiment control, and data acquisition will be housed in a pair of structures located over the beam tunnel as shown in the plan view (Fig. 3.1 (a)). This location minimizes the distance over which cabling and piping must be extended.

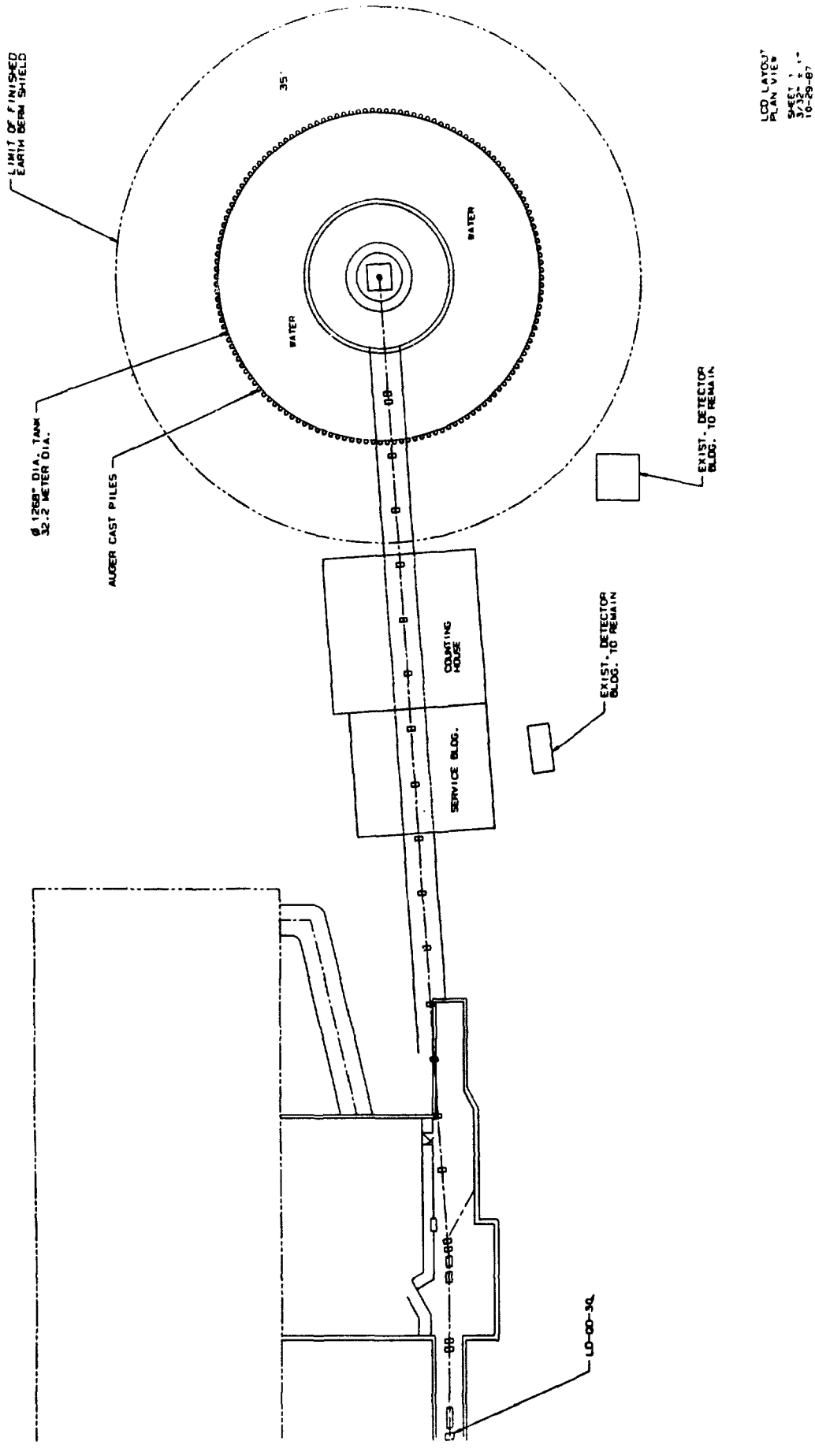

Fig. 3.1 (a). Plan view of the time-separated neutrino source and the Large Čerenkov Detector.

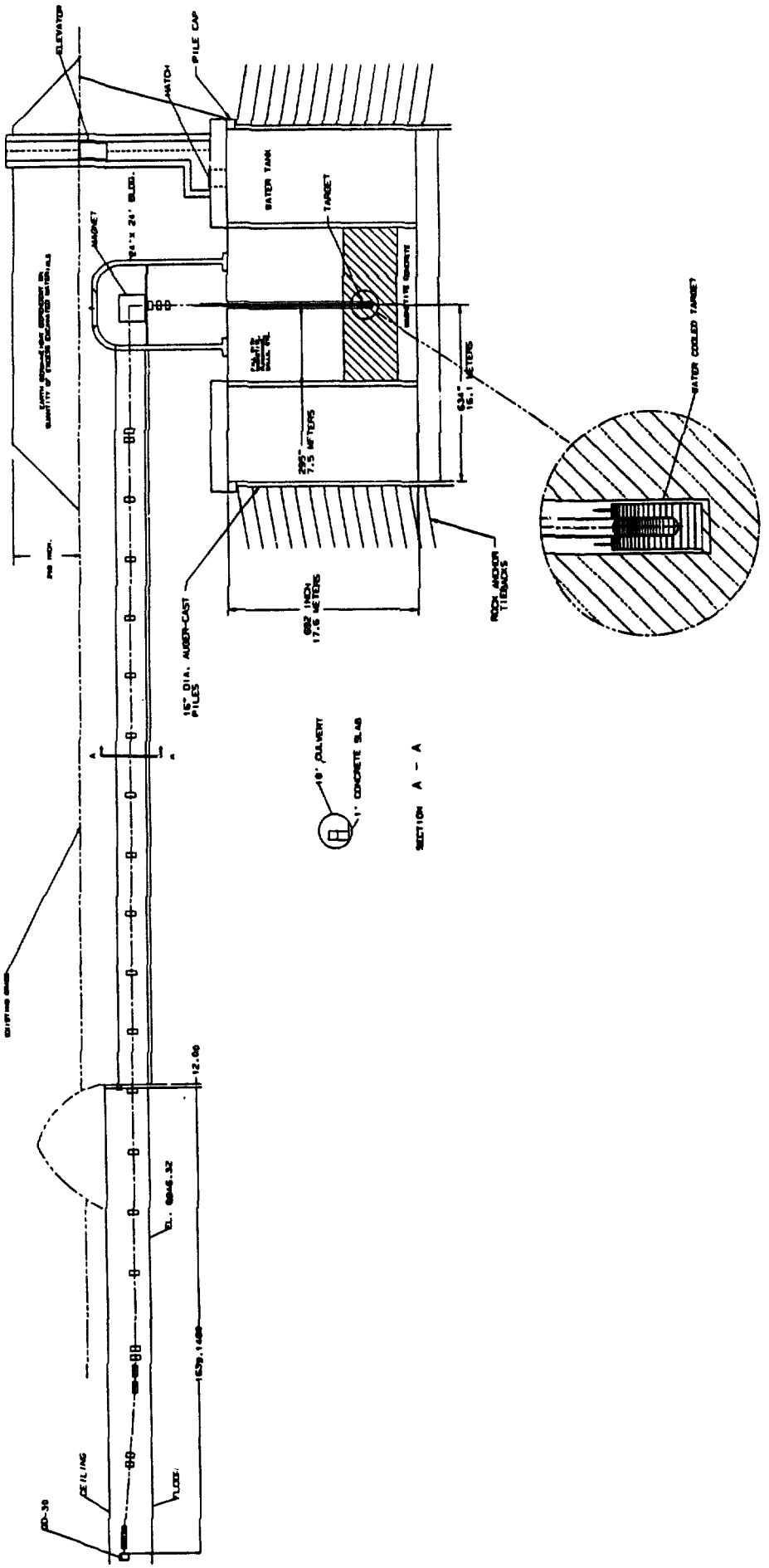

Fig. 3.1 (b). Elevation view of the time-separated neutrino source and the Large Čerenkov Detector.

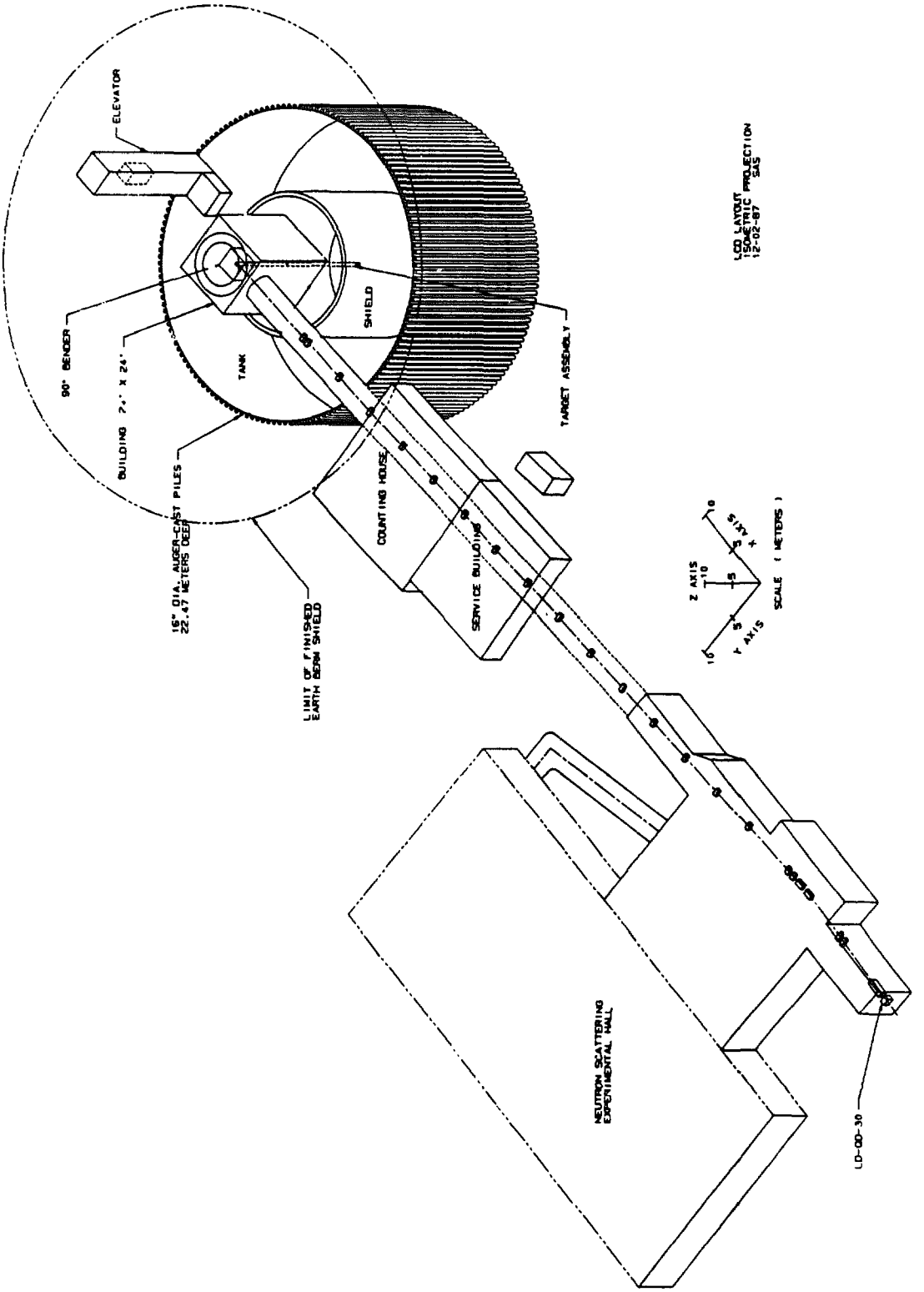

Fig. 3.2. Isometric view of the PSR/WNR facility. The time-separated neutrino source beam begins at LDQD30. This location is indicated in the figure.

3.2 Access

Access to the facility consists of entry through the existing Line D tunnel into the new beam line and separate access to the detector tank.

In order to install the conventional beam line hardware, access to the 10-foot diameter tunnel from the upstream end is adequate, given the size and weight of the magnets and other hardware. Installation of the superconducting dipole will be through the roof of the concrete building which will house it. The tunnel diameter and dipole building clearances are adequate for all maintenance purposes.

Access to the tank must accommodate installation of the phototube supports, cable plant, and phototubes. Occasional access for maintenance must also be possible. Fig. 3.1 (b) shows a vertical penetration of the tank overburden by a concrete shaft containing an elevator. This penetration leads to a hatch in the roof, through which access is made for phototube installation. A suspended elevator bucket in the tank can be used during installation. The vertical penetration can be plugged with a 2500gm/cm^2 cap during data taking, to insure integrity of the cosmic ray shield.

After installation of the detector, occasional entry may be made to the tank using floating platforms to support work at the appropriate level. Such access will not be required often.

3.3 Tube Supports

The phototubes will be supported on a stainless steel cable system. The cables will have a surface treatment consistent with the need to prevent contamination of the tank water. Phototubes will be mounted in groups of nine in plates of PVC plastic, providing support and optical isolation between the regions in front of and behind the tubes. A small fraction of the phototubes will be reversed in the plates to provide the needed veto sensitivity. These plates are then mounted to the tensioned cables. The high-voltage and signal cables are supported on additional stainless steel support cables. This system takes advantage of the rigid tank walls to support the anchored cables, and provides a simple, cost-effective support system for the photomultipliers. Installation will be carried out in the tank, using a commercial personnel lifter for most of the installation.

4 PROTON STORAGE RING (PSR)

The design principles of the Proton Storage Ring are described. Studies carried out during commissioning of the facility have revealed the main obstacles that prevent full current operation of the PSR. Current operations support a physics program at 1/3 of the design intensity. Plans for overcoming current limitations are described.

The layout of the Proton Storage Ring (PSR) and the injection beam line is shown in Fig. 4.1. The principal function of the PSR is to accumulate the entire macropulse from the LAMPF linear accelerator and to compress the time structure of the beam pulses.

The PSR magnets are operated at a constant current, and injection is performed in synchronism with LAMPF. The LAMPF accelerator accelerates H^+ (protons) and H^- species on opposite phases of the same radio frequency. After separation by two kicker magnets and a septum from the positive beam, the H^- beam is deflected through 90° into beam Line D, as shown in Fig. 4.1. The deflection is sufficiently gradual that only a very small fraction of the beam is lost through stripping induced by the magnetic fields.

After any residual halo surrounding the H^- beam is stripped to reduce injection losses in the PSR, the beam enters a 1.5T magnetic field where complete stripping occurs rapidly to the H^o species, inducing a small extra divergence (0.37mrad) in the horizontal coordinate. The neutral beam is further stripped in the PSR by a 200 $\mu g/cm^2$ carbon foil, with a measured stripping efficiency of about 90%. Injection takes place over the full macropulse from LAMPF.

The combination of scattering in the foil and the broadening from H^- stripping is enough to substantially fill the horizontal phase space. The closed orbit is then bumped vertically during injection to provide control of the filling of phase space and to keep injection losses as low as possible.

One orbit of the ring takes approximately 360ns. A beam free gap along the circumference is necessary for low-loss single-turn extraction. Thus, a total beam bunch length of 270ns is desired. This is maintained by a first harmonic RF bunching system. On each turn during injection, a new bunch is added synchronously to the accumulated stack, at zero phase with respect to the RF cycle, whose amplitude is increased through the injection period. Even at the highest circulating currents envisaged (46A), beam loading of the RF is negligible. At high currents the beam bunch evolves from the nearly square shape at the start of injection, to a triangular shape shown in Fig. 5.6. This shape seems to be desirable to prevent

significant beam from being present in the gap in the circulating bunch, and if it is not maintained, beam loss results at extraction.

After accumulation of the entire LAMPF pulse (750μs), the beam is extracted in a single turn. Single turn extraction is achieved by two strip-line kickers, driven by a 45-kV pulser with 60-ns rise time, into a 5-kg septum magnet. Initiation of the pulse is synchronized with the rotation phase of the bunch to within 1ns.

The betatron tunes of the PSR are $Q_x = 3.23$ and $Q_y = 2.21$. These agree with design parameters and it has been verified that there are no resonances near the working point, above fourth order. At present, the measured PSR stored beam lifetime at low currents is much shorter than expected for the design aperture. During accumulation, beam particles pass repeatedly through the stripper foil. Through Coulomb scattering, the beam size grows according to the relation

$$\sigma_1^2 = \sigma_{01}^2 + \beta_1 \beta_s N (\delta\theta)^2$$

where σ_1 is the rms beam size, β_s or β_1 are the x or y beta functions at the stripper foil and observation point respectively, N is the average number of collisions in the foil up to the moment of observation, estimated using a screened Coulomb cross section (about 3000 collisions in 1ms), $(\delta\theta)^2$ is the mean square scattering angle in each transit and σ_{01} is the initial beam size at the point of observation. The important feature to be noted here is that the influence of Coulomb scattering takes place in an accelerator, not in free space.

Even if the protons traverse the foil each revolution, the growth of the beam size is calculated to be well below the aperture, for accumulation times of about 1ms. At present the losses are greater by a considerable factor than this estimate.

Development studies indicate that there are several problems in the PSR. After accumulation, the beam has been bumped off the stripping foil and a lifetime of one second has been observed. The loss rates that have been observed are independent of intensity, indicating that they are due to single particle effects. This lifetime corresponds to a beam loss of about 3×10^{-9} per meter.

Figure 4.2 illustrates the losses during accumulation in normal PSR operation, and in the absence of extraction. The influence of accumulation on the losses is shown separately, as is the effect of extraction.

The maximum beam that can be accumulated in the PSR is limited by four considerations:

a) beam loss during accumulation causing activation of the ring components,

b) instability in the circulating beam,

c) limited brightness in the source (LAMPF),

d) and extraction losses.

Each of these effects merits discussion. The present mode of injection from LAMPF suffers from two major disadvantages. The initial stripping in the magnetic field from H^- to H^0 species increases the emittance of the beam by a significant amount. The neutral beam cannot be manipulated to match the beam emittance to the aperture of the storage ring. In fact, it is now apparent that the mismatch in the emittances is a major cause of loss in the ring during accumulation, for the horizontal aperture is already filled and any growth from Coulomb scattering in the foil will cause losses. This phenomenon now seems to be well understood, and the losses are explained in terms of the beam characteristics in the ring. It appears that improvement in this situation will require changing the mode of injection to H^-, which is then double-stripped to H^+. This will permit the injected beam emittance to be closely matched to the ring acceptance, and the beam can then be bumped continuously to paint the injection aperture in an optimum way. At present, during LANSCE production, the beam has been limited to 30μa, at a repetition rate of 15Hz, so that ring components do not become excessively activated.

In experimental studies of PSR performance, about 2/3 of the design current has been stored. Fast beam loss during accumulation or storage has been observed in the PSR with beam loss occurring in about 50ms. Instability occurs when the accumulated current reaches a threshold value that depends on beam cross section, RF amplitude, and the strength of non-linear elements. The growth rate is much faster than the synchrotron frequency and is almost certainly a transverse instability. At 13-kV RF amplitude, the instability has been observed at 3.5×10^{13} ppp. Further experiments have been performed with octopoles installed in the ring. This succeeded in suppressing the onset of the instability up to a current threshold proportional to the octopole strength. However, with the additional losses during accumulation, it has not seemed appropriate to find the detailed source of the instability or to continue to tune the ring so as to increase the accepted beam.

If the design current is to be achieved with an injection time of 750μs, then the current brightness of the H^- source is a limitation. This is not a fundamental limitation, and it is assumed that this improvement will occur when the other limitations are overcome.

A major accomplishment during the past year has been the identification of a limiting aperture in the extraction system that had caused serious losses. This aperture was improved, and the extraction losses were reduced by a factor of about 30. It may be desirable to further improve the extraction system by increasing the available transverse kick. This will allow an enhancement in the horizontal aperture.

In summary, the PSR-LAMPF combination has operated continuously, for a physics program, at about one-third of the design luminosity. The present limitations in the intensity are understood, and a program of improvement is under way. This program is expected to allow the provision of beam to the LANSCE program as well as to this experiment, at the design current of 5×10^{13} ppp (100μa).

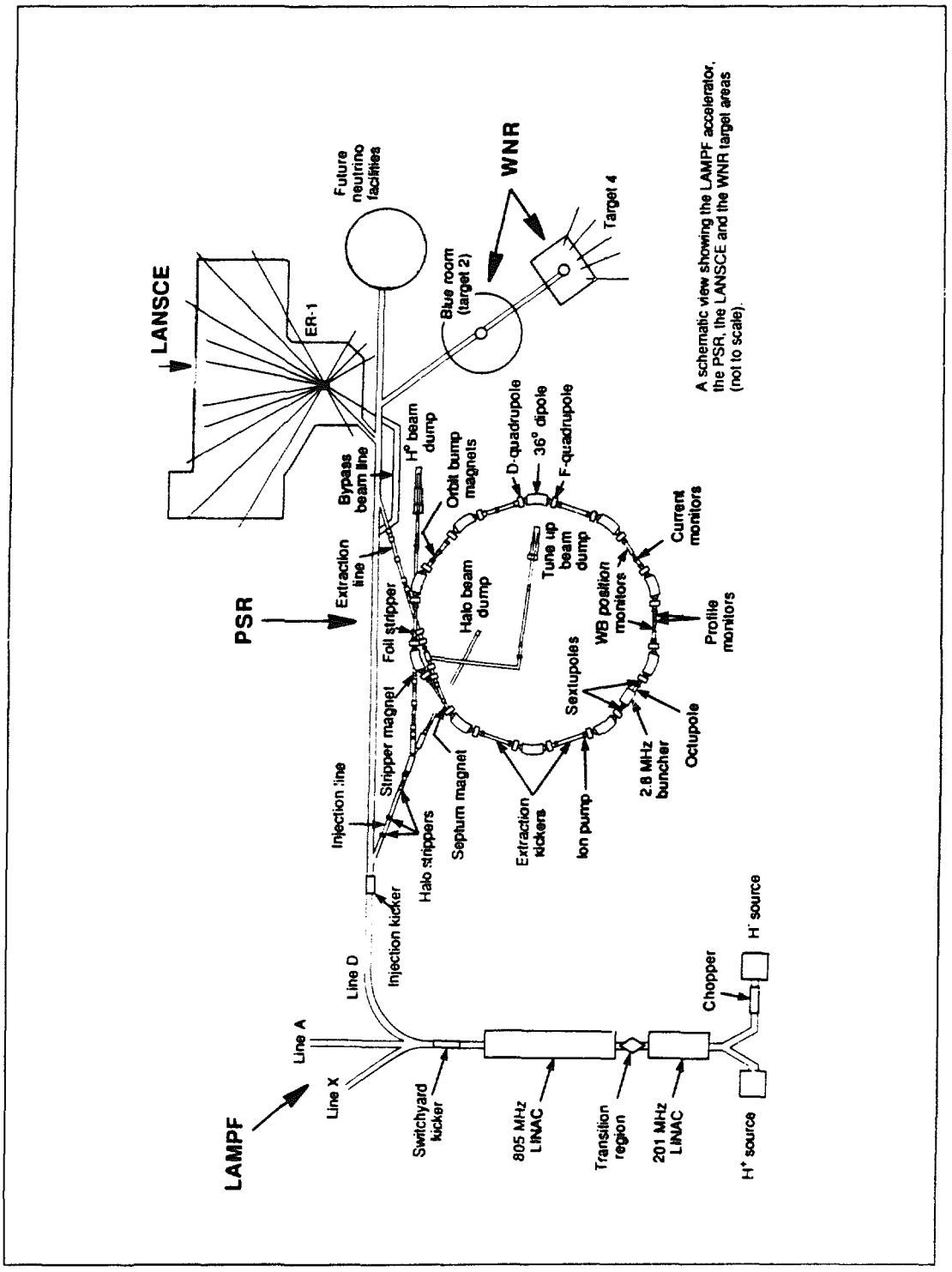

Fig. 4.1. Layout of the Proton Storage Ring, showing the injection and extraction lines, and the LAMPF accelerator.

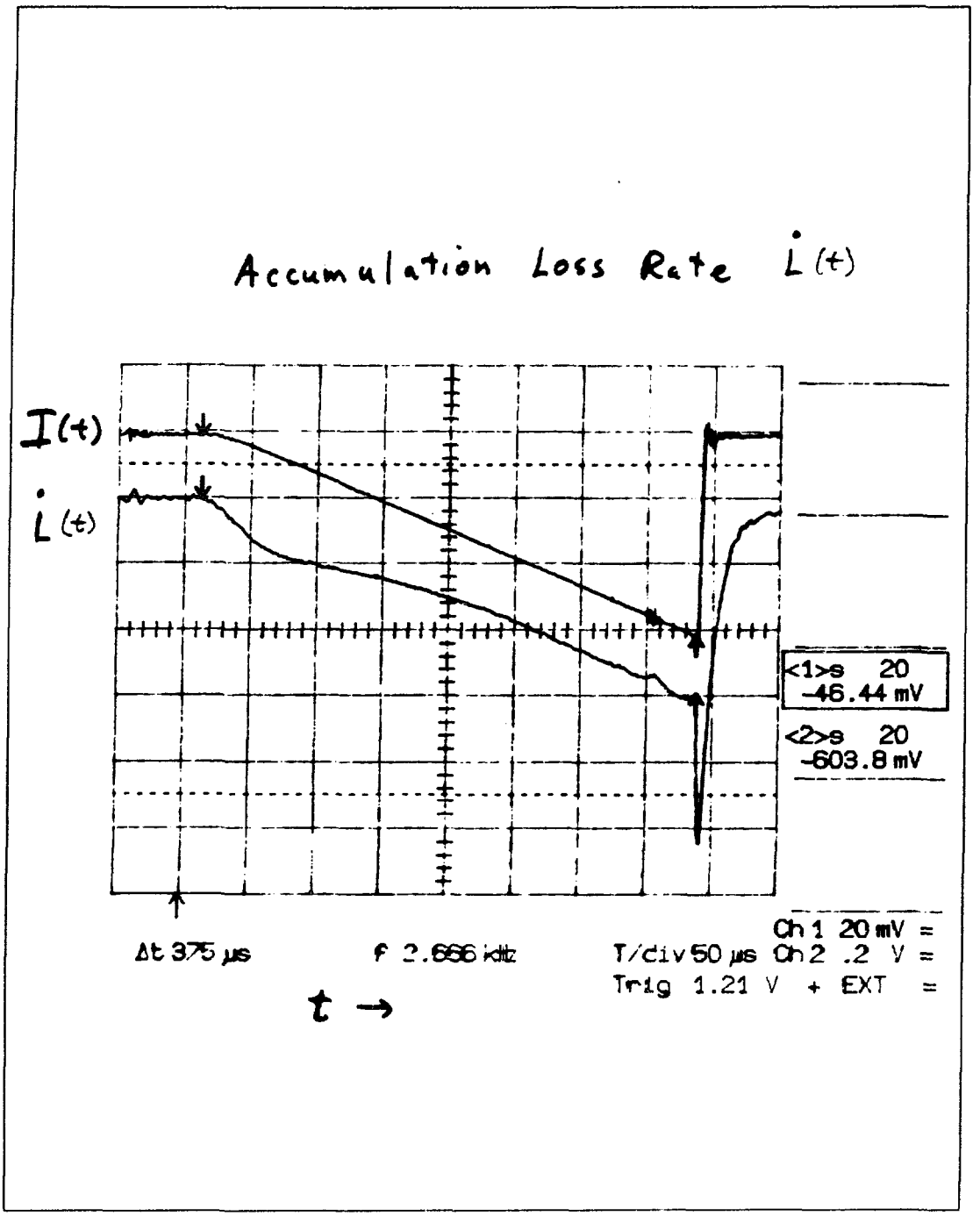

Fig. 4.2 (a). Beam losses during accumulation are shown during typical PSR operation. The upper curve shows the increase of circulating current in the PSR during the 375μs accumulation period. On the same time scale, the sum of all beam losses is shown. The two curves follow approximately the same time dependence. The drop in beam current at extraction is accompanied by a spike in the measured losses, which subsequently decays.

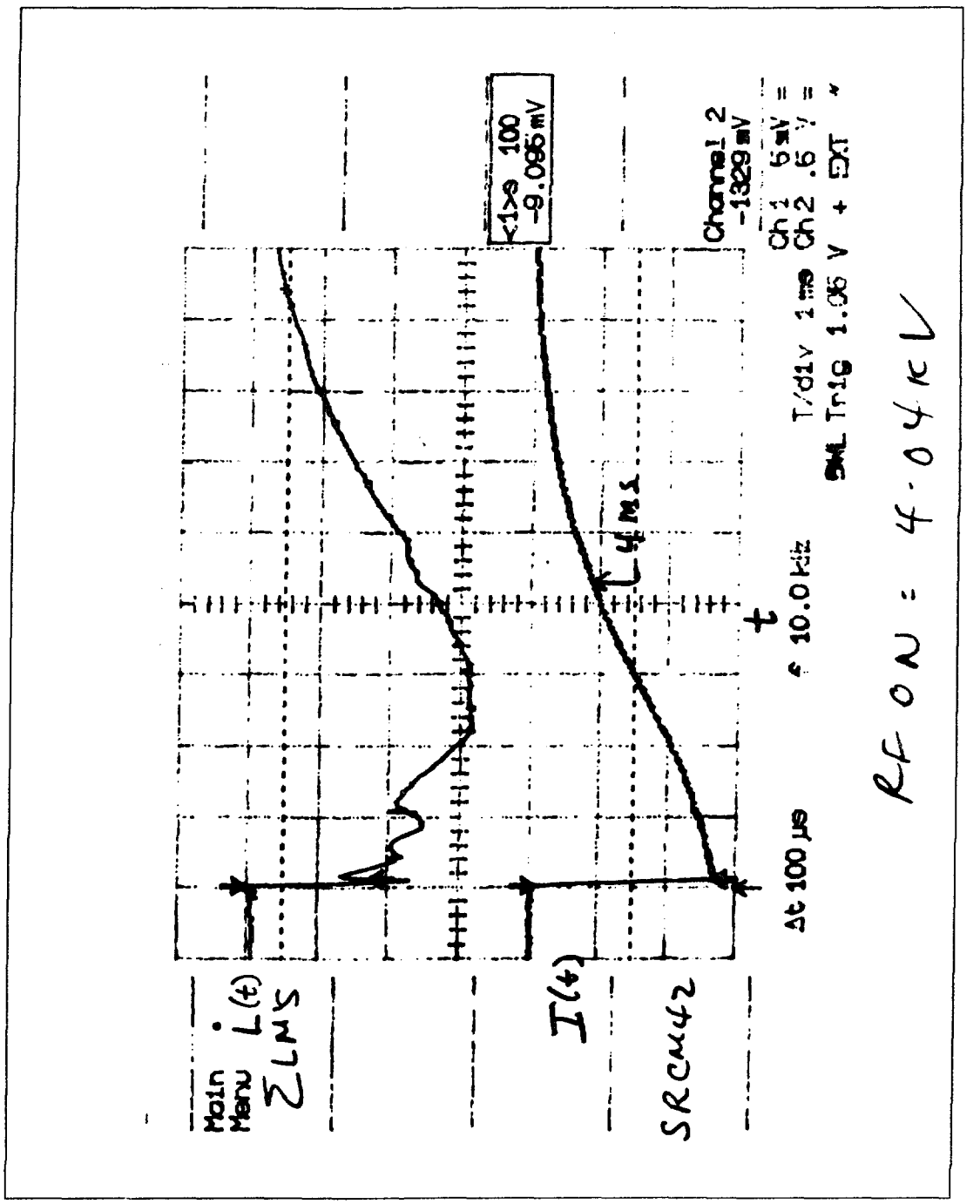

Fig. 4.2 (b). The circulating current I(t), and the total beam losses L(t), are shown as a function of time. This graph differs from Fig. 4.2 (a) in that the beam is allowed to coast without extraction. The entire PSR beam is lost in approximately 9ms. The losses peak in the first 4ms.

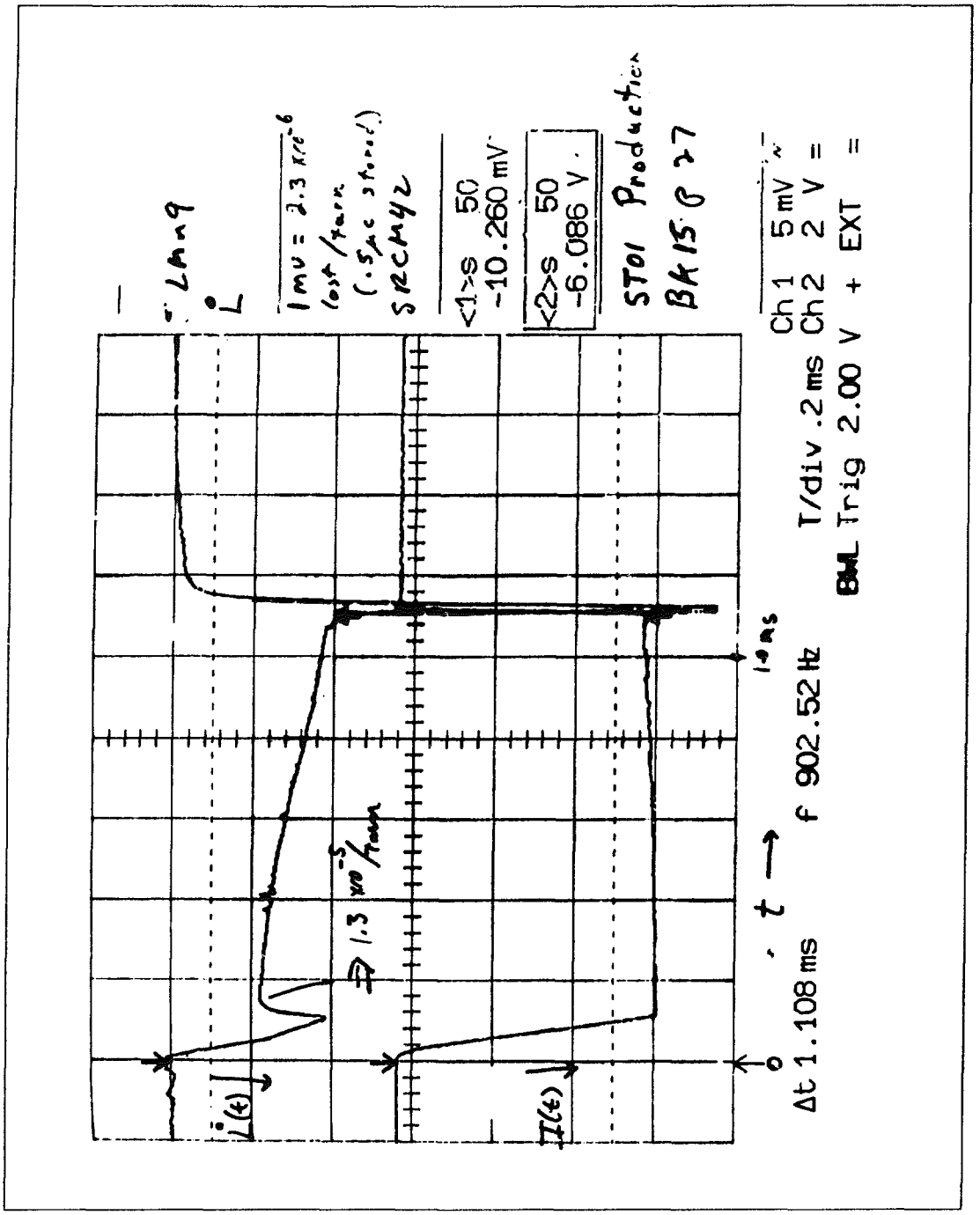

Fig. 4.2 (c). This figure shows the same measurements as in Fig. 4.2 (a), except that the effects of accumulation and loss are cleanly separated. In this measurement, injection and accumulation are limited to the first 100μs only. The lower curve shows the increase in current, paralleled by the losses in the first turn shown in the upper curve. The middle sections of both curves document the current and losses shown in the absence of accumulation. Extraction is shown as in Fig. 4.2 (a).

5 BEAM TRANSPORT AND TARGET

An optical design for the new beam line has been completed. This design meets programmatic requirements at the Proton Storage Ring, has large aperture to aid in achieving low losses, and can be constructed substantially from conventional components. A special superconducting dipole is required to bend the beam down 90° into the target cell. Preliminary studies of emittance growth from space charge effects have been made. These studies will be used to guide a final design of the transport.

The beam line must be designed to transport the extracted PSR phase space, with extremely low losses, to the neutrino production target. The design must meet several requirements. Among these are layout constraints imposed by existing structures, accommodation of shielding, other programmatic commitments at the PSR, the desire to use direct LAMPF beam as well as extracted PSR beam in the new line, optical requirements at the target, and economy. The requirement of extremely low losses and transmission of the entire PSR emittance dictates a large aperture system with high field quality to reduce aberrations. Economy drives the design to the smallest number of simple, small aperture elements. The achievement of extremely low losses in the beam line is not a fundamental problem. Given adequate understanding of the PSR emittance, and a method of transmitting or eliminating beam halo, the design is straightforward. If the input emittance is larger than expected, or if the tails of the beam phase space population are extended, the optical elements will cost more. The design discussed in this chapter illustrates a single, relatively complete design study based on a calculated PSR emittance. Consideration of optical philosophy, space-charge effects, design details of the focusing elements, and all facility instrumentation and costs has been included. As knowledge of the source emittance develops, this design can be readily modified to insure that the final performance criteria can be met. Possible design modifications that may be required are discussed.

5.1 Beam Layout

Figure 5.1 shows the layout of beam line optical elements. Briefly, the transport can be described as an extraction system to remove pulses from the existing Line D, an alternating-gradient quadrupole channel to carry the beam to the detector location, a superconducting dipole to bend the beam down into the detector, and the final vertical target string.

Figure 5.2 shows the layout of the PSR and its extraction line. This figure shows that the location downstream of LDQD30 is the first reasonable point at which beam transported directly from the LAMPF switchyard, bypassing the PSR, and beam from the PSR extraction line, can be selected. While the experiment will be run using only the PSR beam, development studies using the smaller emittance, and more readily available, LAMPF beam will be essential to the timely commissioning of the new facility. A disadvantage of the location downstream of LDQD30 is the influence of the PSR extraction skew magnet immediately upstream of LDQD29. This magnet mixes the orthogonal horizontal and vertical phase space axes, complicating the optical relation of tuning in the PSR, and extraction line to the measured profiles downstream of the skew magnet. Some consideration will be made of the possible means to simplify this system. The location downstream of LDQD30 is also one of the last locations that will not interfere with beam delivery to the LANSCE and WNR facilities.

Table 5.1 lists the principal parameters of all significant optical elements in the new beam line. The apertures listed are selected to accept the input phase space used in the design described here. If a larger phase space is encountered at LDQD30, these apertures can be chosen to be larger. The design is preserved if the same dipole fields and lengths, and quadrupole gradients and lengths, are retained.

Immediately downstream of LDQD30, a kicker is employed to direct alternate PSR pulses out of Line D. The kicker has been designed to be operated up to 48Hz, which should be adequate to accommodate all planned PSR operating modes. The default operating mode is assumed to be a 24Hz repetition rate in the PSR, with the kicker directing every other pulse into the new line. The rise and fall times of the kicker are modest, given the tens of milliseconds separating pulses. This magnet is designed to be an elaboration of the existing Line D injection kickers. The kicker deflects the beam downward, by 5 degrees. This choice is the only feasible extraction direction, given existing physical constraints.

In order to develop adequate separation from the existing Line D, the beam is allowed to drift 5.4 meters to a quadrupole doublet. Due to the minimal separation between adjacent lines, these quadrupoles may have to be built as septum magnets. A more refined design study will have to consider a centroid shift and higher order aberrations before this pair of magnets can be designed in detail. The design presented here employs quadrupoles identical to most of the other lenses. The doublet is used to capture the drifting beam before its transverse size grows unacceptably, and it is tuned to achieve achromaticity in the vertical plane, after the following dipole. This is useful in minimizing vertical dispersion at that location.

Table 5.1. Principal parameters of all optical elements in the LCD beam transport.

ELEMENT	*EFF. LENGTH*	*POLE FIELD*	*BORE OR GAP*
Kicker	2.0 m	+2.13 kg	15 cm
Quadrupole	0.4 m	−6.12 kg	20 cm
Quadrupole	0.4 m	+6.50 kg	20 cm
Bender	2.0 m	+2.13 kg	15 cm
Bender	2.0 m	+1.70 kg	15 cm
Quadrupole	0.4 m	−4.08 kg	20 cm
Quadrupole	0.4 m	+2.53 kg	20 cm
Quadrupole	0.4 m	+2.78 kg	20 cm
Quadrupole	0.4 m	−2.38 kg	20 cm
Quadrupole	0.4 m	+2.90 kg	20 cm
Quadrupole	0.4 m	−2.38 kg	20 cm
Quadrupole	0.4 m	+2.90 kg	20 cm
Quadrupole	0.4 m	−2.38 kg	20 cm
Quadrupole	0.4 m	+2.90 kg	20 cm
Quadrupole	0.4 m	−2.38 kg	20 cm
Quadrupole	0.4 m	+2.90 kg	20 cm
Quadrupole	0.4 m	−2.38 kg	20 cm
Quadrupole	0.4 m	+2.90 kg	20 cm
Quadrupole	0.4 m	−2.38 kg	20 cm
Quadrupole	0.4 m	+2.90 kg	20 cm
Quadrupole	0.4 m	−2.34 kg	20 cm
Quadrupole	0.4 m	+4.54 kg	20 cm
Quadrupole	0.4 m	−3.54 kg	20 cm
Bender	2.0 m	38.35 kg	30 cm
Quadrupole	0.4 m	10.68 kg	30 cm
Quadrupole	0.4 m	−8.93 kg	30 cm
Quadrupole	0.4 m	−5.69 kg	30 cm

The beam then drifts an additional 5.4 meters to a bender that bends up by 5 degrees, thus restoring the beam trajectory parallel to the floor. This bender and the one to follow are identical to the kicker in design and construction, including laminations, but will be operated as DC magnets. This permits construction economy and simple stocking of replacement hardware.

The third dipole is required by the existence of permanent structures at the site that interfere with a direct forward location of the detector. It bends the beam by 4 degrees to beam left. This moves the target location 6.7 meters to the left of the direct forward location, removing any interference with existing structures.

A matching doublet is used immediately downstream of the third dipole, to capture the beam and to achieve a simultaneous horizontal and vertical beam "waist" at the center of the next quadrupole. This is a standard means of "matching" a beam into an alternating-gradient quadrupole channel. We employ two quadrupoles for this purpose, in the interest of simplicity and economy. A more complete and general solution to such a problem requires four quadrupoles to control the horizontal and vertical beam sizes and divergences. By the choice made here, we sacrifice complete symmetry between the horizontal and vertical planes. This does not compromise the performance of the beam line for our purposes, as we shall illustrate in our discussion of the beam envelopes.

A fourteen-quadrupole alternating-gradient channel follows. This is the configuration generally employed for transmission of the maximum phase space over long distances. We have reduced the number of periods in the channel from the optimum, in the interest of economy. This has not compromised the channel performance significantly. In a typical transport of this type, the quadrupole polarities alternate and all magnets of one polarity can be operated at identical settings, and therefore, from a common power supply. The influence of space charge in the extracted PSR beam shifts the tune as the beam travels downstream. Thus individual control of all quadrupoles is necessary.

The alternating-gradient section is followed by another matching doublet. In this case, however, the phase space exiting the previous section is transformed to a simultaneous horizontal and vertical beam waist at the center of a dipole, that follows.

The dipole is a 2-meter long, 3.8-T superconducting magnet with a 30-cm clear aperture. The aperture is curved to conform to the central trajectory. The beam is bent down by 90°. The dipole has been modeled using a standard ideal treatment of a sector magnet with no higher order multipoles, symmetric entry and exit, and edge focusing in the plane orthogonal to the bend plane. These simplifications may not be achievableable in a real magnet. Additionally, stray field from an

air-dominated magnet will be a significant complication. Thus, a detailed design, treating this dipole as a spectrometer magnet, will be required before it can be fabricated. Precision control of field homogeneity and higher order multipoles has been done on large dipoles of this sort in the past, given a complete design study.

Immediately following the dipole, a quadrupole triplet captures the beam before dispersion can produce growth of the beam profile. The triplet focuses the beam onto the experimental target, producing the desired 2.5-cm beam spot. A long drift of 14.2 meters is required following the triplet to separate the elements requiring human maintenance from those made inaccessible by beam-associated activation.

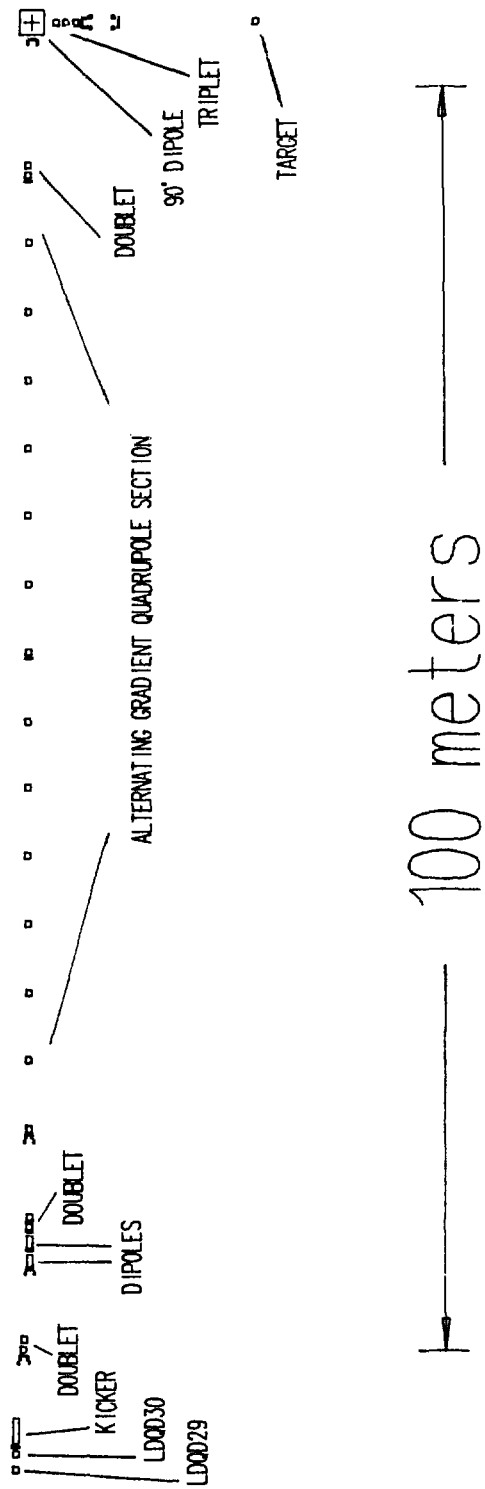

Fig. 5.1. Elevation view of the beam line optical elements.

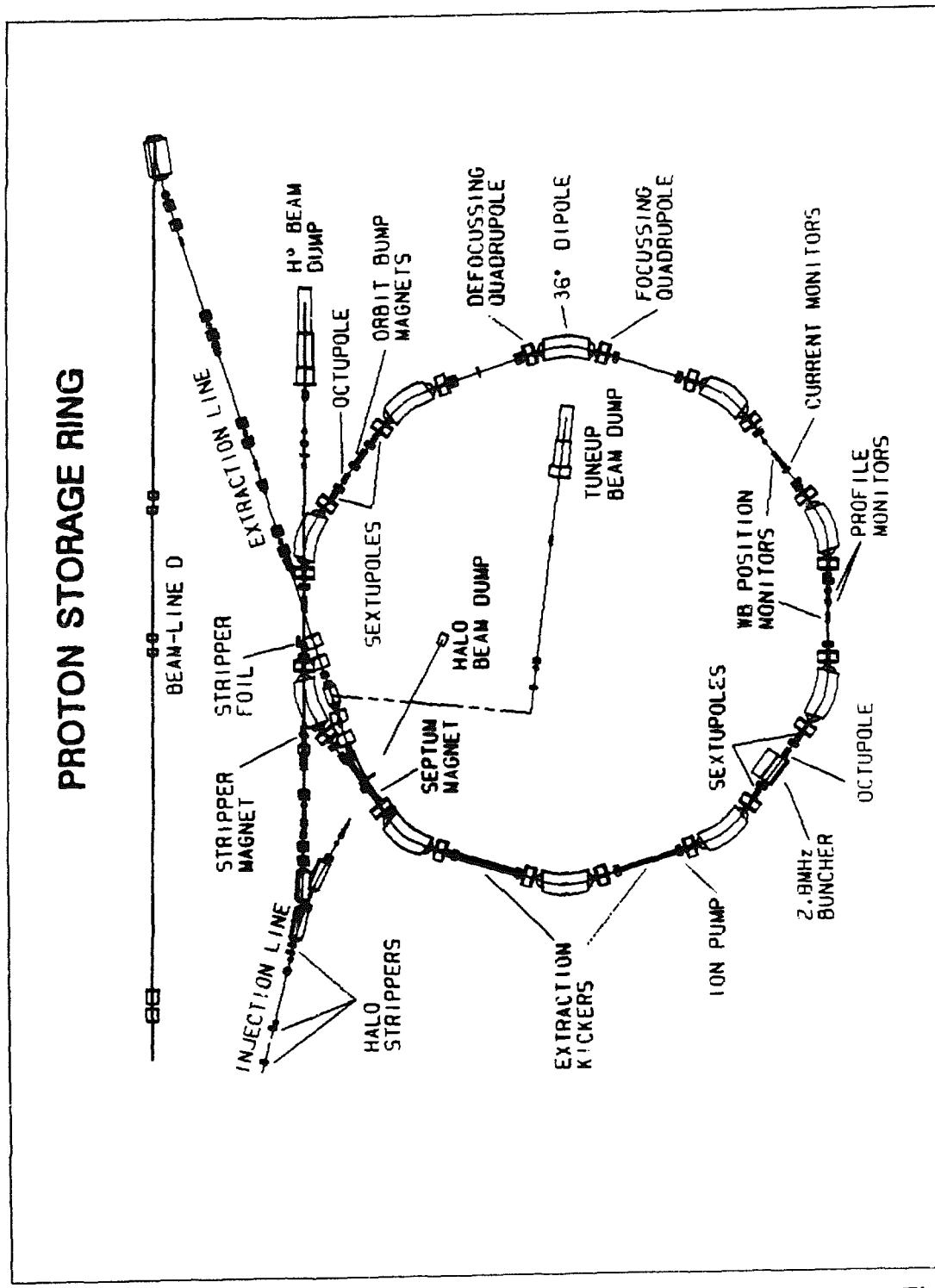

Fig. 5.2. (a). Layout of the PSR and extraction line optical elements. The beginning of the extraction line is shown.

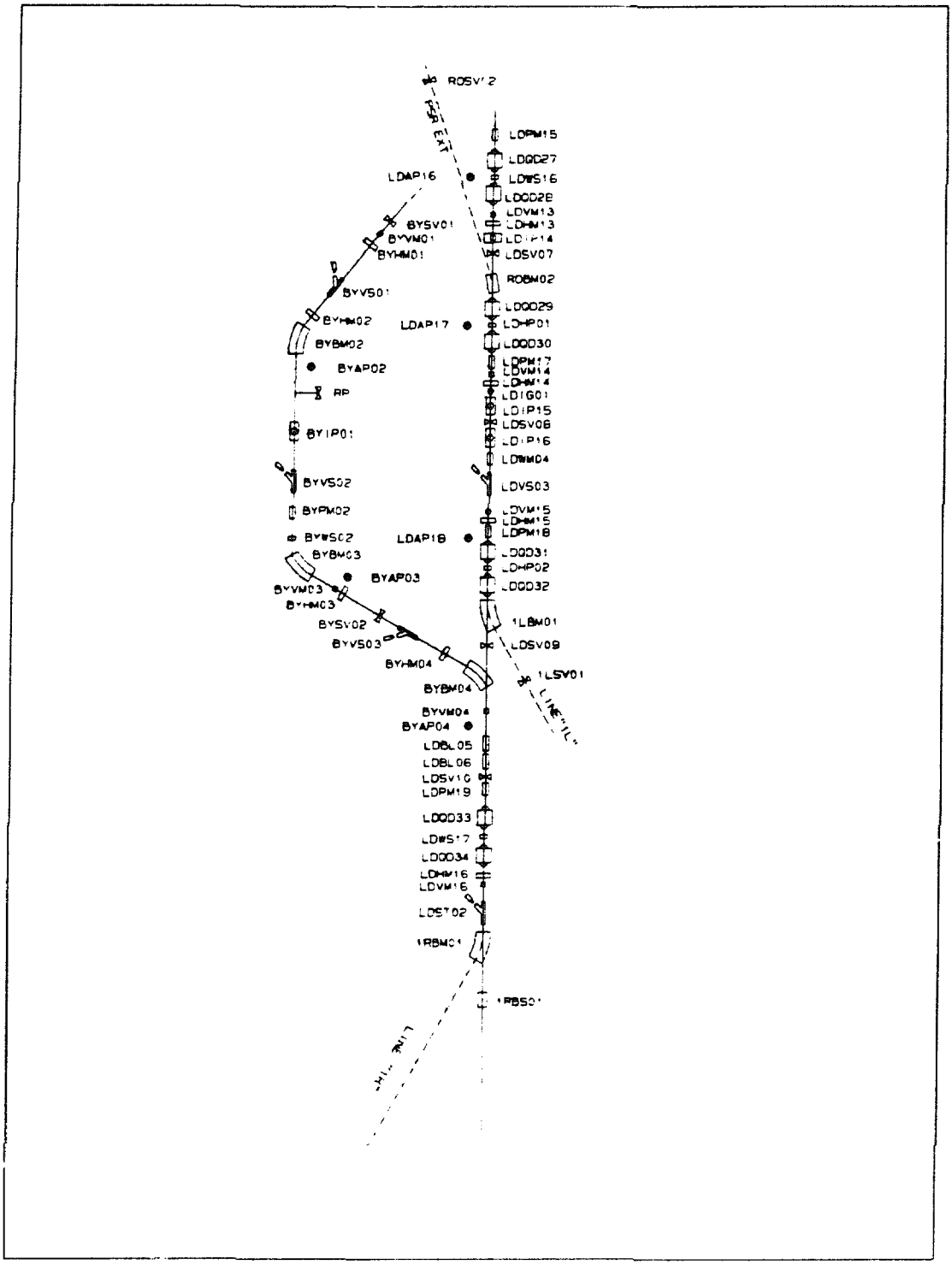

Fig. 5.2. (b). Layout of the extraction line optical elements in Line D. The ... cation LDQD30 is identified.

5.2 Beam Optics

Input Phase Space

This design study has made use of a calculation of the extracted PSR beam phase space carried out by members of the PSR design team. At the time the study was made few measurements of the actual phase space had been carried out, though the PSR has been in operation for two years. The few beam spots measured were consistent, however, with the calculated phase space.

Recently, with new instrumentation installed, preliminary measurements have been made. These indicate, as well, an actual phase space consistent with the calculation. As these measurements mature, they will be included in design revisions. As stated before, the main effect will be to require adjustment of magnet apertures, or consideration of phase space tailoring at the input to the new beam line.

Table 5.2 lists the six diagonal parameters of the calculated input phase space, corresponding to the six basis axes of phase space. The correlations between these coordinates are listed as well. These parameters define the core of the beam, and we take them to be at least inclusive of two standard deviations of the distribution along each axis. The actual distribution, common to storage rings, is a parabolic one. Due to non-linear effects, such as space charge, the beam is predicted by the calculation to have extended tails. This halo will have to be studied carefully in the measurements made of the actual beam.

Results of the Design Calculation

Figure 5.3 shows the horizontal and vertical beam envelopes along the central trajectory. The optics design was carried out using the code TRANSPORT. At no point in the system, except in the dipoles, is the beam larger than 2.5cm radius. In most locations, the size is substantially less. In the input section, far from the detector, the beam is slightly larger. In the superconducting dipole, the vertical size reaches 3.5cm. This is a good location because the strong magnetic field provides shielding, in addition to material used in this location. Additionally, the large size in the dipole is due to the stringent focusing requirement downstream. By permitting a larger beam spot on the target, the size in the dipole can be reduced proportionally. This tradeoff will have to be carried out during commissioning of the beam.

The figure shows the oscillation of the beam envelope characteristic of an alternating gradient quadrupole channel. The peaks and valleys are uniform in the vertical coordinate, but display a beat pattern in the horizontal coordinate that is due to the imperfect matching achieved by using only two quadrupoles at the input end, as discussed previously.

Table 5.2. Parameters of the calculated input beam, including the diagonal elements of the beam matrix expressed as beam sizes along the corresponding half axes, and the correlations in standard TRANSPORT notation. These parameters are taken to be twice the beam standard deviation.

INPUT BEAM PARAMETER	*VALUE*
(1) Horizontal half size (x)	1.11cm
(2) Horizontal angular half size (x')	1.733mr
(3) Vertical half size (y)	0.537cm
(4) Vertical angular half size (y')	4.03mr
(5) Bunch length (l)	270ns
(6) Momentum bite half size (δp)	0.3 %
Central trajectory momentum	1.464 GeV/c

CORRELATION	*VALUE*
x',x	0.791
y,x	−0.003
y,x'	−0.026
y',x	−0.048
y',x'	−0.097
y',y	0.29
l,x	−0.044
l,x'	−0.351
l,y	−0.091
l,y'	0.12
δp,x	−0.088
δp,x'	−0.386
δp,y	−0.067
δp,y'	0.138
δp,l	0.999

Given complete and final knowledge of the input phase space, this design can be used to determine the magnet apertures required to achieve the low losses that can be tolerated by the detector. The magnet designs and cost estimates made for this study have used six-inch gap heights for dipoles at the upstream end, consistent with the current Line D aperture, eight-inch quadrupole diameters through the alternating-gradient section, twelve-inch bore for the superconducting dipole, and ten-inch diameter for the final triplet. This progression is designed to accommodate the emittance growth due to space charge.

Figure 5.4 shows the dispersion matrix elements (x,δp) and (y,δp) along the line. Through most of the transport, momentum dispersion is small, insuring low sensitivity to the possibility that the input beam has a larger momentum bite than predicted.

Figure 5.5 plots the phase advance along the beam line. This quantity is useful in extracting the phase space from beam profile measurements made at selected locations. We shall discuss this later.

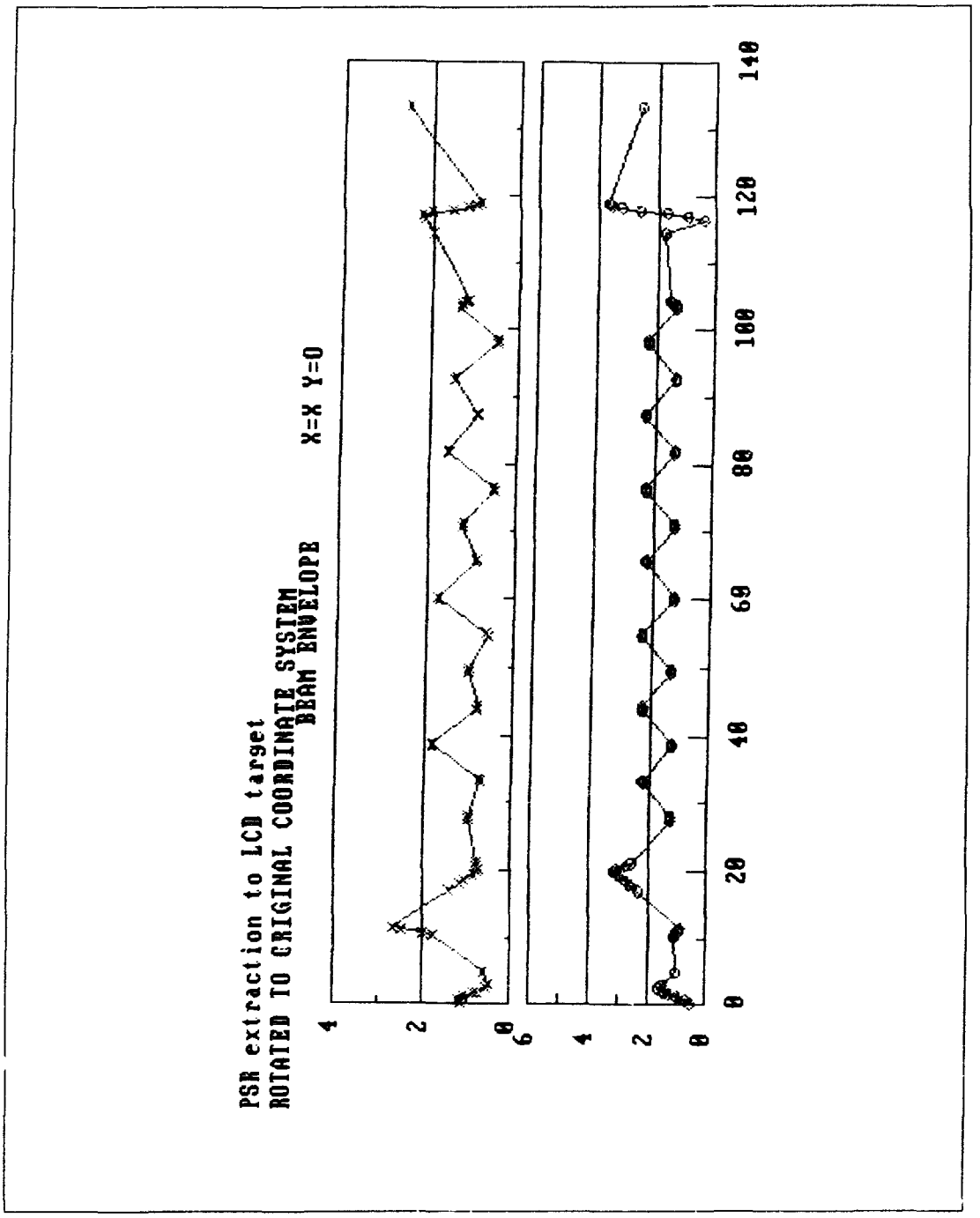

Fig. 5.3. Beam envelope of the calculated tune of the new beam line. The horizontal and vertical beam radii are plotted as a function of distance along the central trajectory. Since the beam is not parallel to the floor at all locations, this coordinate differs from the floor layout positions.

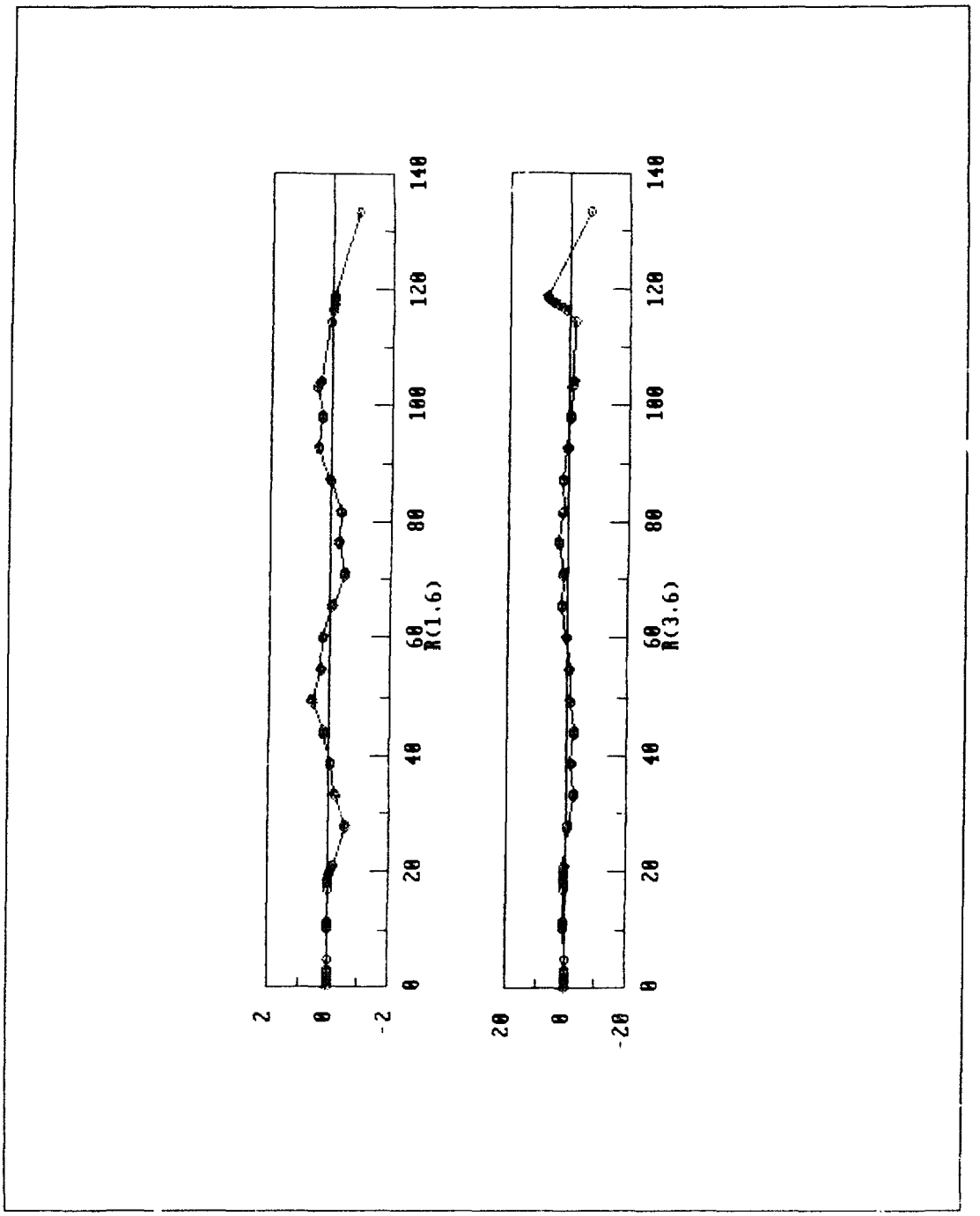

Fig. 5.4. Dispersion along the beam line. The matrix elements for the (x,δp) and (y,δp) correlations are plotted in units of cm-%.

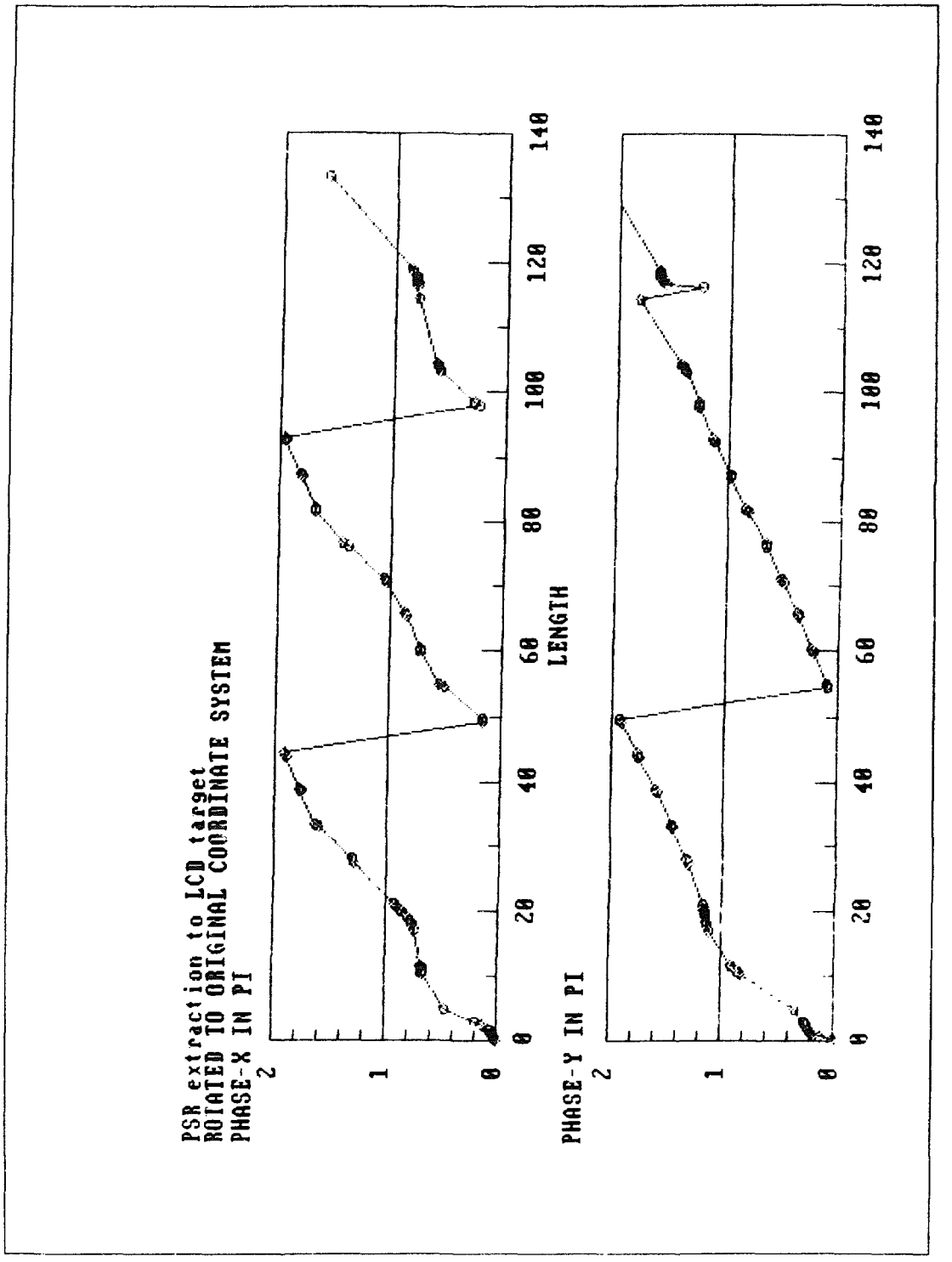

Fig. 5.5. Phase advance of the beam along the central trajectory.

Space Charge

Figure 5.6 shows a typical time distribution of a PSR pulse. The shape is approximately triangular, with a base length of 270ns, and an area of 5.0×10^{13} protons with 100 microamperes circulating. This corresponds to an average current of 100 microamperes, during 12-Hz operation. The peak current in a single pulse is $\sim$ 60 amperes. This very high charge density can lead to instabilities and emittance growth due to space-charge repulsion. Preliminary studies have been made to determine the severity of this effect. These studies indicate that non-linear tails may develop on the beam distribution in space, and that the beam core may grow slightly. This development can be accommodated by increasing the magnet apertures, as previously discussed.

Using the code SCHAR, the input phase described previously was transported through the magnets, up to the superconducting dipole, with all fields set corresponding to the TRANSPORT design described above. The TRANSPORT design did not include space charge. The effect of space charge at half the expected charge density was minimal. However, at the peak charge density of 61 amperes, the core emittance grew by 30%, and non-linear tails were indicated. Figure 5.7 shows a distribution of the beam at the entrance to the superconducting dipole. The non-linear halo is indicated.

This calculation would imply two modifications to the zero-charge-density design carried out using TRANSPORT. First, larger apertures would be required at the output end. For this reason, we have more than doubled the aperture area of the final triplet. Second, the constant but alternate settings of the quadrupoles in the alternating-gradient channel will be progressively inappropriate for the growing phase space. In order to retune the quadrupoles along the channel to account for the emittance growth, but to achieve the same transport performance, an interactive procedure is required. This algorithm must include the effects of space charge accurately and must permit fitting for the same optical requirements used in the TRANSPORT study.

A preliminary study has commenced, using the code TRACE in a form available at Los Alamos. This version includes space charge effects. As the PSR phase space is measured more accurately, an integrated retune of the beam line, including space-charge, will be carried out.

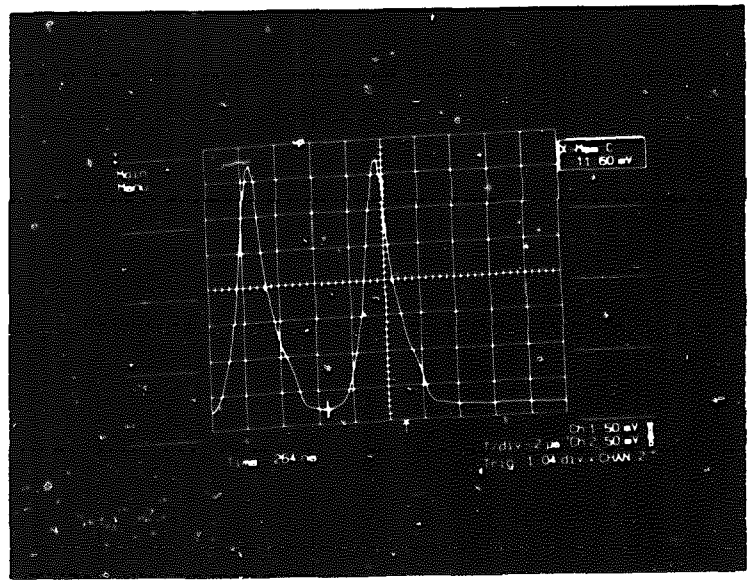

Fig. 5.6. Time distribution of typical PSR pulses.

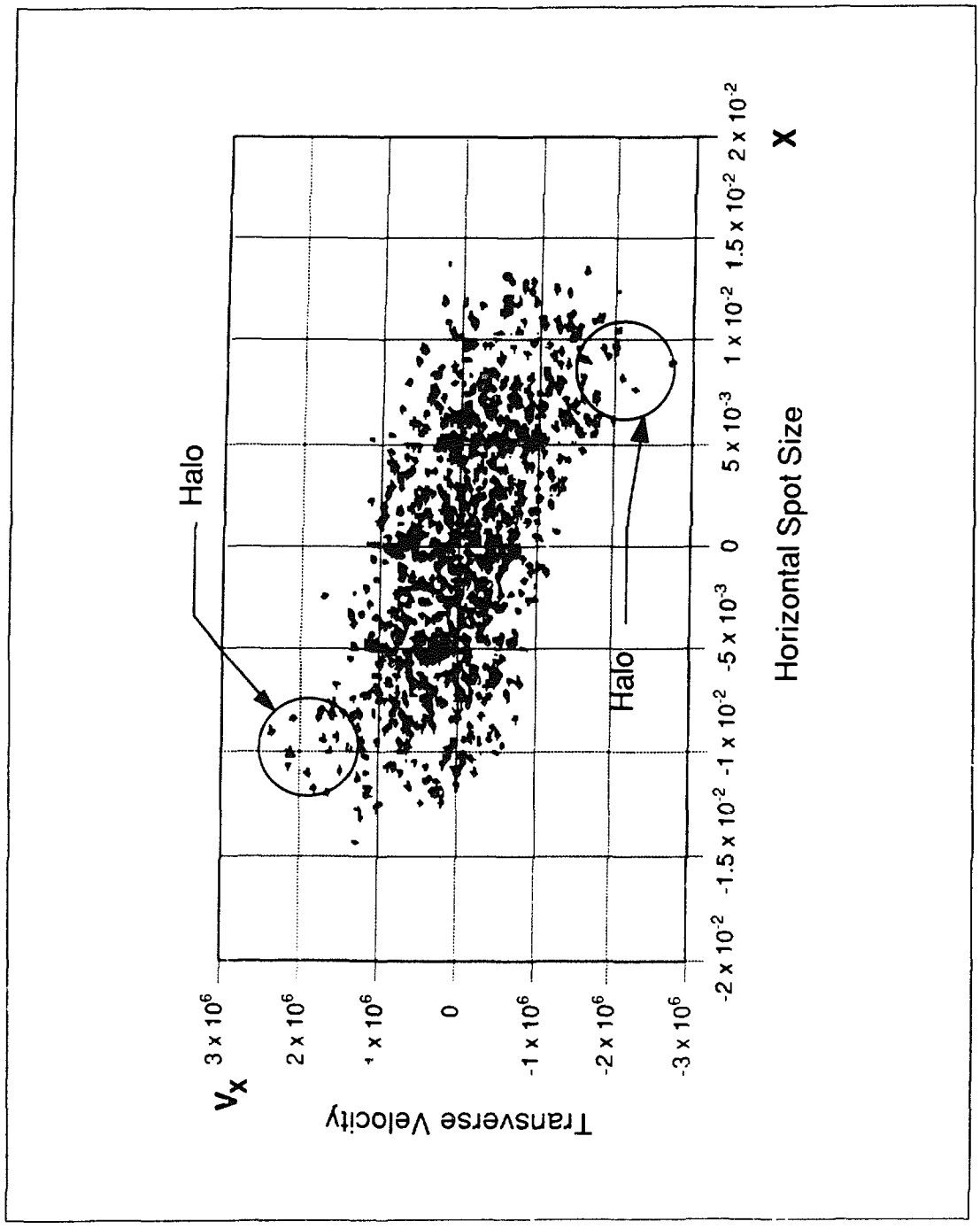

Fig. 5.7. Distribution of the beam in horizontal position vs. horizontal velocity at the entrance to the superconducting dipole. The calculation was done using the code SCHAR, which includes the effect of space charge. The resulting halo is indicated.

5.3 Superconducting Dipole

The 90° bending magnet must introduce no significant distortion of the beam phase space, other than those inherent in a true dipole. While the beam design has been carried out with an ideal TRANSPORT dipole, construction of this magnet will necessarily involve minimizing higher multipoles, tailoring fringe fields, controlling aperture focusing, and preserving high field homogeneity.

Two questions arise immediately in considering a magnet of this type. Have magnets been built sufficiently similar to this dipole to encourage confidence that the necessary technology exists in industry, or is this dipole inherently a development project fraught with risk? Can the required field quality be achieved?

Meetings have been held with seven industrial firms experienced in the design and construction of large superconducting magnets. The firms were from the USA, United Kingdom, West Germany, Switzerland, and Italy. Specifications for the magnet were provided to each firm. Five of the seven firms expressed interest in this project. Several examples were provided of technically similar magnets in production or in the field.

Based on these contacts, it appears that this dipole is a feasible commercial magnet. A pair of dipoles has been delivered to BESSY, for use as a synchrotron radiation source. These magnets are air-dominated, highly corrected for higher order effects, bend the beam by 180°, and have the outside radius of the bore and cryostat open to allow synchrotron radiation to exit the gap. They operate at 4.5T. They were produced by Interatom GmbH, a subsidiary of Siemens.

An iron-dominated dipole, also constructed for synchrotron radiation production, has been produced by Brown, Boveri et cie, and a magnet for application at Darmstadt has been designed by Oxford Instruments. Other complex magnets with related technology have been produced by Ansaldo (Genoa) and GA Technologies.

Prior to opening bidding on this magnet, a detailed design of the required field uniformity will be made using the same codes previously used at LAMPF for the design of the "Clamshell" spectrometer and the Medium Resolution Spectrometer. The results of this study will be combined with other specifications to generate a request for proposals for a full technical feasibility study. We expect to let contracts with two firms for parallel studies. Based upon experience, this is necessary to adequately cover the range of technical choices. The results of these studies will enable the final technical specifications to be determined for production bidding.

The design of the magnet will interact strongly with the facility design, given the location of the magnet under a great deal of shielding and above the central detector assembly. For this reason, it is one of the first items that will require final, detailed design.

These considerations also dictate the cryogenic concept selected. Given the location, it would not be feasible to incorporate a closed-loop Helium liquifier in the system. Close quarters, inaccessibility, and high stray fields dictate a simple, but contemporary, low-loss cryostat to be manually topped up at intervals of several weeks. This may require the use of persistent switches.

5.4 Target System

Since the vertical string containing the final triplet, diagnostics, collimators, and target assembly is difficult to maintain, it must be designed and constructed to the most conservative standards possible. For this reason, the target design is extrapolated from an existing system, with which a great deal of experience has been accumulated.

The target system is based on the LAMPF A-6 beam stop. This design has been in use since 1975 with essentially no operational problems. The beam stop at A-6 has been exposed to the full milliampere of LAMPF beam during that time.

The beam stop consists of multiple plates of high-purity oxygen-free copper, cooled on both sides, contained in a stainless steel shell. It is cooled at the rate of 2.5 gallons/minute for a total flow rate of 75gpm. It is surrounded by stainless steel water-cooled shielding to reduce the heat load to the surrounding structure.

The target capsule is shown in Fig. 5.8, and consists of the target of copper plates contained in a stainless steel or Inconel 718 can with hemispherical heads. Although the present LAMPF A-6 beam stop has flat heads, the extremely high stresses, especially under exposure to a pulsed beam, make the fatigue life of flat heads limited. The target is surrounded by stainless steel water-cooled shielding and has a water-cooled collimator immediately upstream, as shown in Fig. 5.9 and 5.10. The entire assembly will be suspended from above with the upstream vacuum line that, with the water lines, will run a sufficient distance to allow hands-on hookup and maintenance. A number of thermocouples will be placed on the target assembly to monitor all the critical areas, with a high level of redundant coverage.

The design has been made assuming an 800-MeV beam, 200 microampere average current, a 1.27-cm beam spot (σ), and a 12-Hz repetition rate. The assembly was analyzed using the ABAQUS finite-element code. This calculation yielded the temperature distributions in the assembly. Stress calculations were done on the hemispherical windows, and heating calculations were also carried out for the water-cooled shielding and the collimators. All calculations indicated that the design is conservative.

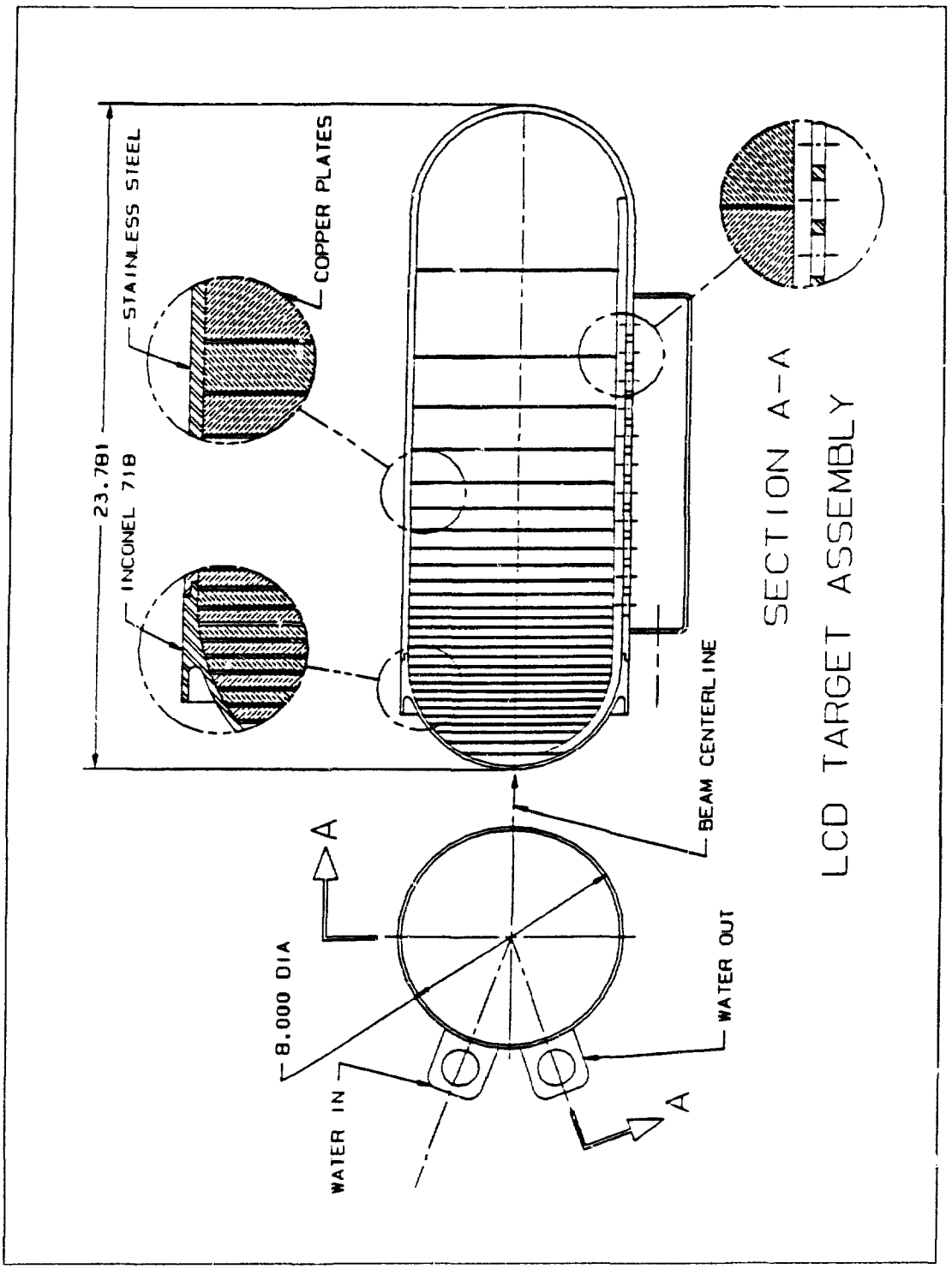

Fig. 5.8. Target assembly.

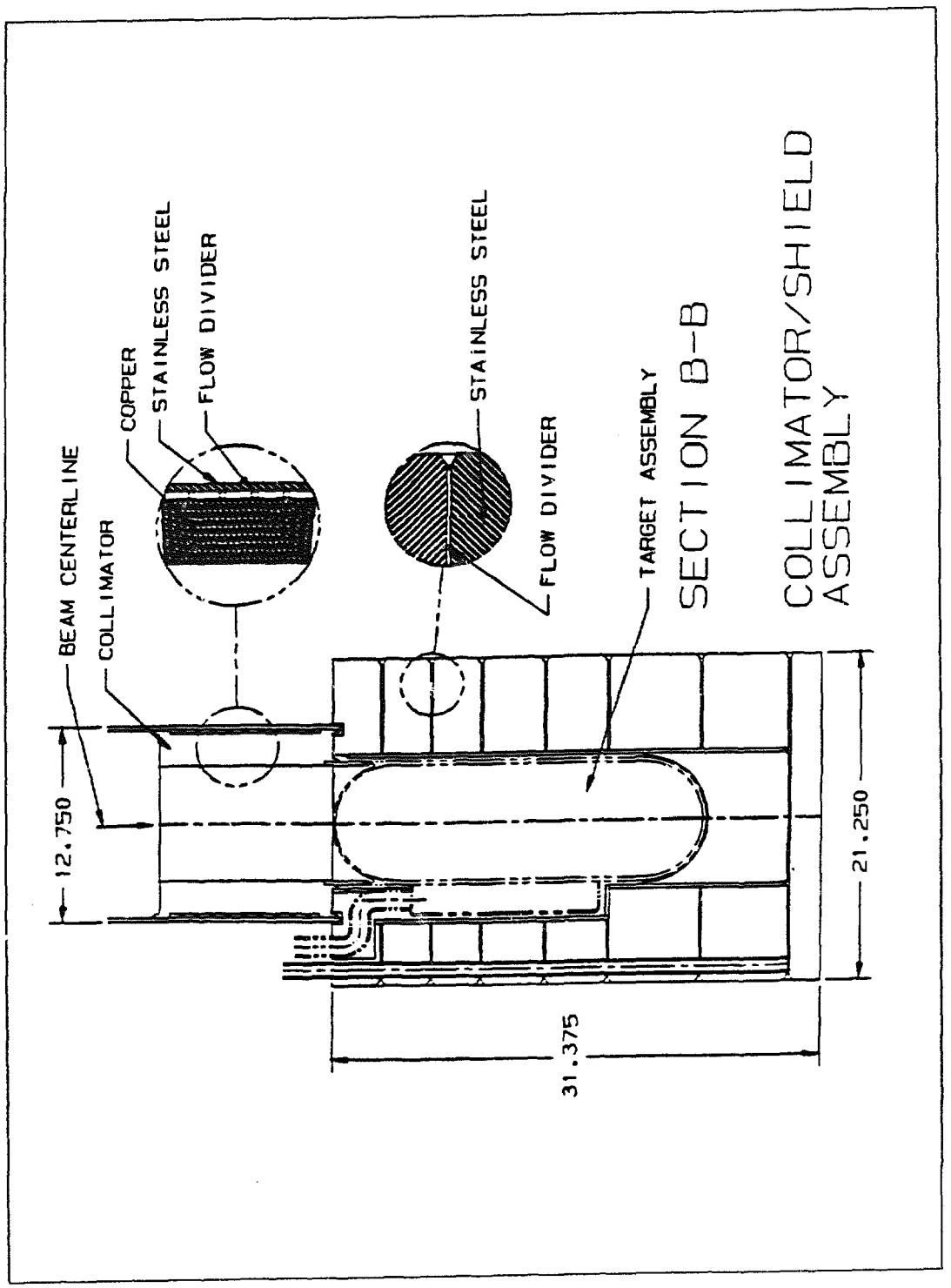

Fig. 5.9. Collimator/shield assembly.

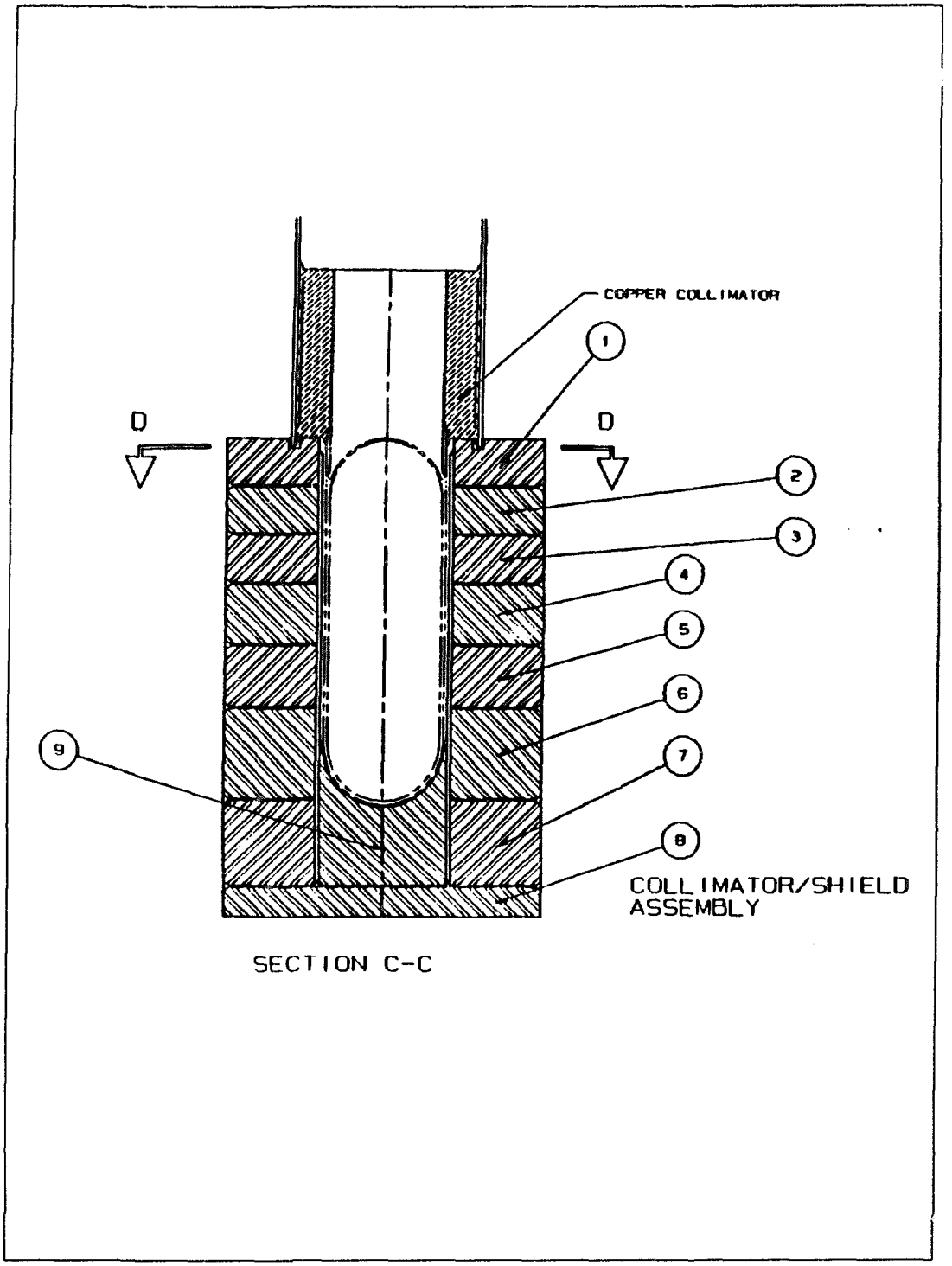

Fig. 5.10. Collimator/shield assembly.

5.5 Beam Controls and Measurement

Control of the facility will be through a MicroVax-based console located in the PSR control room. The hardware and software employed will be fully compatible with the PSR system. PSR operators will be able to monitor and control magnet currents, cooling, vacuum pumps and valves, cryogenics, water-purification, beam profile and position, beam losses, target assembly cooling, personnel access, and detector tank environment.

The diagnostic devices required for beam tuning and monitoring are specified in Fig. 5.11. The system requires ten two-coordinate, 8" aperture harp assemblies on actuators, three current monitors, five fast-protect ion chambers and a secondary emission monitor, and guard-ring system. The locations shown in the Figure are necessary to verify the beam size and position and the optical conditions at key locations and to prevent unacceptable beam spill. Each of the harp locations is specified to verify a required optical condition, typically a beam waist, as well as the profile and position. The current monitors, fast protect chambers, and guard rings are designed to monitor losses.

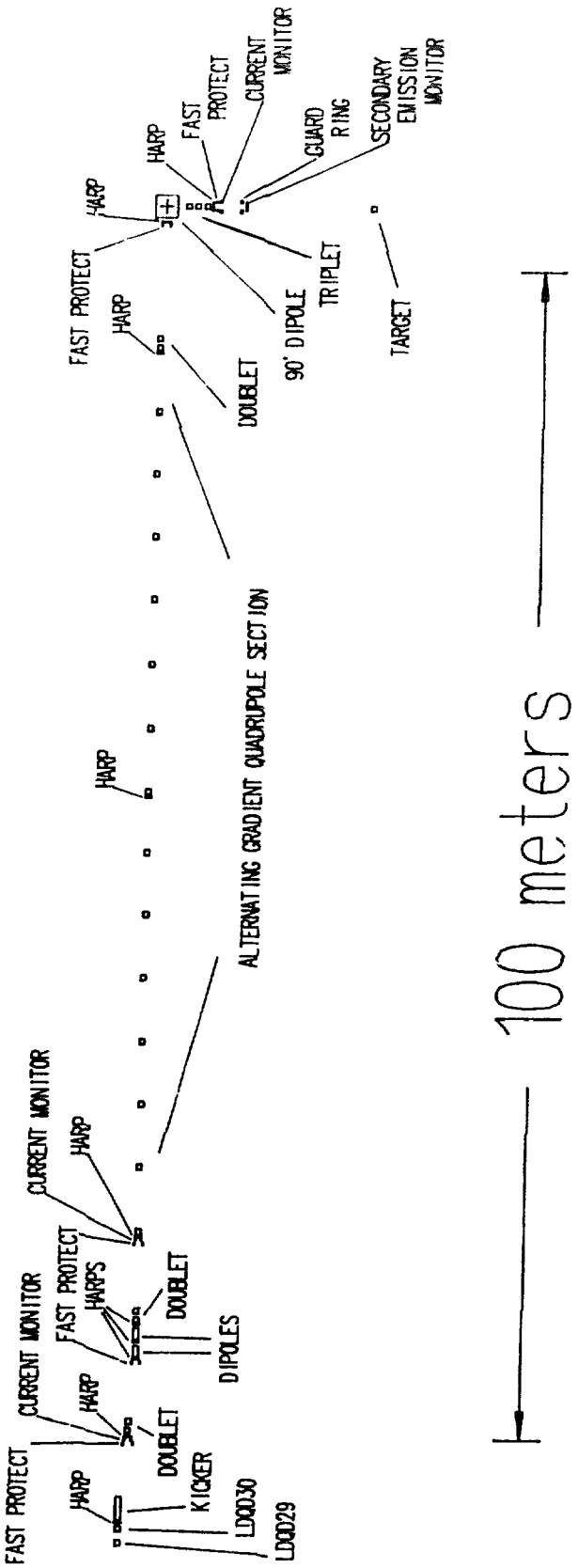

Fig. 5.11. Elevation view of the beam line showing all planned beam diagnostic locations.

6 NEUTRINO AND ELECTRON FLUX

During the "prompt" time interval corresponding to the 270-ns proton beam spill, 95.3% of the ν_μ and 4.8% of the ν_e and $\bar{\nu}_\mu$ are produced. About 70% of the events in this time region are $\nu_\mu e$ events and 30% are $\nu_e e$ and $\bar{\nu}_\mu e$ events. The percentages of the events for the three elastic reactions that result in an electron above threshold (10 MeV) are 59%, 67% and 63%. The systematic error on R due to measurements of the beam-spill shape is estimated to be <0.15%.

6.1 Spill Time Distribution

Pions are created from proton interactions in the beam stop, and the different neutrinos are then produced by the decay of π^+ into ν_μ and μ^+, with subsequent decay of the μ^+ into e^+, $\bar{\nu}_\mu$ and ν_e. Because of the short lifetime of the π^+ (τ_π = 26.03ns), the production of ν_μ closely follows the time profile of the PSR proton beam spill. The production of $\bar{\nu}_\mu$ and ν_e is delayed by the longer μ^+ lifetime (τ_μ = 2197ns), so that most of the $\bar{\nu}_\mu$ and ν_e are produced a few microseconds after the end of the beam spill.

The quantitative rates of ν_μ and ν_e ($\bar{\nu}_\mu$) production as a function of the proton beam spill are given by following integral formulas:

$$N_{\nu_\mu}(t) = N_\mu(t) = \int_0^t \frac{1}{\tau_\pi} N_\pi(t') \exp(-\frac{t-t'}{\tau_\pi})\, dt'$$

$$N_{\nu_e}(t) = \int_0^t \frac{1}{\tau_\mu} N_\mu(t') \exp(-\frac{t-t'}{\tau_\mu})\, dt'$$

where $N_\pi(t)$ is the π^+ production rate in the beam stop target as a function of time, and $N_\mu(t)$ is the corresponding μ^+ production rate. Because the $\bar{\nu}_\mu$ and ν_e are produced in pairs, only the ν_e rate is listed.

An isosceles triangle is taken as the typical beam spill profile (as discussed in chapter 5) and is used as a reference to gauge the effect of spill variations on the composition of the neutrino flux. Figure 6.1 shows the neutrino time distributions from this triangular beam spill. During the 270ns spill, 95.3% of the ν_μ and 4.8% of the ν_e and $\bar{\nu}_\mu$ are produced. Because the $\nu_e e$ elastic scattering cross section is so large, 70% of the events in this time region are $\nu_\mu e$ events and 30% are $\nu_e e$ and $\bar{\nu}_\mu e$ events. In the region after the end of the spill, $\nu_e e$ and $\bar{\nu}_\mu e$ events dominate. Less than 0.5% of the events in this region are from $\nu_\mu e$ scattering.

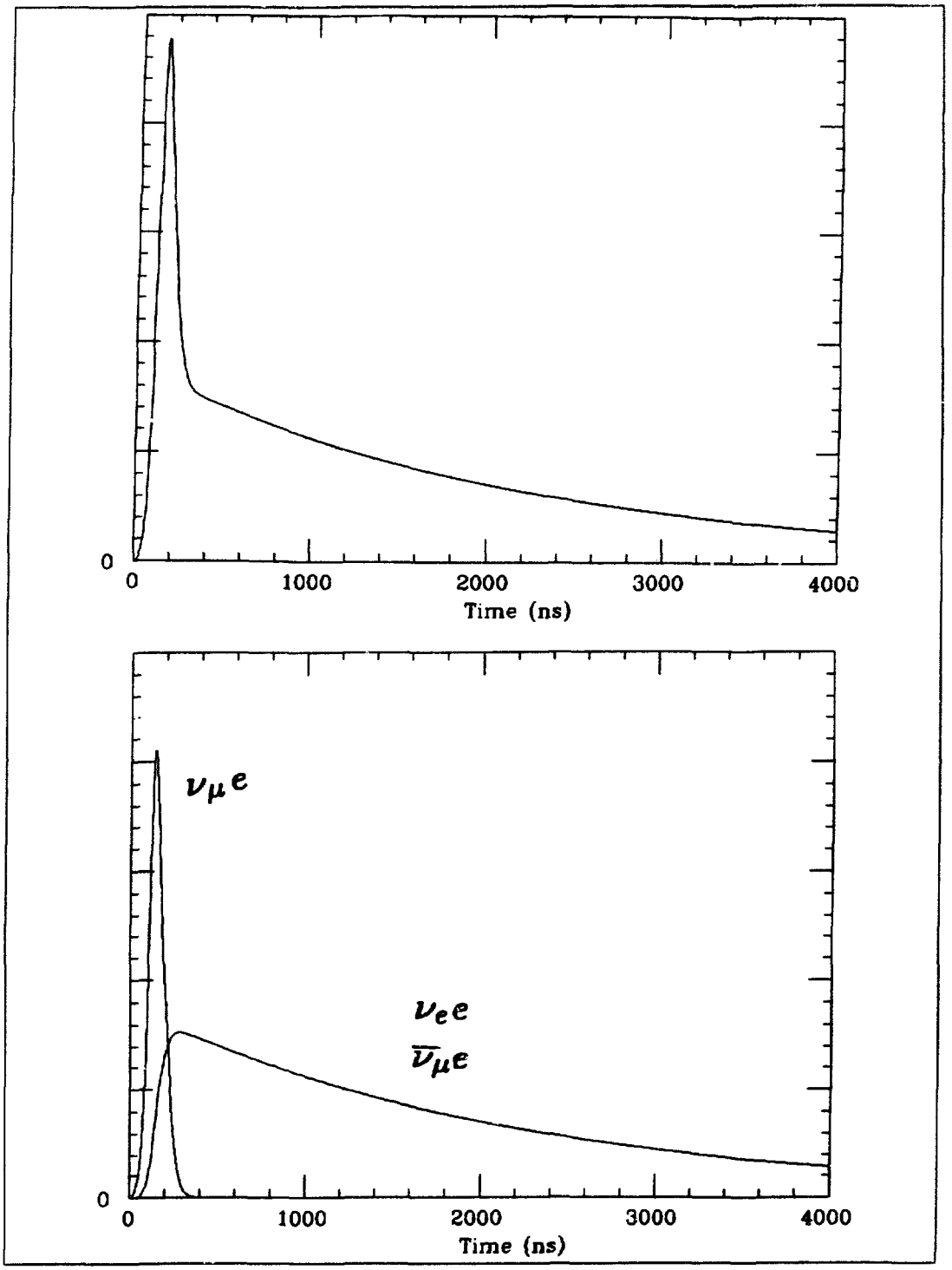

Fig. 6.1. Time distribution of neutrino events from the beam stop in ns.

6.2 Spill Measurement

The actual PSR beam pulse time-distribution will be monitored for every spill, and a digital record will be made. At the end of the run, the time average will be determined by summing over all spills. We expect to measure the absolute time offset to a precision of < 1ns; however, this serves only as a check of our maximum-likelihood fitting technique (see section 7.6), which will fit the time offset to < 0.1ns. The resulting systematic error on our value of R is < 0.08%. Note that it is desirable that we keep the PSR and experiment clocks stable, although we need not know the absolute values. In addition to the absolute time offset, we will measure the average PSR spill shape to high accuracy. We have investigated the effect on R due to measurements of the beam spill shape with varying accuracy. Table 6.1 shows the systematic error on R as a function of time bin size and resolution, assuming a triangular spill. The time bin size is the time interval over which we digitize the spill (averaging over the time interval), and the resolution is the accuracy with which we measure each time bin. We plan to use time bins of $\leq$ 10ns and have amplitude resolutions < 2.5% for each bin. Interpolating from Table 6.1, the systematic error on R is < 0.15%.

Table 6.1. Systematic Error on R Due to Spill Measurement.

Time Bin	*Resolution*	*Systematic Error*
5ns	0%	0%
5ns	5%	$0.23 \pm 0.12\%$
5ns	10%	$0.33 \pm 0.10\%$
5ns	15%	$0.50 \pm 0.09\%$
5ns	20%	$0.67 \pm 0.08\%$
10ns	0%	0%
10ns	5%	$0.23 \pm 0.12\%$
10ns	10%	$0.35 \pm 0.10\%$
10ns	15%	$0.64 \pm 0.09\%$
10ns	20%	$0.78 \pm 0.08\%$

6.3 Neutrino Spectra

Many of the features of this experiment are possible because of the unique characteristics of neutrinos produced from low-energy (nominally 250 MeV) pions that stop in the target. The neutrino spectral shapes are known to high accuracy and are a composite of pion and muon decays at rest and a small component of pion and muon decays in-flight. Because 250-MeV pions have a range and interaction length of about 10cm in copper, the in-flight component arises from decays within the target material before the pions and muons lose all of their kinetic energy. To calculate the in-flight contribution accurately, it is necessary to employ a Monte Carlo simulation. The in-flight neutrino spectrum entering the detector is dependent upon the angular distribution of pions produced in the target, the energy loss of pions in the target, the interaction and absorption of pions in the target, and the kinematics of in-flight pion decays that result in the neutrino spectrum being forward-peaked. A modified version of the CERN program NUBEAM was chosen as the basic simulation code. Measured pion double-differential cross sections off carbon, as shown in Fig. 6.2 were used, and energy loss was added to the program. Figure 6.3 shows the resulting ν_μ spectrum as a function of energy. The spectrum is dominated by the 30-MeV peak containing neutrinos produced from pion decays at rest, and there is a high-energy component of about 1% from in-flight pion decays. The resulting ν_e and $\bar{\nu}_\mu$ energy spectra are also shown in Fig. 6.3. The background from muon decay in-flight is negligible (about .0001%) and is therefore not considered. The average neutrino energies vary from 30 to 35 MeV for the three processes.

6.4 Electron Spectra

Using the neutrino-electron-differential cross sections discussed in section 1.3, we can obtain the electron-energy distributions for a nominal value of $sin^2\theta_W$=0.23. Figures 6.4-6.6 show the electron energy distributions from the reactions $\nu_\mu e$, $\nu_e e$, and $\bar{\nu}_\mu e$, respectively; about 59%, 67%, and 63% of the electrons in the three reactions have energies greater than 10 MeV. (The percentages are 41.8%, 52.1%, and 48.6% for a 15 MeV energy cut.) For events with electron energy greater than 10 MeV that are successfully reconstructed, the average electron energies for the three reactions are 19.7 MeV, 23.4 MeV, and 24.3 MeV, respectively.

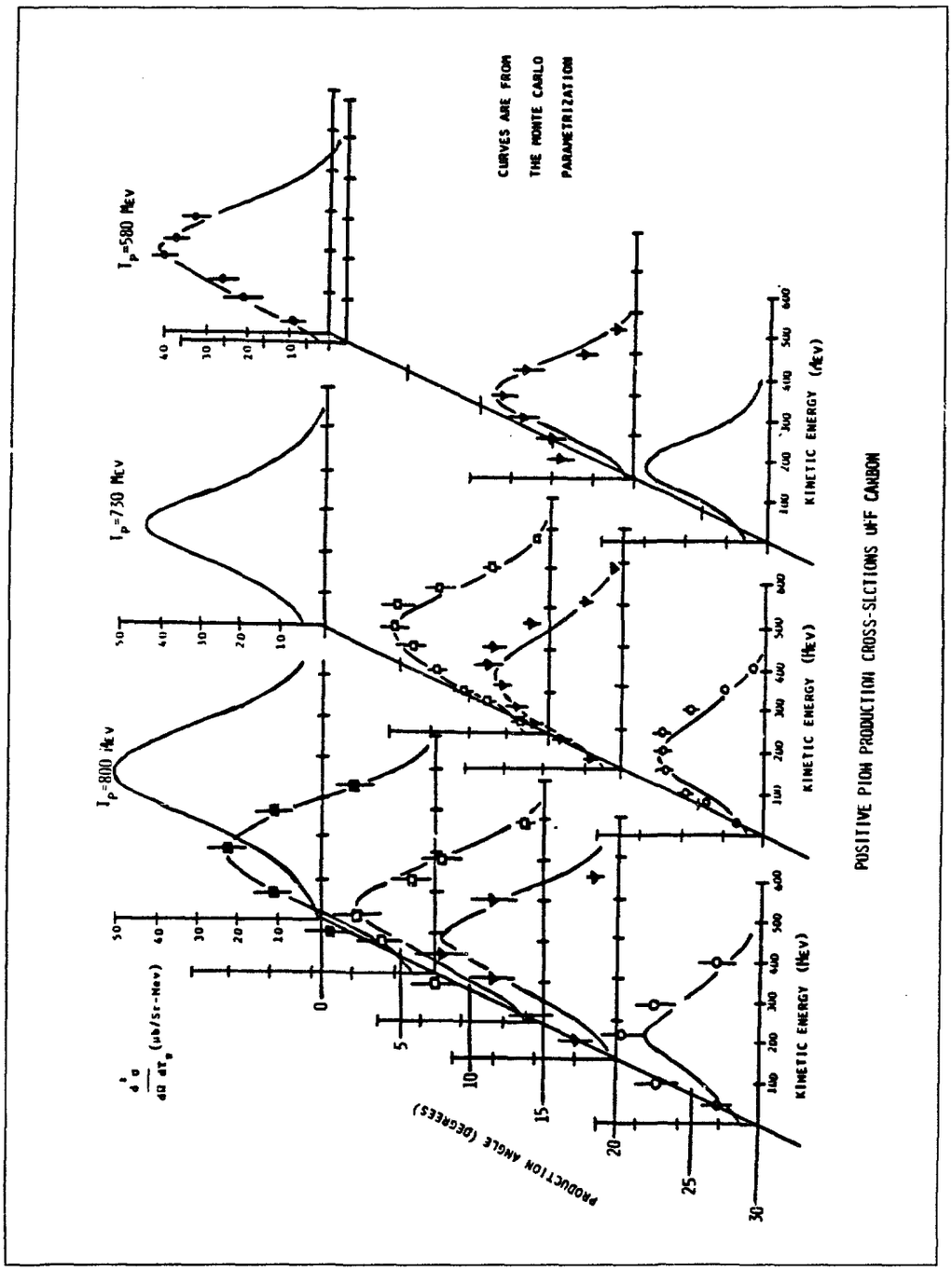

Fig. 6.2. Measured pion double-differential cross sections.

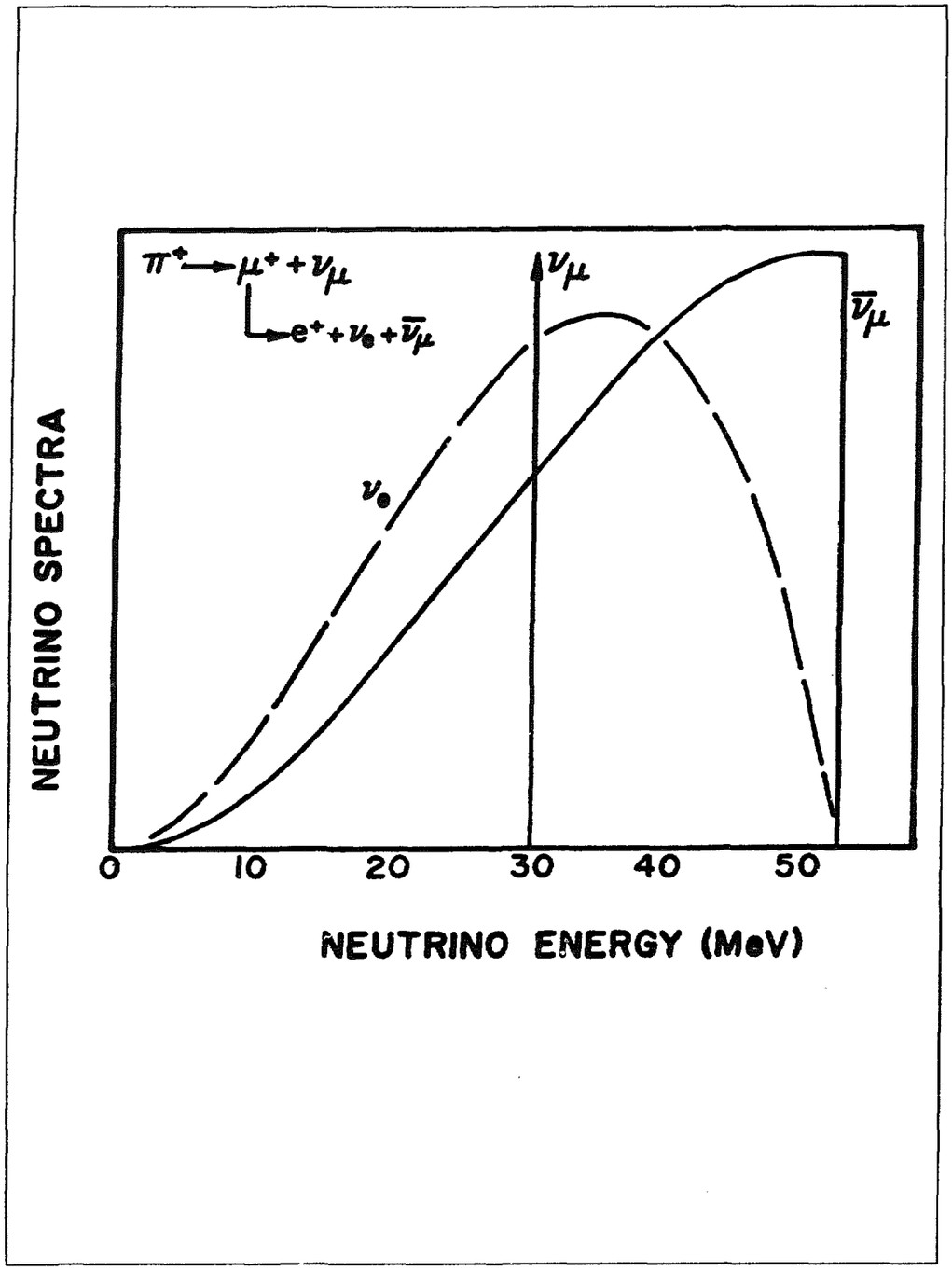

Fig. 6.3. The ν_μ, ν_e, and $\bar{\nu}_\mu$ energy spectra.

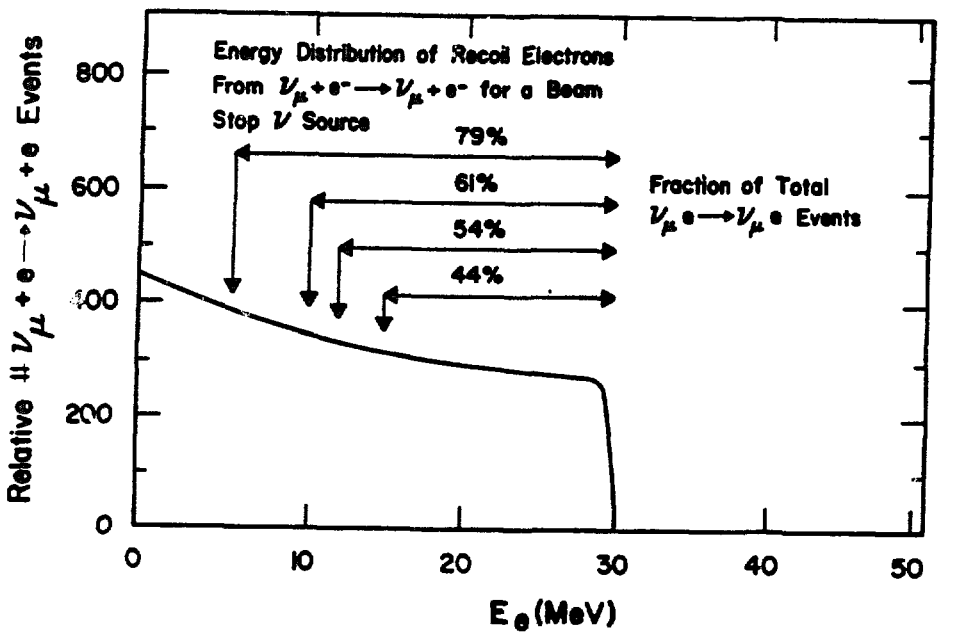

Fig. 6.4. Electron-energy spectrum from $\nu_\mu e$ interactions.

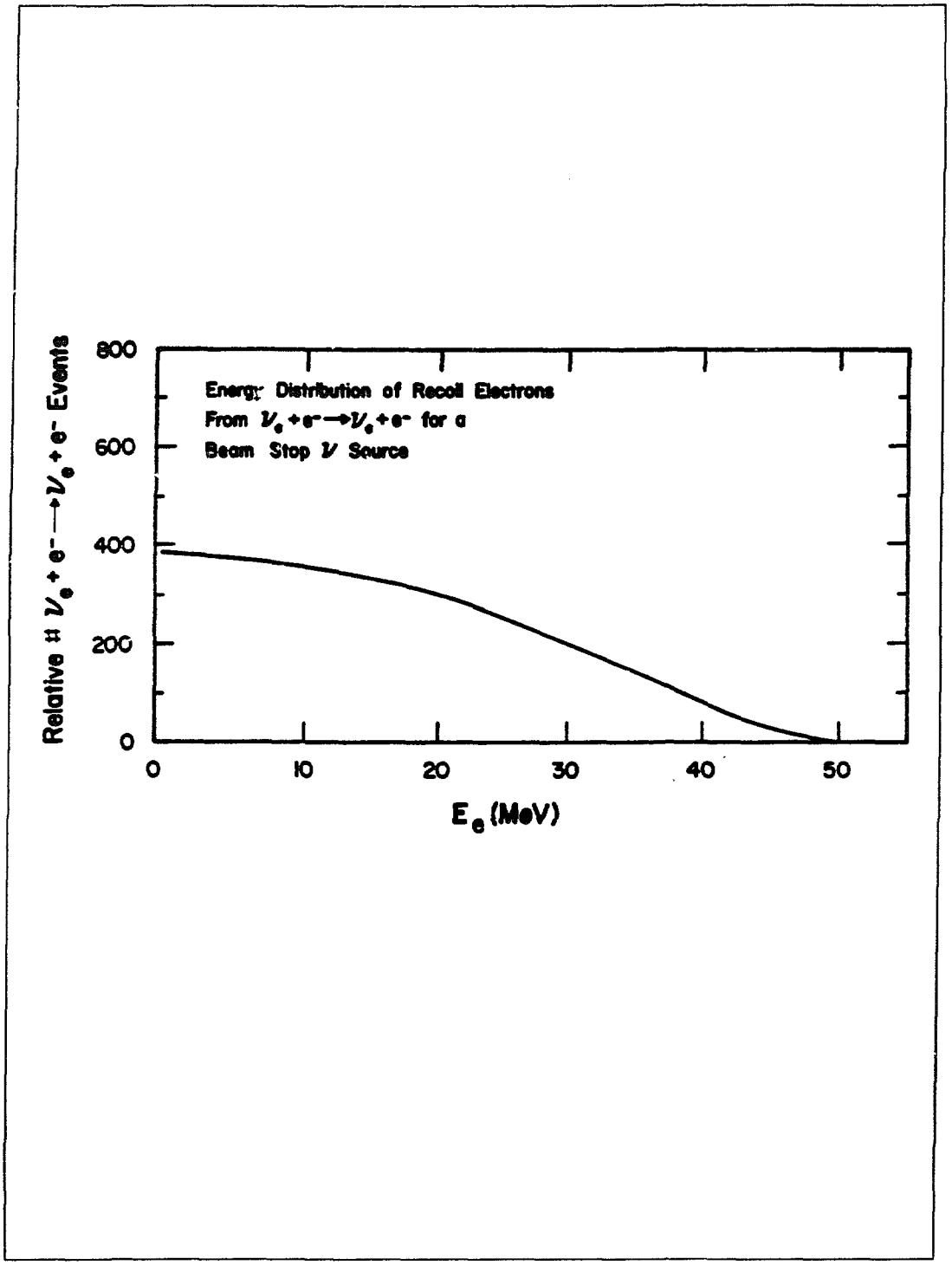

Fig. 6.5. Electron-energy spectrum from ν_ee interactions.

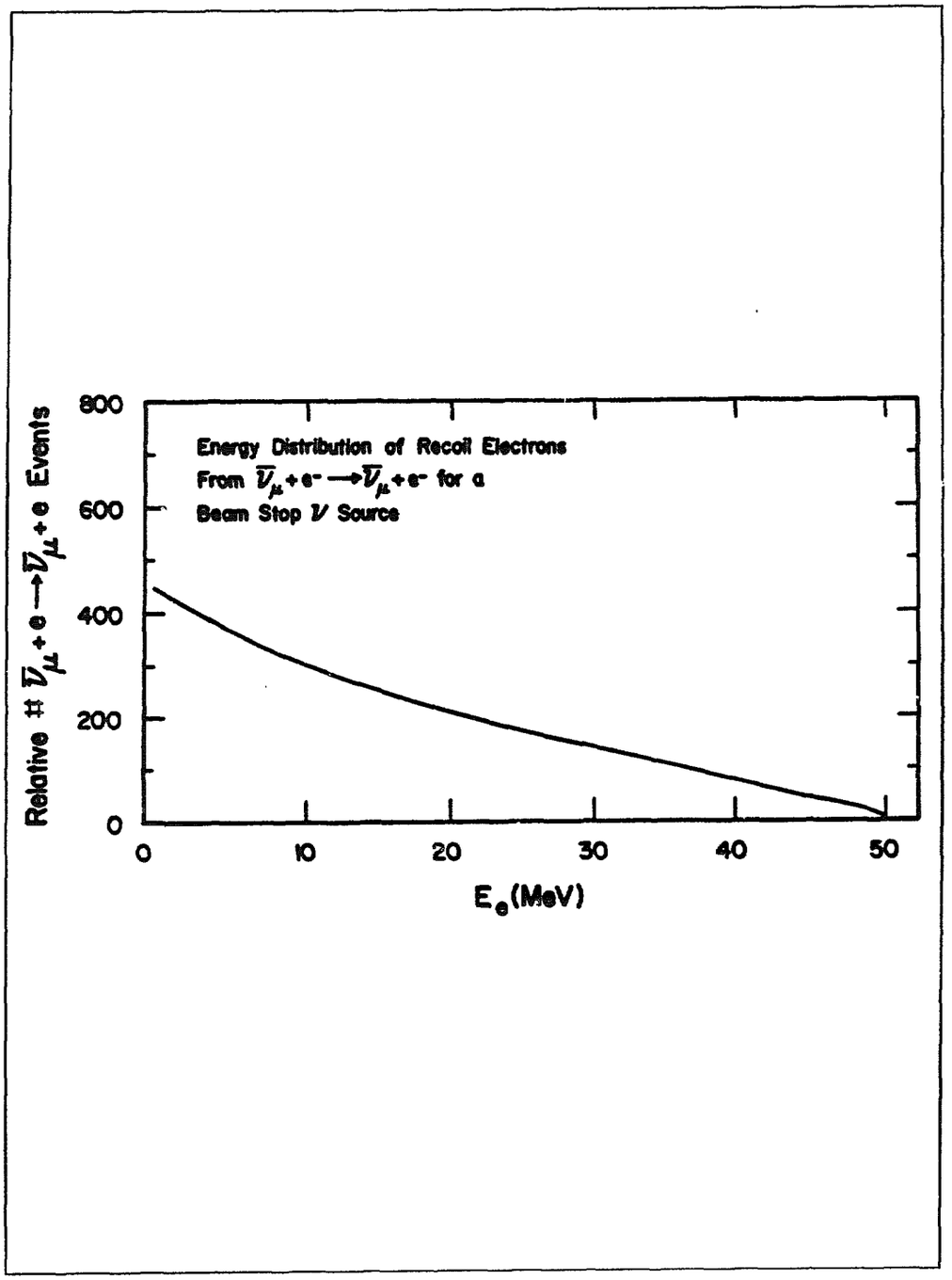

Fig. 6.6. Electron-energy spectrum from $\bar{\nu}_\mu$e interactions.

7 BEAM-INDUCED BACKGROUND

The systematic errors in R due to neutrino-related and neutron-induced backgrounds are: ν_e - O scattering (<0.5%), pion decay in flight (0.12%), neutron-induced photons (0.45%), neutron-induced pions (0.20%). Contributions from neutral-current excitation of ^{16}O and from neutrinos produced in β decay of radioactive isotopes in the target are negligible. Neutron-induced background errors from ground shine and from beam loss in transport can be made much smaller than the errors given above by appropriate shielding.

In this chapter, we analyze background events in the detector that are associated with the proton beam. These events can be broadly characterized as neutrino-related and neutron-induced.

The principal neutrino-related background arises from the charged-current interaction of ν_e with the various isotopes of oxygen, resulting in an electron. Neutral-current excitation of $^{16}0$, resulting in a gamma ray, is also considered. Pion decay in flight is a source of error because the analysis assumes that both the pion and muon decay are at rest. Neutrinos produced by β decay of radioactive isotopes in the target also are a potential background.

Neutrons will produce photons in the detector as well as pions, which produce Čerenkov light themselves and decay, producing background electrons and photons. These events, unlike the neutrino-related background, are directly influenced by the shielding design. The time structure of these events is critical; therefore, "prompt" (~pion lifetime) and "delayed" (~muon lifetime) time intervals are distinguished.

An important tool in analyzing the neutron-induced background is the Monte Carlo code HETC (High Energy Transport Code). Equally important is our ability to normalize the neutron spectrum generated with HETC using existing data from Experiment 225, a previous LAMPF neutrino experiment.

Neutrons primarily enter the detector by directly penetrating the iron shield. Other paths include ground shine and back-scattering in the magnetite column above the shield. Our proposed shielding configuration is very close to optimum; however, we are still fine-tuning the design. The studies described in this chapter are also on-going, and new results will enable us to further improve the shielding design. To test our calculational results, we plan to experimentally determine these production cross sections in the near future, using neutron beams produced at LAMPF.

7.1 Neutron Induced

7.1.1 Neutron Shielding - Calculations

The primary background source emanating from the production target into the sensitive region of the LCD detector is neutrons penetrating the target shield. To characterize the effectiveness of various shield configurations, both empirical and calculational information have been used, with the empirical information providing a normalization of the calculated results. The best method for calculating yields from thick targets and for transporting reaction products through thick shields is the Monte Carlo method. This method allows incorporating all important physical processes, materials, and particles at all relevant energies so that a realistic model description is constructed. It is impossible to achieve the same results using strictly analytic calculations. The Monte Carlo method, however, is slow, and the precision is governed by the details of the input cross sections. In many cases, a lack of good experimental cross section data requires the incorporation of extrapolations from theoretical calculations or extensions of the available data into regions where no data exist. Comparisons with empirical measurements are the only way to determine the validity of the approximations used in the Monte Carlo calculations.

The Monte Carlo codes used are HETC and MCNP. HETC (High Energy Transport Code) is a code originally developed at the Oak Ridge National Laboratory that utilizes the intranuclear-cascade model of Bertini to describe the physics of the nuclear interaction.[1] The intranuclear-cascade products consist of emitted protons, neutrons, charged pions, neutral pions and a residual nucleus. Pion decay into a muon and neutrino is also included, although the neutrino is ignored. The energy and angular distributions of these products are sampled from empirical or theoretical distributions. HETC includes all neutron interactions above 20 MeV. Charged cascade products are included above a user-defined threshold (default values are: protons, 1 MeV; pions, 0.149 MeV; muons, 0.113 MeV), and all interactions above the threshold are included. Any neutron appearing from a reaction below the 20-MeV cutoff energy has its kinematic parameters stored in a file that can be accessed later by MCNP to complete the transport. MCNP (Monte Carlo Neutron Photon transport) is a general purpose, continuous-energy, coupled neutron-photon Monte Carlo code developed at the Los Alamos National Laboratory that is used to transport neutrons and photons with energies less than 20 MeV. The LANL versions of HETC and MCNP both use the same input geometry routines, so the coupling of the two codes provides a means of determining the neutron transport through the shield for all neutron energies. Both of these codes have been extensively tested

in a variety of empirical situations at accelerator laboratories, so confidence at the level of factors of ~ 2 or so is justified.

The primary mechanism for attenuating high-energy neutrons is by inelastic interactions with the shield. The most effective materials for removing neutrons are high-density materials such as uranium and tungsten. However, these materials are expensive and thus should not be used for massive shields. Instead, the most commonly used shield material is iron, because of its cost effectiveness. The goal of the design calculations is to define a composite shield of iron and, possibly, uranium that is cost effective and provides sufficient protection against neutron-induced background events, while being as thin as possible to minimize the number of phototubes.

To carry out the design, the target and shield configuration was divided into three regions. The first region includes the target and the surrounding water-cooled shielding out to a radius of 60cm. The second, intermediate, region may contain depleted uranium to provide the largest attenuation in the smallest volume. The third region is the remaining iron shield beyond the uranium. The iron will provide the bulk of the shielding while the uranium will minimize the shield thickness. The final configuration will be dictated by the relative costs of iron and uranium and the impact the shield radius will have on the cost of the building, phototubes, and electronics. The backgrounds computed herein assume no uranium; however, we show the effect on the neutron flux of replacing iron with uranium.

Although the Monte Carlo codes at our disposal are expected to give an adequate representation of the transport through thick targets and shields, they cannot be used to transport neutrons through the expected shield thickness of approximately 7m. About 1 hour of CRAY running time is required to reach attenuation factors of 10^{-5} to 10^{-6}. As attenuation factors of 10^{-15} are needed, we were required to find alternative methods to transport the neutrons through the remaining shield. We have chosen to use the Monte Carlo codes to define the neutrons exiting the target region, to use the codes to define the attenuation lengths in iron and uranium, and to use analytic techniques to transport the neutron flux through the bulk of the shield. This procedure is workable because the neutron spectrum shape is essentially unchanged after a few attenuation lengths in a material.

Target Volume

The target volume is arbitrarily defined to be everything within a 60-cm radius sphere whose origin is located at the intersection of the beam axis and the entrance face of the target. A schematic of the target volume is shown in Fig. 7.1. The target consists of copper disks, 1-cm thick, separated by 1-mm thick water-cooling passages. This design is similar to the beam stop design presently used for the

LAMPF high-intensity H^+ beam line, for which a vast amount of operating experience exists. Surrounding the target is a water-cooled iron shield. The remaining material, to a radius of 60cm, is either iron or uranium. The neutron flux at the 60-cm surface, for both the iron shield and the composite iron-uranium shield, both exhibit exponential attenuation. It is for this reason that the target boundary is defined to be at the 60-cm surface, and beyond this surface analytical techniques using exponential attenuation are used. The angle-energy distribution for neutrons at the 60-cm surface for the iron shield is shown in Fig. 7.2. The spectra show a decrease in neutron yield as a function of angle, with the energy distribution falling off more rapidly as the angle from the production target increases. This behavior is reasonable because the available energy for the scattered neutrons decreases as the scattering angle increases. The general shape of the neutron spectra as a function of angle is considered to remain constant as the neutrons are transported through the shield. To include some averaging as the neutrons travel into the shield, the neutron spectra are averaged over a 55° angle from 75°–130°. The resulting spectrum is then used for determining the background from neutrons entering the detector volume.

Calculation of Attenuation Lengths

Neutron transport through the bulk shield is simulated analytically by determining the attenuation lengths in uranium and iron, which were found to be 14.7 and 21.6cm, respectively, for high-energy (E_n > 20 MeV) neutrons. The neutron attenuation in uranium and iron is shown in Fig. 7.3. The attenuation length is insensitive to scattering angle, and an analysis of the attenuation length as a function of energy reveals very little dependence on energy within an energy group. The use of a constant attenuation for iron and uranium, independent of angle and energy, greatly simplifies the extension of the neutron transport through bulk shielding. The neutron-energy group below 20 MeV is transported with the MCNP code; the attenuation length in iron was found to be 32.5cm. The results are also shown in Fig. 7.3. The low-energy group is fed by downscattered neutrons from the high-energy group and depleted by inelastic events and capture. Low-energy neutrons (<20 MeV) produced directly from the target have an attenuation length less than 21.6cm and are removed in the first few meters of shield; therefore, they do not contribute to the total neutron flux at the shield boundary.

Neutron Attenuation in a Composite Shield

The calculations for the yield of neutrons from the target, together with the evaluated attenuation lengths for the composite materials, yield a family of curves that can be used to determine the required shield thickness. The results of the calculation are shown in Fig. 7.4 for $E_n > 20$ MeV. The curves represent the bulk shield of iron with the addition of 0.0,0.5,1.0 meters of uranium. The replacement of 1m of iron with 1m of uranium provides one order of magnitude of additional attenuation. The uranium, if used, would be located as close to the target as possible to reduce costs, but far enough away so that fission heating from neutron interactions would be at an acceptable level. The total number of neutrons (E_n >20 MeV) entering the water for a pure iron shield of 7.25m radius, in the 75°- 130° angular range, is equal to 1.6×10^4. This includes the attenuation due to 30cm of water in the veto region. If a normalization factor of 0.49 from experiment E225 (discussed in the next section) is included, then the total number of neutrons in the specified energy and angular ranges is ~8000 per day.

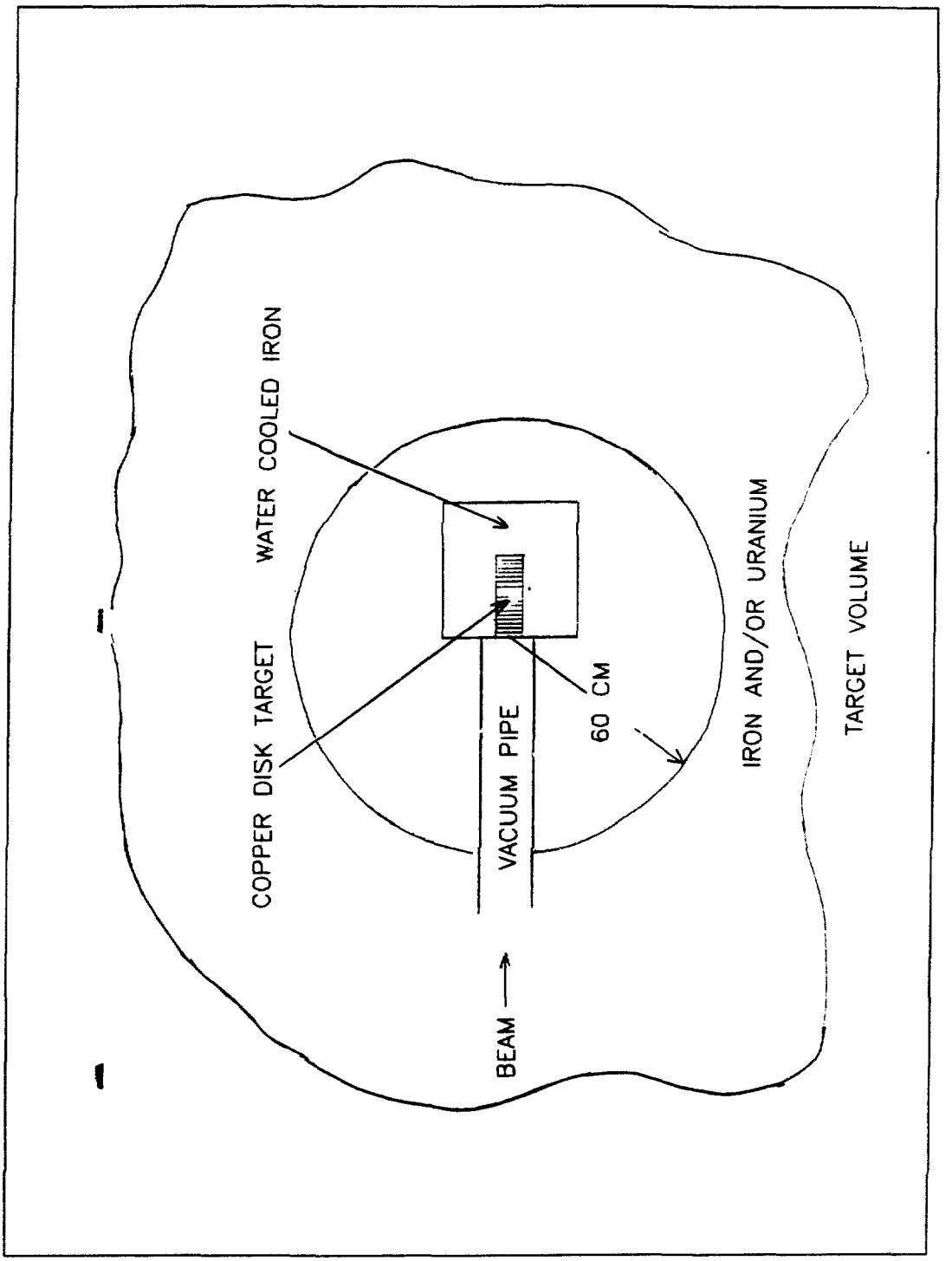

Fig. 7.1. The target volume consists of a central target of copper disks surrounded by water-cooled iron shielding and uncooled iron out to a radius of 60cm.

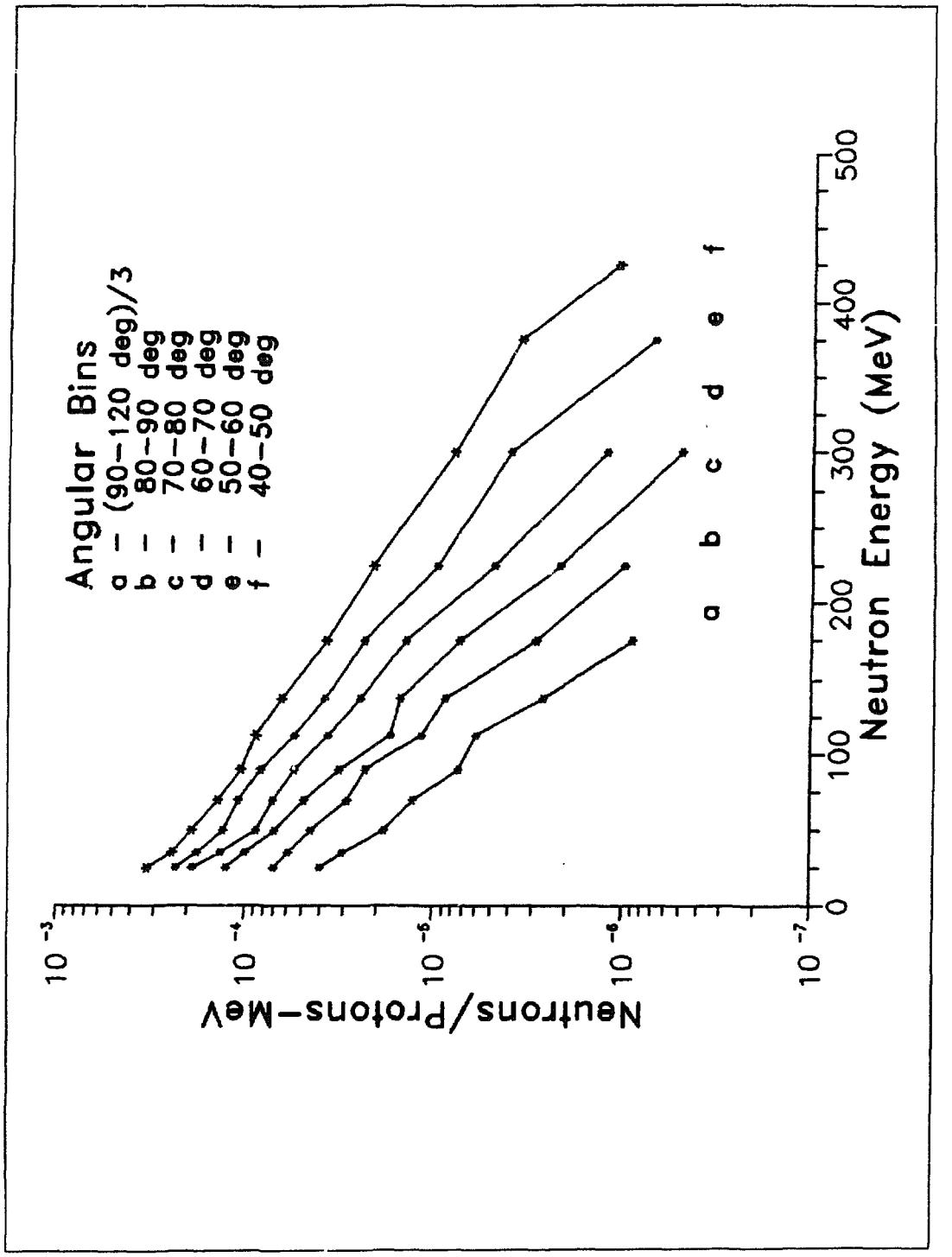

Fig. 7.2. Neutron-energy distributions for different production angles at the boundary of the target volume. Results of a HETC calculation for neutron energies $E_n > 20$ MeV.

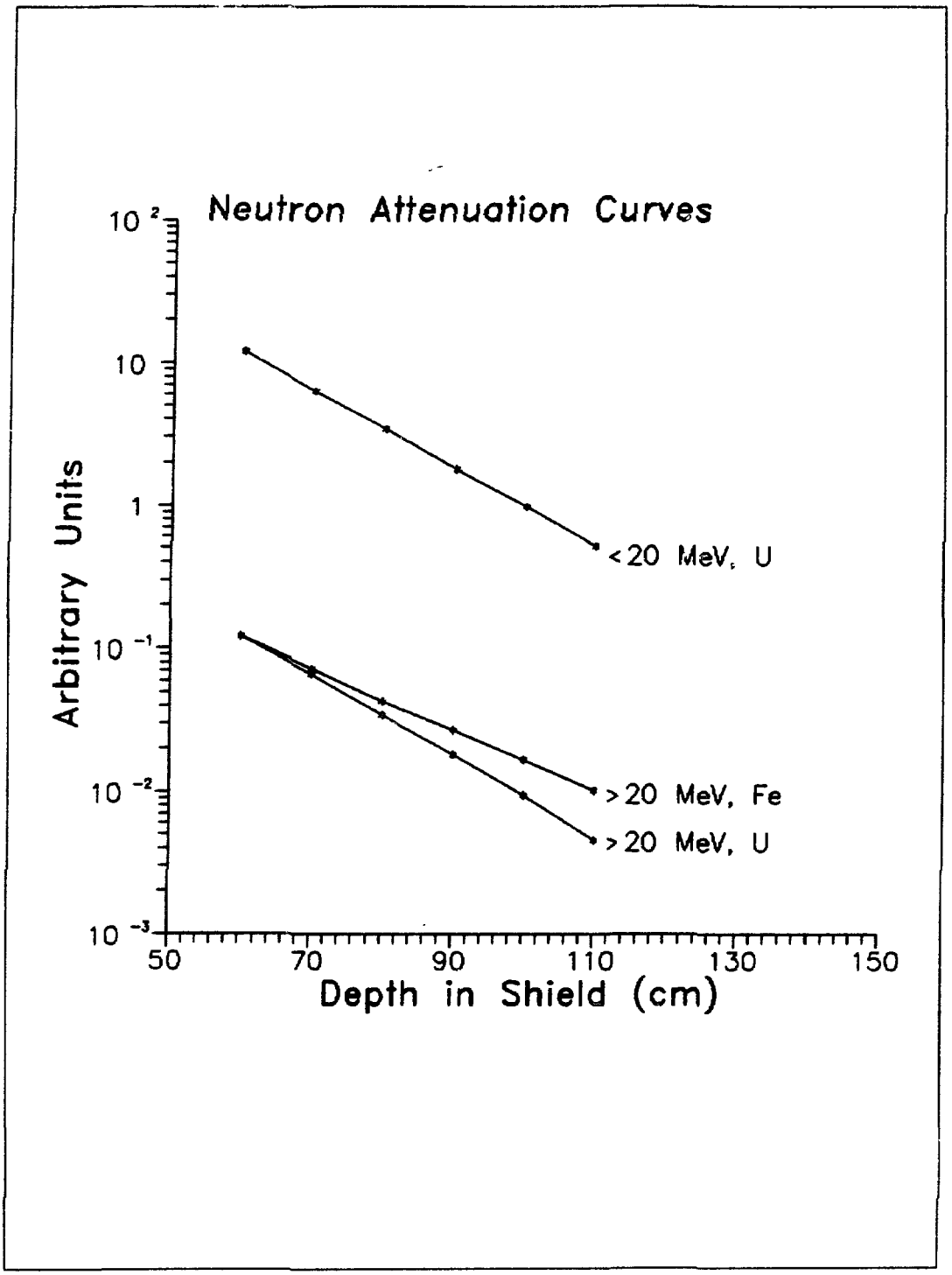

Fig. 7.3. Neutron attenuation in uranium and iron.

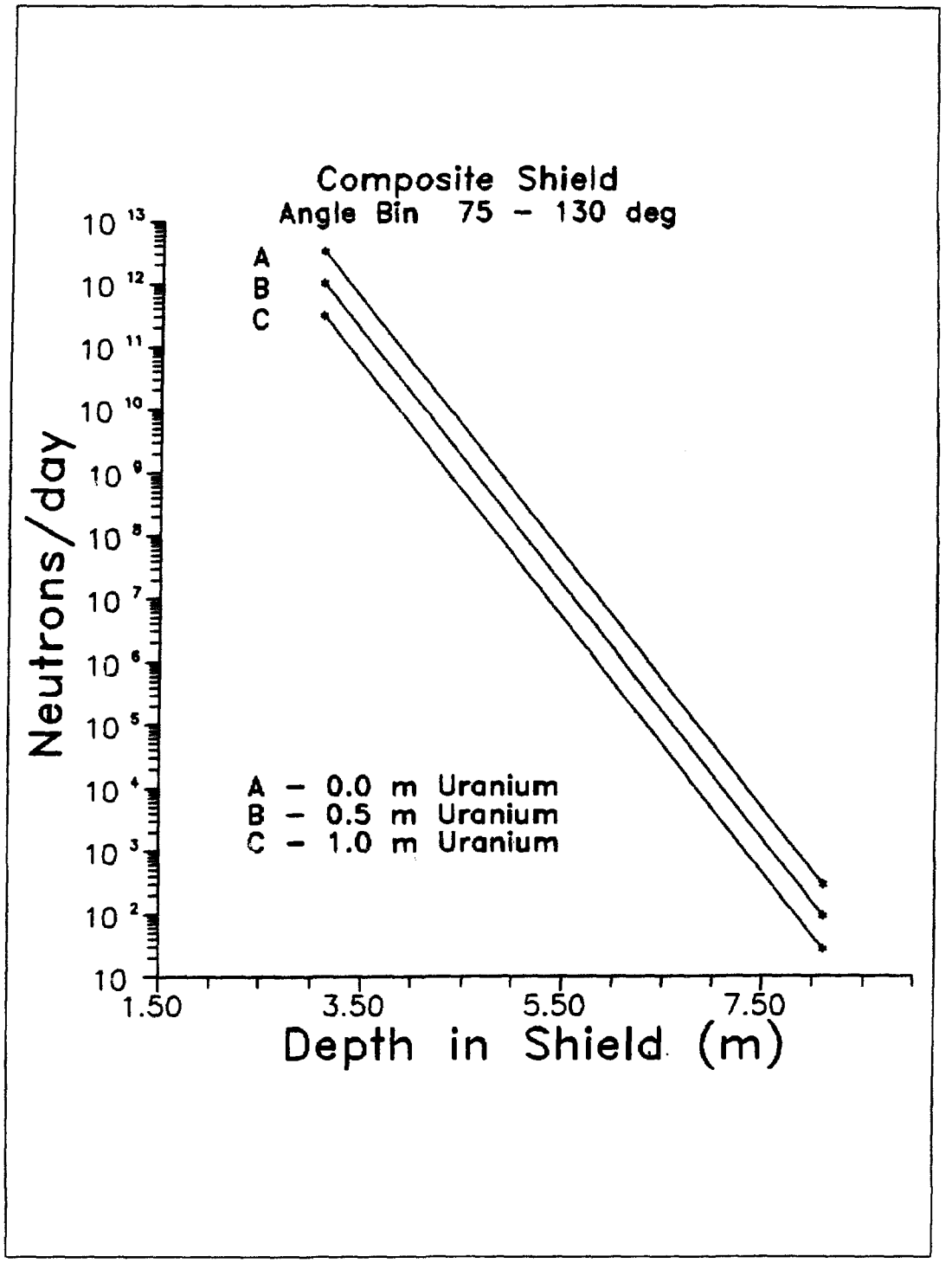

Fig. 7.4. Transport of neutrons through the LCD shield. The results are for the angular interval 75-130 degrees and neutron energies $E_n > 20$ MeV.

7.1.2 Measured Neutron Flux

The LAMPF neutrino experiment E225 was sited at 90° to the Line-A beam stop and was shielded by an equivalent of 6.5m of steel. It thus represents a close approximation to the LCD shielding geometry, so that measurements of neutron flux made by E225 can be used to predict with confidence the fluxes to be expected in LCD. Neutron flux measurements for a differential shielding change were made by both E225 and the earlier neutrino experiment E31. The E225 detector also recorded the absolute neutron flux at the full 6.5m shielding configuration.

Differential Measurement

When E31, which was a 2 × 2 × 2m water Čerenkov detector, was first installed, background rates were measured with 4.0m and 5.0m of iron shielding. The measured rate reduction was a factor of 105 for the 1.0m of cast iron; this gives an attenuation length of 169gm/cm^2. This measured number from E31 agrees well with the value of 170gm/cm^2 from HETC calculations.

The E225 detector was a 3 × 3 × 3.4m sandwich, comprised of 40 layers, each with 2.5cm (2.6gm/cm^2) of scintillator and 6.0cm (1.4gm/cm^2) of flash chamber. Neutron-produced recoil protons were detected by running without an upper level discriminator that normally vetoed proton signals. Data were taken in 1985, before and after 13.75" of iron was replaced by 12" of uranium. HETC calculations predicted that the fast neutron flux would be changed by a factor of 0.54. The measured proton-recoil event rate was 56 ± 2 events per mA-hr before the replacement of steel with uranium, and 25 ± 2 events per mA-hr after the replacement. The experimental reduction of 0.45 is in reasonable agreement with the HETC prediction of 0.54.

Absolute Measurement

The same data from E225 used for the differential measurement yield an absolute neutron flux as produced by the LAMPF proton beam in the Line-A beam stop and subsequently shielded by 6.5m of iron. Events other than proton recoils were found to be completely negligible.

We can then take the average event rate before the iron was replaced, 56 ± 2 events per mA-hr, as the absolute rate for neutron-proton recoils in the E225 detector. The trigger requirement in E225 was at least a three-layer coincidence, corresponding to a minimum proton energy of 150 MeV; thus, the E225 detector was sensitive to neutrons in the energy range 150 MeV to 400 MeV. A Monte Carlo calculation, using the Kent State code,[2] was done to determine the actual detector

response. The neutron detection efficiency was calculated by counting proton recoils that had a projected range of 13.6cm or greater, and that did not escape the detector. Pertinent average properties of the E225 detector include a density of $0.47 gm/cm^3$ and a hydrogen/carbon ratio of 1.35. Neutrons were generated normal to the detector face with uniform initial position and with energies between 50 MeV and 400 MeV.

A graph of the efficiency as a function of neutron energy is shown in Fig. 7.5. The curve is the result of a fit to a cubic equation:

$$\epsilon(E) = -.3826 + .0054\ E - (1.194 \times 10^{-5})E^2 + (8.444 \times 10^{-9})E^3\ . \qquad (7.1)$$

This parameterization of the efficiency was used to form the "average" efficiency by integration over an assumed incident neutron-energy distribution. In general, the neutron-energy spectrum is observed to build up to a characteristic shape that depends upon the incident particle energy, but is insensitive to the depth in the shield. Between E_{min} = 20 MeV and the upper cut-off energy E_{max}, the energy distribution is assumed to be given by

$$\begin{aligned} \phi(E) &= \phi_0 E^{-\gamma} && E_{min} \le E \le E_c \\ \phi(E) &= \phi_0 \left\{C_0 + C_1 E + C_2 E^2\right\} E^{-\gamma}, && E_c < E \le E_{max}\ , \end{aligned} \qquad (7.2)$$

where E is the neutron energy and γ is called the spectral index. The constants are determined by continuity of the flux and the first derivative at the junction energy E_c. The junction energy is taken to be 2/3 of the maximum energy, and measurements typically give a spectral index γ = 1.8. This assumed shape has been tested with data from E645. We find that the measured recoil spectra of E645 is in good agreement with Eq. (7.2) for γ = 1.8 and E_{max} = 400 MeV, as is shown in Fig. 7.6. This neutron spectrum was then used with Eq. (7.1) to calculate an average efficiency for the E225 detector. The efficiency, averaged over neutron energies from 150 MeV to 400 MeV, was found to be ϵ = 0.29.

We can now use the measured proton recoil rate in the E225 detector of 56 $\pm$ 2 per mA-hr to get

$$\text{Neutron Rate } (150 < E_n < 400 \text{ MeV}) = \frac{56}{\epsilon} = \frac{56}{0.29} = 193 \text{ neutrons/mA-hr.}$$

This rate can be compared to the HETC calculation, and used to normalize that calculation, for 6.5m of iron shielding. The calculation gives a rate, in the same

energy range, of 3.13×10^{-16} neutrons/proton into the angular ranges 80°-100° in θ and 360° in ϕ. The E225 detector subtends 20° × 20°, centered at $\theta = 90°$. Thus, we have for the HETC calculation:

$$\begin{aligned} \textit{Calculated Neutron Rate} &= 3.13 \times 10^{-16}(\frac{20}{360})(2.25 \times 10^{19}) \\ &= 391 \text{ neutrons/mA} - \text{hr} \ . \end{aligned}$$

The agreement with the E225 measurement of 193 neutrons/mA-hr is remarkable, especially in view of the reduction factor of 8.5×10^{-14} in the calculation for the 6.5m of steel shielding. We shall use the E225 result to normalize the numbers from the HETC calculations by a factor

$$\text{Rate (E225)/Rate (HETC)} = 193/391 = 0.49 \ .$$

This normalization factor is uncertain to about 20%. We shall apply this normalization factor to the HETC-generated neutron spectrum used in the background estimates in the following sections.

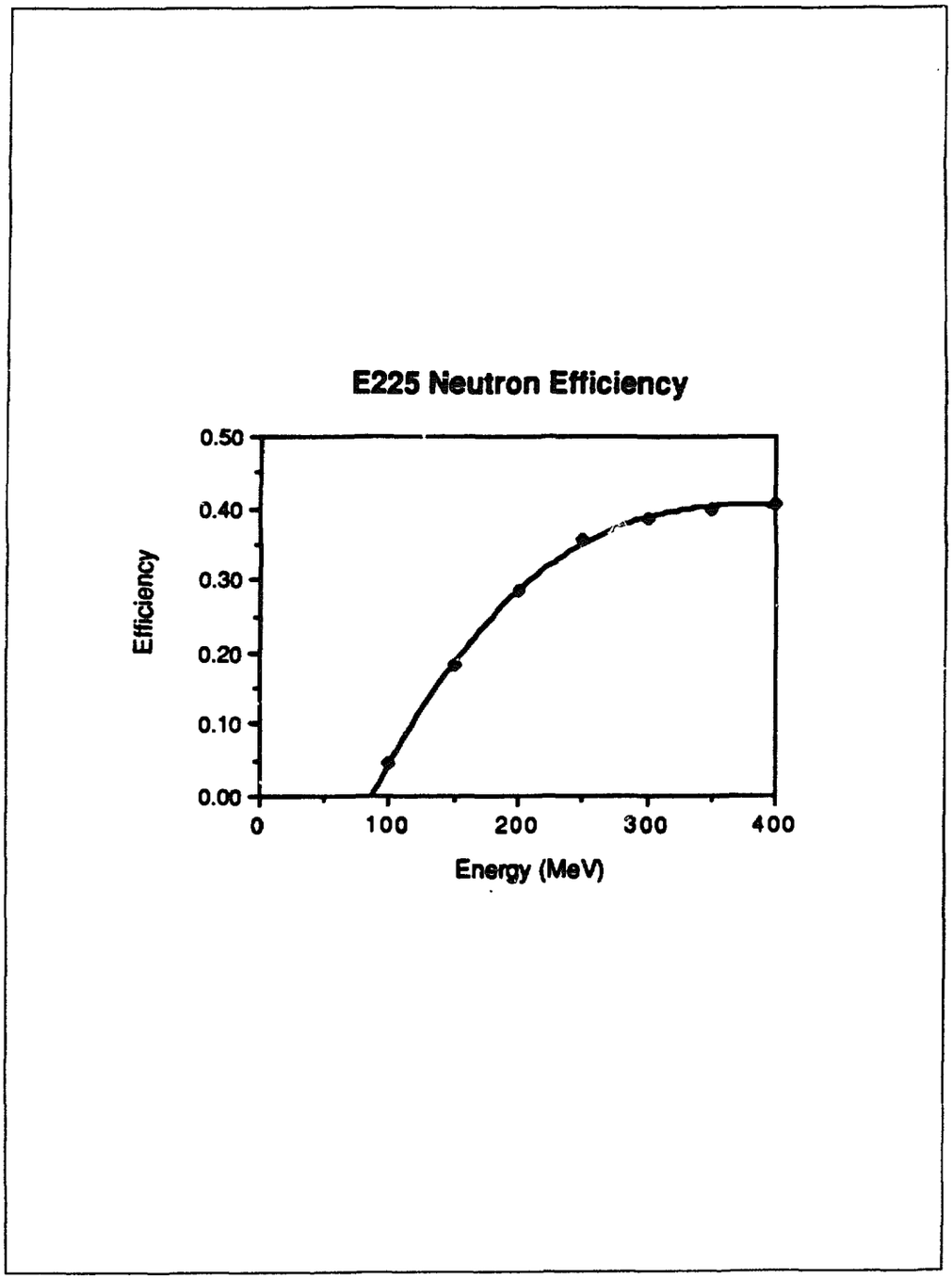

Fig. 7.5. Efficiency for detection of recoil protons from energetic neutrons for the E225 detector. The calculation is from a detailed Monte Carlo simulation.

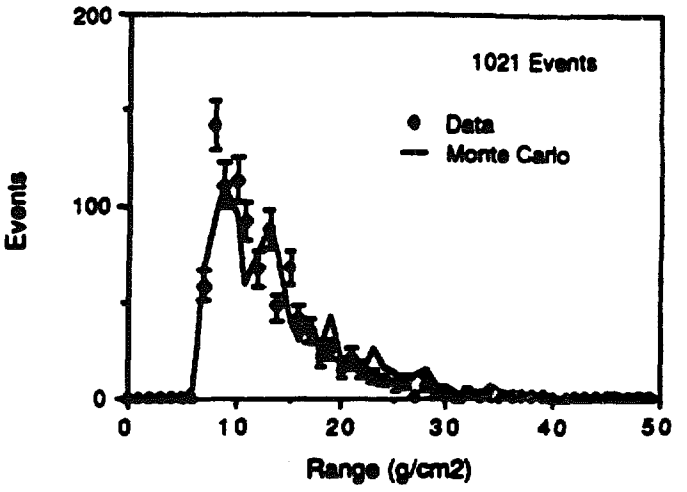

Fig. 7.6. Recoil proton spectrum from E645 detector. The data are compared to Monte Carlo results using the neutron spectrum of Eq. (7.2) with $\gamma = 1.3$ and E_{max} = 400 MeV. The Monte Carlo events are normalized to the 1021 events observed in the detector. The range axis has not been adjusted. The χ^2 between the Monte Carlo and the actual data was 82 for 49 degrees of freedom.

7.1.3 Photon Production by Neutrons in Water

Photons produced in the water by neutrons provide a prompt background for ν_μe events. The experimental goal is to have this background rate be $\lesssim$ 10% of the ν_μe rate ($\sim$ 11 per day), and then to perform a background subtraction with less than 10% error. The photon energy range of interest extends from threshold (10 MeV) to the maximum energy of neutrinos resulting from μ decay (53 MeV).

The spectrum of neutrons, $S(E_n)$, with energy $E_n > 20$ MeV emerging from the iron shield (radius = 7.25m, iron equivalent) in the angular range $75° < \theta < 130°$ is shown in Fig. 7.7. In the water, we assume that the spectral shape remains constant; the attenuation length is $\lambda = 1.26$m. Accounting for this attenuation, the thick-target correction for 6m of water is given by

$$x_f = \int_0^6 dx \exp(-x/\lambda) = 1.25\text{m} \ .$$

The photon spectrum for a specific process is given by

$$\frac{dg}{dE_\gamma} = x_f \int dE_n \left[\frac{d\sigma_\gamma}{dE_\gamma}(E_n, E_\gamma)\right] S(E_n) K \ ,$$

where g is the number of photons and

$$K = (6.02 \times 10^{23}/18g)(10^{-24}\ \text{cm}^2/\text{b})(1\text{g/cm}^3)(10^2\ \text{cm/m}) = 3.34/\text{b}\cdot\text{m} \ .$$

Thus,

$$\frac{dg}{dE_\gamma} = 4.18 \int dE_n \left[\frac{d\sigma_\gamma}{dE_\gamma}(E_n, E_\gamma)\right] S(E_n) \ . \qquad (7.3)$$

The most important processes for neutron-induced photon production are: (1) np bremsstrahlung; (2) n + p $\rightarrow$ d + γ; and (3) ^{16}O (n, γ) X. We discuss the contribution from each process below.

np Bremsstrahlung

Experimental data for neutron-induced bremsstrahlung are not plentiful. Studies of neutron-proton bremsstrahlung (npγ) at beam energies of 140 MeV and 208 MeV found total cross sections of 8μb[3] and 30μb[4], respectively, for photons with energies greater than 40 MeV. Bremsstrahlung from protons on nuclei has been studied at 185 MeV[5]. From this experiment, we conclude that the cross section is proportional to the neutron number. If we assume charge symmetry, we then estimate the bremsstrahlung cross section for neutrons on ^{16}O to be $\sim$2/3 that for npγ. We need an estimate of the energy dependence (both neutron and photon) of npγ.

There is no accepted theory for npγ, so the energy dependence is uncertain. We make the simple approximation that the npγ cross section is proportional (with proportionality constant C) to the product of the np elastic cross section, σ_{el}, and the photon yield per np collision, as given by classical electromagnetism. From Ref. 6, we write

$$\frac{dI}{d\Omega_\gamma} \approx \frac{e^2}{4\pi^2 c}|\Delta\vec{\beta}|^2 \sin^2\theta_\gamma \quad ,$$

where I is the energy per frequency interval, $\Delta\vec{\beta}$ is the change in velocity of the proton, and θ_γ is the photon angle with respect to $\Delta\vec{\beta}$. This is a non-relativistic expression. As the proton is the target, $\Delta\beta = \beta$, and can be approximated, as an average quantity, by

$$\beta^2 \approx \frac{2}{m}(\frac{1}{2}E_n - E_\gamma) = \frac{E_n}{m}(1 - 2E_\gamma/E_n) \quad .$$

Rewriting in terms of photons/MeV $\cdot$ sr,

$$\frac{dN_\gamma}{dE_\gamma d\Omega_\gamma} = \frac{\alpha}{4\pi^2 m} \cdot \frac{E_n}{E_\gamma}(1 - 2E_\gamma/E_n)\sin^2\theta_\gamma \quad ,$$

where α is the fine structure constant and m the nucleon mass. To obtain the experimental total cross section of 30μb at E_n = 200 MeV (for E_γ > 40 MeV), the constant of proportionality must be seven, which yields a cross section of 10μb at 140 MeV, in good agreement with the experimental value. Thus, the final expression is

$$\frac{d\sigma_\gamma}{dE_\gamma} = C\sigma_{el}\frac{dN_\gamma}{dE_\gamma} = \frac{14\alpha}{3\pi m}\frac{E_n}{E_\gamma}(1 - 2E_\gamma/E_n)\sigma_{el} \quad , \tag{7.4}$$

which yields the observed shape for the photon spectrum. Folding this expression with the neutron spectrum as per eq. (7.3) yields the photon spectrum shown in Fig. 7.8. The photon angular distribution is assumed to be isotropic.

$n + p \rightarrow d + \gamma$

Deuteron photodisintegration has been studied extensively and is related to n-p capture by detailed balance:

$$\sigma(np \rightarrow d\gamma) = \frac{3}{2}\left(\frac{k}{p}\right)^2 \sigma(\gamma d \rightarrow np) \quad , \tag{7.5}$$

where k and p are the center-of-mass (cm) momenta of the photon and nucleon, respectively. The photon lab energy, E_γ, can be approximated as $E_\gamma \approx (\frac{1}{2}E_n + B)(1 + \beta\cos\theta_{cm})$, where B is the deuteron binding energy (2.2 MeV)

and β is the velocity (c = 1) of the cm frame, $\beta = \left(E_n/(E_n + 2m)\right)^{1/2}$. Assuming the photon is produced isotropically in the cm frame, we can then write

$$\frac{d\sigma_\gamma}{dE_\gamma} \approx \frac{4\pi}{(E_n + 2B)\beta}\frac{d\sigma_\gamma}{d\Omega_\gamma} = \frac{\sigma_\gamma}{(E_n + 2B)}\sqrt{\frac{E_n + 2m}{E_n}} \quad . \tag{7.6}$$

A compilation of total cross sections for deuteron photodisintegration, over the energy range of interest, is given in Ref. 7. Using Eq. (7.5) in Eq. (7.6), and folding with the neutron spectrum as per Eq. (7.3) yields the photon spectrum shown in Fig. 7.8.

Very low-energy neutrons produce photons with $E_\gamma \approx 2.2$ MeV by n-p capture. Although these photons are below our threshold, they can possibly cause problems. We estimate that 2.3×10^{11} neutrons per day with energies $E_n < 20$ MeV emerge from the surface of the steel shield at r=7.0m. After passing through 0.50m of boron-loaded magnetite-concrete (attenuation length = 7.75cm), 3.5×10^8 n/d remain. We assume that all of these neutrons produce 2.2 MeV photons either in the inner veto region between the concrete surface and the fiducial volume or within the fiducial volume itself. In either of these extreme cases, the PMT rate is less than or comparable to the noise rate. Therefore, low-energy neutrons converting to photons by capture do not represent a problem.

$^{16}O(n,\gamma)X$

The principal contribution to photon production from nuclear excitation arises from the giant-dipole-resonance (GDR) reaction $^{16}O(n,\gamma)^{17}O$. To our knowledge, there are no data available for this reaction, so we assume charge symmetry and use data[8] for $^{16}O(p,\gamma)^{17}F$ (GDR). The data for $d\sigma_\gamma/d\Omega$ vs E_p were fitted with the function

$$\frac{d\sigma_\gamma}{d\Omega} = \left(\frac{d\sigma_\gamma}{d\Omega}\right)_0 \frac{E_p^2\Gamma^2}{(E_p^2 - E_0^2)^2 + E_p^2\Gamma^2} \quad , \tag{7.7}$$

with $E_0 = 22$ MeV, $\Gamma = 8$ MeV, $(d\sigma_\gamma/d\Omega)_0 = 9\mu$b/sr. From the angular distributions, we estimate a solid angle factor of ~ 6 sr. Because of the near identity of laboratory proton (neutron) energy and $^{17}F(^{17}0)$ excitation energy, we assume $d\sigma_\gamma/dE_\gamma \approx \sigma_\gamma\delta(E_n - E_\gamma)$. Then, the photon spectrum is given by

$$\frac{dg}{dE_\gamma} = (4.18)(6)\left(\frac{d\sigma}{d\Omega}\right)_0 \frac{E_\gamma^2\Gamma^2}{(E_\gamma^2 - E_0^2)^2 + E_\gamma^2\Gamma^2} S(E_\gamma) \quad , \tag{7.8}$$

which is shown in Fig. 7.8.

In addition to the broad GDR, the de-excitation spectrum also contains several very narrow lines arising from nuclear levels. These lines generally lie below the 10-MeV threshold and are easily subtracted because they are so sharp.

Photon Yield

In Fig. 7.8, we show the photon spectra resulting from the three processes described above. The integrated total photon yield, in the range 10-60 MeV, is 4.1 photons/day, with 67% coming from the bremsstrahlung reaction. A factor of 0.79, due to the attenuation in the 30-cm water veto region, has been applied. An additional factor (0.12) for the angular cut (40° forward cone) has not been included here. The assumption of isotropic photon production overestimates the number of background events in the forward direction. Model calculations indicate that the photon spectrum is broadly peaked near $\theta_\gamma = 90°$. Also, choosing a 40° forward cone for the angular cut is very conservative because the ν_μe events with which the background is being compared are forward peaked and steeply falling with angle.

The principal uncertainties in this calculation involve the neutron spectrum and the photon-production cross sections. From Experiment 225 (see section 7.1.2), we were able to normalize the HETC-generated neutron spectrum, and the calculations reported herein include the normalization factor of 0.49. The residual, unexplained background events in Experiment 225 amounted to ~100 events/A-hr, which represents an upper limit for photon events. Applying the present analysis to that experiment, we obtain a detectable photon production rate of ~150 events/A-hr. The good agreement in this comparison gives us confidence in the accuracy of our background estimates.

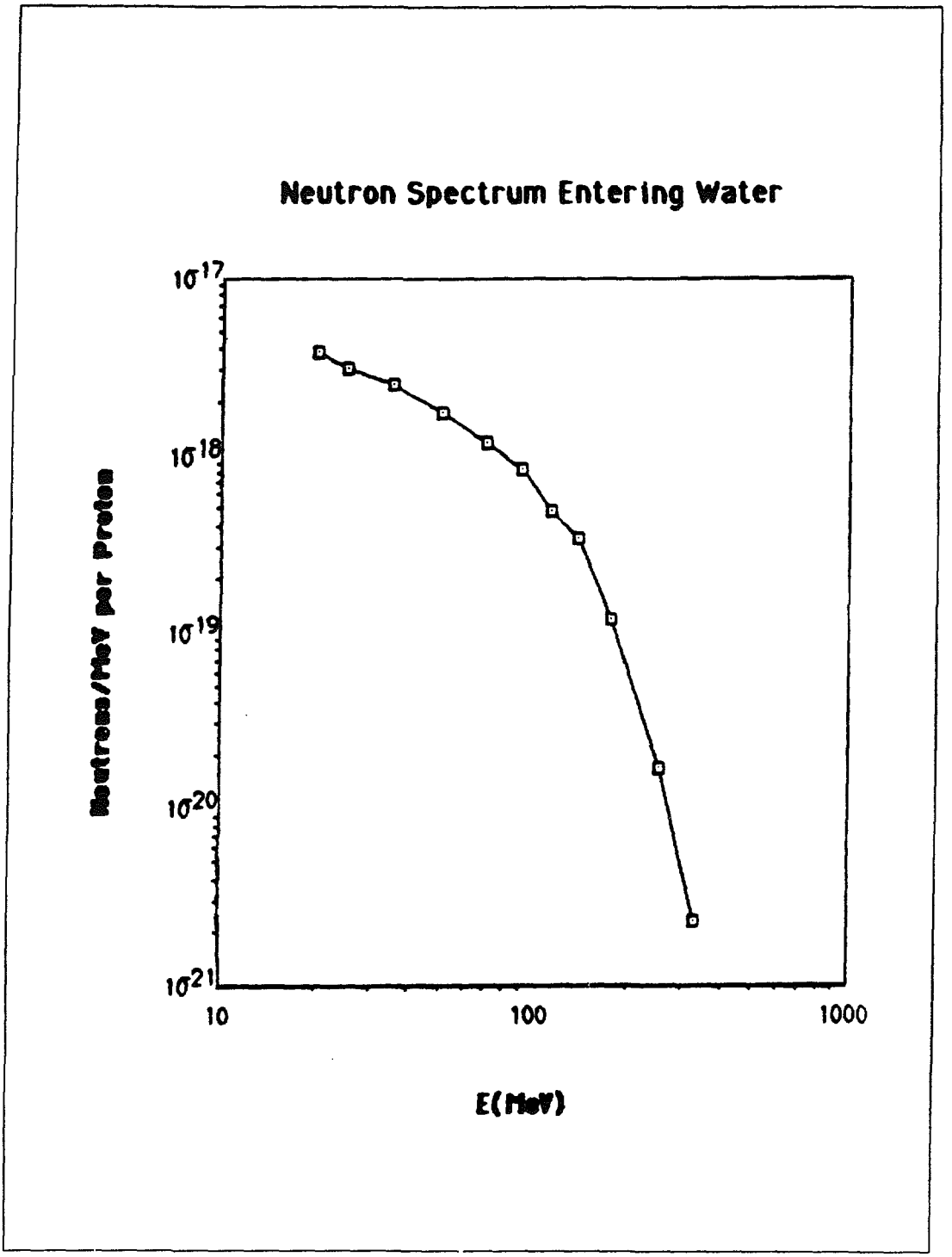

Fig. 7.7. Calculated neutron spectrum entering water after passing through a shield of radius 7.25m iron equivalent, angular range is $75^{\circ} < \theta < 130^{\circ}$. A normalization constant of 0.49 from Experiment 225 is included.

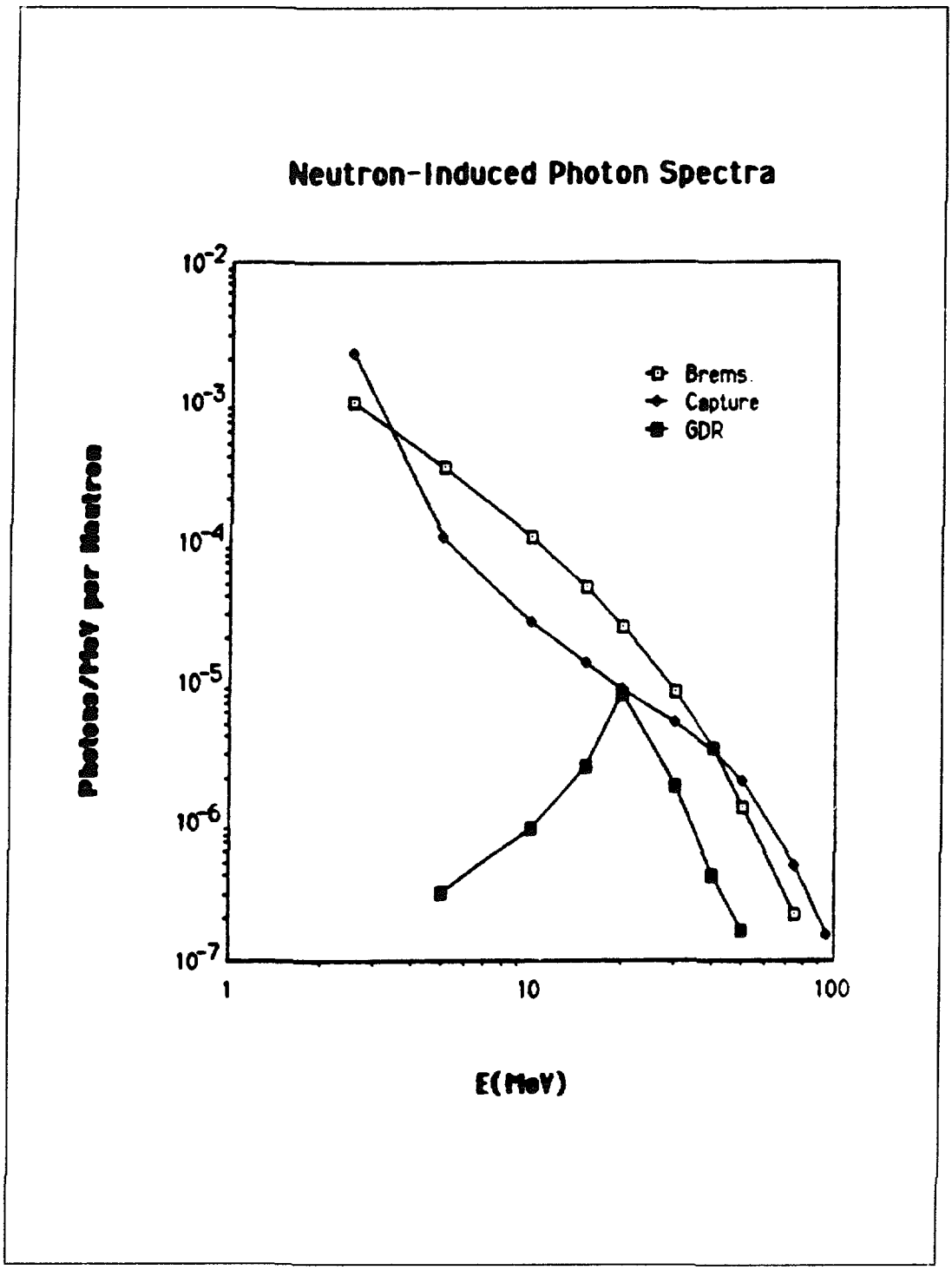

Fig. 7.8. Calculated photon spectra produced by neutrons in 6m of water.

7.1.4 Pion Production by Neutrons in Water

Even after attenuation in the shield, a nonnegligible flux of neutrons above 200 MeV exists. Thus, pion production in the water is considered as a source of background. The pions will produce a signature that will mimic a true event in a number of ways.

Positive pions can decay to muons, which subsequently decay to positrons. The positive pions generally will come to rest before decay, so the muon and neutrino will share the rest energy of the pion. The positron energy from the decay of the muon exhibits a Michel spectrum with an end point of 53 MeV. This positron will be indistinguishable from the electrons of interest; therefore it will be an unwanted background. Coupling the angular distribution of the neutrons entering the water with the angular distribution of pion production, and including the asymmetry in the muon decay, produces an angular distribution for the positrons that is essentially isotropic. Most positrons from muon decay, therefore, can be eliminated by angular cuts.

Neutral pions decay into two high-energy photons, each with energy greater than 70 MeV. Two high-energy photons produce an easily distinguished signature in the detector. However, we conservatively estimate that $\sim$ 10% of the time, only one photon is observed, and $\sim$ 10% of these lie within the angular cut. Thus, we estimate a net discrimination factor of 1% for these events.

Negative pions generally will come to rest before decay and will be captured by either an oxygen or hydrogen nucleus. The capture by oxygen will lead primarily to the emission of two low-energy nucleons that will be invisible to the LCD detector. A small fraction (2%) of the time, the negative pion will be radiatively captured by hydrogen or oxygen. In radiative capture, a low-energy neutron and a high-energy photon (E_γ >50 MeV) are emitted. The high-energy photon will be seen by the detector; however, energy discrimination will eliminate most of these background events.

The most serious background from pions is the Čerenkov light produced directly by energetic pions. Pions above about 110 MeV will produce sufficient Čerenkov light to appear to the detector as a good electron event. A calculation of the number of Čerenkov photons produced as a function of pion (or electron) energy is shown in Fig. 7.9. An assumption was made that the energy loss is a constant of energy (2.2 MeV/cm) for the energy range of interest. A detection threshold for electrons of 10 MeV is equivalent to a detection threshold for pions of 110 MeV. Positive pions above 110 MeV will have a distinctive signature: the pion will produce a Čerenkov event, and the electron from the subsequent muon decay will produce an additional Čerenkov event at a later time (determined by the muon lifetime of 2.2μs). This

distinctive signature will allow most high-energy positive pions events to be distinguished. Negative pions that produce Čerenkov light will generally proceed via nuclear capture (98% of the time) and will produce no additional signature. These high-energy negative pions will appear to be candidate events. Integrating the pion spectrum above 110 MeV, we find that 8% of the negative pions produced through neutron interactions in the water will produce a visible background event.

HETC was used to determine the pions produced in the detector water by high-energy neutrons. Because the neutron spectrum falls steeply with energy, the region of interest ranges from the production threshold at ~200 MeV to about ~500 MeV. Very little experimental data exist in this region, so the HETC code relies on the isobar model of Sternheimer and Lindenbaum.[9] Data near the interval of interest exist only at 585 MeV.[10] A comparison of these data with the predictions of HETC is shown in Table 7.1 The agreement is generally quite good, with the HETC code giving 1.4 times as many negative pions from oxygen as the data.

Table 7.1 Total pion production cross sections at 585 MeV.

	π^+		π^-	
Target	*HETC*	*Experiment (a)*	*HETC*	*Experiment (a)*
C	26mb	28.5mb	6.3mb	4.7mb
Al	48mb	43.8mb	14.3mb	9.8mb
O	40mb	34.6mb	8.9mb	6.4mb

(a) Ref. 10

The validity of this code in the threshold region is not tested. The prediction of the HETC code for pion production as a function of neutron energy is shown in Fig. 7.10. This spectrum was folded with the neutron-energy spectrum to determine the yield of pions in the water volume for neutrons exiting the shield; Fig. 7.11 shows these results. The sharply falling neutron spectrum, coupled with the spectrum of Fig. 7.10, gives a pion spectrum in the water that peaks at approximately 300 MeV neutron energy.

Summary of Backgrounds from Pions

Listed in Table 7.2 is a summary of the background rates due to neutron-induced pion production, with discrimination factors included. (From section 7.1.1 the total neutron rate is $\sim$ 8000 per day.) The background events have been integrated over the angular acceptance of the detector and the detector thickness. The primary source of background in the prompt-time interval is the charged pions, which produce Čerenkov light; neutral pions are less important. Positive pions also contribute to the background in the delayed-time interval. The discrimination factors include the expected reduction in the background rates due to the intelligence of the detector. For the charged pions, the factor of 0.08 represents the fraction that produce Čerenkov light. No additional reduction has been included for angular cuts or for differences in the ring pattern of the Čerenkov light on the detector phototubes. For the neutral pions, the factor 0.01 includes energy discrimination and angular discrimination. No discrimination factor has been included for positive pions in the delayed-time interval, although angular cuts can be applied.

Table 7.2 Backgrounds due to pions.

Source	*Rate(Pions/Neutrons)*	*Discrimination*	*Comments*
π^-	2.0×10^{-5}	.08	prompt time
π^o	2.5×10^{-6}	.01	prompt time
π^+	5.5×10^{-6}	.08	prompt time
π^+	6.8×10^{-5}	1.00	delayed time

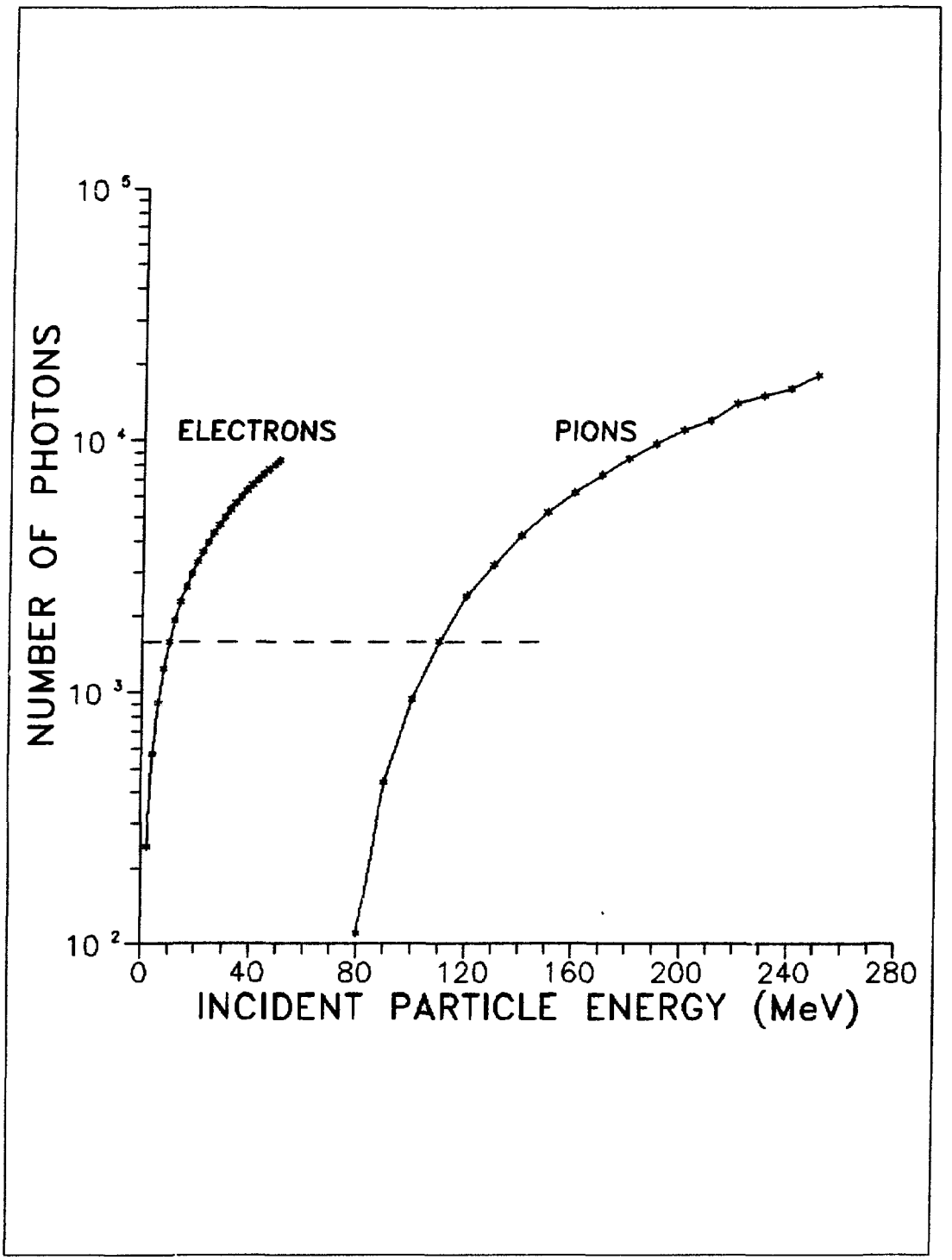

Fig. 7.9. Čerenkov photons produced in water by relativistic electrons and pions. The dashed line represents the LCD detection threshold.

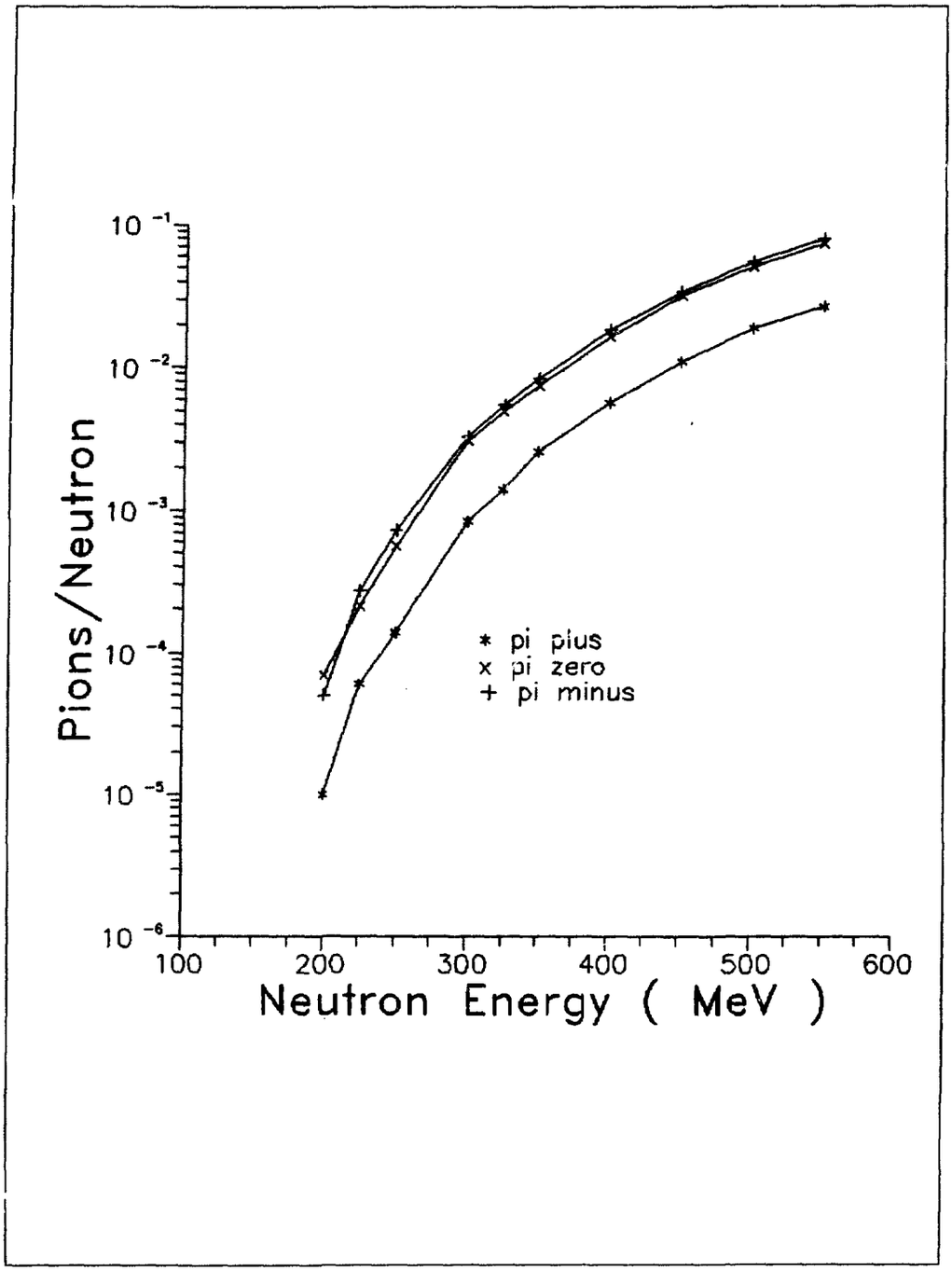

Fig. 7.10. Pion production as a function of neutron energy from the HETC calculations.

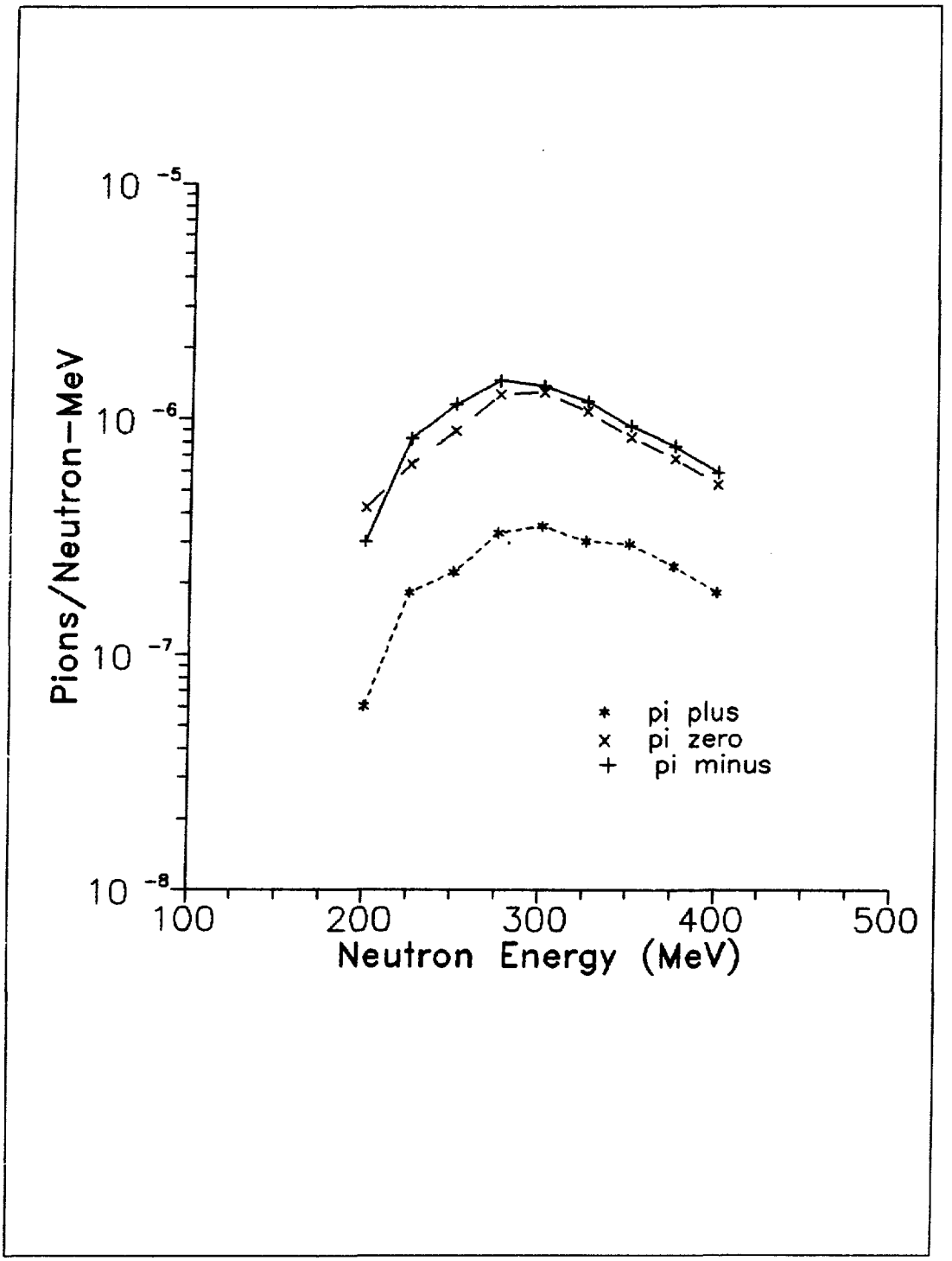

Fig. 7.11. The yield of pions in LCD as determined from combining the results of Fig. 7.10 with the neutron-energy spectrum.

7.2 Losses in Beam Transport

The neutron current due to losses in the beam transport down the vertical column was calculated using a numerical integration based on the Moyer model:[11]

$$I = \int_{\Delta\Omega} \int_{150}^{800} I_0 \; a \; b \left\{ \frac{d^2n}{d\Omega dE} \right\} dE d\Omega \quad , \tag{7.9}$$

where a is the attenuation obtained using the HETC-derived attenuation lengths, b=3 is the build-up factor in the forward direction, and the double-differential distribution of secondary neutrons is given by the Ranft distribution.[12]

$$\begin{aligned} \frac{d^2n}{dEd\Omega} = & \left\{ \frac{A}{P_0} + \frac{BP}{P_0^2} \left[1 + \gamma_0 - \gamma \left(\frac{P_0}{P} \right) \right] \right\} \\ & \times P^2 \left\{ 1 + \gamma_0 - \frac{PP_0}{\rho m^2} \right\} \\ & \times \left\{ \frac{E+m}{P} \right\} exp\left(-CP^2\theta^2\right) \quad , \end{aligned} \tag{7.10}$$

which has units of neutrons per GeV per steradian per interacting particle. The other parameters are defined as:

P_0 is the momentum of the incident particle in GeV/c,
P is the momentum of the neutron secondaries in GeV/c,
m is the neutron rest mass (0.9395 GeV/c^2),
E is the energy of the neutron secondaries in GeV,
θ is the angle made by the neutron secondaries to the incident beam direction,
A, B, and C are constants which depend upon the shield material,

$$\gamma = \sqrt{1 + (P/m)^2},$$

$$\gamma_0 = \sqrt{1 + (P_0/m)^2}$$

For iron or magnetite: A = 0.92, B = 0.75, and C = 2.9.

The neutron current into the water as a function of Z-position is shown in Fig. 7.12. The total current is 3.1 $\times$ 10^{-8} neutron, normalized to a loss of one proton per meter. If the beam current is 5.4 $\times$ 10^{19} protons per day (100μA), and the detector can tolerate 2 $\times$ 10^3 neutrons per day (the directly penetrating rate is 8 $\times$ 10^3 n/d), then this loss must be kept below 10^{-9} of the incident beam per meter.

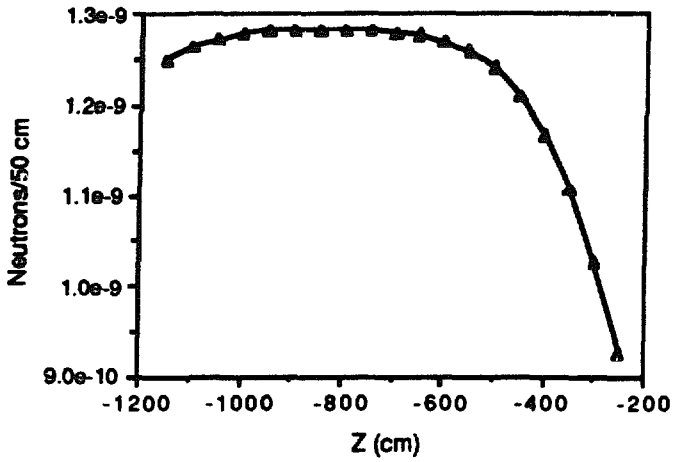

Fig. 7.12. Neutrons in the detector from beam loss in the transport through the vertical pipe. The Z-direction is along the beam with the origin being the center of the beam stop. The neutron current into the water for each 50cm bin along Z is calculated assuming a constant loss of one proton per meter. The last point at Z = -250cm corresponds to the top of the iron shielding.

7.3 Ground-Shine Neutron Current

The ground shine is defined here to be neutrons that reach the detector after one bounce. In the case of the magnetite column above the beam stop, there will be both a ground-shine and a direct component. In the case of the tuff below the detector, there is only a scattered component. The ground shine from the magnetite above the beam stop was not calculated in the present analysis.

Before calculating the total ground-shine current from the tuff and magnetite concrete below the detector, a comparison was made with the HETC Monte Carlo for the simple, cylindrically symmetric geometry shown in Fig. 7.13. In the HETC problem, 600- MeV neutrons were incident straight down along the Z-axis, and the neutron current across the annular surface per incident neutron was tallied. This was done using a reduced and variable density for the reflecting material, so that some neutrons could escape. The numerical integration for the ground-shine current was performed using the formula

$$\frac{d^2 I_{gs}}{d\Omega_s dz} = \left\{\frac{\rho}{\lambda}\right\} exp\left\{-\frac{\rho z}{\lambda}\right\} \frac{1}{P_0}\left\{\frac{dP(\theta_s)}{d\Omega_s}\right\} exp\left\{-\frac{\rho r}{\lambda}\right\} \quad , \tag{7.11}$$

where λ is the attenuation length and ρ the density. The angular power distribution is given by

$$\frac{1}{P_o}\frac{dP(\theta_s)}{d\Omega_s} = 1.75\exp(-3.337\theta_s) + 8.8 \times 10^{-3} \quad ,$$

where θ_s is in radians. Equation (7.11) represents the neutron current scattered by the material between z and z+dz into the solid-angle increment of $d\Omega_s$, which is the solid angle for the annular ring along the tally surface between radius R and R + dR:

$$d\Omega_s = \frac{dA}{r^2} cos(\pi - \theta_s) = \frac{2\pi R\, dR}{r^2}\left[\frac{R}{r}\right] \quad .$$

The total ground-shine current is then

$$I_{gs} = \int_0^{2000}\int_{700}^{1500}\left\{\frac{d^2 I_{gs}}{d\Omega_s dz}\right\}\frac{2\pi R}{r^2} dR dz \quad . \tag{7.12}$$

The results of Equation (7.12) are presented in Fig. 7.14 for several values of the density. The two calculations agree to within a factor of five, and they both show that the ground shine is the worst for a density of about $0.1 g/cm^3$. The difference is due to the neutrons that can scatter in even though they are parallel to the tally surface (double scatters). The ground shine drops rapidly for densities

greater than this and more slowly for lesser densities. Therefore, the way to control ground shine is to make the material as dense as possible.

The final ground-shine calculation is done by integrating over the entire region below the detector and using a different solid-angle treatment for the first interaction length of material below the target. The result is that the high-energy ground-shine current is 5.0×10^4 n/d for the magnetite concrete and 1.4×10^4 n/d for the tuff, for a total of 6.4×10^4 n/d. As the most copious source is the magnetite concrete immediately below the target, the ground shine could be reduced by replacing 1.5m of magnetite concrete with iron. This action will reduce the ground-shine neutron background to $< 10^3$n/d, which is small compared to the directly penetrating rate of 8.0×10^3 n/d.

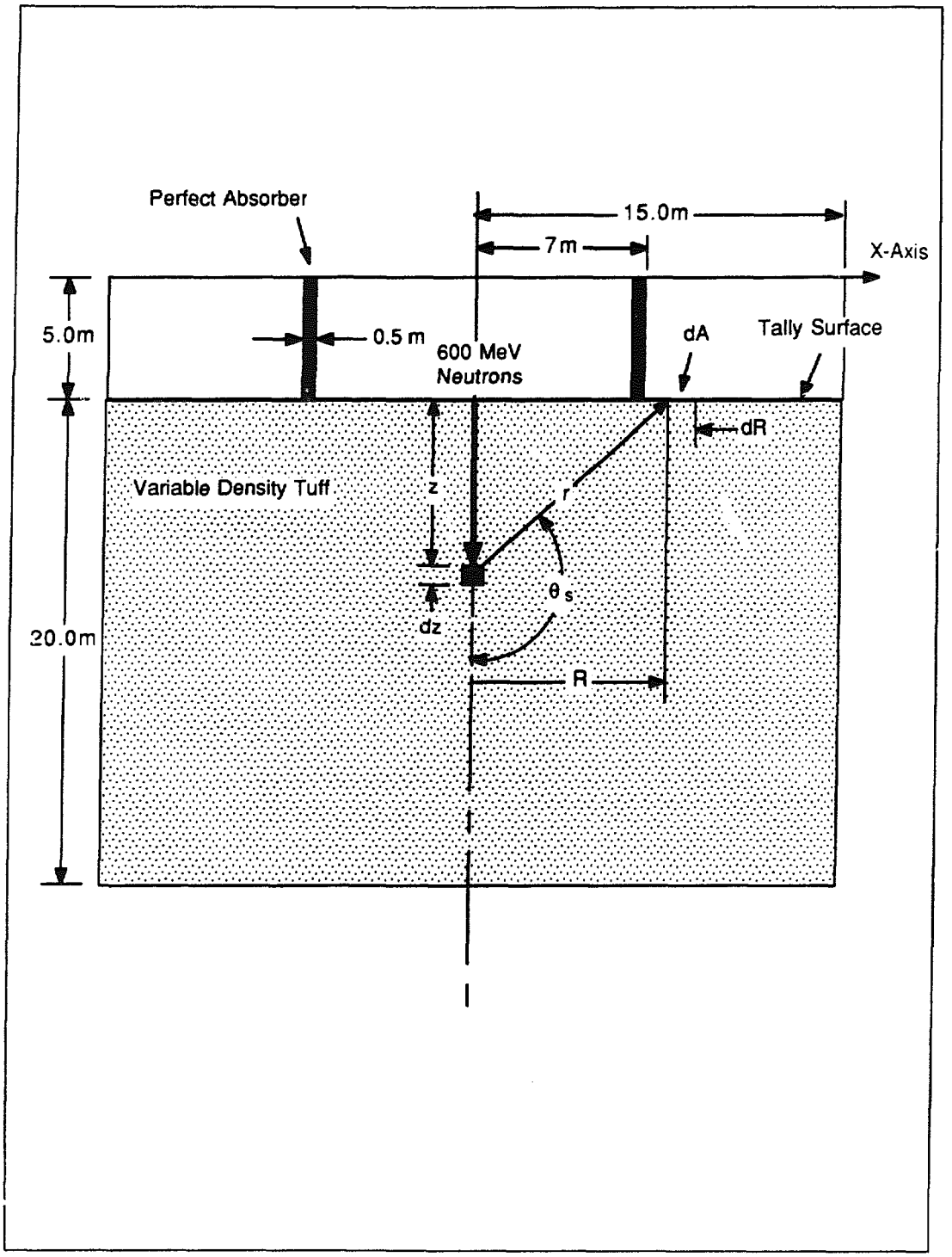

Fig. 7.13. Geometry used for comparison of numerical integration with the HETC Monte Carlo code. 600-MeV neutrons are started straight down along the z-axis. Ground-shine neutrons are tallied that cross the annulus between R = 700cm and R = 1500cm.

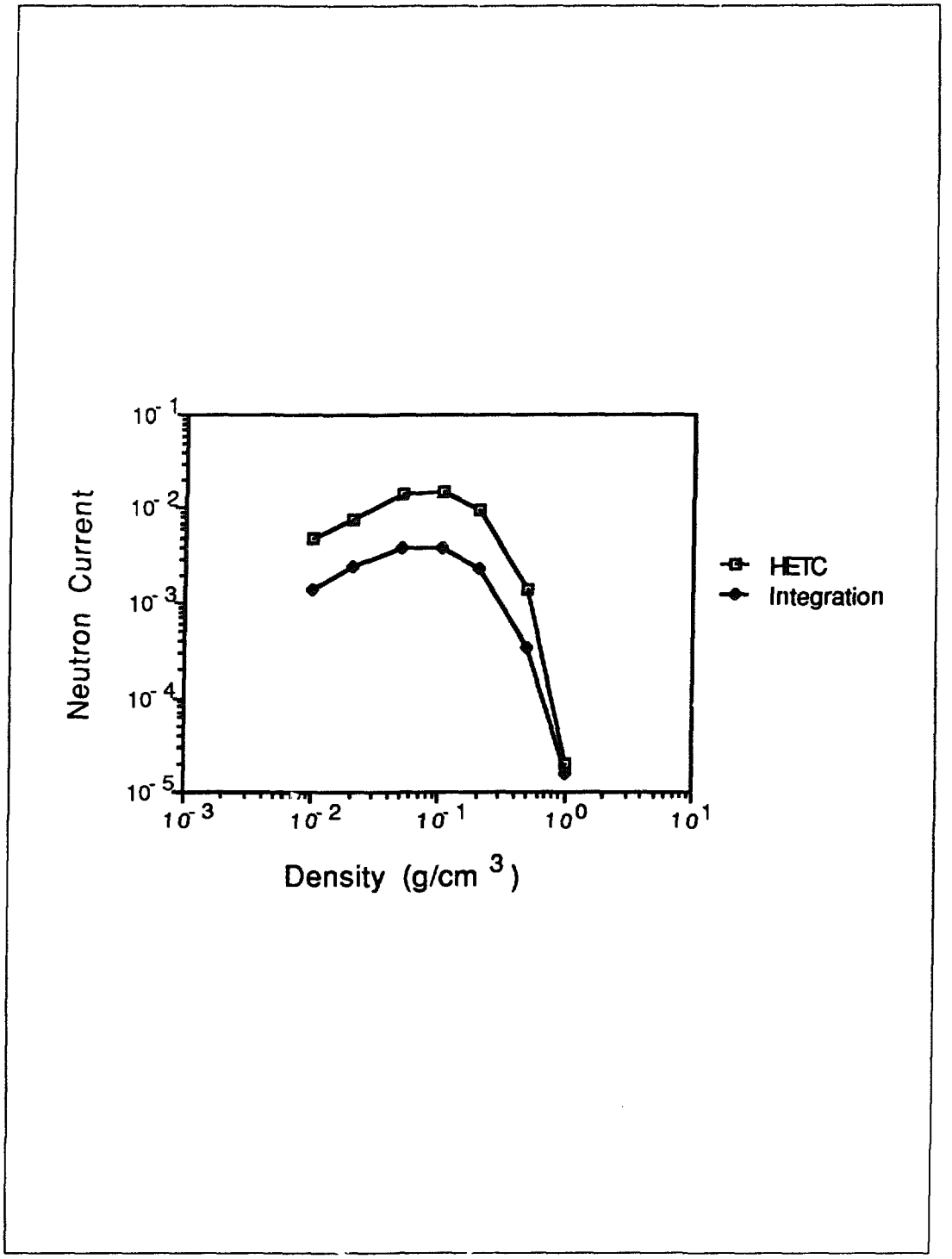

Fig. 7.14. Neutron ground-shine current for the geometry of Fig. 7.13. The numerical integration is compared with the HETC Monte Carlo. The density of the tuff (silicon dioxide) is allowed to vary from 10^{-2} to 1.0g/cm^3. The actual density of tuff is about 1.6g/cm^3.

7.4 Backscattering from the Target

Neutron attenuation is not constant in all directions for the current cylindrically-symmetric shielding design. In optimizing the shielding configuration, an estimate of the effectiveness of the attenuation for various neutron directions is required. The most effective way of calculating the neutron attenuation is by Monte Carlo transport in a geometry closely matching the proposed LCD detector. As noted above, it is not computationally possible to transport through the entire shielding volume. It is found, using HETC, that after about 60cm, the attenuation factor is independent of energy. Neutrons were transported through a 60cm iron thickness, and then the attenuation was calculated analytically. The geometry of the iron shield/magnetite column was scaled by $\sim$ 10 (we used 60cm of iron at 90°, for example), giving computationally manageable material thicknesses. This strategy yields relative neutron survival fractions for comparison of the neutron attenuation in various directions. Three HETC calculations were done for neutrons with initial angles of 105°, 135°, and 158° with respect to the initial proton beam. Neutrons were tallied if they passed through various surfaces at the water interface. The results are shown in Fig. 7.15, where the neutrons entering the water per source neutron is plotted as a function of z-position (z=0 at the target). The source neutron distribution shown in Fig. 7.16 has been folded into the survival distributions shown in Fig. 7.15.

The number of neutrons entering the water decreases with increasing neutron angle (Fig. 7.15), so the shielding in the backwards direction is deemed sufficient. The "thinnest" shielding is in the direction perpendicular to the proton beam (θ = 90°). The proposed shielding is a design benchmark — it should be possible to preserve attenuation characteristics while incrementally decreasing cost by introducing future design refinements such as a uranium "belly band" near the target.

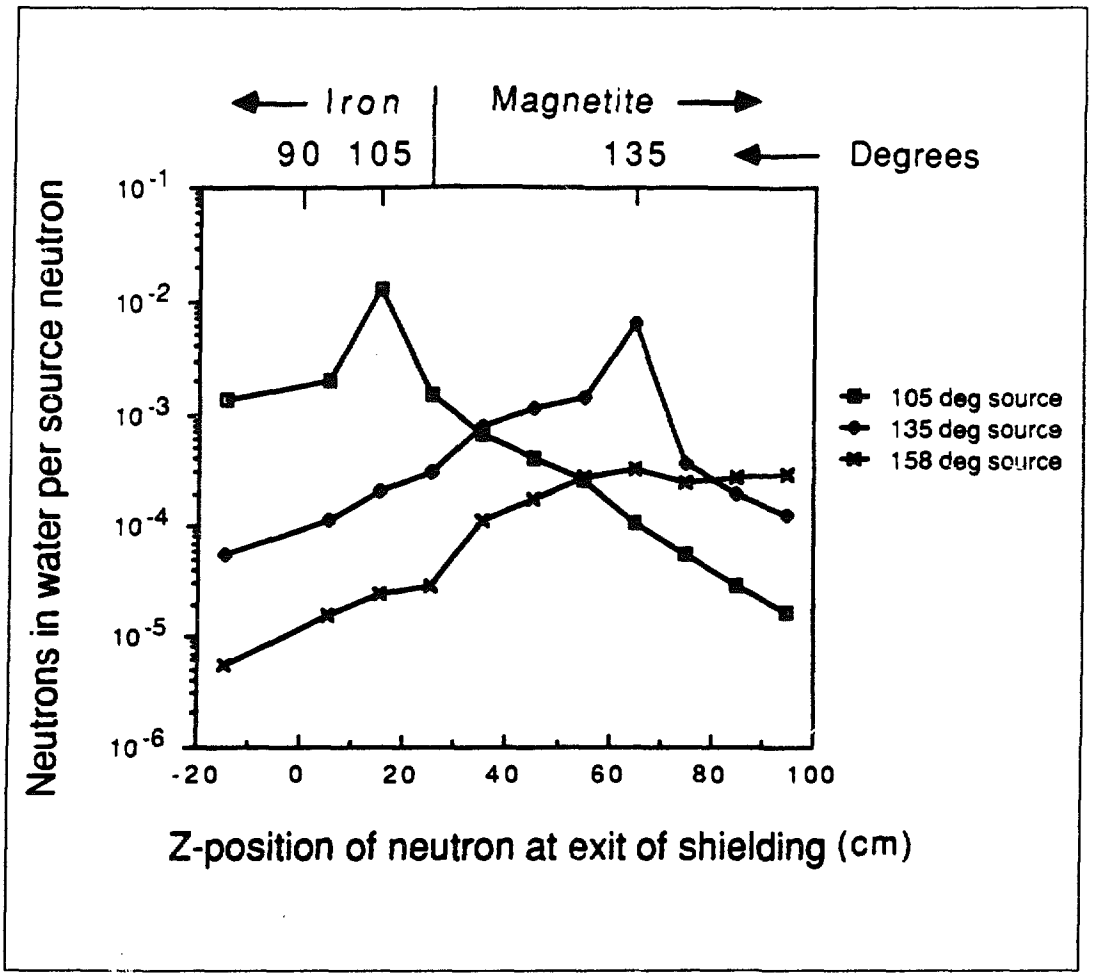

Fig. 7.15. Three HETC calculations showing the z-position of neutrons entering the water after surviving passage through the LCD iron and magnetite shielding. For each calculation (105°, 135°, and 158° with respect to the proton beam direction), 500,000 neutrons with initial energy in the 20 to 100-MeV range were transported. Only those surviving neutrons with greater than 20-MeV energy are shown here. Both the 105° and 135° results exhibit a peak corresponding to the original neutron angle, attributed to neutrons traveling a roughly "direct" path to the water; the neutrons in these peaks have a significantly more energetic spectrum. Zero in z-position is at the target, with the units in cm; the detector was approximately one-tenth the size of LCD for modeling purposes. The calculations shown here have been weighted by the source distributions shown in Fig. 7.16. While no calculation was done specifically for 90° incident neutrons, the maximum surviving flux would be near this angle since both the incident flux is highest, and the iron is thinnest.

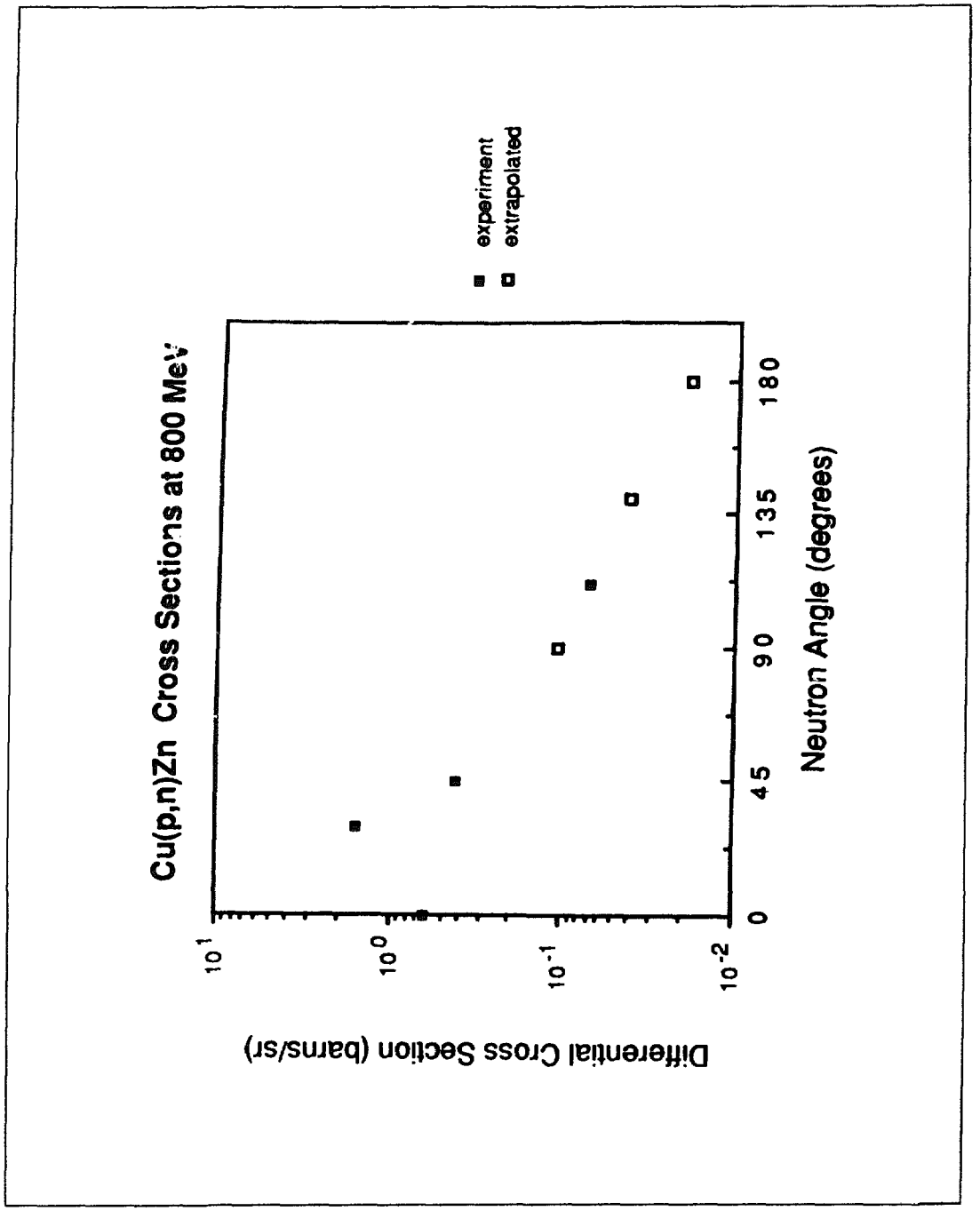

Fig. 7.16. Cu(p,n)Zn-differential cross sections for 800-MeV incident proton energy, summed over neutron energies 20 MeV to maximum. Four of the points are experimental,[13] and three were extrapolated from a logarithmic fit to the two highest-angle data points. This distribution was used to weight the HETC calculations in Fig. 7.15 according to the relative number of source neutrons for a particular angle.

7.5 Proton Beam Interactions with Gas in the Beam Pipe

The proton beam travels through about 16m of beam pipe within the LCD shielding before striking the target. Significant background rates are possible arising from interactions of the proton beam with the small amount of gas contained in this evacuated beam pipe. It is straightforward to estimate the vacuum necessary to hold the beam-gas backgrounds to an acceptable level. The desired target density, ρ, can be found by writing the total cross section as

$$\sigma = (I_s/I_o)\,(A/N_o\rho d)\,,$$

where I_s and I_o are scattered and incident intensities, A is the target atomic weight, N_o is Avogadro's number, and d is the pipe length. The total proton-scattering cross section on ^{14}N is 390mb (Particle Properties Data Booklet). The constraint on allowable beam losses on the pipe wall is 10^{-9}m^{-1} (see section 7.2), so the value taken here for the ratio I_s/I_o is 16×10^{-9}. This gives the result that the poorest allowable vacuum in the beam pipe corresponds to $\rho_{max} = 6.0 \times 10^{-10}$g/cm^3, or 0.50$\mu$m-Hg gas pressure. The vacuum requirement can be relaxed to 1.6μm-Hg by replacing 0.5m of magnetite with 0.5m of steel. A vacuum quality of 1μm-Hg or better can be achieved, so we do not expect significant background arising from beam interactions with the residual gas in the beam pipe. We have not estimated the background associated with beam loss due to space-charge expansion of the beam. Replacing magnetite adjacent to the beam pipe with steel would also reduce this source of background to acceptable levels. For example, replacing a meter of magnetite with a meter of steel relaxes the beam loss requirement of 10^{-9}m^{-1} to 10^{-8}m^{-1}.

7.6 Background from ν_e - O Scattering

An equal number of ν_μ, ν_e, and $\bar{\nu}_\mu$ emerge from the beam stop. Only the ν_e will interact with oxygen in the water to produce electrons in the final state. At the neutrino energies of this experiment, the charged-current cross sections are much reduced from the free-nucleon values. This is especially true of nuclei such as oxygen, where the ground state is a good approximation to a closed shell. However, even though the cross section for ^{16}O is small, it is not negligible. Furthermore, because some of the transition strength (allowed axial vector) is suppressed, the calculation of it is not straightforward. This question is discussed in this section along with the simulation of the data analysis of this background that we have performed. Although a small number of $\bar{\nu}_e$ will be produced from μ^- decay, the existence of the reaction $\bar{\nu}_e + p \rightarrow e^+ + n$ will be more a test of neutrino oscillations, as is discussed

in chapter 15, than a background in the experiment. Muon neutrinos produced from decay at rest cannot undergo charged-current interactions. Neutral-current excitation of ^{16}O from muon and electron neutrinos is discussed in section 7.9.

Haxton[14] has recently performed an extensive analysis on the ν_e - oxygen cross section as it will appear in this experiment. We now summarize his conclusions; the equation numbers below refer to his paper.

a) The major contribution to the cross section comes from the first forbidden transitions to odd-parity states in ^{16}F: $0^+ \rightarrow 1^-$ and $0^+ \rightarrow 2^-$. The $0^+ \rightarrow 1^-$ cross section (equation 10) goes to zero as the momentum transfer goes to zero in the forward direction. The transition $0^+ \rightarrow 2^-$ (Eq. 9) gives an enhanced cross section at backward angles, where the cross section is dominantly transverse. The contribution of the 2^- states is almost 60% of the negative-parity cross section near $\theta = \pi$. This calculation is similar to that of Donnelly,[15] which was used by us previously, with a normalization to agree with recent electron-scattering data.

b) The $\Delta J^\pi = 0^-$ contribution vanishes at backward angles and is dominated in the forward direction by the axial-charge operator, the leading correction to the allowed approximation in the long-wavelength limit. There are two relevant 0^- states in ^{16}F, the first is at 190 keV and the second is expected at 13 MeV above the ground state. The cross section for the 190-keV state is sharply constrained by the analog β-decay transition ^{16}N$\rightarrow^{16}$O(gs). The second state contributes 56% of the $0^+ \rightarrow 0^-$ neutrino capture rate in the Haxton calculation, in spite of the reduction in phase space. The principal issue at stake here is the renormalization of the time-like part of the axial current, which is expected to be strongly renormalized by pion exchange currents. However, over the past three years this subject has become well understood theoretically[16] and been verified by experiment.[17] The energy distribution of the electrons will also be reduced by the 13-MeV excitation energy.

c) The closed-shell approximation for ^{16}O is known to be inadequate because several magnetic-dipole transitions to excited states have been observed. The analogues to these excited states presumably have Gamow-Teller (GT) transitions in the ν_e charged-current scattering. The $\theta = 0$ allowed cross section depends only on the $\Delta J^\pi = 1^+$ GT matrix element, which is gently peaked in the backward direction ($d\sigma/d\Omega \approx 1 - 1/3\ \cos\theta$). In principle, the GT distribution in ^{16}O can be calibrated in forward (p,n) reactions. The GT transition is weak in ^{16}O, as expected, so that a precision determination has not been made, although as we shall discuss below, it is not necessary. Those involved with the (p,n) program believe they have demonstrated that this technique measures

relative GT strengths in light nuclei to an accuracy of 5-10%, although there is no known GT transition in ^{16}O to use for normalization. Such measurements would provide a crosscheck on the calibration procedure we describe later in this section.

d) The net contribution of ^{17}O and ^{18}O to the forward-angle cross section is about 0.5 of the ^{16}O GT or axial-charge transitions. The strong GT transitions to the ^{18}F ground state and first excited state are calibrated by β-decay measurements. These transitions are 90% of the ^{18}O cross section. The relative amounts of ^{17}O and ^{18}O in water are small, but the cross sections are large enough that they must be taken into account. Empirical calibration from β decay is straightforward, and it is also noted that the sum of Fermi and GT transitions yields a cross section that is almost flat with θ.

The dynamics of the electron angular and energy distributions are known very well. The main uncertainties are the cross sections of the different components, which are known to $\leq 25\%$. Of the four components, the principal concerns are the axial-charge to the 13-MeV excited state and the ^{16}O GT contribution. The axial-charge contribution could have been pernicious because its angular distribution peaks at $\theta = 0$. Table 7.3 gives a summary of the calculation by Haxton of the magnitudes of these contributions as well as the contribution at 0°. We have ignored ν_eD interactions, which are similar to ν_e ^{18}O interactions in electron energy and angle but contribute only 5% the number of events.

Table 7.3 Calculation of the oxygen cross sections.

Isotope	*Contribution*	*Total Cross section* ($10^{-41} cm^2$)	*Cross section x Abundance* ($10^{-41} cm^2$)	*0° Cross section x Abundance* ($10^{-41} cm^2 cos\theta^{-1}$)
^{16}O	− parity 1^-,2^-	0.908	0.908	0.035
^{16}O	+ parity GT 1^+	0.149	0.149	0.042
^{16}O	axial charge 0^-	0.042	0.042	0.042
^{17}O	+ parity GT	8.24	0.003	0.001
^{18}O	+ parity GT	18.4	0.037	0.012

Figures 7.17a-d show the angular distribution of each of these contributions, weighted by the naturally occurring abundance in water. Figure 17.18 shows the composite cross section of all of the isotopes together. Figure 7.19 shows the same

distribution after the detector resolution has been folded in and cuts applied. It is important to note here that the distribution of events as a function of $\cos\theta$ between $\cos\theta = 1$ and $\cos\theta = 0$ is very close to linear. Deviations from the straight line occur in the backward hemisphere, but as will be seen, the extrapolation process using the forward hemisphere alone is remarkably accurate and tolerant of substantial variation in the input-oxygen cross sections. The oxygen interactions have the same time distribution as the neutrino-electron scattering from muon decays, which are the events in the denominator in R. In Figs. 7.20a,b are shown a simulation of the events that are expected to occur in the detector as a function of $\cos\theta$, including neutrino-electron scattering: Figure 7.20a is the generated distribution and 7.20b is after reconstruction.

The simulation was extensive and included energy acceptance, finite energy resolution, multiple scattering, full-track reconstruction, random noise in the photomultiplier tubes, 16% photocathode coverage, and 1ns-σ timing jitter per tube. In order to separate the ν_μe, ν_ee + $\bar{\nu}_\mu$e, and ν_eO components we have performed a maximum-likelihood-analysis fit in time and angle for $\cos\theta > 0$. Two time dependences were used, a prompt-time dependence based on pion decay convoluted with the PSR spill for the ν_μe component, and a delayed-time dependence based on muon decay and the PSR spill for the other components. For the angular dependence, three simple functional forms shown in Table 7.4 were used.

Table 7.4 Three functional forms used for the angular dependence.

Time	*Reaction*	*Functional Form*
Slow	$\sigma(\nu_e O)$	A + B$\cos\theta_e$
Fast	$\sigma(\nu_\mu e)$	C exp (D$\cos\theta_e$) + Eexp(F$\cos\theta_e$
Slow	$\sigma(\bar{\nu}_\mu e) + \sigma(\nu_e e)$	Gexp (H$\cos\theta_e$) + Iexp (J$\cos\theta_e$)

The ratio R, the result of the experiment, was fit for a number of possible combinations of oxygen-cross-section contributions. The axial-charge contribution was adjusted, for example, by $\pm$ 25%. In Table 7.5 we show the results of fitting for R with different hypotheses for the oxygen cross section.

Table 7.5 Results of fitting for R.

Hypothesis	*Fitted value for R*	*Difference in fit value*
Normal oxygen	0.1217± 1.8%	
No oxygen	0.1221± 1.6%	$+3.3 \times 10^{-3}$
25% more axial	0.1214± 1.8%	-2.5×10^{-3}
25% less axial	0.1219± 1.8%	$+1.6 \times 10^{-3}$
25% more ^{16}O GT	0.1220± 1.8%	$+2.5 \times 10^{-3}$
25% less ^{16}O GT	0.1217± 1.8%	$< 1.0 \times 10^{-3}$

The error on the fitted value for R is statistical only and based on 5500 accepted ν_μe events, less than the 7500 events we expect after 1.5 A-Hr. (We generated approximately $2.3 \times 10^5 \nu_e O$ events and $1.0 \times 10^5 \nu e$ events.) The third column is the difference from the Haxton calculation for normal oxygen. It is remarkable that the fitting procedure is tolerant of removing the oxygen contribution altogether, and still the value of R remains close to the expected value. The error in the second column is consistent with the statistical error (see section 12.8.3); therefore, the difference in fit value, which is shown in column 3, is a good representation of the systematic error in the fitting process. Because there are about 22 ν_eO events with $\cos\theta > 0.76$ and 101 ν_ee plus $\bar{\nu}_\mu$e events per day, a 0.5% systematic error implies that we can effectively subtract the oxygen background to better than 2%.

In conclusion, we have found that a simple parameterization, linear in $\cos\theta$ over a limited range, gives a good fit to the oxygen cross section computed by Haxton and is tolerant of substantial variation in the component cross sections. This variation comes mostly from a lack of knowledge of the relative amplitude of the component contributions and not from a lack of knowledge of the angular distributions (or energy distributions — inclusion of energy should further improve the fit). The success of the fitting procedure is not ascribed to detailed knowledge of the cross sections, but is due to the very different shapes of the cross sections for neutrino-electron scattering and charged-current neutrino-oxygen scattering. Even the simple fitting prescription that we have used is sensitive to the difference in these shapes. By varying each component in the calculation by 25% of itself we have induced an error in R of $< 0.5\%$, which is clearly adequate for our purposes.

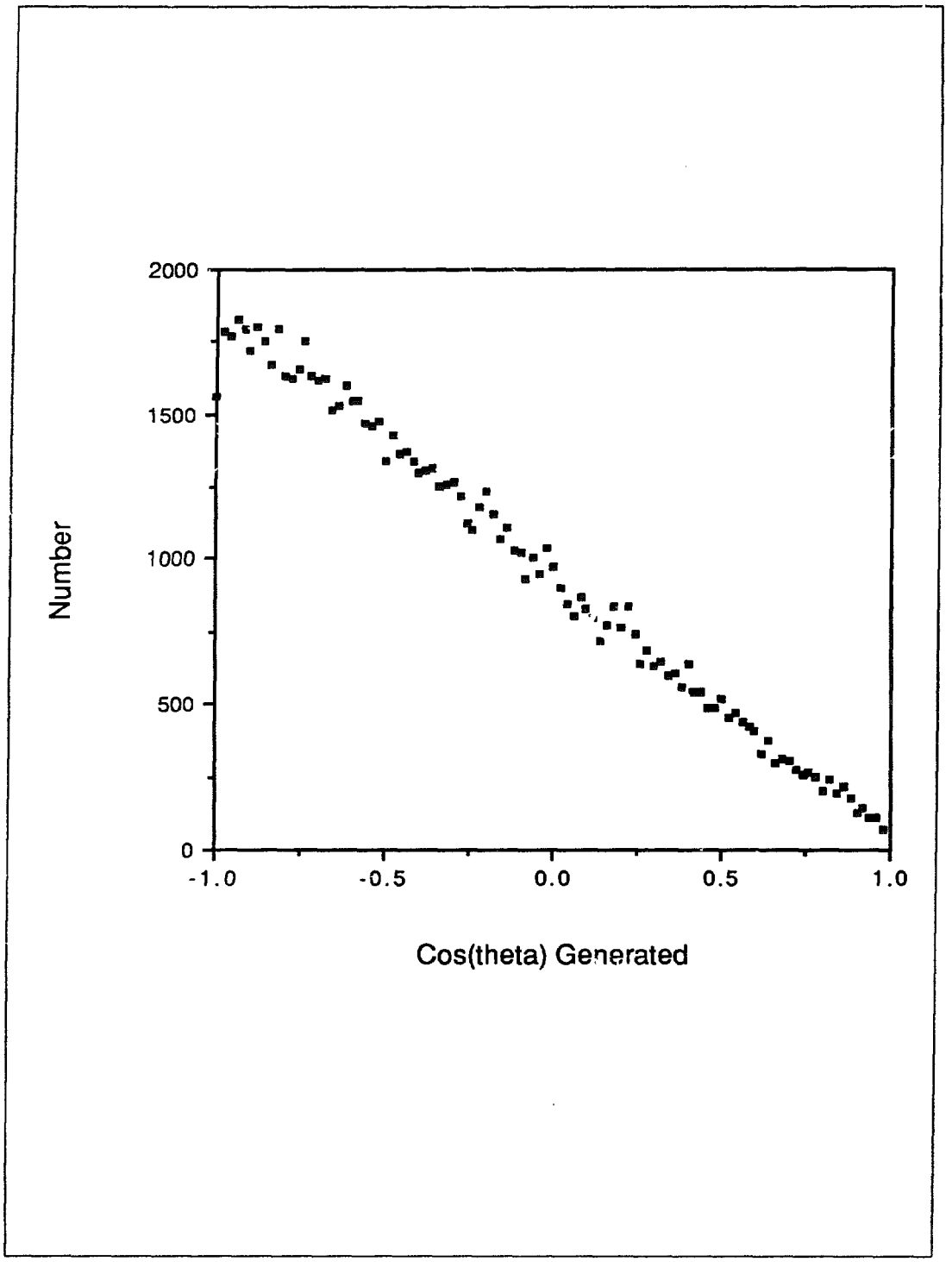

Fig. 7.17 (a). Angular distribution of the ν_e $^{16}O^-$ contribution.

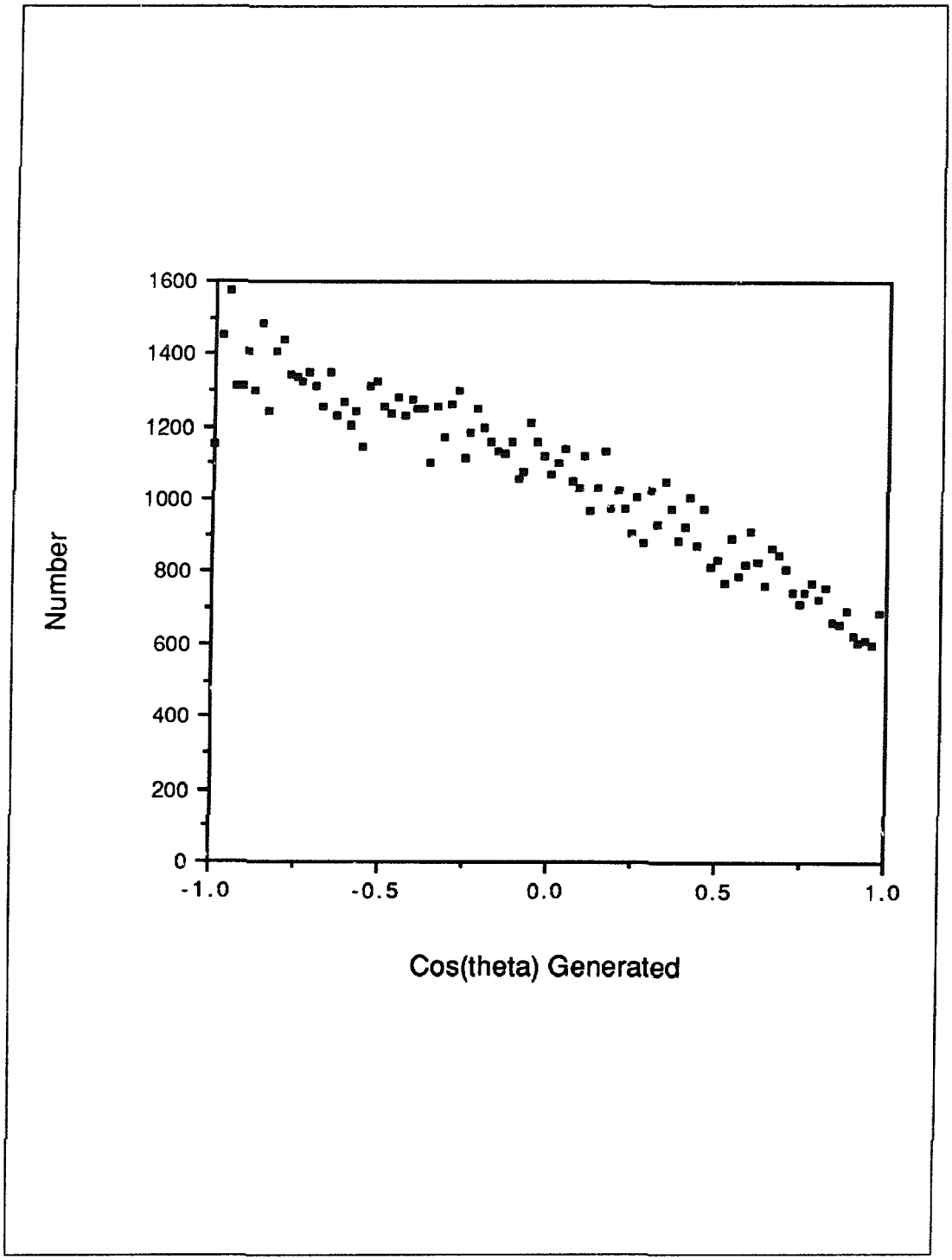

Fig. 7.17 (b). Angular distribution of the ν_e $^{16}O^+$ GT contribution.

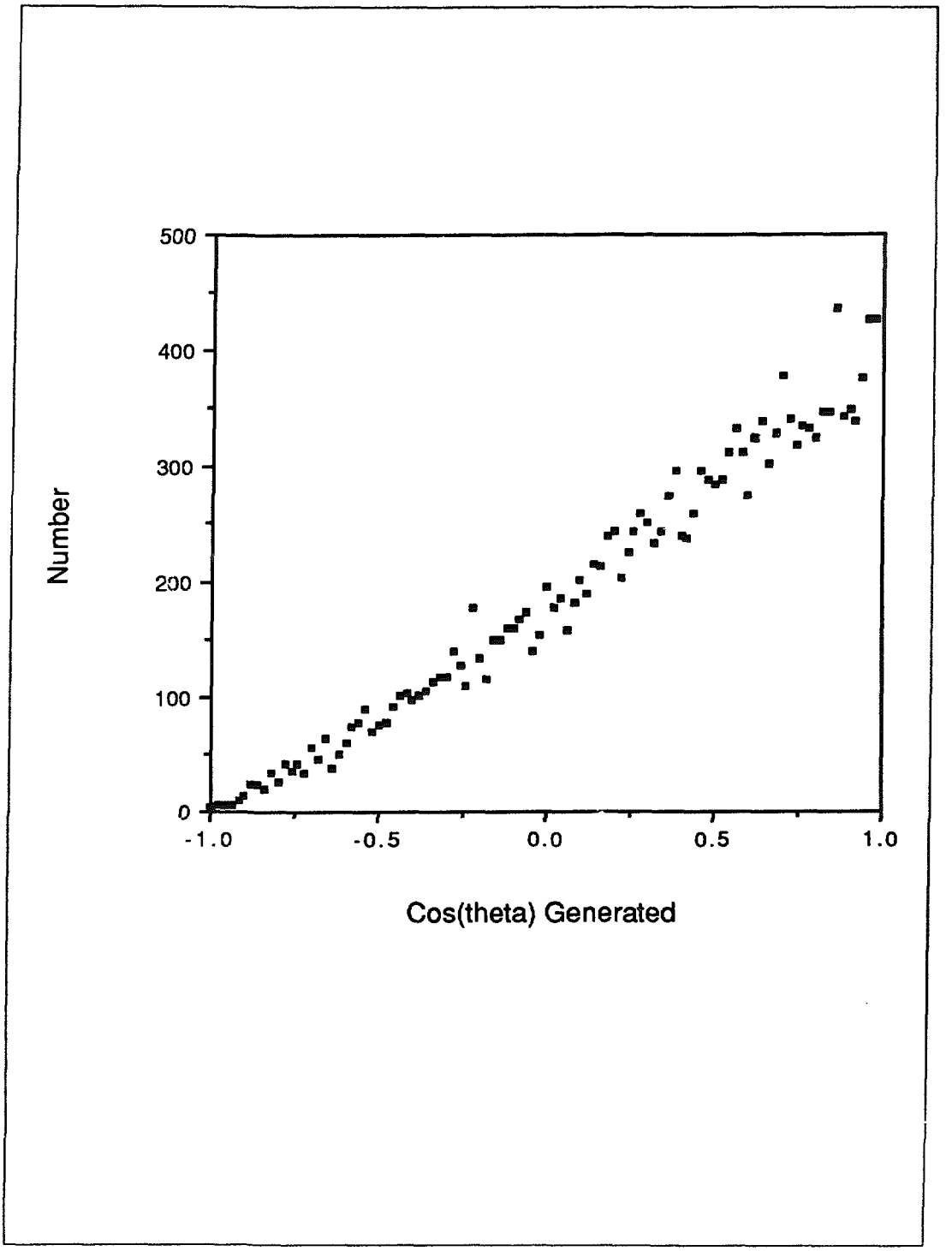

Fig. 7.17 (c). Angular distribution of the ν_e $^{16}O^-$ axial-charge contribution.

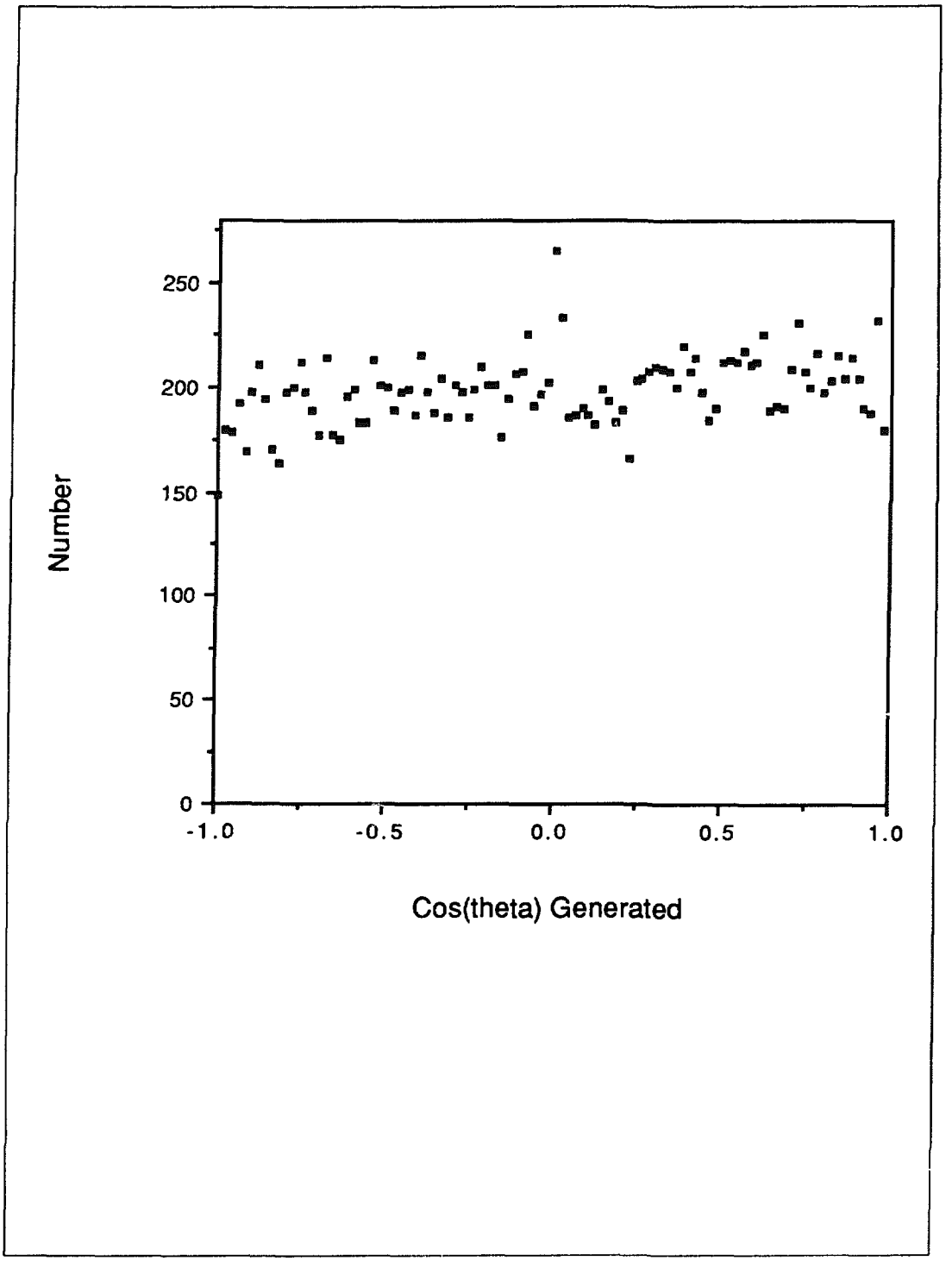

Fig. 7.17 (d). Angular distribution of the ν_e $^{17,18}O^+$ contribution.

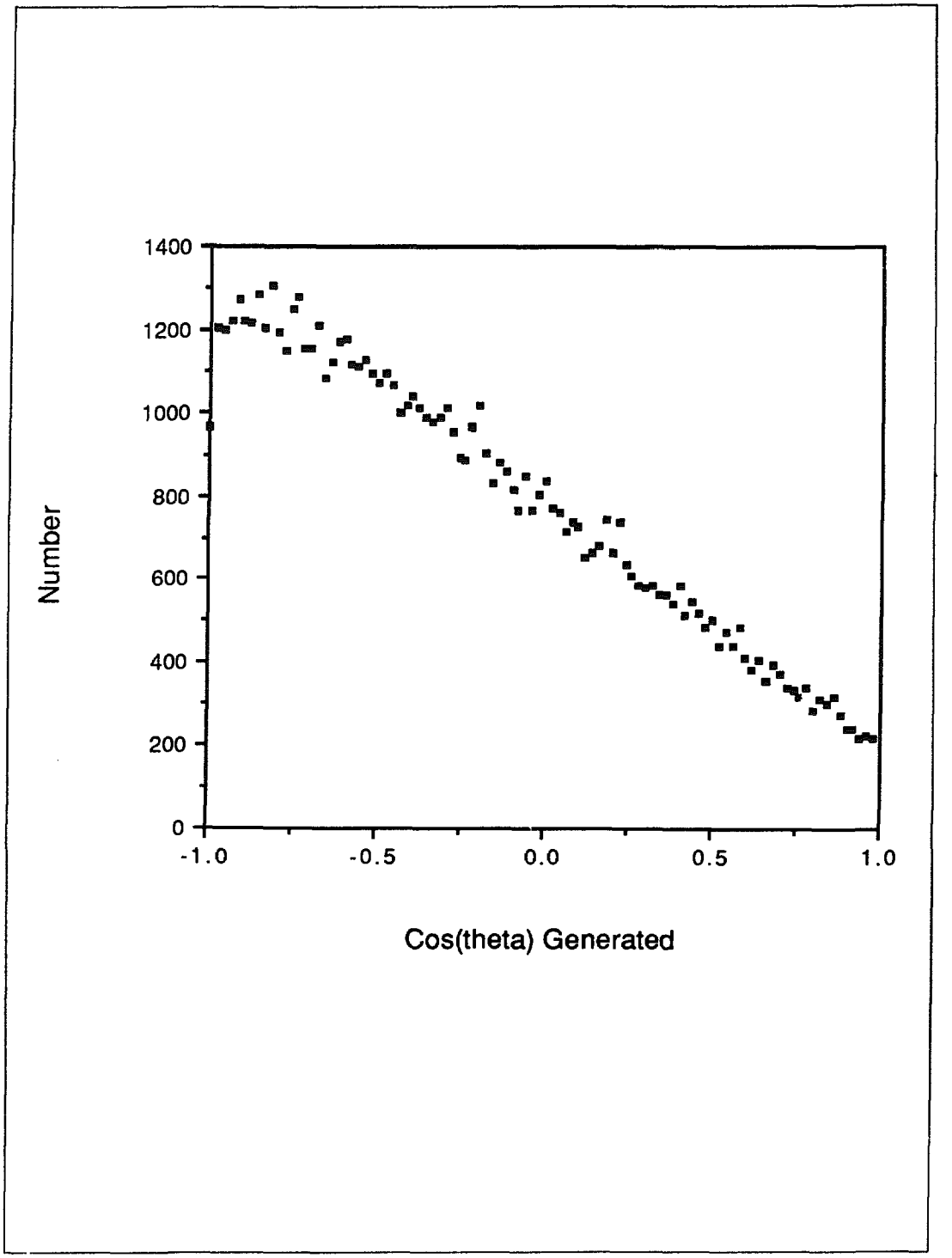

Fig. 7.18. Composite $\nu_e O$ angular distribution of all isotopes together.

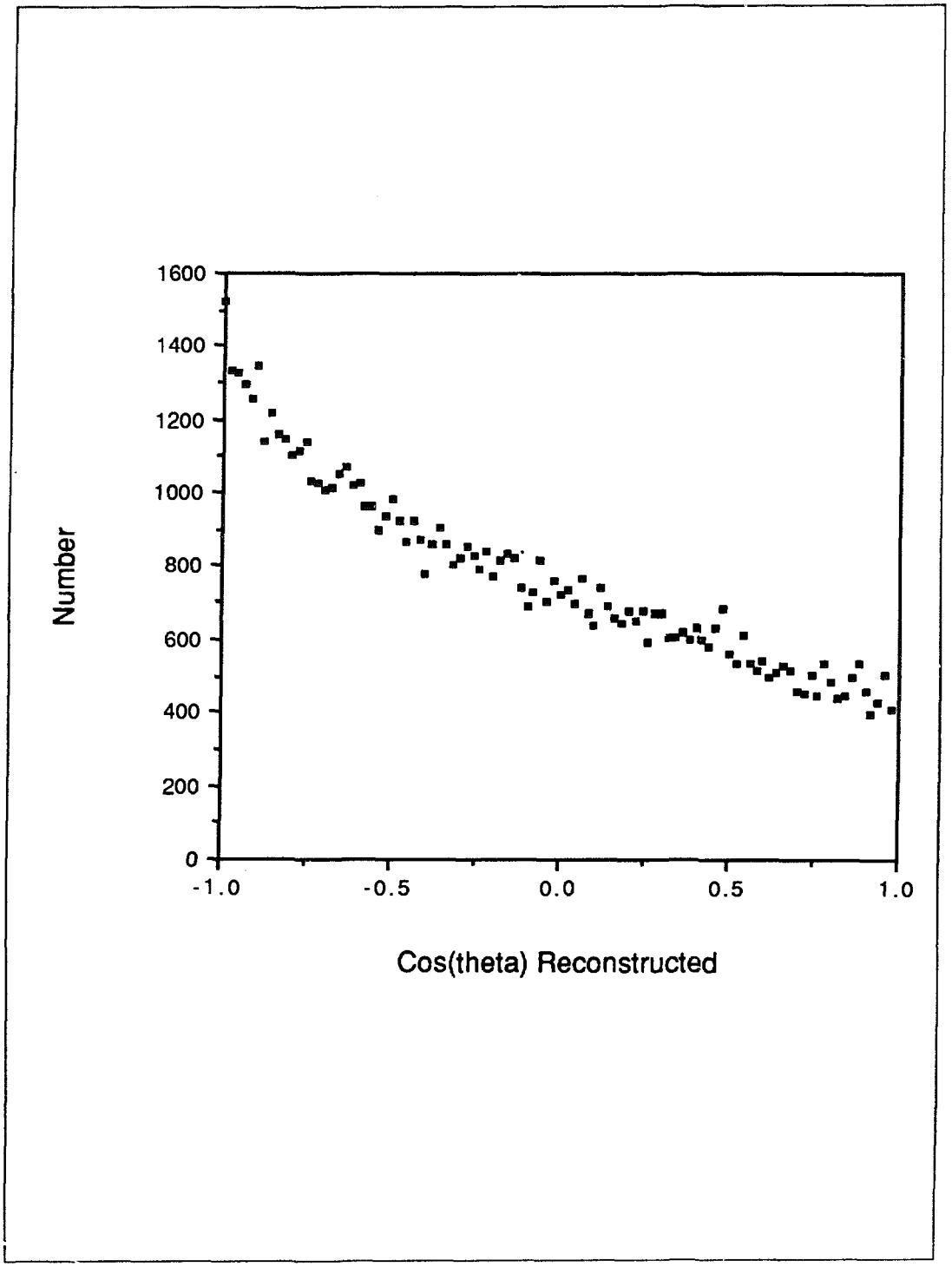

Fig. 7.19. Composite ν_eO angular distribution after reconstruction with the detector resolution folded in.

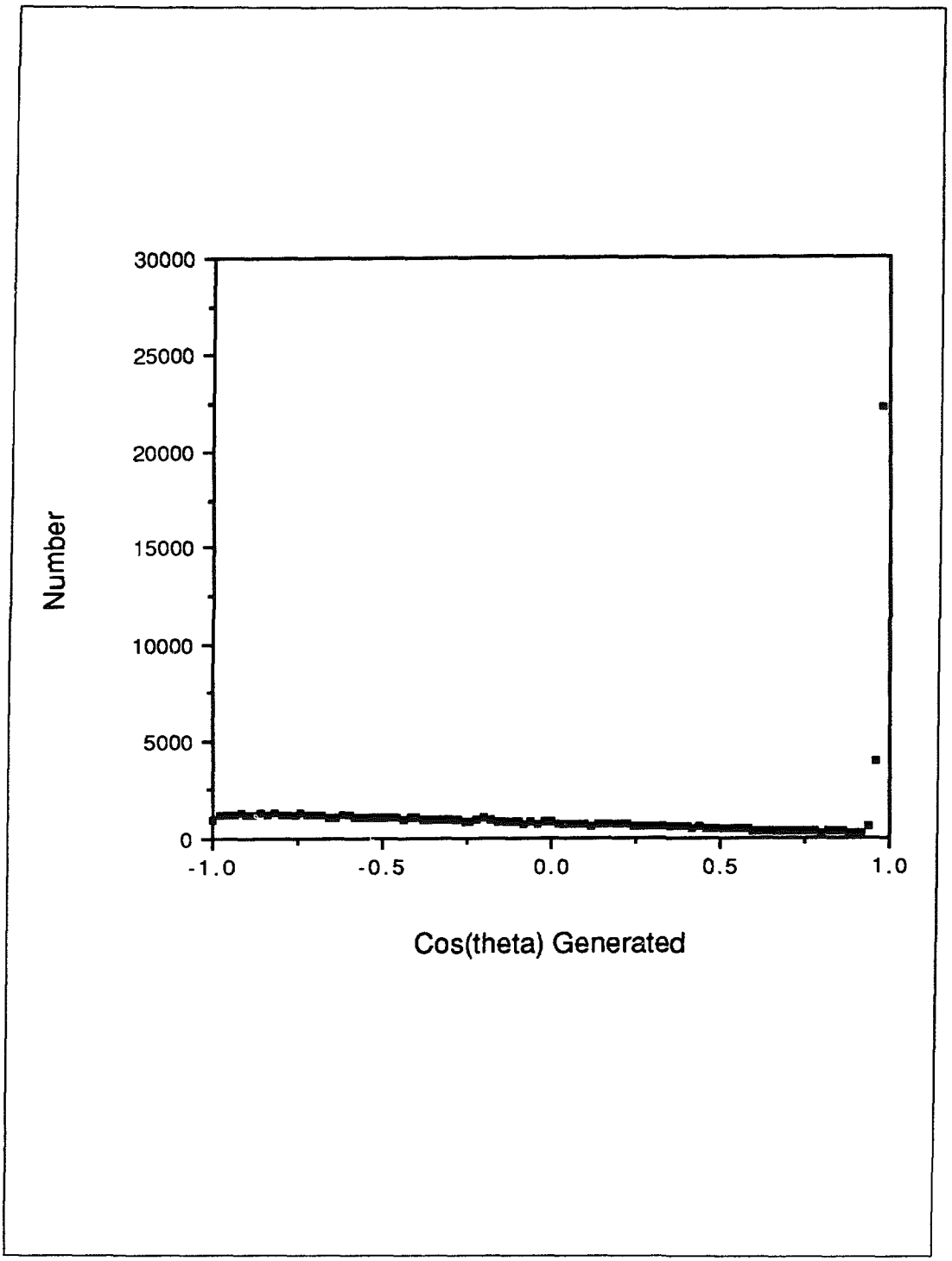

Fig. 7.20 (a). The generated angular distribution of νe and ν_eO events combined.

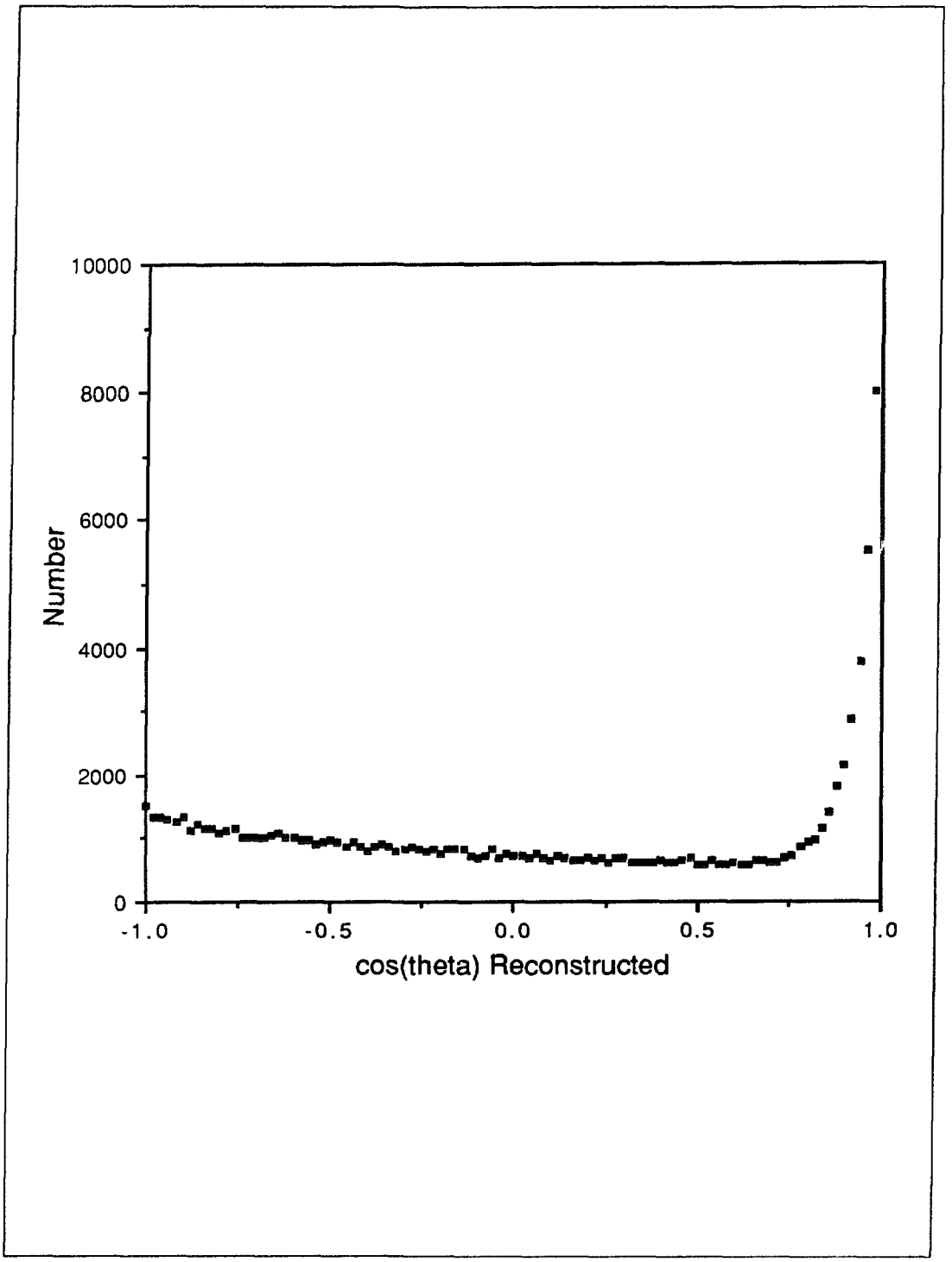

Fig. 7.20 (b). The reconstructed angular distribution of νe and $\nu_e O$ events combined.

7.7 Decay-In-Flight Background

As mentioned in the previous chapter, about 1.1% of the pions produced in the target dump will decay in flight before coming to rest. Because we nominally assume that the neutrinos come from stopped pions and muons, it is necessary to correct the data for this background. Note that we can ignore in-flight muon decay because only about 10^{-6} of the muons produced in the target dump will decay before stopping. We consider seven separate processes: three involving π^+ decay in flight, three involving π^- decay in flight, and the decay $\pi^+ \rightarrow e^+\nu_e$.

π^+ Decay-In-Flight Background

As described in chapter 6, the production and decay of pions in the target have been modeled in detail. About 1.1% of the pions will decay in flight before coming to rest, and 20% of the neutrinos from pion decay-in-flight will enter the fiducial volume of the detector compared to pion decay at-rest. The first background we consider is a neutrino from in-flight pion decay interacting in the detector. This process will occur at $1.1 \times 0.2 = 0.22\%$ the rate of neutrinos from pion decay at rest. Therefore, the effect of this background is to increase R by 0.22%. If the neutrino energy is over 130 MeV, then muons can be produced by the neutrino-oxygen charged-current process, which has a cross section several orders-of-magnitude larger than neutrino-electron scattering. The resulting muons are non-relativistic and do not emit Čerenkov light; however, the positrons from muon decay are relativistic and do emit Čerenkov light. Fortunately, only a very small fraction of these high-energy neutrinos enter the detector, as is shown in Fig. 7.21, which gives the ν_μ energy distribution at an angle of 63^o. (Note that the fiducial volume of the detector covers the angular range $75 - 130^o$.) Hence we estimate that this background will decrease R by less than 0.1%.

Another π^+-induced background is neutrino interactions from stopped muon decay, where the muon comes from pion decay in flight. This process gives the largest decay-in-flight background, but depends only on the 1.1% fraction of pions that decay in flight. As almost all muons decay at rest, this background will cause R to be decreased by 1.1%.

The last π^+-induced background is the rare decay $\pi^+ \rightarrow e^+\nu_e$. Although it is not a decay in-flight background, the effect of this rare decay is quite similar to the other backgrounds discussed in this section. The branching ratio for this decay is 1.2×10^{-4} and the cross section ratio $\sigma(\nu_e e)/\sigma(\nu_\mu e) \sim 10$ due to the higher ν_e energy and the larger intrinsic cross section. This background will therefore increase R by about 0.1%.

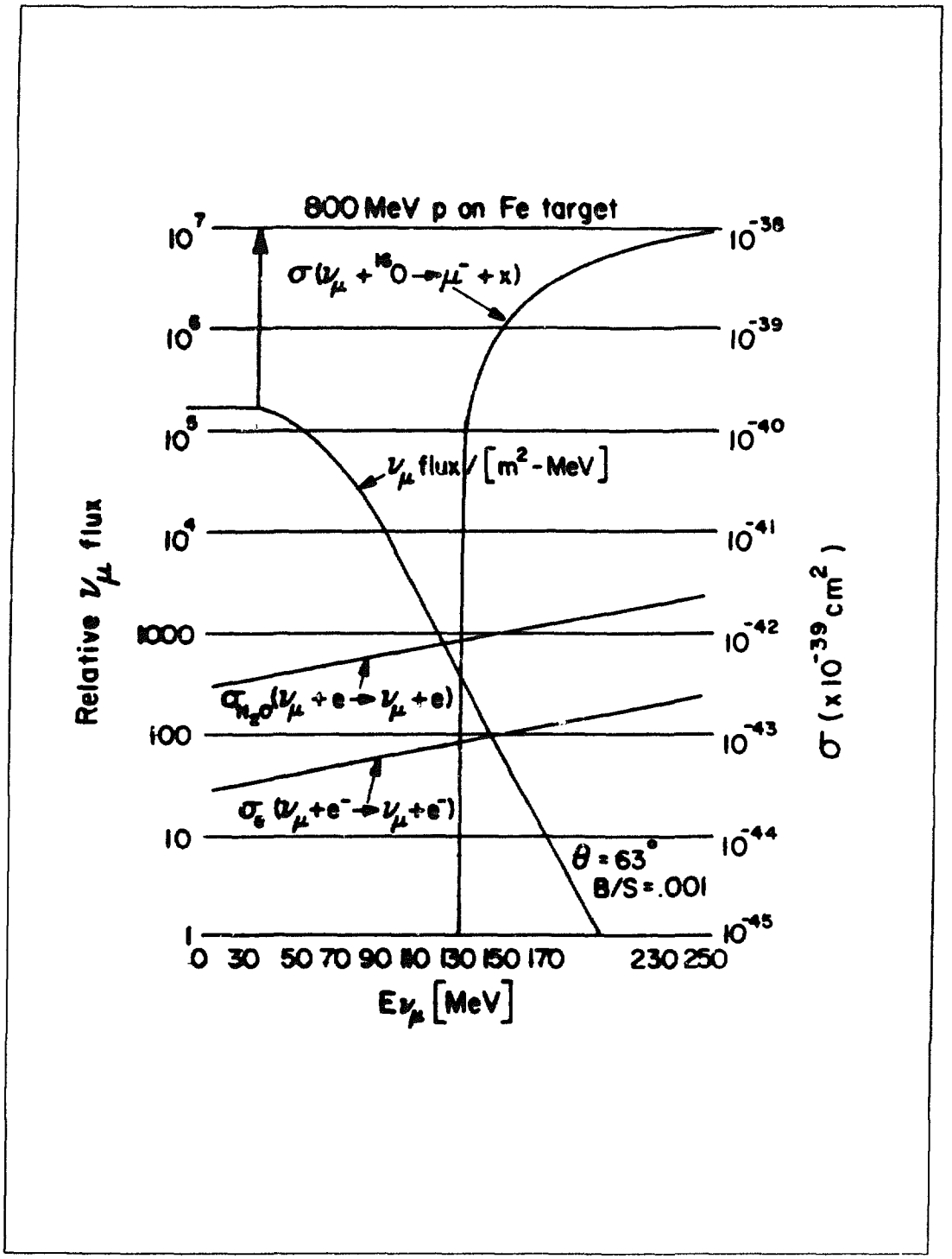

Fig. 7.21. The ν_μ energy distribution from pion decay at rest and in flight. Also shown are the cross sections for $\nu_\mu e$ scattering and ν_μ O charged-current interactions.

π^- Decay-In-Flight Background

The probability that a π^- will decay in flight is 1.1%, and the π^-/π^+ ratio in the target is 1/6. Because the $\bar{\nu}_\mu e$ cross section is similar to the $\nu_\mu e$ cross section, and the probability that the neutrino from pion decay in flight enters the detector is 20% of the decay at rest probability, neutrino interactions from in-flight pion decay cause R to be increased by $1.1 \times 1/6 \times 0.2 = 0.04\%$. Another background to consider is neutrino interactions from stopped muon decay, where the muon comes from pion decay in flight. Only about 5% of the muons will decay before absorption; however, the $\bar{\nu}_e p$ charged-current cross section is approximately 40 times as large as the neutral-current ν_ee cross section, taking into account the free proton to electron ratio of 1/5. As only about 10% of the positrons from $\bar{\nu}_e p$ interactions are in the forward direction, we estimate the change in R to be $-1.1 \times 1/6 \times 0.05 \times 40 \times 0.1 = -0.04\%$. The final background we consider is $\nu_\mu e$ interactions from μ^- capture, which occur more or less promptly. Neutrinos from muon capture have a much harder spectrum than neutrinos from pion decay, although for now we shall assume that they contribute equal numbers of events for electron energies less than 55 MeV. We therefore estimate an increase in R of $1.1 \times 1/6 \times 0.95 = 0.17\%$.

Summary of the Decay-In-Flight Background

Adding up all of the above contributions, we estimate that the pion decay-in-flight backgrounds will cause R to change by $\sim -0.7\%$. Assuming we can correct this change to 10%, the systematic error on R becomes 0.07%. A more conservative approach is to add up each component in quadrature and then multiply the square root by the 10% correction factor. The resulting systematic error on R is 0.12%.

7.8 Spallation in the Target

Protons from the PSR will interact in the copper/graphite target to produce pions, which in turn decay to make the neutrino source. Approximately 0.1 π^+ is produced for each 800-MeV proton incident. The interactions of the protons result in secondary nuclei, which principally decay strongly through particle emission in a very short time.

After the particle-emitting channels are exhausted and de-excitation by gamma rays is complete, the residual nuclei are either stable or β emitters. In fact, because copper has a neutron excess, most often the residual nucleus will emit an e^-, and the associated neutrino will be $\bar{\nu}_e$.[18] These neutrinos will primarily interact in the water of the detector through the reaction

$$\bar{\nu}_e + p \rightarrow e^+ + n$$

on free protons, with a threshold of 1.8 MeV. It is a good approximation[19,20] to assume that every proton will produce one β emitter. Although some of the end products are stable, heavy nucleus fragmentation occasionally produces more than one β emitter, and these effects apparently compensate.

Immediately after the proton beam spill, the residual nuclei will β decay with an end point to the neutrino spectrum limited by the particle-unstable threshold. A lifetime of about 10ms exists for light elements (for example, ^{12}B, has a lifetime of 20ms and a Q value of 13 MeV and is an allowed transition). The fraction of the β emitters formed that will decay in the 10μs following the beam spill will be 0.5×10^{-3}, and that is to be compared to the fraction of 0.1 that produce π^+. A background of less than 0.5% of the ν_e flux with a mean $\bar{\nu}_e$ energy below 6 MeV will occur after the spill, uniformly through the gate. The ratio of the cross section for the neutrino-induced reaction from ^{12}B neutrinos to that for ν_e-e scattering is $3.64\ E_\nu/m_e = 43$, so there will be low-energy clusters at a level of about 20% of the ν_e-e events. These events are mostly below threshold, but will occur accidentally and be rejected in the fitting process. One hundred milliseconds later, the next pulse arrives from the PSR after many of the allowed β decays have taken place; those remaining will produce a small noise component that also will be rejected by the fitting process.

Estimates made using the measured radioactivity in the target taken in routine operations at LAMPF soon after the beam is turned off are consistent with this picture. A detailed calculation of the probability of producing β emitters from appropriate target constituents will be made.

It seems amusing to try to detect these neutrinos from the radioactivity in the target. To do so it will be necessary to lower the threshold of 20-hit tubes and look for an increase in the number of small clusters of coincident tubes for a substantial period after the proton spill. The effective lifetime of these events will allow identification of the source of the events and also an estimate of the neutrino energy. It is not inconceivable that a competitive neutrino-oscillation measurement could emerge from these events.

7.9 Neutral-Current Excitation of ^{16}O

It is possible for all three neutrino types produced in the beam-stop source (ν_e, ν_μ, and $\bar{\nu}_\mu$) to excite levels in ^{16}O via weak neutral-current interactions. For example, the reaction $^{16}O(\nu_\mu, \nu_\mu^{'})\ ^{16}O^*$ (16.209 MeV, 1^+, T=1) is analogous to the well-studied[21] axial-vector, isovector transitions in ^{12}C. These inelastic-scattering processes represent potential background to the neutrino reactions of interest, through the emission of high-energy gamma rays. The ^{12}C (15.4 MeV 1^+, T=1)

level, as an example, decays through roughly isotropic emission of a 15.11-MeV gamma ray.

The cross section for such a transition in ^{16}O is comparable to the charged-current backgrounds treated at length in this proposal, being typically a factor 1/3 as large. However, the rates for high-energy gamma-ray emission are quite small. At the momentum transfer available for 0-53 MeV neutrinos, the neutral-current excitations from 0^+ ground states are dominated by axial-vector transitions.[20] Within the standard model, these transitions are restricted to be isovector as well; hence, the interest in the ^{12}C (1^+, T=1) excitations. For ^{16}O, these O^+ $T = 0 \rightarrow 1^+$, $T = 1$ axial-vector, isovector transitions lead to states at 16.204, 17.140, and 18.79 MeV. These states are all particle unstable, with typical Γ_γ widths of a few eV, compared to total Γ widths of tens of keV. Hence, the rates for high-energy gamma emission will be reduced by a factor of 10^{-4} and will be negligible.

Excitation of giant dipole states by neutral currents would proceed through a vector operator. The strength is expected[20] to be down by $(q/M_n)^2$, where q is the momentum transfer (about 60 MeV), compared to the axial-vector transition. This very reduced cross section for neutrino energies below 50 MeV is shown in an explicit calculation by Dadayan.[21] We would again expect negligible background rates from this neutral-current channel.

7.10 Summary of Backgrounds

The principal neutrino-related background is the charged-current interaction of ν_e with the various isotopes of oxygen. A good fit to the Haxton calculation of this background is obtained by a simple $\cos\theta$ parameterization. A 25% uncertainty in the ^{16}O-axial contribution leads to a systematic error in R of less than 0.5%.

The systematic error in R due to all of the pion decay-in-flight backgrounds is conservatively estimated to be 0.12%.

Backgrounds associated with neutral-current excitation of ^{16}O and neutrinos from β decay of radioactive isotopes in the target are negligible.

Neutron-induced photons are produced in the fiducial volume of water at a rate of 4.1 per day (at 100μA beam current) in the energy range $10<E_\gamma<60$ MeV. Assuming isotropy, the contribution in the forward 40° cone will be $0.12 \times 4.1=0.49$. We expect to be able to subtract this contribution with less than 10% error by fitting the neutron background in the same way as the oxygen background. (Note that this neutron background has a different time distribution than the oxygen background.) These events occur in the "prompt" time interval. This leads to an error in the numerator of R, which comprises ν_μe events, occurring at a rate of 11 per day.

Thus, the error contribution to R of neutron-induced photon production will be 0.45%.

The contribution to the numerator of R ("prompt" time interval) from events related to neutron-produced pions in the fiducial volume of the water is given by:

$$[2.0(\pi^-) + 0.55(\pi^+) + 0.25(\pi^o)] \times 10^{-5} pions/neutron \times (8.0 \times 10^3 \; neutrons/day)$$

$$= 0.22 \; events/day$$

These events will be mostly contained in the forward 40^o cone. Again, subtracting this contribution with less than 10% error and comparing with a ν_μe rate of 11 per day, we obtain an error in R of 0.20%.

The pion contribution to events in the "delayed" time interval, which appear in the denominator of R, is very small. Assuming that this contribution can be subtracted with less than 10% error, the resulting systematic error is less than 0.01%.

The neutron-induced background is sensitive to the shielding design, as well as to the neutron spectrum. We have used a 7.25m-radius (iron equivalent) shield and 30-cm water veto region before the fiducial volume of the detector. From Experiment 225, we have included a normalization factor of 0.49 for the HETC-generated neutron spectrum. As a guide, the neutron-induced background rates are changed by a factor of 10 by 0.5m of iron shield.

References

1. H. W. Bertini and M. P. Guthrie, *Nuclear Physics A* **169,** 670 (1971).
2. R. M. Edelstein et al., *Nuclear Instruments & Methods in Physics Research* **100,** 355 (1972); M. W. McNaughton et al., ibid **161,** 439 (1979).
3. J. A. Edgington and B. Rose, *Nuclear Physics* **89,** 523 (1966).
4. F. P. Brady, J. C. Young, and C. Badrinathan, *Physical Review Letters* **20,** 750 (1968).
5. C. Cohen, B. J. Moyer, M. C. Shaw, and C. N. Waddell, *Physical Review* **130,** 1505 (1963).
6. J. D. Jackson, Classical Electrodynamics, Section 15-1, John Wiley and Sons, Inc., New York, 1962.
7. F. Partovi, *Ann. Phys.* **27,** 79 (1964).
8. M. N. Harakeh, P. Paul, and Ph. Gorodetzky, *Physical Review C* **11,** 1008 (1975).
9. R. M. Sternheimer and S. J. Lindenbaum, *Physical Review* **123,** 333 (1961).
10. J. F. Crawford, et al., *Physical Review C* **22,** 1184 (1980).
11. B. J. Moyer, "Evaluation of Shielding Required for the Improved Bevatron," Lawrence Radiation Laboratory Report UCRL-9769, June 1961.

    B. J. Moyer, "Method of Calculating the Shielding Enclosure of the Bevatron," in Premier Colloque International sur la Protection Aupres des Grands Accelerateurs (Presses Universitaires de France, Paris, 1962), p. 65.
12. J. Ranft, "Improved Monte-Carlo Calculation of the Nucleon-Meson Cascade in Shielding Material," *Nuclear Instruments and Methods* **48,** 133-140 (1967).

    Keran O'Brien, "Tables for the Determination of the Lateral Shielding Requirements of High Energy Accelerators," United States Atomic Energy Commission Report HASL-203, November, 1968.
13. S. D. Howe, Kansas State University Dissertation, 1975.
14. W. C. Haxton, *Neutrino Reactions on Oxygen and the Proposed LAMPF Measurement of the Weinberg Angle*, (1987).
15. T. W. Donnelly, *Physics Letters* **43B,** 93 (1973).
16. I. 3. Towner, *Annual Review of Nuclear and Particle Science* **36,** 115 (1986).
17. G. T. Garvey, " $O^+ \rightarrow O^-$ Transitions in A=16", in Nuclear Spectroscopy and Nuclear Interaction Proceedings of the International Symposium, Osaka, Japan (March, 1984) p. 193.
18. R. Mundis, HSE Division, Los Alamos, private communication; M. Barbier, Induced Radioactivity, North Holland Publishing Company, 1969.
19. T. W. Donnelly and R. D. Peccei, *Physics Letters* **65B,** 196 (1976).
20. T. W. Donnelly and R. D. Peccei, *Physics Reports* **50,** 1 (1979).

21. N. A. Dadayan, *Soviet Journal of Nuclear Physics* **24,** 216 (1976).

8 DETECTOR MONITORING

Descriptions are given of (1) monitor systems for photomultiplier-tube rates and high voltages; (2) the water purification system necessary to maintain a low attenuation length for Čerenkov light in the 2.5 million-gallon tank; and (3) the small effects anticipated from the decay of natural uranium present in the local water supply.

8.1 Detector Systems

Monitoring of the operational status of the photomultipliers and logging will be done at the crate level by local microprocessors. These microprocessors will have direct access to each PMT channel and, as such, will coordinate and log the measuring of singles rates. The microprocessors will report their values to the host computer, which will histogram the rates and generate the PMT activity maps. These will be stored in files available for use on-line to determine the health of the detector.

Photomultiplier tube high voltage will be distributed in a separate set of racks from the data acquisition electronics. This will allow greater channel density and the use of less expensive connectors for both high voltage and anode signals. The high voltage will be derived from simple fixed-voltage supplies. The individual PMT voltages will be set by inserting fixed dropping resistors into sockets on the high voltage distribution boards. To monitor the voltages an analog multiplexing switch and an ADC on each distribution card will report to the host computer the voltage on any channel. This is illustrated in Fig. 8.1.

8.2 Water

8.2.1 Water Purification

The LCD tank will hold approximately 2.5×10^6 gallons of water, and will present typically 8-10m path lengths for Čerenkov radiation. A convolution of the Čerenkov spectrum, the transmission characteristics of water, and the tube photocathode response, result in a detected photon spectrum that peaks at 400nm. In order to achieve a high photo-electron count, we require the water to have an attenuation length of about 40m. Water of this purity has been achieved in a number of large detectors, e.g., Kamioka and IMB.

A detailed discussion of a purification system that will produce water of 40m attenuation length is given elsewhere.[1] Briefly, several stages of treatment are required because no single process can remove all contaminants. The flow diagram

in Fig. 8.2 shows the main components of the system, which consists of the following: one series of units for processing the raw water during the initial fill at a flow rate of 25gpm; a slow recirculation loop at 50gpm; a fast recirculation loop at 200gpm.

The water is first passed through depth filters to remove particulate matter of size above 10μm. The second step is either softening or injection of anti-scaling chemicals. The water is then filtrated through granular carbon to remove organics and chlorine.

The reverse-osmosis system contains thin-film composite membranes. It is designed to produce 25gpm of permeate with a total dissolved-solids reduction of 95% or above. The overall product water recovery is 50%. The permeate water flows into a 3,000 gallon storage tank and is pumped to portable exchange deionizers. These anion and mixed-bed deionizers consist of two parallel banks to be used one as running and one as stand-by. The deionized water is filtered through a 3μm cartridge filter and passed through U.V. sterilizers for bacteria. A 0.2μm final filter removes remaining particles, as well as dead bacteria, left after the sterilization process.

The first part of the system from the depth filters to the reverse-osmosis unit is to be used only during the initial filling of the 2.5 million gallon detector tank at a flow rate of 25gpm. The filling time will be 70 days. The water is then to be recirculated through the 3,000 gallon storage tank, the deionizers and the U.V. sterilizers at a flow rate of 50gpm, which corresponds to one detector volume per 35 days. A fast recirculation system including a U.V. sterilizer and a cartridge filter is designed to prevent bacteria from growing in the tank. Working at a rate of 200gpm, it corresponds to one detector volume recirculated every nine days.

8.2.2 Effects of Natural Radioactivity in Water

Water drawn from the supply wells on the Los Alamos site had been examined for radiochemical quality in an extensive program of measurements[2] over the past several years. These results are available in numerous Laboratory documents. The wells are 1000 to 2000 feet deep, and analysis shows that the water is relatively old, 50 to 300 years, and thus free of man-made radioisotopes. The only measurable radioisotopes in the water are those of natural uranium and its daughters. The

concentration of uranium varies appreciably from one well field to another, with two of the available fields (Guaje Field and Pajarito Field) producing water relatively free of uranium. Typical values for total uranium are about 1 microgram per liter for water from these fields. At this level of activity, one should consider possible background events in a water-filled Čerenkov detector due to: energetic electrons from beta decay, energetic electrons produced by gamma rays from spontaneous fission or the uranium decay sequence, and possibly other background processes.

In the following discussion it is assumed that the uranium concentration in the two million gallons of water will be reduced by a factor of 1000 through use of a deionizer (see Section 8.2.1). Thus, an equilibrium uranium concentration of 1 nanogram per liter (8mg total) will be the basis for numerical estimates. In addition, it will be assumed that the uranium decay sequence is in secular equilibrium, although this may not be a completely sound assumption for the radioisotope content of the water drawn from these deep wells. The dominant secular rate (93 decays/sec.) is ^{238}U, so the ^{235}U decay sequence (4.3 decays/sec.) is not discussed here.

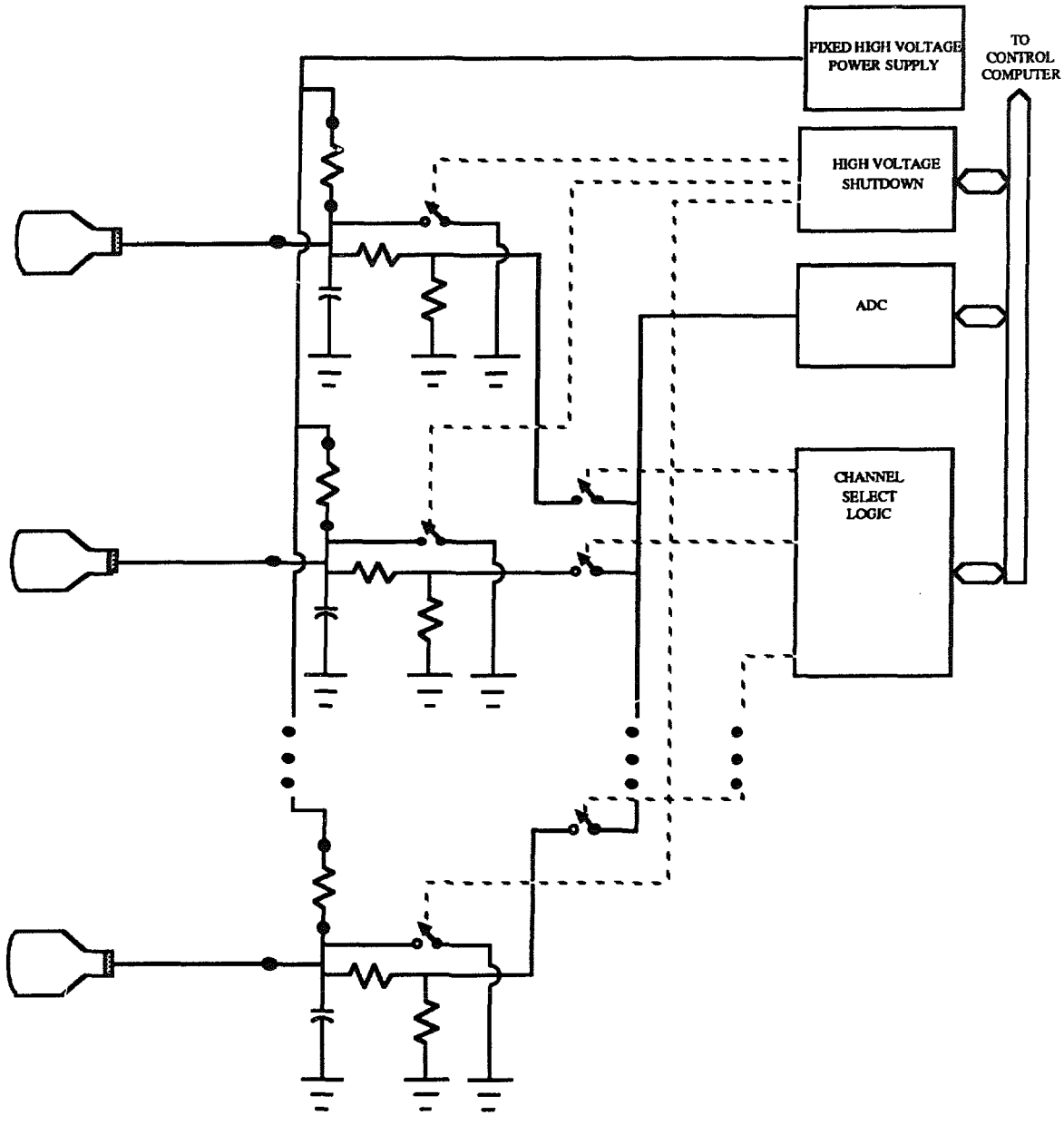

Fig. 8.1. Photomultiplier high voltage distribution and monitoring.

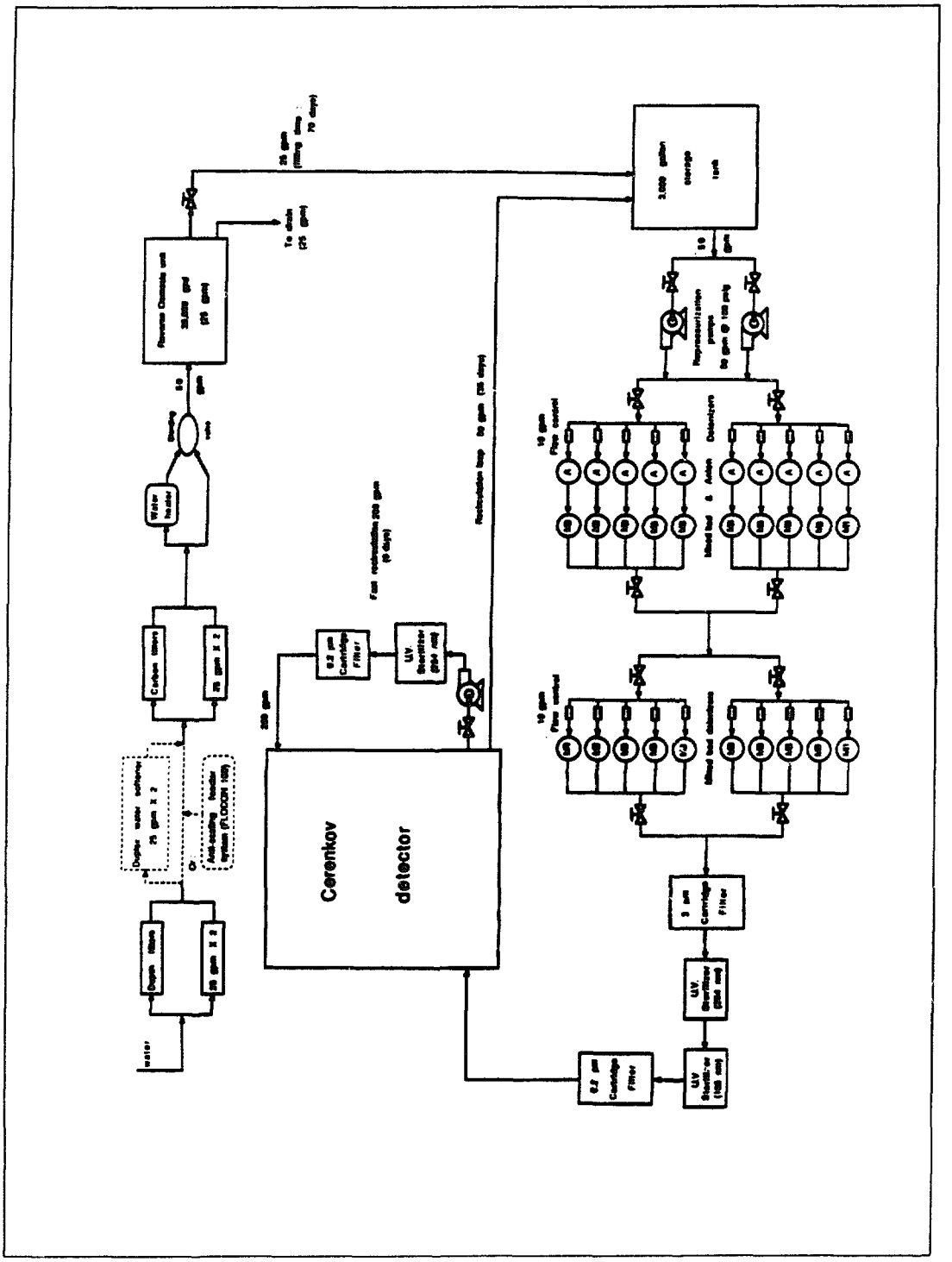

Fig. 8.2. Flow diagram of the main components of the water purification system.

Beta Decay Electrons

Alpha decay of ^{238}U ($t_{1/2} = 4.5\times 10^9$ years) initiates a chain (Fig. 8.3) of several alpha and beta decays; the decay of dominant interest is that of ^{214}Bi because of its near–100% branch and the 3.2-MeV beta endpoint for 19% of the beta decays, substantially higher in energy than that of any other beta decay in the sequence.

Under the assumptions stated above, there will be 1.5×10^6 of these 3.2-MeV ^{214}Bi decays per day in 2 million gallons of purified water. The number will be reduced by several factors, including: a detector duty factor of 3.2×10^{-6} for ν_μ or 6×10^{-5} for ν_e plus $\bar{\nu}_\mu$, and 0.12 from a forward-angle requirement. These two factors reduce the potential event rate to 0.5 per day for ν_μ and 11 per day for ν_e plus $\bar{\nu}_\mu$. The typical number of photoelectrons from a 3-MeV electron is 8.1. Application of Poisson statistics gives a probability of $< 10^{-5}$ that a 3-MeV electron will exceed the 27 photoelectron threshold. Most beta-decay electrons from the uranium sequence will have an energy of 2 MeV or less, and hence a much smaller probability of triggering the detector. The number of triggers generated by uranium sequence beta-decay electrons appears to be completely negligible. The background from ^{232}Th is comparable to ^{238}U. The average energy from ^{232}Th is slightly higher than from ^{238}U; however, the ^{232}Th decay rate is a third of the ^{238}U rate.

Gamma Rays in the Uranium Decay Sequence

The most energetic gamma rays in the decay of natural uranium all follow the beta decay of ^{214}Bi. The most abundant of the higher-energy gamma rays and their overall branching ratio (% of ^{214}Bi decays) are listed below.[3,4]

E(MeV)	BR
2.448	1.5%
2.204	5.0%
2.119	1.2%
1.765	15.8%
1.729	3.0%

These are all obviously much less important than the beta-decay electrons from the highest-energy group, having a 3.2-MeV endpoint, which were shown above to be negligible.

Spontaneous Fission

Spontaneous fission of uranium and decay of the resulting fission fragments produce both γ-rays and β-decay electrons with energy spectra extending up to

about 8 MeV (Fig. 8.4). The spontaneous fission halflives of ^{238}U and ^{235}U are 8×10^{15} years and 3.6×10^{17} years, respectively. Thus, there will be about 4.5 spontaneous fissions per day from 8mg of normal uranium. It is estimated that these beta and gamma decays will result in about 10 electrons per fission with energies in the MeV region. Including a livetime factor of 6×10^{-5} and a forward angle factor of 0.1, the event rate from spontaneous fission is estimated to be 3×10^{-4} per day, with most events being small compared to the 10-MeV threshold. Thus, it is most probable that no spontaneous fission events will exceed threshold during the experiment.

Noise Hits on A Real Event

In addition to masquerading as a real event, the possibility exists that a uranium sequence decay event may coincide in time with a real (or background) event and confuse the event fitting process. An upper *limit* to the probability of this will be estimated as follows. There are 97 uranium decays per second in the detector. There are six β-decays in the ^{238}U sequence and four in the ^{235}U sequence. Each β-decay has a total energy of 3.2 MeV or less, which may be divided in a variety of ways among the electron, the neutrino, and possibly one or more gamma rays. As the energy is divided among more entities, it becomes less harmful, hence the noise-hit probability will be calculated assuming that no γ-rays are emitted. A 20ns time window is used to test for trigger conditions, although 2ns time resolution is expected for the final fitting of events. (The 20ns is an off-line time window; the on-line time window is approximately 100ns.) The estimate is:

$$\text{Noise hit probability} \approx 20 \text{ ns} \times 6 \times 97 \text{ s}^{-1} = 1.2 \times 10^{-5}.$$

It is concluded that noise hit distortion of true events by uranium radioactivity in the water is not significant.

Infusion of Ambient Radon

Infusion of ambient radon could create an additional background event rate associated with ^{214}Bi decay. We see no way to calculate this contribution, but it must be noted that LCD in normal operation will be sealed and radon penetration is expected to be small.

Summary

Signal-to-background ratios for the various background processes due to radiochemical content of the water are:

	ν_μ	$\nu_e + \bar{\nu}_\mu$
Beta Decay Electrons	$> 1.5\times10^6$	$> 7\times10^5$
Gamma Rays	$> 1.5\times10^6$	$> 7\times10^5$
Spontaneous Fission	$> 8\times10^6$	$> 4\times10^6$
Ambient Radon	?	?

It should also be noted that these contributions will be evaluated during the course of the experiment to a high degree of precision because they will be observed outside of the duty-factor time, thereby giving relatively good statistical determination of their magnitude. Therefore, this background can be removed along with the cosmic ray background.

References

1. P. Bystricky, "The Water Purification System," Los Alamos Scientific Laboratory, unpublished data, 1987.
2. W. D. Purtymun, N. M. Becker, and M. Maes, "Water Supply at Los Alamos During 1982," Los Alamos National Laboratory report LA-9896-PR(1982).
3. R. L. Heath, Gamma-Ray Spectrum Catalog, Third Edition (1974), Aerojet Nuclear Company, see the Gamma-Ray Spectrum of Natural Uranium.
4. Tables of the Isotopes, Seventh Edition, Edited by C. M. Lederer and V. S. Shirley (1978) John Wiley & Sons, see the Decay Scheme of ^{214}Bi, p. 1367-1369.

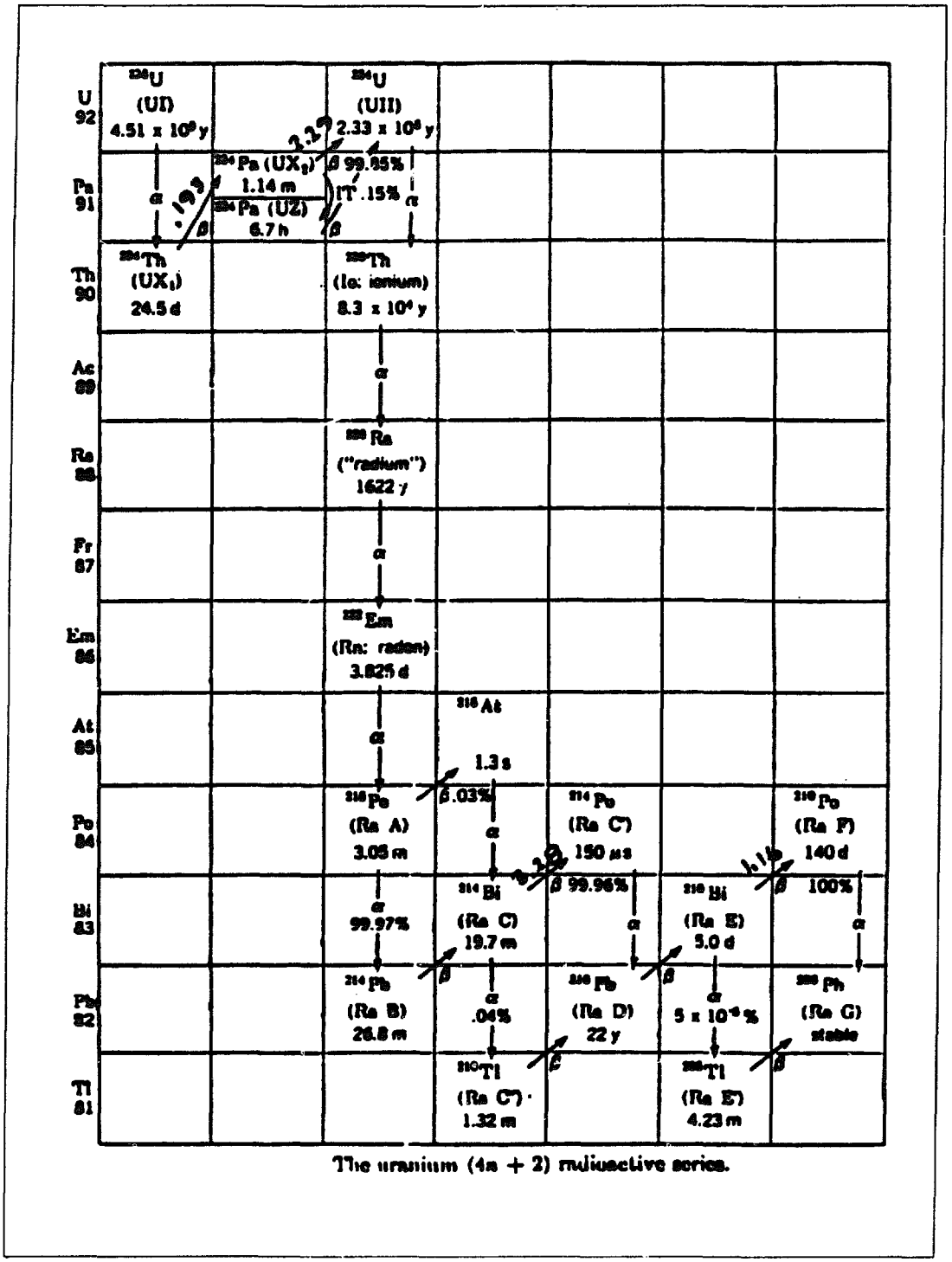

The uranium (4n + 2) radioactive series.

Fig. 8.3. The uranium radioactive decay series (from: R.B. Leighton, Principles of Modern Physics, McGraw Hill, 1959).

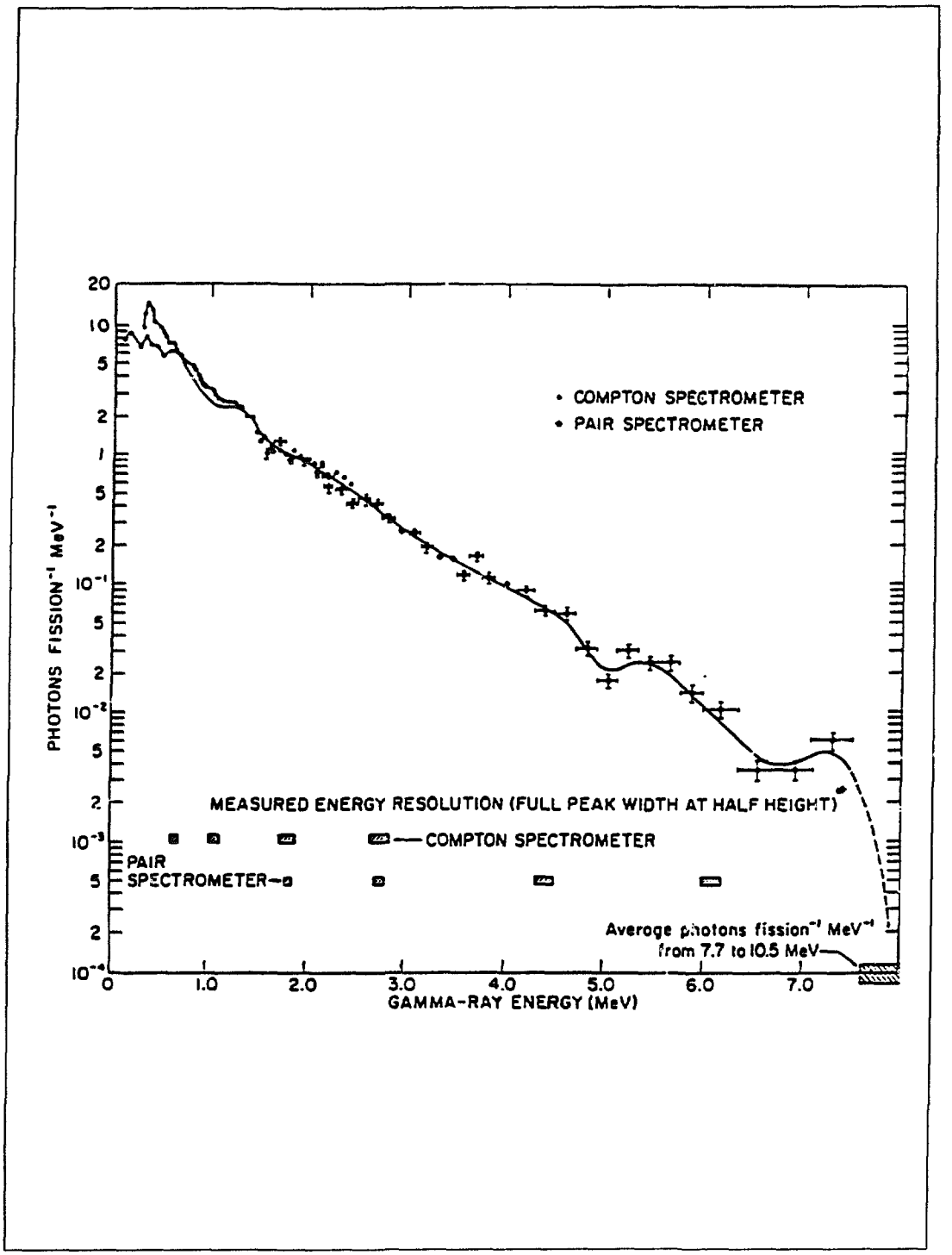

Fig. 8.4. The energy spectrum of prompt γ rays from thermal-neutron fission of ^{235}U (from: R. Vandenbosch and J.R. Huizenga, Nuclear Fission, Academic Press, 1973).

9 COSMIC-RAY-INDUCED BACKGROUND

A discussion of the several backgrounds arising from the cosmic-ray flux in the LCD detector. Expected cosmic rates are calculated by Monte Carlo and compared to measurements at LAMPF. The rates and energy depositions are given for through muons and for muon-produced decay electrons, spallation products, pions, and neutrons. The resultant cosmic-ray background rate is about one per day within a 5μsec gate.

Cosmic radiation at the Earth's surface consists of a hard component of muons and a soft component (N and E) of hadrons, leptons, and gammas that accounts for about 1/4 of the intensity. The muon flux underground falls exponentially with an attenuation length of $\lambda = 1400\text{g-cm}^{-2}$ until a depth of about 2000g-cm^{-2}, below which the curve flattens and λ becomes 4000g-cm^{-2}. Figure 9.1 shows this gradual attenuation below the break in the slope. The neutrino detector (LCD) will be situated beneath an effective depth of 2300g-cm^{-2} below sea level (2500g-cm^{-2} below the surface at Los Alamos), where the average muon energy is about 10 GeV. The angular distribution of these muons varies as $\cos^2\theta$ down to 10^5g-cm^{-2} and this gives 38/sec through a sphere of 1m^2 projected area. The effective projected area of LCD is 400m^2 giving a muon counting rate of about 15kHz in the fiducial volume and about twice that rate in the full volume, including the veto. Of these muons, about 55% are positive and 41% stop and decay into electrons or positrons. This muon activity dominates all others and affects the experiment by creating background electrons and deadtime in the system.

The N-component has two parts, the part created by primary cosmic rays and the part created by muon-nucleus interactions. The former is still present at sea level but is almost completely attenuated in the first 1000g-cm^{-2} of overburden as shown in Fig. 9.1. The latter is regenerated continuously by muons and is present in the flux at a level of about 1%. The muoproduction cross section rises slowly with energy so that this fractional component increases with depth. In Fig. 9.2. is shown a calculation, interpolating actual data, of neutron production as a function of depth, which we expect to primarily reflect inelastic muon-induced hadron processes. It can be concluded that at the depth of LCD, hadrons arise primarily from muoproduction processes both from real and virtual photons.

The electromagnetic (e,γ) component is also created in two parts; the part created in the atmosphere, π^0 decay, μ decay, bremsstrahlung, and the part due to direct muon processes (mu-e elastic, direct pair production, and bremsstrahlung). The former are attenuated with $\lambda = 50\text{g-cm}^{-2}$ and do not penetrate, the latter are carried with muons. In Fig. 9.2 the sum of the electromagnetic processes (with

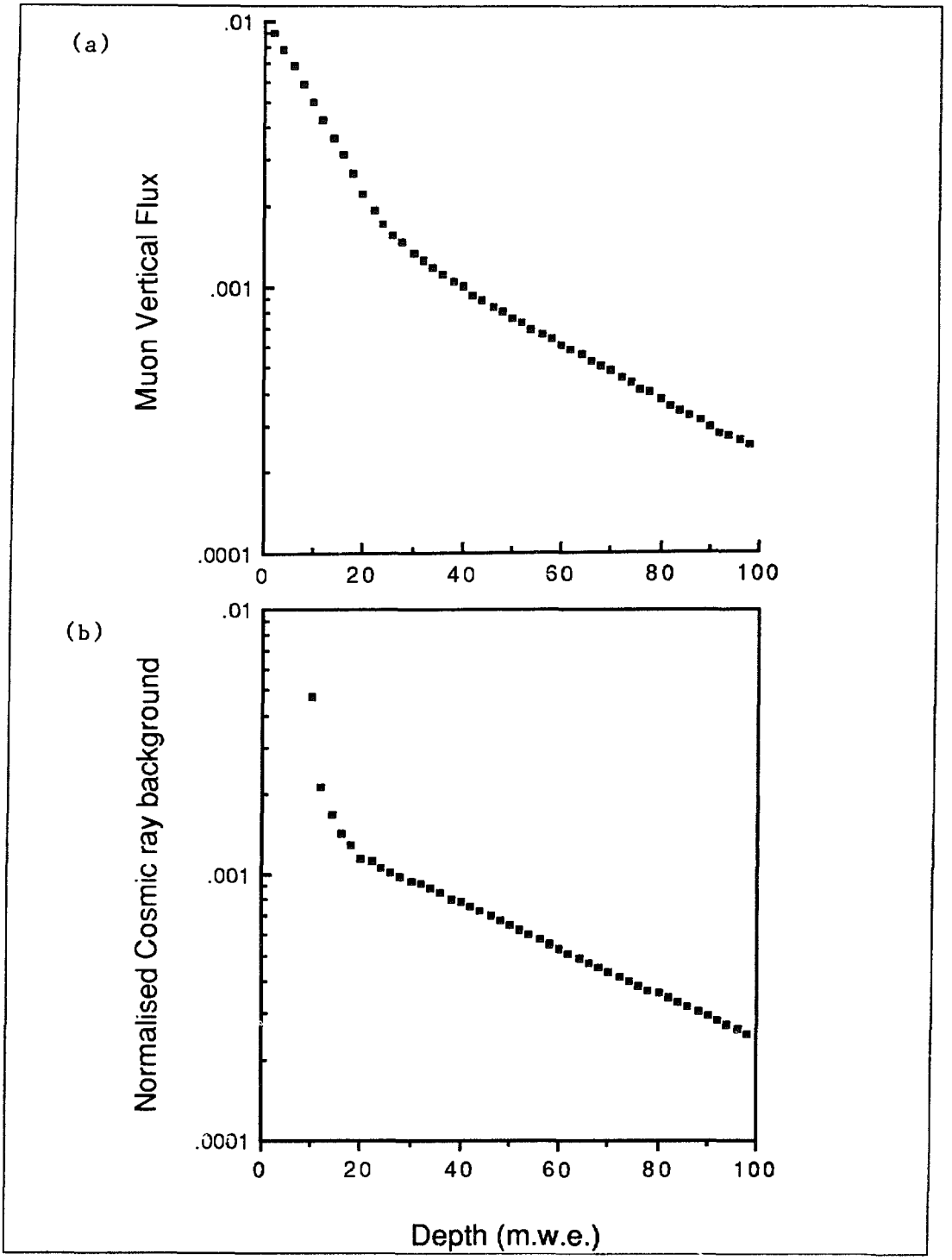

Fig. 9.1. (a) Muon flux as a function of the depth below sea level in hg/cm^2. (b) Cosmic-ray background as a function of depth below sea level in m.w.e.

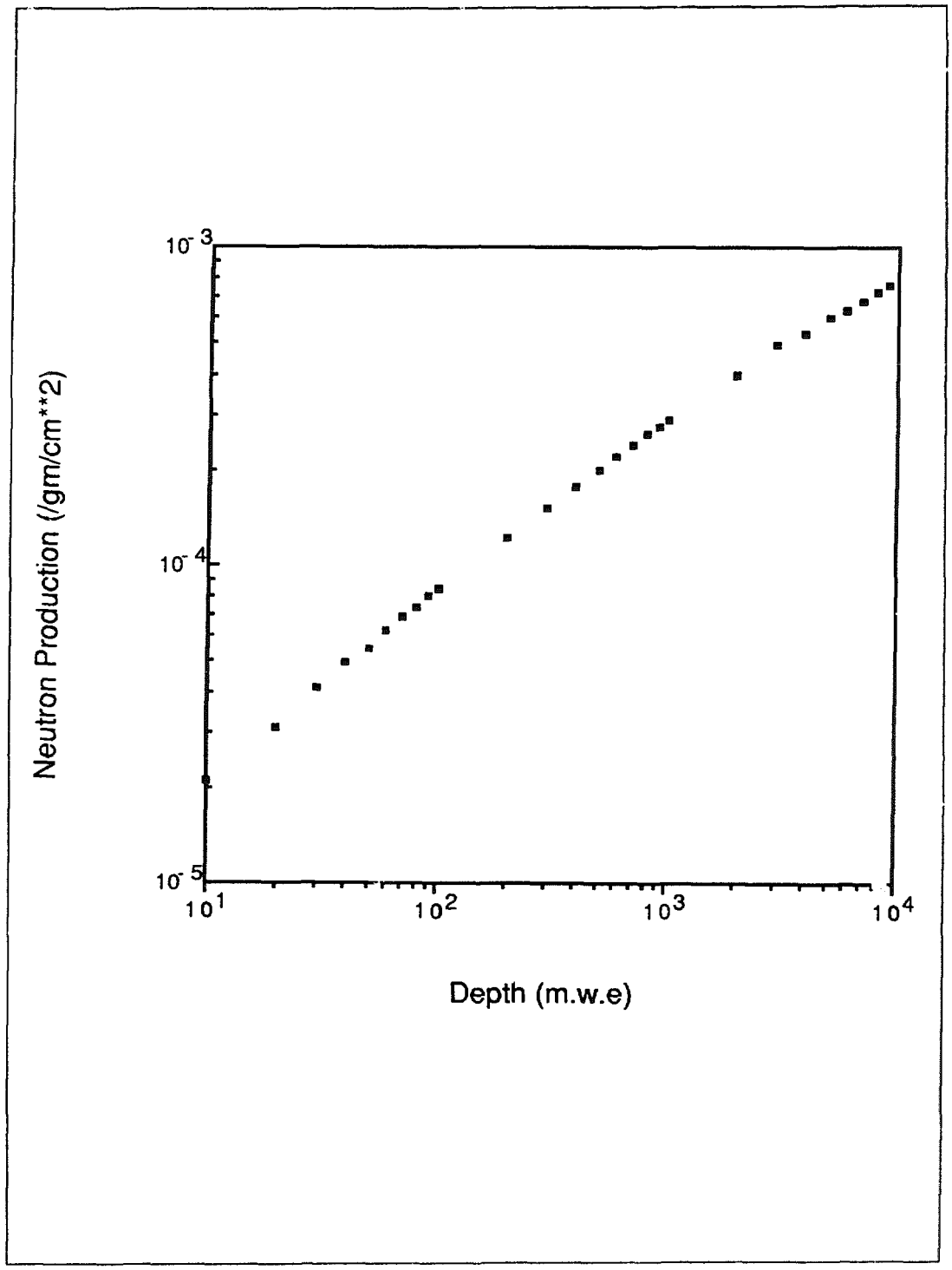

Fig. 9.2. Dependence of neutron production from cosmic rays as a function of depth in meters of water equivalent.

subsequent showers and interactions folded in) creates 1/3 as many neutrons as direct muoproduction, and the energy dependences track fairly well.

As a result of our understanding of these processes we are able to identify the main sources of backgrounds in LCD from cosmic-ray sources. If these can be kept below about 1 count per day there will be little effect on the accuracy of $\sin^2\theta_W$.

a) Muons stop in the fiducial volume of the detector and decay, giving an electron of energy determined by the Michel spectrum.
b) Muons interact inelastically in the water leaving spallation products that subsequently beta decay giving electrons above the threshold of the experiment.
c) Muons interact outside the veto in the ground, producing prompt neutrons or gamma rays that penetrate the veto and create electrons in the detector that are not separable from signal electrons.
d) Muons enter undetected due to incomplete veto coverage. This source differs from the type a) events because the parent muon is not observed.

Muons passing through the detector produce an effective dead time. Afterpulsing following a large pulse in a phototube from muons traversing the detector produces a dead time in that particular channel. Tests have been conducted on the transient response of the phototubes, and are discussed in chapter 13. However, for the present discussion it is sufficient to observe that a dead time of 500ns is sufficient for phototube recovery from the larger pulses that are likely to be seen in this detector.

In order to estimate the potential background from cosmic-ray muons, the expected data-taking mode is now described. Beam from the PSR is delivered at a rate of 12Hz or a multiple of this rate (x2). Useful signal will occur in LCD for about 5μs after the start of the beam spill of 270ns. It is prudent to take data for an additional 5μs after the beam gate. In order that an incoming muon will register in the detector and be identified as the source of an electron, it is planned that data be taken for about 30μs before the beam gate start. As is noted above, 1.3×10^9 muons traverse the fiducial volume of LCD each day. Of these,

$$1.3\ 10^9\ \text{x}\ 12\ \text{x}\ 5\ 10^{-6}\ \text{x}\ 0.41\ \text{x}\ 0.9\ (10\%\ \text{capture}) = 2.9 \times 10^4$$

produce decay electrons in the detector uniformly in the gate width in which neutrino-electron scattering events may occur. We now discuss in detail our calculations of the muon flux and associated backgrounds.

9.1 Muon Flux in LCD

The primary source of information on the cosmic-ray muon flux is Allkofer's compilation.[1] This compilation includes four distinct experiments that are sub-

stantially in agreement. Figure 9.1 shows the muon vertical flux as a function of depth. On this plot there is a 'break' at 2500g cm^{-2}, which is a reflection of the muon energy spectrum shape. An estimate of the hadron contribution to cosmic-ray background from Davis[2] is also shown in Fig. 9.1b, which is in agreement with a similar feature identified by Cocconi[3] as the N component. For depths greater than 2000g-cm^{-2}, the slope of the muon curve is close to λ = 4000g-cm^{-2}, mostly indicative of the energy spectrum of the muons rather than absorption length. We assume that the depth of LCD below the surface is 2500g-cm^{-2}, or about 3300g-cm^{-2} below the top of the atmosphere. At this depth the cosmic muon vertical intensity is 1.8×10^{-3} $cm^{-2}s^{-1}$ str^{-1}. The angular distribution varies as $\cos^2\theta$, until depths well below 3300g-cm^{-2} are reached, so that the flux of muons crossing a sphere of unit cross sectional area is 38m^{-2} s^{-1}.

9.1.1 Measurements of Muon Flux

This flux has been verified in other experiments at LAMPF, notably E225, the $\nu_e e$ scattering experiment, E764 the decay in flight neutrino experiment, and in E645 that is presently on line searching for neutrino oscillations. The relevant rates are shown below in Table 9.1:

Table 9.1 Measurements of cosmic-ray muon flux.

Source	*Vertical Flux*	*Depth*	*Rate in Sphere*
	m^{-2} $s^{-1}str^{-1}$	g-cm^{-2}	$m^{-2}s^{-1}$@ 2500 g
E225	62	1400	43
E764	199	850	24
E645	79	2440	78
C R Tables			38

The rates in the last column are directly comparable; the spread probably reflects the uncertainty in establishing the depth parameter and, to a lesser extent, the purity of the muon sample. For estimations, the number from the cosmic-ray tables are used, but the spread of a factor of two in the local experiments should be borne in mind.

9.1.2 Monte Carlo Program for Muons

The cosmic-ray flux penetrating the overburden and traversing the sensitive volume of the detector has been calculated with a Monte Carlo program. Cosmic rays are generated over an area of about 70m × 70m at the surface. A volume including the detector and neighborhood is divided into a cubical array with a cell size of 0.5m typically. The content of the array element is the density of the material in the cell. A second array is used to identify the box as part of the sensitive region, part of the veto region, or part of the central pillar.

The momentum of individual cosmic-ray muons is chosen according to a spectrum shown in Fig. 9.3 The angular distribution is weighted as $\cos^2\theta$, appropriate for muons penetrating to the level of the detector. Rays are tracked linearly through the volume, stepping through each appropriate box in the geometry including energy loss for each type of material. The prescription for energy loss is taken from Ref. 4. Particles are identified if they pass through the sensitive volume, the veto region, or the central pillar.

Output from the program consists of the number of rays that entered the sensitive region, the number of rays that entered the water (including the veto region), the number of muons that stopped in the water, the number of rays passing through the pillar and entering the water, and the average path length of a ray in the sensitive region.

The calculations have also been extended to estimate the neutral background from muon interactions outside the active detector volume. There are some preliminary results on the contribution of muon bremsstrahlung to the background. The requirement that there be no count in the veto region and the sensitive region have an energy deposit similar to that of a signal electron (from 10 to 60 MeV) reduces the bremsstrahlung contribution by a factor of 0.4×10^{-3}. This results in negligible background. It is expected that the dominant neutral cosmic-ray related rates are from neutrons. In section 9.5 this point is discussed further.

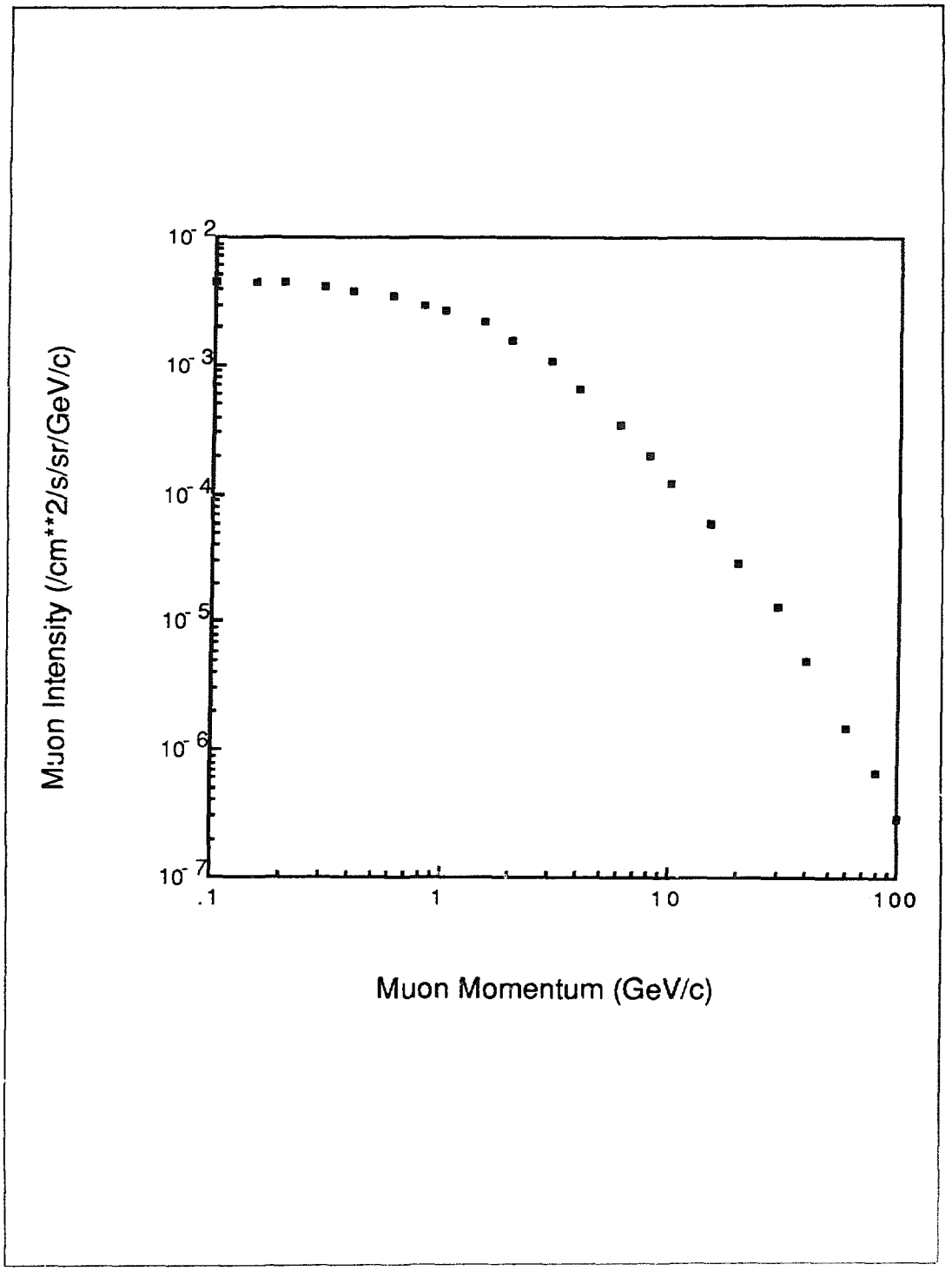

Fig. 9.5. Momentum spectra of individual cosmic-ray muons.

9.1.3 Results

The current values of the program results and other useful quantities are listed below:

$402m^2$	fiducial area
$492m^2$	sensitive area
$609m^2$	veto area
$4672m^3$	fiducial volume
7363	sensitive volume
10560	total volume sensitive and veto region
11.2m	mean path length in fiducial region
15.0	mean path length in sensitive region
15.3kHz	counting rate, fiducial region
18.7kHz	counting rate, sensitive region
41%	fraction of stopping muons in fiducial region
45/55	ratio of μ^-/μ^+
$30s^{-1}$	muons down pillar entering water with < 200 MeV
12 GeV	mean energy of muons entering the water
5s per day	LCD live time for the long spill.

9.2 Afterpulsing in Photomultipliers

The discussion is limited first to muons that actually traverse the sensitive volume of LCD. These muons copiously produce light that is collected by the same PMT's that observe electrons at much lower light level in a single channel. The frequency of these cosmic rays is about 19kHz, so that the accidental probability of observing a cosmic-ray muon less than $0.5\mu s$ before an electron is 1%. We expect to eliminate from consideration any electron events with a muon up to $0.5\mu s$ ahead in time, giving a dead time of 1% from this source. From PMT pulsing tests described in chapter 13, it appears that this delay is enough to efficiently recognize electrons after a large light deposition characteristic of relativistic muons. We also draw on experience in Kamiokande II (KII) in considering this question. In KII there are approximately 3×10^4 muons per day traversing the detector, of which 1% stop, and 3/4 of the decays are detected. The observed momentum spectrum from this muon flux is given in Fig 9.3. The energy spectrum peaks at about 14×10^3 pe (there are about 4 pe per MeV) and then falls to a low at 40×10^3 pe. Nevertheless, there exist muon events with energy deposition extending beyond 100×10^3 pe. A small fraction ($\sim 1\%$) of all through-going muons interact inelastically

in the water, giving rise to π^+, among other products. Most, in turn, initiate the decay chain $\pi^+ \rightarrow \mu^+ \rightarrow e^+$, and e^+ are observed in KII as prompt (i.e., within 30μs) followers of through-going muons. We show in Table 9.2 the ratio of the number of through-going muons with ≥ 1 prompt followers to the number of through-going muons with zero prompt followers, as a function of the energy (Q_μ in pe) of the muon event. Note that π^- and π^0 are produced in roughly equal numbers as π^+, so that the total energy of very energetic muon events receives appreciable contributions beyond the ionization deposited by the muon.

Table 9.2. Ratio R_t of the number of through-going muons with ≥ 1 prompt followers to the number of through-going muons with zero prompt followers as a function of Q_μ (in pe).

Q_μ (x 10^3)	0 - 20	20 - 40	40 - 60	60 - 80	80 - 100	>100
Total Muons (x 10^3)	4	664	71	12	4	2
R_t%	0.6	2.0	5.5	9.5	13	17

One sees from the first two columns in Table 9.2 that 88% of all muons in the sample considered have $Q_\mu \leq 40 \times 10^3$ pe, and that 2% of these have ≥ 1 prompt followers. Furthermore, a plot of the time interval between the through-going muons and those prompt followers is shown in Fig. 9.4, which yields a half life of 2.2μs consistent with the known μ^+ lifetime. A prompt follower from KII with $\Delta t = 2.3\mu s$ of a through-going muon with $Q_\mu \leq 103 \times 10^3$ pe is shown in Fig. 9.5. The decay-electron signal is clear, with the number of hit PMT away from the electron ring consistent with the Rayleigh scattering of Čerenkov light. We conclude from Fig. 9.5 that afterpulsing of the tubes used in KII does not appreciably distort the electron signal 2.3μs after the passage of the muon, and that a 0.5-μs deadtime (an analysis cut used to exclude after pulses, not a hardware deadtime) is probably sufficient to maintain detection efficiency. The 8" tubes that are proposed for LCD are likely to be fully efficient after 0.5μs, given the tests reported in chapter 13.

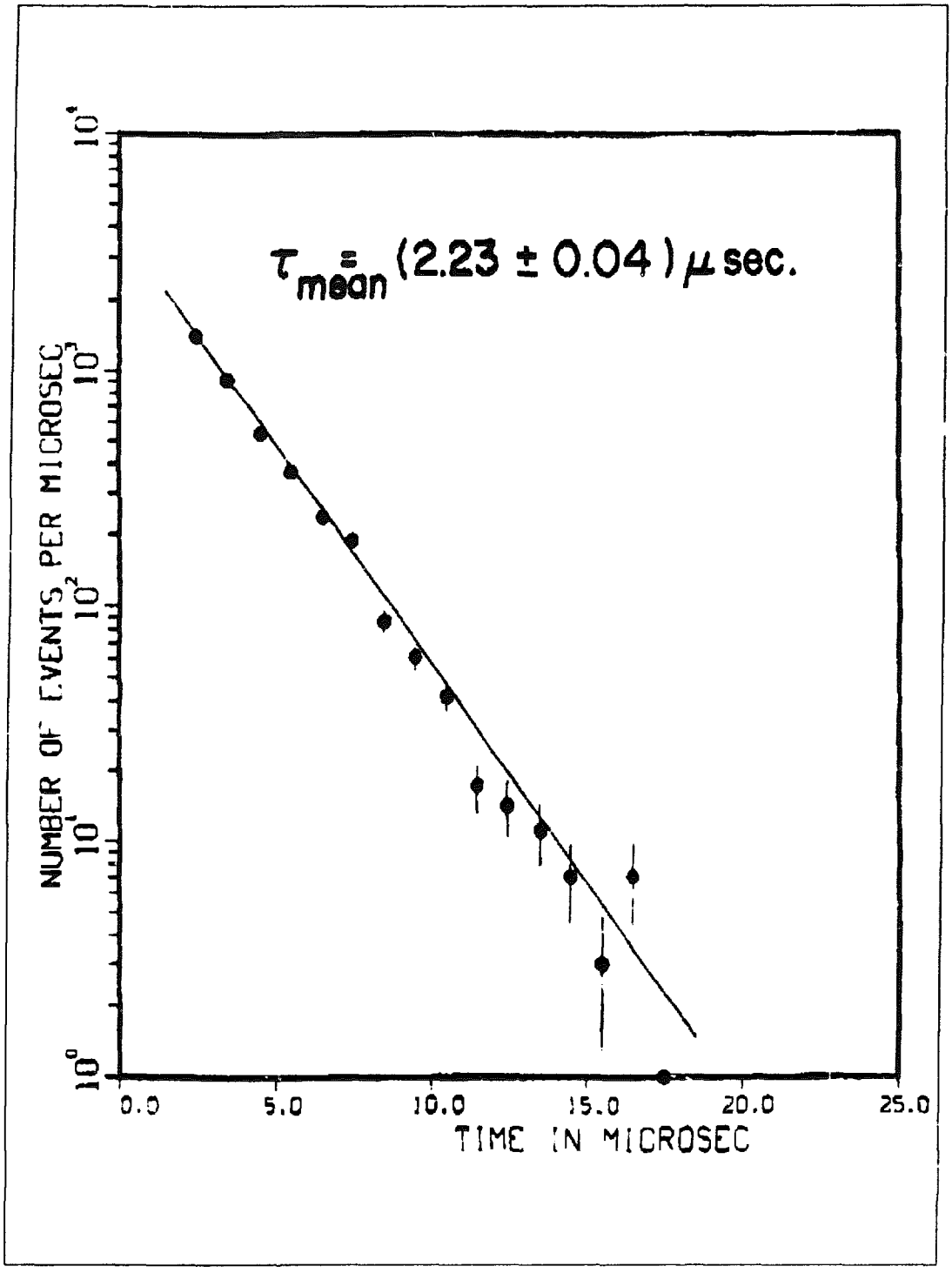

Fig. 9.4. Time interval between through-going muons and the prompt followers

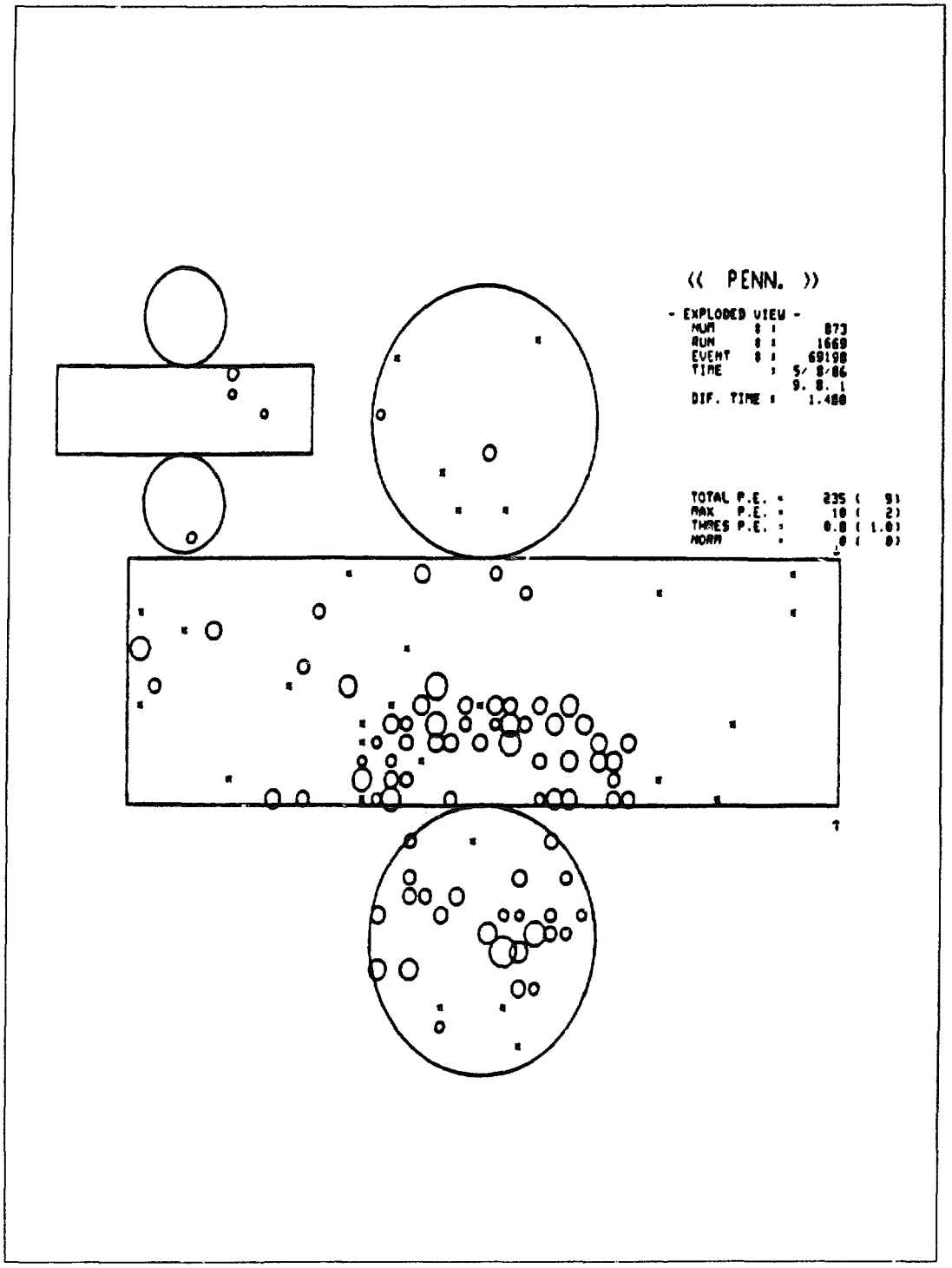

Fig. 9.5. A prompt follower from KII with $\Delta t = 2.3\mu s$ of a through-going muon with $Q_\mu \leq 103 \times 10^3$ pe.

9.3 Electrons from Muon Decay

Approximately 4.9×10^8 muons will stop and decay in the fiducial volume of LCD per day, and it will be necessary to remove the electrons from these decays from the event sample. A large factor is gained from the live time of the experiment. For example, the decay electron rate in the signal gate of $5\mu s$ at 12Hz is 2.9×10^4 per day; a further cut restricting the electron angle to the forward direction gives 2.9×10^3 per day. After reconstruction, the muon stopping point will be known to about 1/2 m, (see chapter 12). If we take this to be the rms radius of a statistical distribution, and reject all muons stopping within the 5σ radius of 2.5m, then the rejection inefficiency of this background will be 6×10^{-7}. After this cut there remain $2.9 \times 10^3 \times 6 \times 10^{-7} = 0.002$ events per day that remain as background to be subtracted. It is important to note that 35% of the electrons from νe interactions have no cosmic muons in the total 40-μs time interval, and 90% have no muons in the same octant. Therefore, almost all of the cosmic-muon background can be eliminated by simple cuts.

A cut radius of 2.5m includes a volume of $65m^3$, or about 0.014 of the total detector volume. The probability of an unrelated mu decay in this region in each 30-μs gate is $15300 \times 0.41 \times 30 \times 10^{-6} \times 0.014 = 0.003$ (0.3%). Thus, the reduced volume lowers the deadtime from stopping muons to an acceptable level. There is another source of deadtime that is caused by the 0.5-μs recovery period for the PM tubes, which was mentioned above to be 1%. The sum of dead times is then 1.3%, which we consider acceptable.

The final background from muon decay results from muons that live longer than $30\mu s$, thereby escaping the veto. This rate is:

$$15300 \times 0.41 \times e^{-30/2.2} \times 5s \text{ x } 0.1 \text{ (for angle cut)} = 0.004 \text{ per day.}$$

We conclude that the background can be reduced to 0.01 per day by simple rejection criteria, and these cause an additional deadtime of only 0.3%.

9.4 Electrons from Nuclear Beta Decay

A separate problem from directly decaying muons is posed by radioactive products from muon interactions. This problem is different in principle from stopped muons because it is difficult to correlate the electron candidate with the parent muon. This difficulty stems from the fact that the cosmic-ray rate in the detector is greater that the beta-decay lifetimes of interest. In KII a correlation was possible because the cosmic-ray single muon rate was low enough. To identify spallation events it may be possible to make a correlation with relatively infrequent

hadronic muoproduction events depositing large amounts of energy in the detector (e.g. $Q_\mu > 40,000$ p.e. in Table 9.2). In Fig. 9.6 we plot electron like events that fall in the time interval 0.1ms to 50ms. A clear signal with $\tau_{1/2} = (16 \pm 1)$ ms is seen, which can be attributed to the beta decays of ^{12}B (25%) and ^{12}N (75%), with half lives of 20.3ms and 11.0ms, respectively. The energy spectrum of the events in Fig. 9.6 is shown in Fig. 9.7, consistent with an allowed beta spectrum with end point energy about 16 MeV, as from ^{12}N. A further search out to 10s shows evidence of decay from ^{8}B, for example, with $\tau_{1/2} = 1.0$s and an end point of 13.7 MeV, as in Fig. 9.8. The rate for this reaction is 1/2 the rate for the 16-ms component. The component with a decay time of 16ms occurs once for each 2000 muons. The energy dependence of muoproduction and the relative thickness of KII and LCD allow a direct conversion into LCD background (see section 9.4.1).

In addition, there is another process that produces long-lived beta-decay nuclei of the same type. μ^- capture is a common process in LCD, and it has channels available to ^{16}N (7s, 10 MeV) and ^{12}B. The neutrino takes away most of the energy, and major disruptions of the nucleus are uncommon. Branching ratios for these reactions were determined from existing capture experiments and, to a lesser extent, from KII which has a very small fraction of stopping muons (1%). Background calculations from these sources are made in section 9.4.2.

9.4.1 Interactions of Through-Going Muons

The overall inelastic muon rate observed in KII is approximately 1% of the single through-going muon rate, as noted above. Almost all of that rate (95%) is manifested in energy deposits within a few microseconds of the primary event and are referred to as prompt followers in KII. These are presumably $\pi - \mu - e$ decays and can be directly eliminated, as with decays of stopping muons. Inelastic scattering on O yields the radioisotopes shown in Fig. 9.6 and 9.7, with a factor of 1 beta per 2000 muons. The mean energy of muons[5] at the depth of KII is 100 - 300 GeV, and 10 - 15 GeV at LCD. The energy dependence of the muoproduction cross section results in a smaller relative production of β-decay nuclei in LCD. Kalchukov et al.[6] have published a calculation of neutron production per muon vs depth that has been verified at a depth of 550mwe and is shown in Fig. 9.2. From this we expect a relative factor of ten reduction of β unstable isotopes over KII.

A possible concern in the estimation of these general trends comes from the nature of the Weiszaker-Williams approach used in Ref. 6,7. We have repeated the calculation using specific inelastic form factors for the nucleon. There are several relevant considerations in such a calculation:

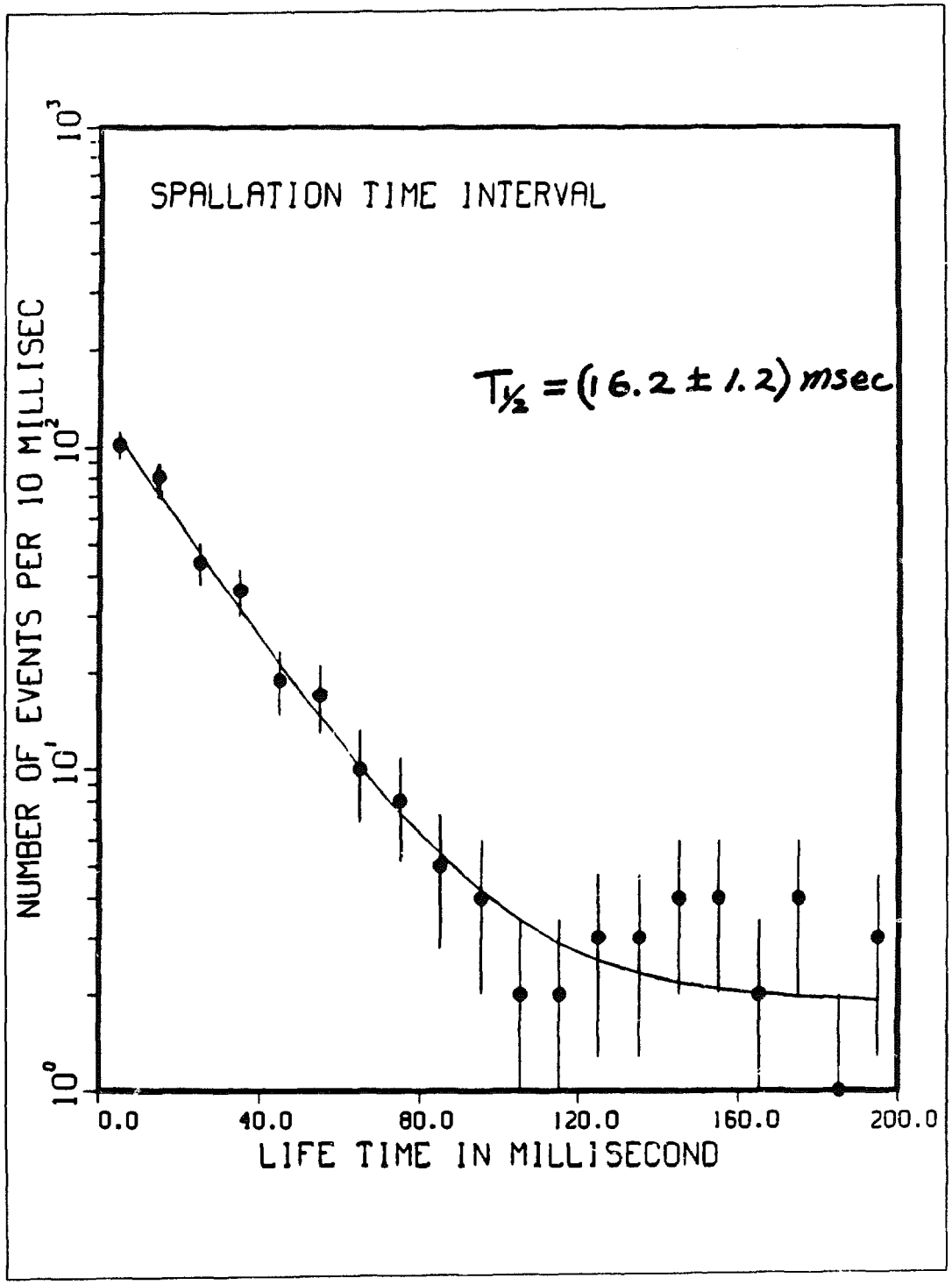

Fig. 9.6. Electron-like events that fall in the time interval 0.1ms to 50ms.

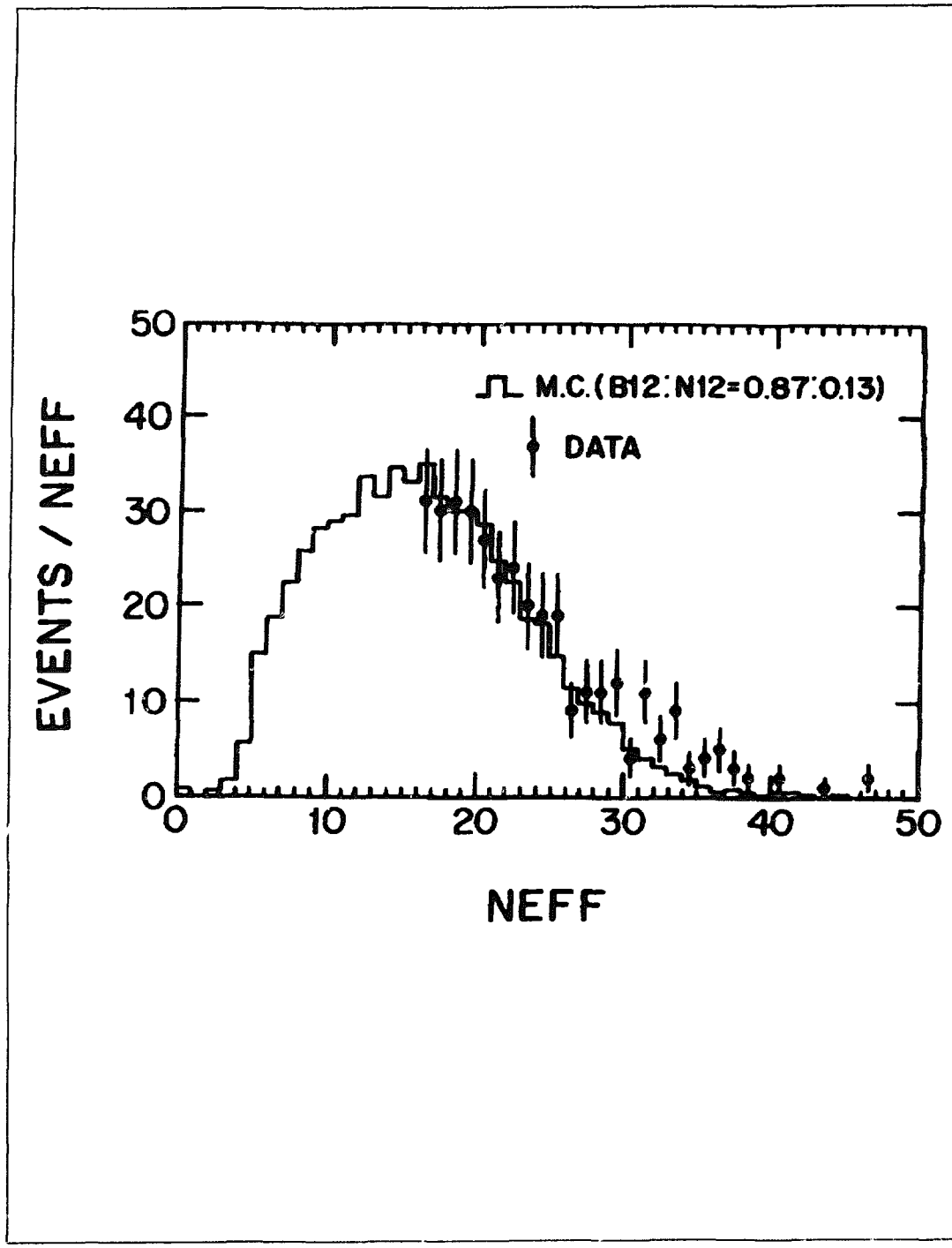

Fig. 9.7. Energy spectrum of the events from Fig. 9.6. N_{eff} is the corrected number of photoelectrons detected.

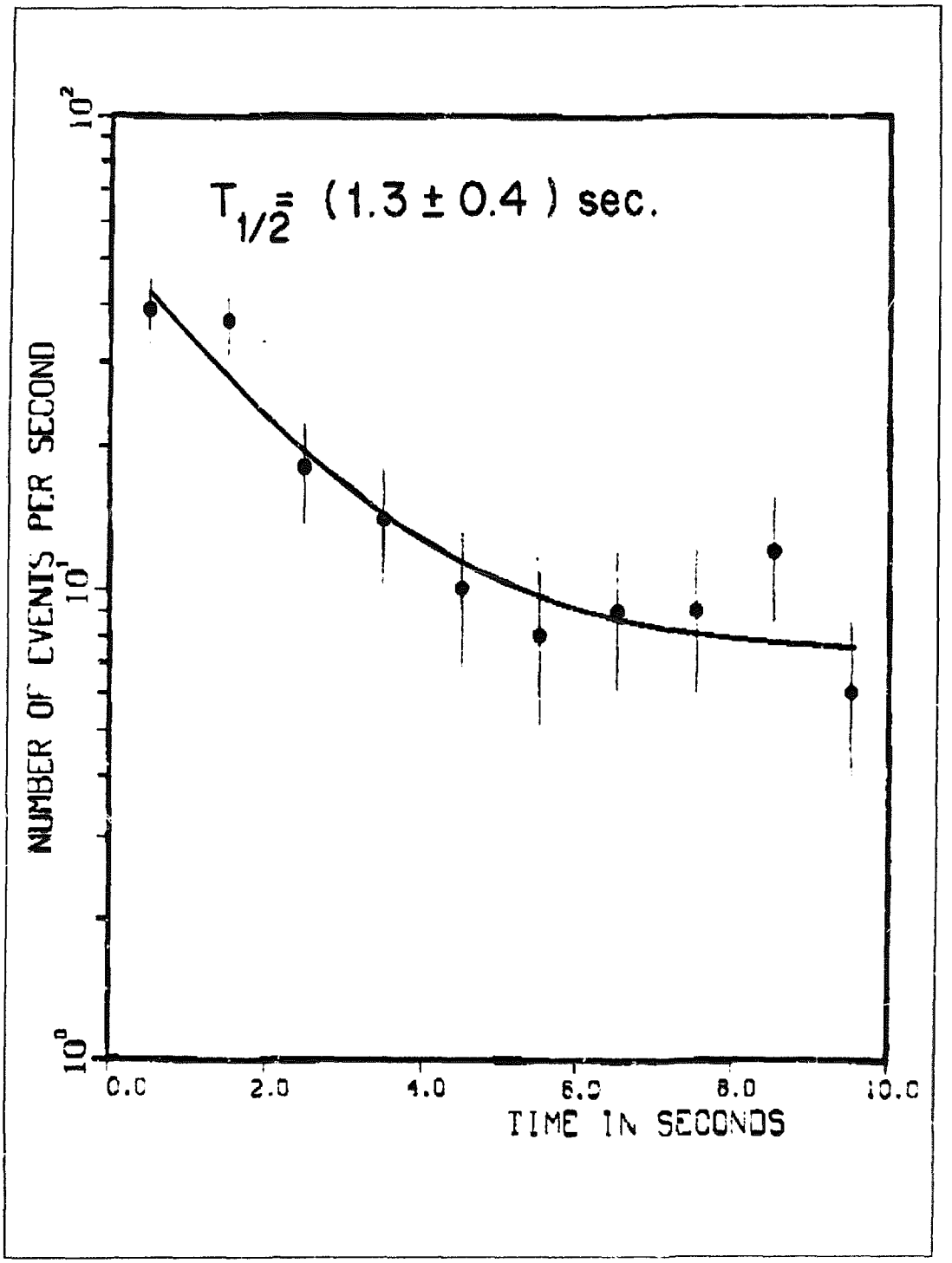

Fig. 9.8. Evidence of beta decay from ^{8}B with $\tau_{1/2} = 1.0$s.

1. The energy dependence of inelastic muoproduction $\sim (ln[E])^n$, n = 1 to 2.
2. Multiplicity of hadrons in muoproduction goes like ln E or $E^{0.25}$.
3. The average energy of the hadrons (should be proportional to the hadron track length).

The product of 2 and 3 is essentially the energy of the hadrons, which is the energy loss in the detector and is proportional to the hadronic path length. This, in turn, is proportional to the production of radioactive nuclei. Therefore, the production of nuclei should be proportional to $K\Delta\sigma$.

$$\Delta\sigma = \int\int (d^2\sigma/dq^2\ dk)dq^2\ dk,$$

the muoproduction hadronic cross section

$K = E - E'$, the virtual photon energy

$$d^2\sigma/dq^2dk = \Gamma_T\sigma(k,q^2)$$

$$\Gamma_T = \alpha/(2\pi q^2)\ (k/p^2)\ (1 - 2m^2/q^2 + (2EE' - q^2/2)/(k^2 + q^2))$$

(the virtual photon spectrum)

$$\sigma = \sigma_\gamma\ .$$

Case I: σ_γ is an average photoproduction cross section
Case II: σ_γ is proportional to $(1 + q^2/0.6)^{-1}$, an experimental fit.

Case I assumes that the form factor is independent of Q^2, which is probably what was used in the Kalchukov calculation. Case II is an approximation of experimental data from 12-Gev muoproduction from SLAC.[8] The results show very little sensitivity to which form factor was used, as is shown in Table 9.3.

Multiplying $\Delta\sigma$ by K and integrating over phase space, we obtain an estimate of the energy dependence for the reaction of interest to be $\sim$ E lnE. This gives an energy dependence roughly in agreement with the Kalchukov result, but steeper.

Table 9.3. The energy dependence of muoproduction and radioactive nuclei.

	Case I	*Case II*
$\sigma(k, q^2)$	σ_γ=120μb	$\sigma_\gamma/(1 + q^2/0.6)$
$\Delta\sigma$	$\alpha\sigma_\gamma/2\pi \ln(aE)\ [\ln(aE) - 2]$	$\alpha\sigma_\gamma B/\pi\ [\ln(E/m_\pi) - 1]$
		B = 3.42
$\Delta\sigma$ at 10 GeV	4.6μb	3.1μb
$\Delta\sigma$ at 300 GeV	12.1μb	6.3μb
E lnE at 10-15 GeV (n.b. the average energy is difficult to determine well)	23 - 41	
E lnE at 100 - 300 GeV	460 - 1711	
Ratio of high E/ low E	11 - 74	

Our $\Delta\sigma$ also can be used to estimate the number of interactions per muon at KII, using an average path of 14m:

$$\begin{aligned} \mathrm{Nint}/\mu &= 1400\ ((6.3 - 12.1) \times 10^{-30}) \times 6 \times 10^{23} \\ &= 0.005. \end{aligned}$$

This is in agreement with a number from KII of a little less than 1%. We feel that this agreement is sufficiently good to accept the more complete calculations of Kalchukov for the correct energy dependence. Using a factor of 10, our β production rate in LCD should be reduced to about one per 20000 muons for the same path length as KII (14m). Thus, the path length for production is 10 × 20000 × 14 = 280000m at our depth, and we can calculate the production rate in LCD:

R=15200s^{-1} × 11.2m /280000 = 0.69 per sec
counts per day in the 5s live time = 5 × R = 3.5
the angle cut gives 90% rejection → 0.35 per day
a 10-MeV threshold rejects 60% → 0.15 per day
the ^{8}B contribution adds 50% → 0.25 per day.

There is one more opportunity to remove these events because of their association with large, infrequent muoproduction reactions. These reactions occur for

1% of the muons in KII and should scale down a factor of 2 to 3 in LCD due to the energy dependence. Therefore, the rate of these events is 18700 s^{-1} × 1/500 = 37s^{-1} or 1 every 27ms. This is longer than the 16-ms life of most of the background. It is thus conceivable to establish a correlation and remove many of the events by observing large energy deposits. We possibly could cut any event that has a big pulse within 2.5m of the electron within 27ms. The efficiency of removal is $e^{-27/16}$ = 0.78 and the dead time incurred is the ratio of rejection area to detector area = 20 / 492 = 4%.

We conclude that this background can be made small.

9.4.2 Muon Capture Reactions

Nearly one-half of the muons are negative, and about 0.4 of these muons stop. Of these about 17% are captured on ^{16}O; capture on Hydrogen is unimportant. It is known[9] that 2.9% of captures on ^{16}O result in ^{16}N, which has an endpoint of its β decay spectrum of 10.4 MeV and a half-life of 7.1s. An intensive search in KII for the presence of ^{16}N has not yet yielded a positive result. We may estimate an upper limit for the production of ^{16}N through the process.

$$\mu^- + {}^{16}O \rightarrow \nu_\mu + {}^{16}N \ \beta(7s,\ 10.4\ MeV)$$

Muon rate (Hz) = 15300

Fraction that are negative = 0.45

Fraction that stop = 0.41

Fraction that are captured = 0.17

Fraction that give ^{16}N = 0.029

Efficiency for detecting 10.4-MeV β = 0.05

Branching Ratio to 10.4-MeV decay = 0.26

Angle cut = 0.1

Live time per day = 5 sec

Number of ^{16}N per day = 0.09 .

We can check this using Fig. 9.9. On this plot we have 2400 stopped muons. ^{16}N production would be observed in the left half of the figure, which contains 1200 ± 35 background counts. If 50 β decays occurred we would expect to see them in this plot and set a limit of 1 event for 80 stopped μ^-. The upper limit for LCD is then

$$R_\beta({}^{16}N \rightarrow \beta) = 1/80 \text{ x } 14000 \text{ x } 0.1 \text{ x } 0.05 = 0.9 \text{ per day} .$$

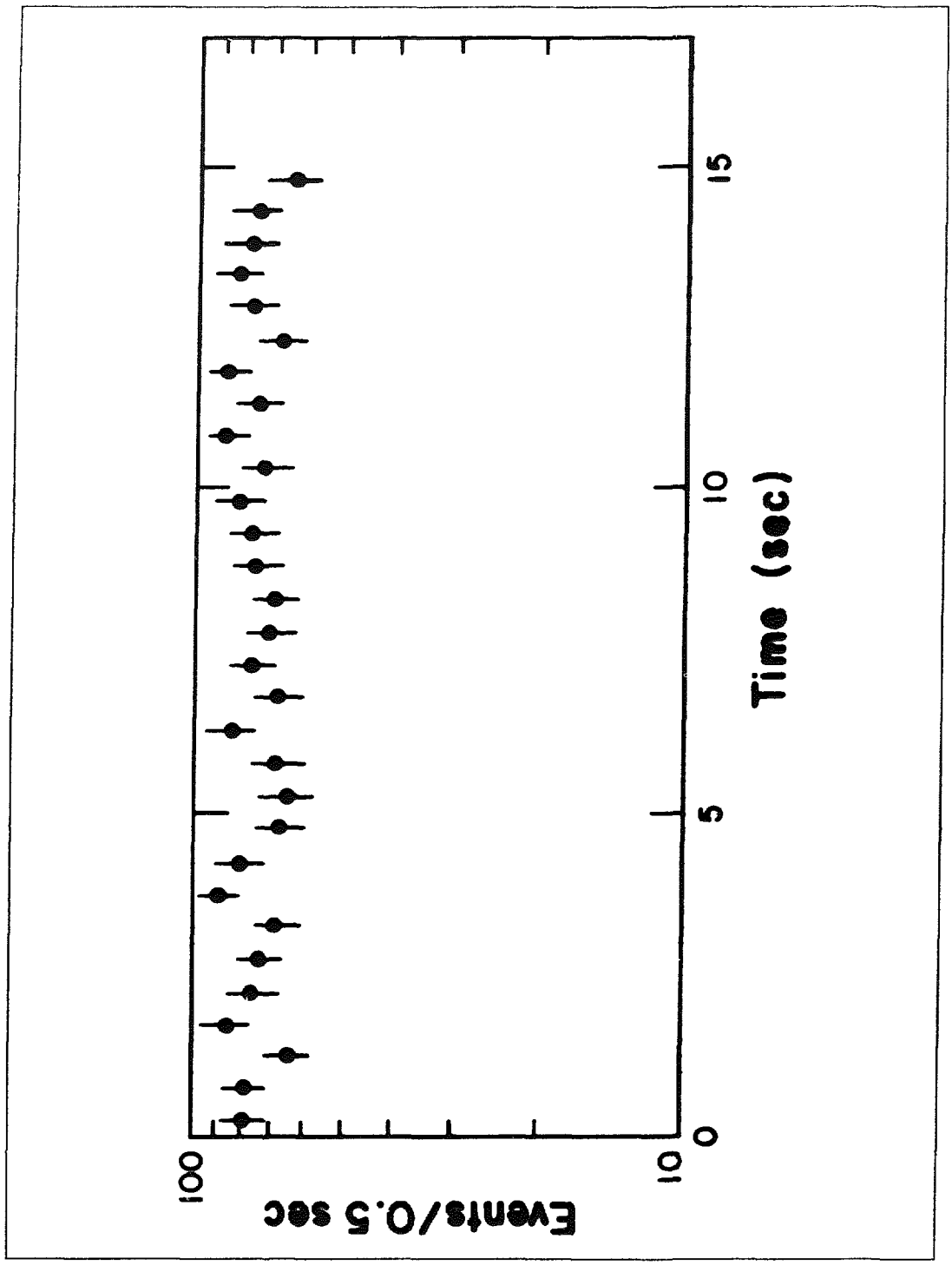

Fig. 9.9. The followers in time of 2400 stopped muons.

The limit on ^{12}B decays from

$$\mu^- + {}^{16}O \rightarrow \nu_\mu + \alpha + {}^{12}B\ \beta\ (20ms, 14MeV)$$

can be derived from noting that they should all appear in the first energy bin in which there are 80 $\pm$ 9 events. Assuming that we can see 10 events in that bin, we have a sensitivity of 1 β for 400 μ^-. This gives

$$R_\beta({}^{12}B \rightarrow \beta) = 1.4 \text{ per day}$$

with the same angle cut and a factor of 0.3 for the energy threshold. These upper limits are almost certainly high by an order of magnitude. We expect that muon capture reactions will give a background of approximately $\sim$ 0.2/day.

This background also seems negligible, particularly as the energy threshold is a very sensitive criterion for acceptance. More data from KII would make a significant improvement on these upper limits, which are already not a severe problem. Furthermore, direct measurements of these stopped rates are possible in a pulsed μ^- beam at LAMPF.

9.5 Neutrals from "Near Miss" Muons

Muons that miss the detector may create neutral secondaries that leak into the detector without counting in the veto. Muon bremsstrahlung, μ-e scattering, and direct muon-electron pair production will usually result in a shower. A background event in LCD occurs if a 10-50 MeV gamma converts in the sensitive region and no event deposit greater than 20 MeV appears in the veto. Another important process is muoproduction of hadrons, which results in a cascade. If a neutron produced in the interaction produces a gamma ray in the sensitive region without energy deposition in the veto, then LCD will record a background event.

Scaling of experiments E225, E31, and E764 is a direct way of estimating gamma backgrounds. This was done in the original proposal (blue book) for a larger LCD and a larger duty factor, but the method is unchanged here. Factors for overburden, area, tracking, and duty factor have been applied to the neutral cosmic-ray rates (with some recent small changes for E31) in the individual detectors. The resulting estimates of neutral background in LCD are shown in Table 9.4.

Table 9.4 LCD neutral background calculated from other experiments.

Experiment	*Rate (counts/day)*
E225	0.05
E31	0.1
E764	1.1

These experiments have quite different properties, especially in the veto construction and tracking capabilities. E764 consists of liquid scintillator, so that the neutral sensitivity is expected to be greater than the other two detectors. We have directly calculated this background for LCD from the cosmic-ray Monte Carlo.

9.5.1 Gammas from Showers

The attenuation length of gammas in tuff is about 40cm, and we take this to be the approximate transverse spreading of showers from near-miss muons. The muon flux on an annulus of width 40cm and length equal to the circumference of the detector is 1400/sec, and the average path length is about L=16m. The muon radiation length is 11,500 × 1.7cm in tuff at 10 GeV, and the number of gammas emitted between 10 MeV and 10 GeV is:

$$N = (1/L_{\mathrm{rad}}) \times (\ln(10000/10)) = 0.015 \text{ for } 16\mathrm{m} .$$

Therefore, there are $1400 \times .015 = 21$ showers s^{-1} that spread into LCD. Our Monte Carlo results give a fraction of 0.4×10^{-3} that give an electron recoil in the right energy range and no veto. This corresponds to a rate of $.008s^{-1}$. Using a detector active time per day of $5s^{-1}$ and a reduction from the directional requirement of 0.1 we find a rate of:

$R_\gamma = 0.004$ events per day from muon bremsstrahlung.

This implies that cosmic-ray neutrons dominate neutral cosmic-ray background.

9.5.2 Neutrons from Hadronic Interactions

A calculation similar to that for gammas gives a muon flux of 3300Hz in an annulus of radial width L=1m (the collision length of neutrons in tuff). A similar calculation by Khalchukov[6] gives 2×10^4 neutrons per year, above 700 MeV, through a vertical wall of $100m^2$ at 550mwe. We scale this rate by factors of:

14 for area
200 for flux at 25mwe
1/4.6 for cross section at LCD depth
1/3 for veto efficiency on neutrons
0.1 for angle cut

giving a rate of 0.29 s^{-1} into all energies in LCD.

If we assume that 10% of these give a count from 10-50 MeV, and that, as before, the detector live time is 5s, then we get an estimate of:

R_n = .14 per day neutron cosmic background.

This does not include low-energy neutrons; however, we do think this shows that the scaled backgrounds from other experiments are approximately correct.

9.6 Veto Region

A potentially serious background occurs from cosmic-ray muons that penetrate the shield into the detector with only enough residual energy to travel a short distance. If the energy of the muon is near or below threshold for Čerenkov radiation (54 MeV), then the muon will not be detected. The decay electron, however, will be detected and will be a candidate event. The range of a 54-MeV muon is about 20cm. The electrons from these penetrating but undetected muons will be at the edge of the fiducial volume and could be removed by the fiducial cut. However, the number of muons emerging from the central pillar with energies below 200 MeV is 35Hz, and so it seems prudent to veto these muons directly in a separate system. We have modeled the cosmic-ray flux in the geometry of the detector and calculated the rate of muons stopping in the sensitive volume. In Fig. 9.10 is shown a histogram of the number of photoelectrons from Čerenkov radiation of muons that pass through the central-pillar veto region and that stop in the sensitive volume of the detectors. The central-pillar veto region is 30cm thick. Photocathode coverage of 1% (about 500 PM's) and a phototube quantum efficiency of 20% will allow sensitivity to 500 photons emitted, at the one photoelectron level. For a background estimate from this source, we have assumed that events with 2500 photons (or 5 photoelectrons) would be detected with unit efficiency, and from Fig. 9.10 it is noted that the number of muons that escape this cut together with the duty factor ensures that this background will be negligible.

It can be argued that this approach is unnecessarily conservative and that the spatial resolution will be adequate to reject electrons within 30 to 50cm of the walls, and so reject these muon-decay events that way. We are reluctant to assume this at this time and, until a great deal of further study has been accomplished, we include a veto system in our design and cost estimate.

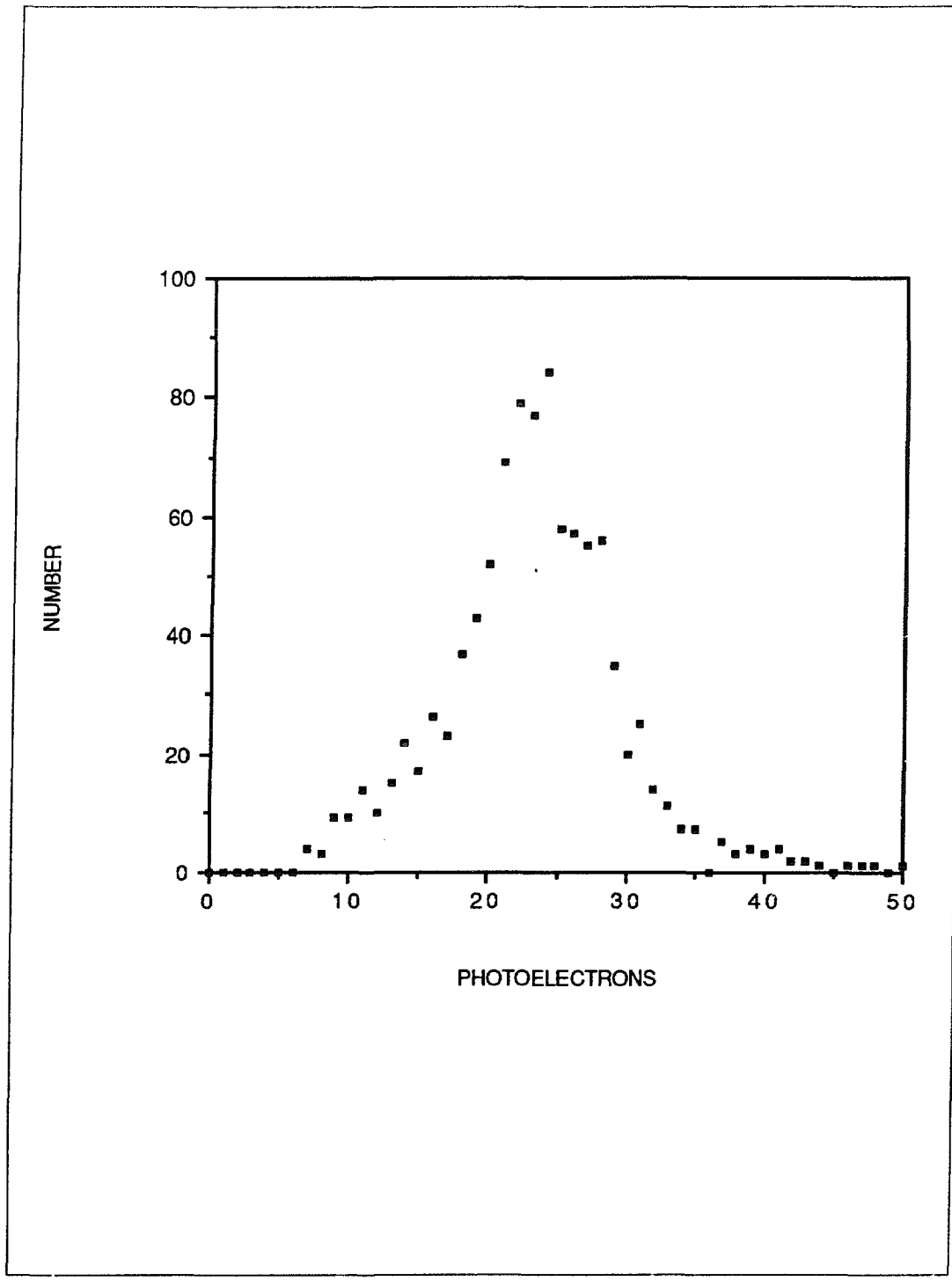

Fig. 9.10. Histogram of the number of photoelectrons from Čerenkov radiation of muons that pass through the central-pillar veto region and that stop in the sensitive volume of the detectors.

9.7 Summary of Cosmic-Ray Backgrounds

Cosmic rays constitute a background of the order of 1/day (or $\sim$ 1% of the number of νe scatters) in the long ($5\mu s$) gate. As we plan to subtract this background to 1%, the systematic error due to cosmic rays is $\sim$ 0.01%. Deadtimes of a few % due to the 20KHz muon singles rates do not create any major problems. The best estimates of the backgrounds are as follows:

1) muon decay $\sim$ 0.01/day
2) neutrals from near miss muons $\sim$ 0.1/day
3) nuclear interactions from through muons $\sim$ 0.3/day
4) muon capture reactions $\sim$ 0.2/day

References

1. Allkofer & Grieder, Cosmic Rays on Earth, Fachsin-informationzentrum, Karlsruhe (1984).
2. R. Davis, Pvt. Communication to Neutrino Oscillation for E764.
3. Cocconi & Tongiori, *Physical Review* **84**, 29 (51).
4. Lawrence Berkeley Laboratory "Particle Properties" (1986).
5. Stearns, et al., *Physical Review* **106**, 1043 (57).
6. Khalchukov, et al., NC **66**, 320 (83).
7. Hayakawa, S., Cosmic Ray Physics, Wiley Interscience (1969).
8. B. Dieterle, et al., *Physical Review Letters* **23**, 1191(1969), M. Perl, et al., *Physical Review Letters* **23**, 1187 (1969).
9. Guichon et al., *Physical Review* **C19**, 987 (1979).

10 CALIBRATION OF ENERGY SCALE AND TIMING

Calibration techniques are described for absolute energy and for relative timing. The energy calibration measurements rely upon the Michel-spectrum of electrons and positrons from stopped muon decay and upon 8-9-MeV neutron-capture gamma sources. The timing calibration will be done with laser-excited scintillator balls.

The methods we describe are those successfully used in calibrating the KAMIOKANDE II (KII) detector; as participants in KAMIOKANDE are also working on LCD, we see no obstacle to transferring the technology. It has been demonstrated that a 3% energy-scale calibration can be achieved and maintained over long periods of time. We do need better timing calibration, particularly if the 20.3-cm (8-inch) Burle photomultipliers are used, but the techniques for timing calibration are also well developed.

A 3% uncertainty in the energy scale translates into 0.3% in R, or 0.15% in $\sin^2\theta_W$. When combined in quadrature with other uncertainties, this will contribute only 0.04% to the final uncertainty in the LCD measurement of $\sin^2\theta_W$. The modifications needed for LCD will not affect the overall performance of the KII methods.

The method for establishing the energy scale is based on using Čerenkov light from physical processes that deposit an appropriate range of energies in the water. These are the Michel spectrum from muon decay, the conversion of gammas (of about 6- to 9-MeV energy) from neutron capture in nickel, and the beta spectrum of spallation-produced nuclei. By comparing the pulse-height spectra obtained from these processes with the prediction of the simulations, we shall calibrate the detector over the range from 0 to 50 MeV, which is the critical range for us. For timing, we will use multiple "scintiballs"—balls of diffusing scintillator pulsed with UV light piped to the balls in quartz fibers.

10.1 Stopped Muon Decay Calibration

Figure 10.1 shows the results achieved in simulating the energy spectrum of electrons from events in which a muon stopped in KII and subsequently decayed. Events per bin of 1.8 N_{eff} are plotted versus N_{eff}, the corrected number of photoelectrons detected. The success in fitting the Monte Carlo simulation to the data is obvious. Parameters fitted include optical absorption in the water and the quantum efficiencies of individual photomultiplier tubes.

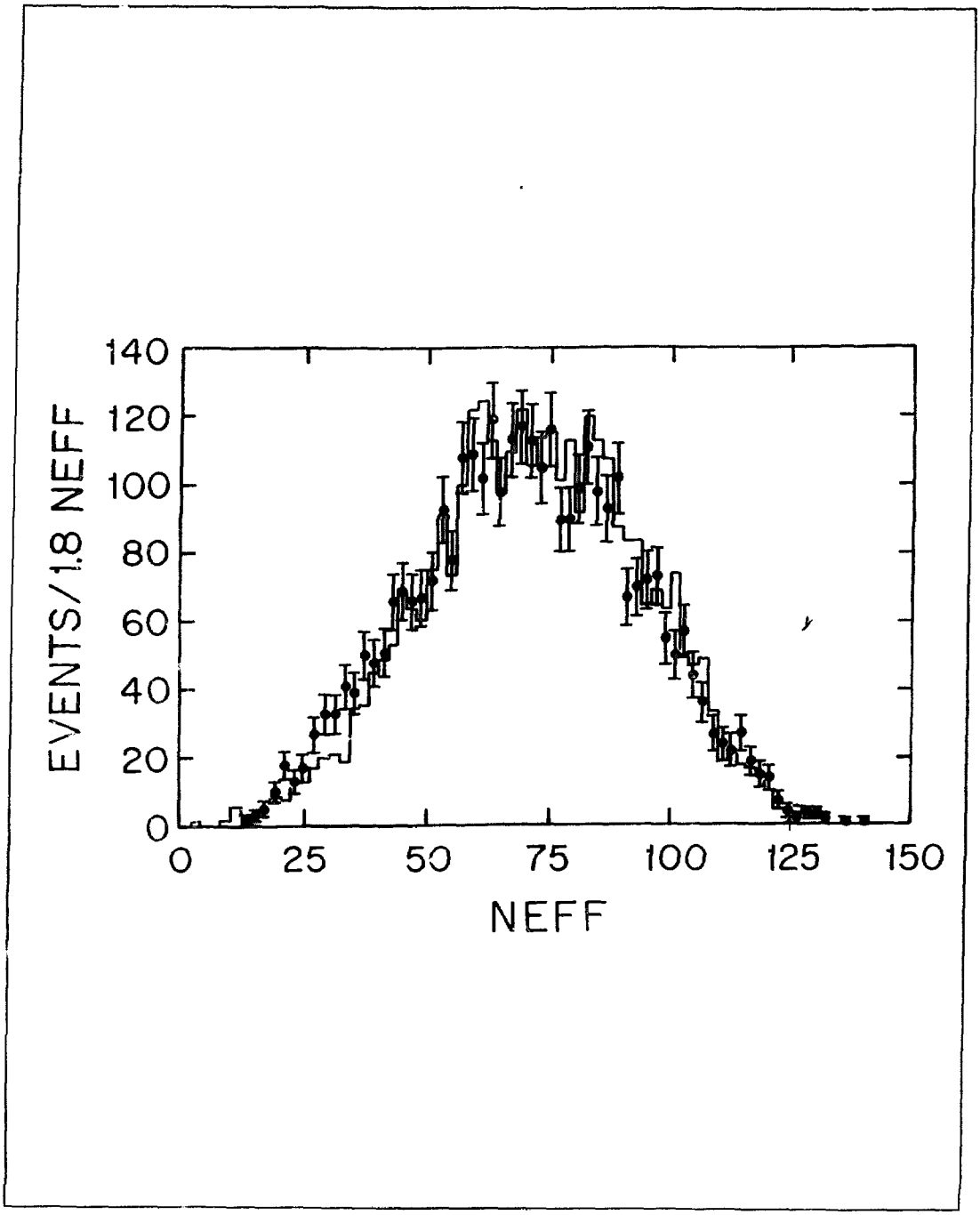

Fig. 10.1. Spectrum of light collected from stopped muons in KII. Events/bin of 1.8 N_{eff} are plotted versus N_{eff}, the corrected number of photoelectrons detected. The points indicate the data; the histogram, the simulation.

It will be straightforward for us to trigger on stopped cosmic-ray muons between beam bursts, so a large sample of events covering the entire detector volume will be collected. The geometry of LCD is topologically toroidal, and so is more complex than that of KII (a cylinder), but it is nevertheless straightforward to simulate.

10.2 Neutron Capture on Nickel

From experience in KII, we know that this method produces a reliable calibration point, so little more need be said. However, we summarize here some design considerations.

The neutrons will be produced by decay of ^{252}Cf, which undergoes spontaneous fission with a branching ratio of 3.1%; it has a half-life of 2.65y. The fission yields a variety of radiations besides the fission fragments.[1] There are 10 prompt photons per fission, with an average total energy of about 8.5 MeV.[2] There are 3.70 prompt neutrons per fission, with an average energy of 2.2 MeV; the spectrum is peaked at low energy (below 1 MeV) with a long, high-energy tail. From study of fission in other nuclei, about six beta decays per fission will occur over time, with an average energy of about 8 MeV. Thus a ^{252}Cf source is quite active for photon and electron emission in the 0- to 8-MeV energy range. A difference technique must be used. The spectrum from ^{252}Cf plus nickel is measured, then that from ^{252}Cf alone. The difference is the spectrum from neutron capture in nickel.

In water, the fast neutron from ^{252}Cf is moderated to thermal energies in a typical distance of 5.7cm.[3] This will take several nanoseconds. After being thermalized (or at least being reduced in energy to 1–10keV), the neutron will capture on hydrogen (with emission of a 2.2-MeV gamma) or on nickel. The cross section for (n,γ) on hydrogen is 5.2×10^{-4}b, whereas for nickel it is around 2.6b. The mean free path of a slow neutron in water is very much longer than the above slowing-down distance, so an enclosure of nickel of 5- to 10-mm thickness will absorb a significant fraction of the neutrons without absorbing the resulting photons. The spectrum of gamma rays from natural nickel (constructed from the spectra of individual isotopes, normalized to the natural abundances) is shown in Fig. 10.2.

Figures 10.3 and 10.4 show the results achieved by the KII group using this technique. Figure 10.3 shows the spectra without the nickel can, and Fig. 10.4 shows the difference spectrum. A solid calibration point at 9 MeV is achieved.

For a reasonable trigger rate (10kHz), an activity of 1mCi would suffice. It is also conceivable that the fissions could be detected and used as a trigger, although this was not done at KII. Otherwise, to trigger on these low-energy events we need to lower our threshold to 5 MeV (about 12 to 15 tubes firing). A PMT mounted

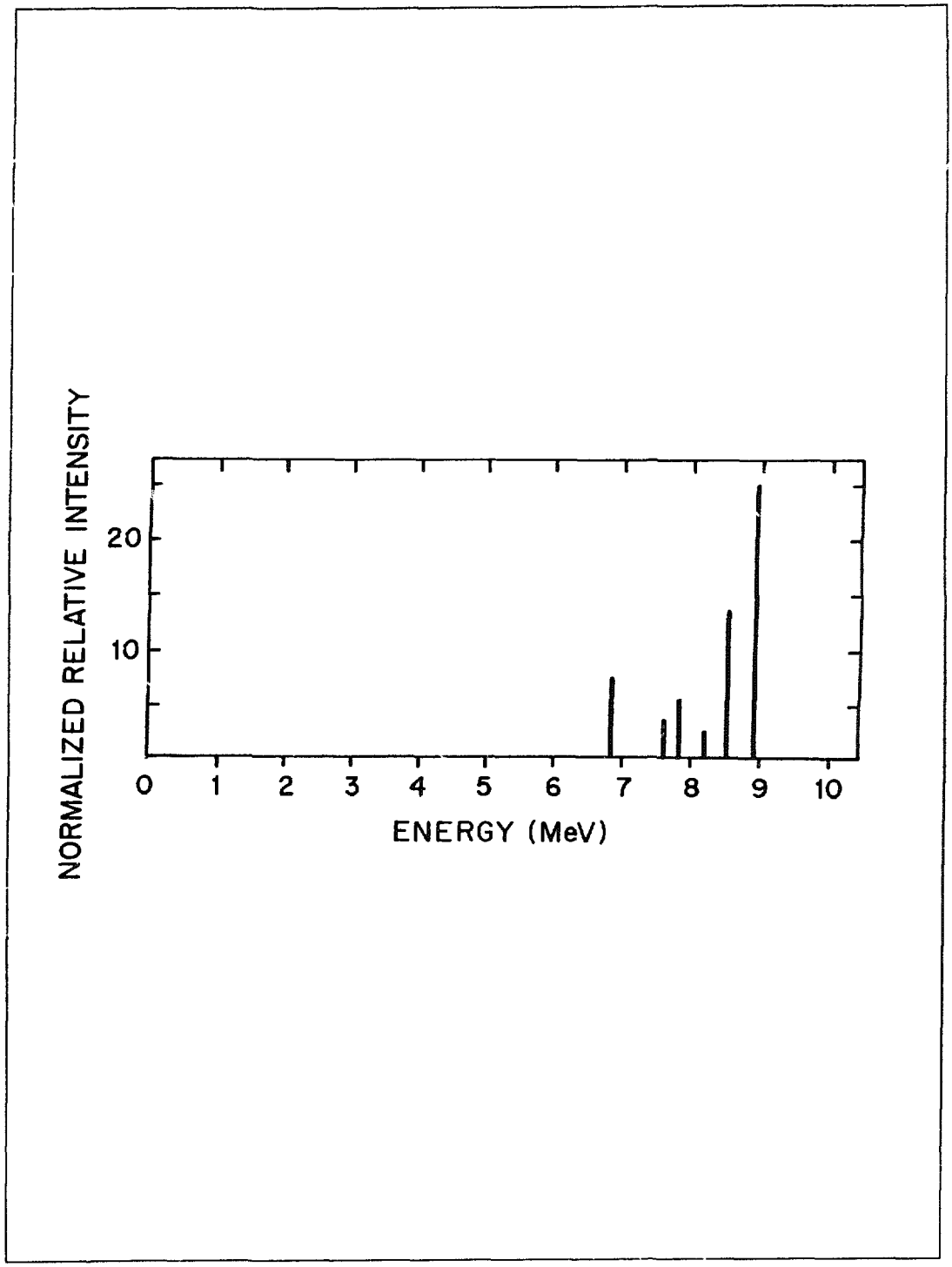

Fig. 10.2. Spectrum of gamma emission from neutron capture in natural nickel (relative intensity versus energy in MeV).

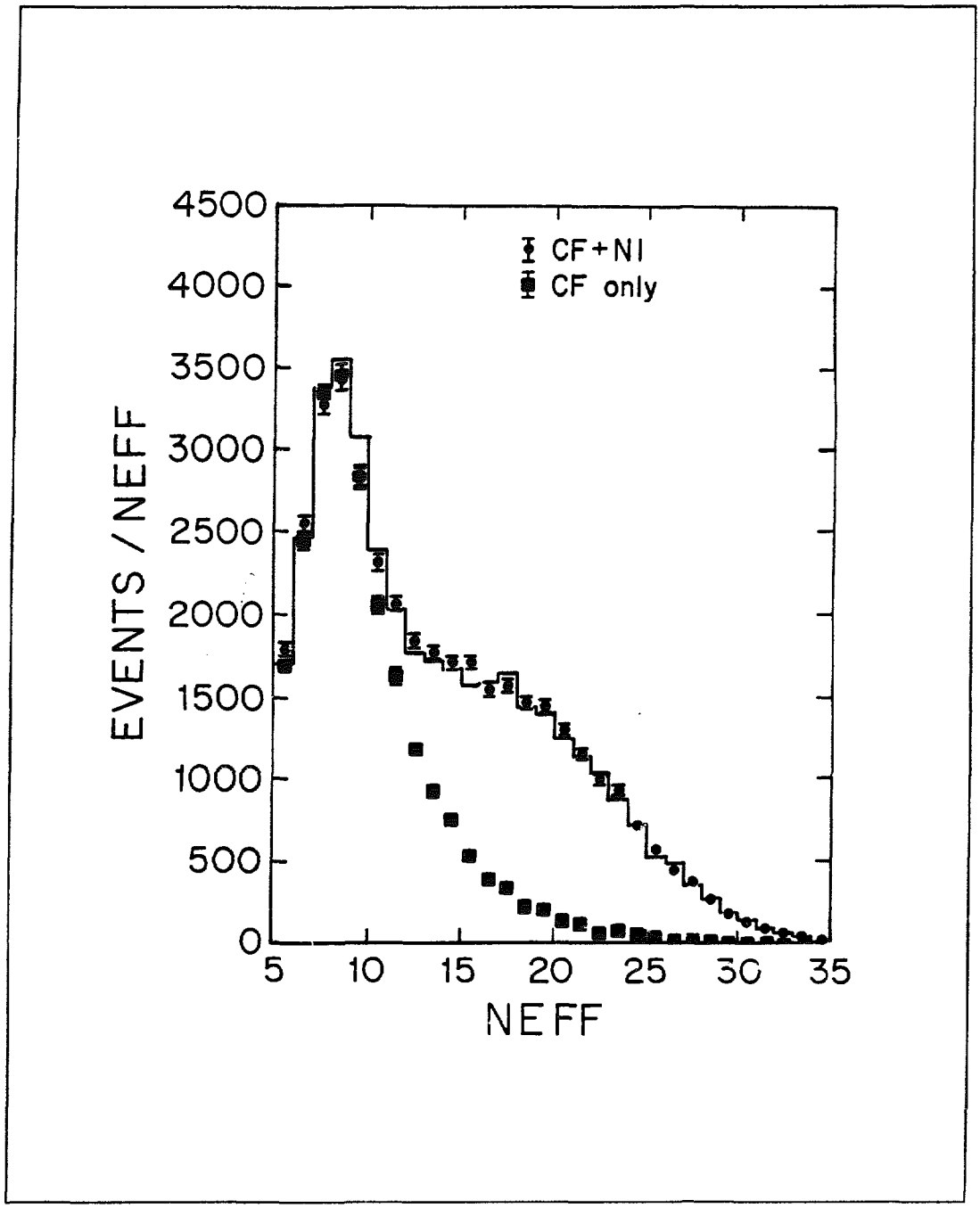

Fig. 10.3. Corrected number of photoelectrons from the californium-nickel source in KII, normalized to the same peak value. The points indicate the data; the line, the simulation. Circles indicate data taken with the nickel can around the californium source; squares, data taken with the nickel can removed.

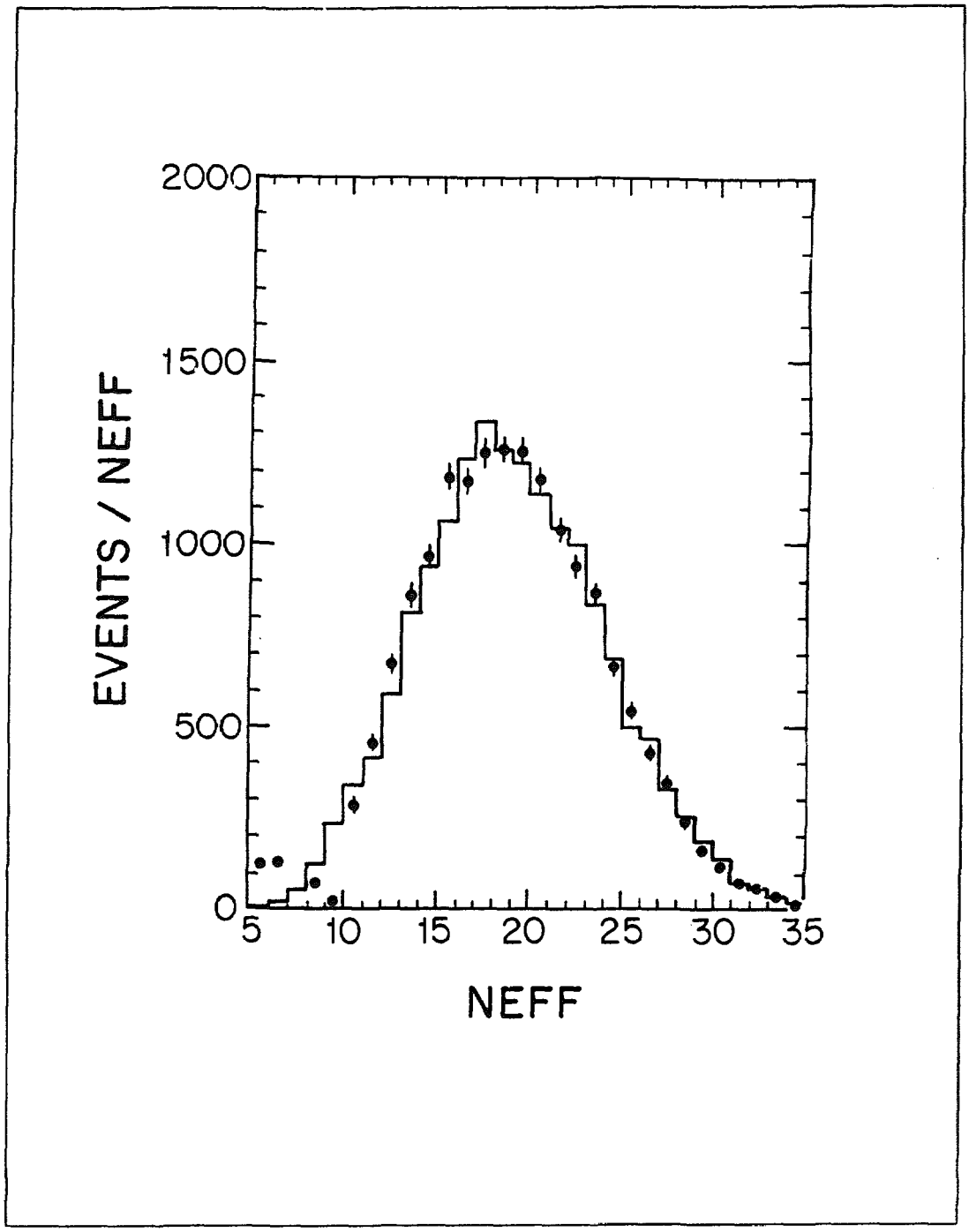

Fig. 10.4. Difference between the spectra of Fig. 10.3. This is the spectrum of gammas from neutron capture in nickel. The points indicate the data; the line, the simulation.

close to the californium-nickel source could be used as a trigger, although that would shadow some of the detector.

To implement this method for LCD, we need to have mechanical systems that can lower a californium source, surrounded by a hollow nickel can, into one of several positions (six is a likely choice) around the detector and also remove the nickel can from the vicinity of the source. (The KII group used manual access, which is not practical for LCD.) There appears to be no obstacle to this; the Laboratory's remote-handling experience at Los Alamos will be essential to making a reliable system.

10.3 Alternative Gamma Sources

Although the californium-nickel source method has been demonstrated to be successful, we are considering other approaches to the (n,γ) reaction. A polonium-beryllium neutron source is attractive because of its relative cleanliness. To give the same number of neutrons per second (300kHz), we would need, however, 100mCi of polonium. Polonium-210 has a half-life of 138d and emits alphas of 5.4 MeV, whereas ^{208}Po has a half-life of 2.93y, with alphas of 5.0 MeV. Iron (say, ^{54}Fe) has a similar capture cross section to nickel and emits gammas of 9.3 MeV (66%) and 8.9 MeV (12%). Chromium-50 has a large cross section (17b) and emits 8.5-MeV gammas (55%). There may be corrosion-resistant alloys that would give us a better overall system than californium-nickel; nevertheless, the californium-nickel method is proved in practice.

10.4 Timing Calibration

We plan to calibrate the timing of the tubes by using the scintiball technique developed by the KII group. A pulsed UV laser will drive several quartz fibers, each of which will excite a scintillator radiator. The radiator will be in the shape of a ball and contain diffusing pigment. The resulting emission of light is quite isotropic, and the spectrum is similar to that of Čerenkov light. Some such system is essential for testing and monitoring all channels independently of the detailed analysis necessary to establish the energy scale. The method can be automated, possibly using the same remote-handling devices used for the (n,γ) source. We see no difficulty in using this method (probably with six remotely handled sources that can be pulsed independently) to give us calibration of the timing channels to better than 0.5ns.

References

1. AIP Handbook, 3rd edition, (1972).
2. AIP Handbook, pp. 8-275.
3. I. Kaplan, *Nuclear Physics*, 530 (1955).
4. C. M. Lederer et al., Eds., Table of Isotopes, (Wiley, 1978).

11 DATA ACQUISITION AND REDUCTION

Data acquisition and reduction are discussed with particular emphasis on event and trigger definitions. The estimated trigger rate is less than one event per second, and the amount of data written to storage is less than a gigabyte per day.

Cosmic-ray muons and the decay of stopped muons to electrons are the main and almost exclusive contribution to the trigger rate. Figure 11.1 illustrates two possible event scenarios. The middle plot shows two cosmic-ray muons entering the detector during a 40-μs interval about the spill. One muon goes straight through the detector, while the other muon stops and decays to an electron. The electron is created only a few microseconds after the end of the PSR spill and therefore simulates a neutrino-electron-scattering event. This background from muon decay dominates the LCD trigger rate.

The lower plot shows a genuine neutrino-electron-scattering event with an unassociated through-going cosmic-ray muon. The electron appears shortly after the PSR spill and is uncorrelated in spatial position with the muon.

11.1 Event Definition

For an appropriate trigger, we assume the following information, which was discussed earlier. The cosmic-muon rate entering the sensitive region of the detector is 18.7kHz, of which 41% are stopping muons. Because we are planning a 0.5μs interval between a muon and the next event, the effective stopping muon fraction is 33%. The sensitive region of the detector is the volume of water defined by the phototube surfaces. There is also an active veto region that is outside and optically isolated from the sensitive region, and there is a 500-ns deadtime after each hit phototube in the detector.

The PSR cycling rate is 12-Hz (100μA), and the data analysis is based on a 40-μs interval per PSR spill, 30μs before the spill and 10μs afterwards. (A PSR cycling rate of 24Hz doubles the average trigger rates; however, this can easily be handled by the data-acquisition system.) There will be only about 0.1 electrons per day after the PSR spill, from muon decay before the 40μs-interval (muon decay lifetime greater than 30μs).

All phototube hits associated with events are stored during this 40-μs interval, up to a limit of about 8 hits per tube. Events are defined, for example, as at least 20 hits occurring within a 200-ns interval. The 20-hit threshold serves to reduce stored data, prevents random-noise hits from contaminating the sample, and corre-

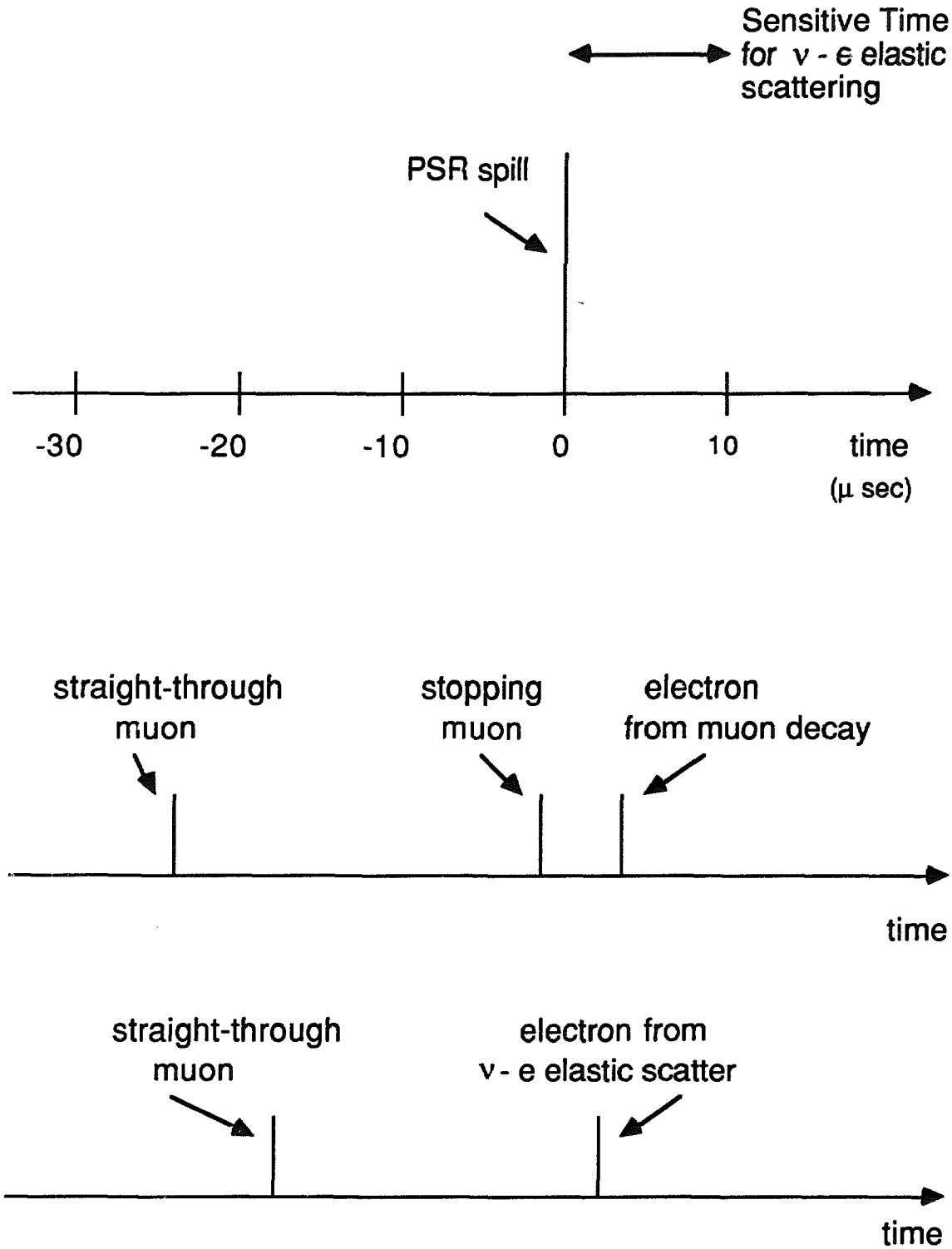

Fig. 11.1. Cosmic ray activity associated with two typical events.

sponds to an energy just under the 10-MeV energy cut we plan to use in the off-line analysis.

Cosmic-muon events, which can be recognized by the active veto surrounding the detector, fire typically 2000-4000 phototubes during the 200-ns interval. These muon events are analyzed by ACP on-line computers between spills, so that the muon information can be written to storage (magnetic tape or optical disk) in compressed form.

Electrons from νe elastic scatters fire between 20- and 200-phototubes, or 100 phototubes on average. We expect to define an electron candidate event as one with 20 to 200-hit phototubes during any 200-ns interval that occurs within 10μs after the beginning of the PSR spill and is not associated in time with activity in the veto surrounding the detector.

11.2 ACP Data Reduction

All electron events will be recorded unless they are associated with a cosmic-ray muon by the ACP computers. Because these events may be electrons from stopped muon decay, it is necessary to store previous muon information in the gate. Therefore, cosmic-muon events and other events will be recorded only if they occur before an electron event in the same PSR spill.

The ACP on-line computers will compress the data of cosmic muons from 32 000 bytes (corresponding to 4000-hit phototubes, as each hit is stored in 8 bytes of data) to 100 bytes, which summarizes the position, angle, energy, and time of the muon. An ACP node will perform this compression in approximately 1s. Because we shall have to compress on average about one muon per second (see below), an array of 10 to 20 nodes should suffice. Due to correlations between the muons and electrons, all data from one spill will go to one node. The ACP can also flag electron events that are associated with cosmic muons in time and position and, therefore, are consistent with electrons from muon decay. These electron events may then be either rejected or written to storage with the information of the associated muons.

11.3 Trigger Definition

The actual trigger could consist of two levels. In the first level an electron event (no active veto signal) with between 20- and 200-hit phototubes in a 200-ns interval is required to occur within a 10-μs interval starting at the beginning of the spill. This multiplicity requirement will be made with fast electronics using majority logic. The second level trigger will use the ACP system to flag events that have a cosmic muon correlated in position within approximately 50cm during the previous 10μs. Flagged electron events can then be rejected or written to storage

with the correlated muon information and processed in a single ACP node. (Note that in the off-line analysis, we probably will veto all events with a correlated muon during the previous 30μs.) If the trigger is satisfied then all events occurring before the neutrino-electron event are written to storage. In addition, we plan to sample electron events from stopped cosmic-muon decays for use in calibration.

11.4 Trigger Rates and Event Lengths

The resulting average trigger rates are shown in Table 11.1. The incident cosmic-muon rate during the 40-μs intervals about the PSR spills is 0.75 per spill (9Hz), which is the rate at which the fast electronics must process data. The stopping cosmic-muon rate is 0.31 per spill (3.7Hz), while the rate of electrons from muon decay in the 10-μs interval after each PSR spill is 0.078 per spill (0.9Hz).

Taking into account the 0.5-μs interval after the muon stop, the total level 1 trigger rate is 0.06 per spill (0.7Hz). The level 2 trigger making use of the ACP system is capable of reducing this by at least an order of magnitude, giving a final trigger rate of 6×10^{-3} per spill (0.07Hz), or 7000 events per day. The average amount of data in a triggered spill is about 1000 bytes, corresponding to 800 bytes for the electron event and 200 bytes for the two cosmic-muon events after data compression by the ACP system. (On average there is approximately one cosmic muon per spill and about two cosmic muons in spills that contain a triggered electron event.)

The amount of data written to storage is then (see Table 11.2) approximately 70 bytes/s (7 Mbytes/day) if the level 2 trigger is imposed, or 700 bytes/s (70 Mbytes/day) if not. Note that a PSR cycling rate of 24-Hz (200μA) increases the average trigger rates and data lengths by a factor of 2, which can still be easily handled by the data-acquisition system.

It is important to note that, using Poisson statistics and the average trigger rates discussed above, we estimate that about 37% of the spills will be empty (i.e., have no cosmic-muon events). This implies that 37% of the time, genuine neutrino-electron-elastic-scattering events will be unaccompanied by cosmic muon background. Furthermore, the fraction of spills with one, two, three, and four or more cosmic muons are 37, 18, 6, and 2%, respectively.

11.5 Random Phototube Hits

It is interesting to calculate the first-level trigger rate (or probability of 20 phototube hits) due to random hits in a 14 000 phototube system. If the noise rate is 1000Hz per tube, the number of extra hits in any 200-ns interval is 2×10^{-4} per

tube, or 2.8 for all 14 000 tubes. The rate, R, of getting 20-hit tubes from noise is then approximately

$$R = (1000\ \text{Hz})(14\,000)[e^{-2.8}(2.8)^{19}/19!] = 2.2 \times 10^{-3}\text{Hz} \ .$$

Therefore, random triggers from noisy tubes should not be a problem if the average noise rate of each tube is less than 1000Hz.

Table 11.1 Trigger rate.

	Trigger Rate per Spill	*Trigger Rate per Day*
Incident cosmic muon in 40-μs interval	0.75	7.8×10^5
Stopping muon rate in 40-μs interval	0.31	3.2×10^5
Electron (from μ decay) in 10-μs interval	0.078	8.1×10^4
Electron (from μ decay) $> 0.5\mu$s after muon	0.060	6.2×10^4
Electron not correlated with muon (level 2)	0.006	6.2×10^3

Table 11.2 Data written to storage.

	Data Written to Storage (Bytes/s)	*Data Written to Storage (Bytes/d)*
Data processed by fast electronics	3×10^5	3×10^{10}
Data processed by ACP system	4×10^4	4×10^9
Data written to storage (no level 2)	700	7×10^7
Data written to storage (level 2)	70	7×10^6

12 EXPERIMENT SIMULATION

The simulation of the experiment and the event reconstruction are described. For neutrino electron elastic scatters, the total acceptance is about 50%, the average angle of the electron is 19°, the average position error is 40cm, and the energy resolution is approximately 20%. The total statistical error in $\sin^2\theta_W$, after subtraction of background, is estimated to be $\pm 1.6\%$.

12.1 Monte Carlo Calculation

A precision experiment requires a detailed simulation so that the operating performance of the detector can be understood in sufficient detail that the proposed precision can be evaluated. In addition, because the detector is a substantial commitment, the optimization of the details of the detector needs to be carried out with care. An integral part of this procedure involves a Monte Carlo simulation of the entire detector, which is described in this section. This proposal is based on water Čerenkov technology that has been proved in two experiments, Kamioka (referred to as KII in this document) and IMB. Both of these detectors have run for extended periods, and the design of this experiment borrows from their experience. These experiments in which proton decay was searched for are only partly applicable to this experiment, although the successful observation of low-energy electrons is directly of interest. In KII, a nominal photocathode coverage of 20% has yielded a threshold of 7.5 MeV in a search for ^{8}B solar neutrinos.

There are two notable differences between the LCD design and the precursors. The first is that a substantial pillar passes through the center of the detector, so that any phototube views only a portion of the detector volume. The second is that the LCD preferred design uses 8" tubes with superior time resolution, higher photoelectron efficiency, and better spatial granularity. Following the KII design, a comparable photocathode coverage is proposed. The photomultiplier tubes (PMT) are modeled as flat discs, which is a close approximation to the actual design (Burle). The geometry of LCD is modeled closely, following the apparatus description in chapter 3. The photoelectron yield from Čerenkov light has been assumed to be similar to KII with the exception that a slightly higher photocathode efficiency has been used for Burle tubes following the manufacturers published data.

The following reactions are modeled in the program.

1. Neutrino-electron scattering.

The cross sections in the Standard Model are calculated for neutrino energies from a stopped pion source. Events are weighted by these elastic cross sections.

2. ν_e-Oxygen charged-current scattering.

Cross sections from the calculations of Haxton[1] are included in the program, following the description in chapter 7.

3. Output from selected calibration sources is included.
4. Electrons or gamma rays may be selected by energy, position, and angle.

The energies of the neutrinos are chosen from the appropriate decay spectrum. ν_μ is a delta function at 29.8 MeV, ν_e is given by 52.83 $\times^2$ (1 - x) and $\bar{\nu}_\mu$ as 52.83 $\times^2$ (3-2x) where 0 < × < 1. These spectra model the stopped pion source but do not include the effects of decay in flight, and the effects of the small π^- contamination.

The spatial distribution of the neutrino flux is isotropic; again, the non-uniform distribution from decays in flight is not modeled here directly in the program. The target is a point source.

The range of wavelengths of PMT sensitivity for Čerenkov light is taken to be 300nm to 700nm and an average photocathode efficiency is used, which is taken from the manufacturers data sheets and calibrated directly against KII performance.

Particle tracking is accomplished using the electron and gamma-shower code EGS4, simulating the electromagnetic processes. The step sizes were limited to less than 2mm. Fig. 12.1a shows a set of electrons at 12 MeV tracked in water by this code, and in Fig. 12.1b is a 30-MeV set of electrons. EGS4 includes all of the electromagnetic energy-loss mechanisms, Fig. 12.2 shows the energy loss due to ionization and the output of the program showing the extra loss due primarily to delta rays. A linear fit to total energy loss yields 0.85 ($T_e - T_{thresh}$) where T_{thresh} is the Čerenkov energy threshold.

A charged particle travelling with velocity β, through a medium having index of refraction n, will produce Čerenkov light provided that

$$cos\theta_c = \frac{1}{n\beta} \leq 1 \ .$$

This gives a threshold kinetic energy for electrons in water of 0.26 MeV; by 1 MeV the Čerenkov angle is 37°, nearly 41.4°, the value for $\beta = 1$.

The number of Čerenkov photons generated in each increment of track depends both on β and the wavelength window that is accepted. As discussed above, wavelengths between 300nm and 700nm are accepted. After a step size of d cm, the number of Čerenkov photons generated is given by a Poisson distribution with a mean

$$N = 872 \ d \ sin^2\theta_c \ .$$

These photons are thrown uniformly around a Čerenkov cone of appropriate angle and propagated to the phototube surface of the detector. These photons are

absorbed with an absorption length of 40m, appropriate to the water purity that is expected, and scattered isotropically also with a scattering length of 40m. The effects of the water-glass interface at the phototube have not been included. The principal effort has been in modeling the Burle 8" phototube; the photocathode surface is expected to be almost flat in these tubes, and we have assumed them flat for this simulation.

The inherent jitter of the phototube has an important effect on the reconstruction accuracy. The Burle 5" tube has a measured spread of 2.5ns (section 13.1.1), and simulations of the proposed 8" tube indicate that jitter will be very close to the tubes that we have measured. This parameter is discussed in detail in section 13.1.1; for the principal simulation, 2.5ns FWHM has been used. For PMT's that detect more than one photoelectron, the earliest photon arrival time is recorded. This causes a systematic shift in the event time for these PMT's, and a time correction is applied during analysis based on the number of photoelectrons observed in the PMT. Noise measurements on the Burle 5" tube indicate a very satisfactory noise level of less than 1kHz. In the Laboratory, noise rates of 0.5kHz have been observed at the 0.2 photoelectron threshold level. The simulation takes this into account by including a random number of PMT hits for each event. The noise rate is taken to be 1kHz for 8" tubes.

Analysis of the raw PMT data is done successively at two levels. The first level simulates the detector hardware trigger described in chapter 14. It is envisaged that the hardware will be capable of selecting a number of hit tubes, defining a threshold energy. An upper limit to the number of hit tubes may also be used to eliminate events that have small probability of being neutrino-electron scattering. The time period for which the hit threshold is exceeded must be long enough to allow for variation in flight time. Any event that passes the trigger requirement is then reconstructed. At present, the reconstruction program fits electrons as if they were a point source. For electrons less than 50 MeV, the length of the track is less than 0.3m.

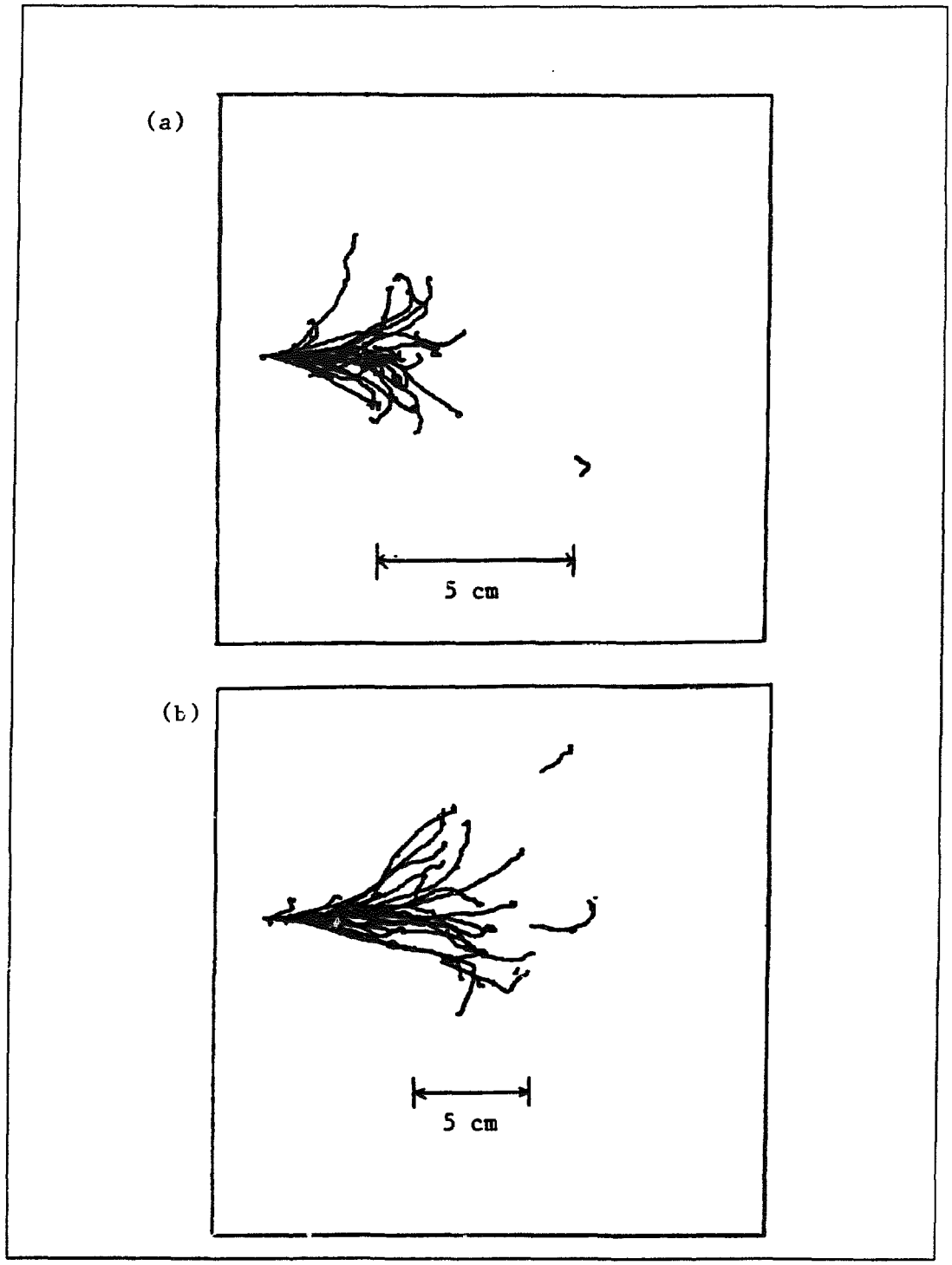

Fig. 12.1. (a) A set of 12-MeV electrons generated by the Monte Carlo (b) A set of 30-MeV electrons.

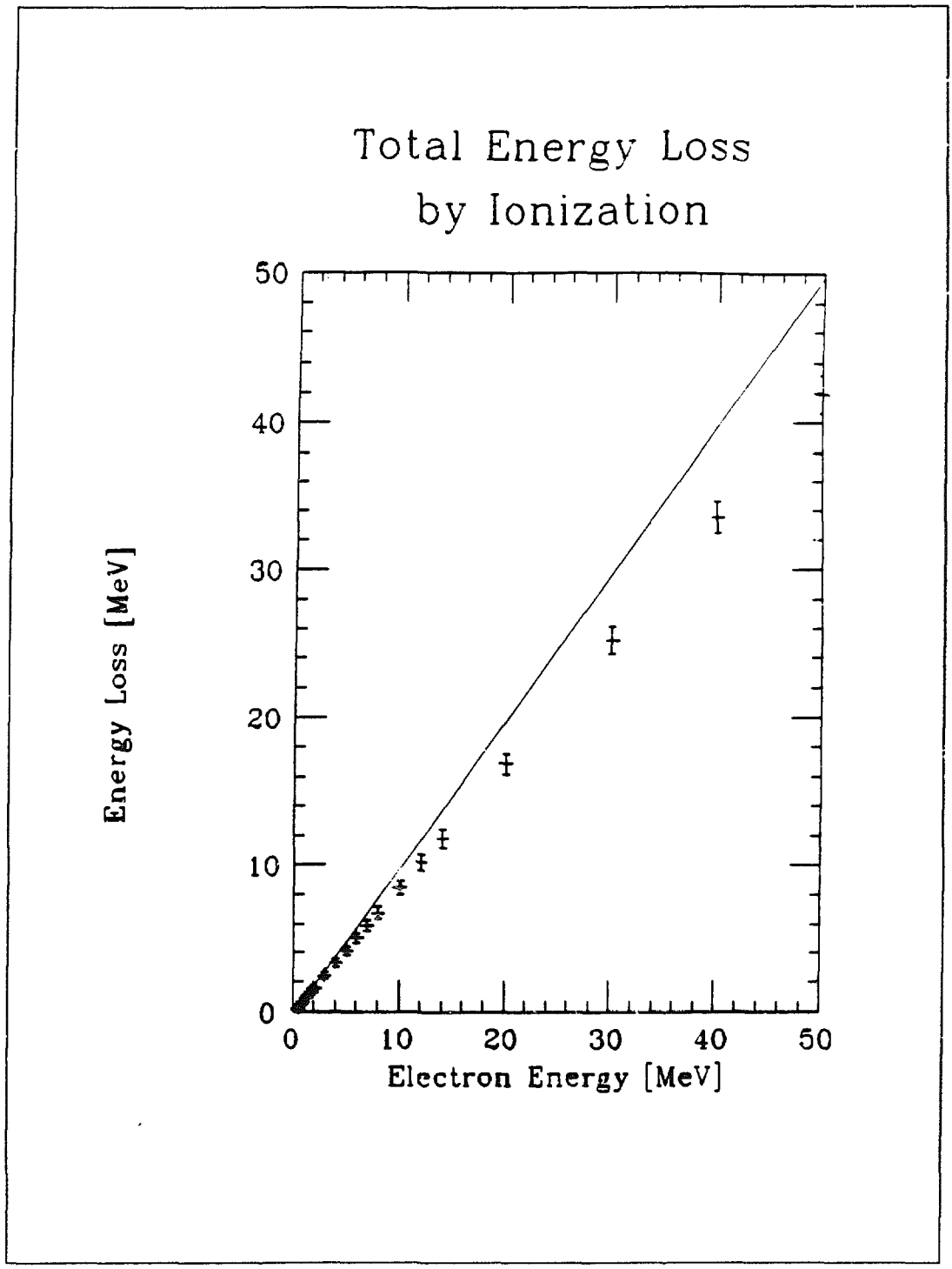

Fig. 12.2. Energy loss due to ionization in the Monte Carlo.

Calculation of Residuals

For reconstruction, the basic assumption is made that each event is described by a single space-time point, (x_i, y_o, z_o, t_o), which is the origin of all the Čerenkov photons observed by the PMTs. Using the physical coordinates, (x_i, y_i, z_i), of the individual PMTs in the data set and the time information derived from the PMT activity, t_i, the starting point can be calculated by minimizing a residual function, R, of the form

$$\begin{aligned} R &= \sum_{i=1}^{NPTS} R_i \\ &= \sum_{i=1}^{NPTS} (r_i - \Delta T_i \frac{c}{n}) \\ r_i &= \sqrt{(x_i - x_o)^2 + (y_i - y_o)^2 + (z_i - z_o)^2} \\ \Delta T_i &= t_i - t_o \end{aligned}$$

where $NPTS$ denotes the total number of PMTs involved in the event. The reduced χ^2 (χ^2 per degree of freedom) can be calculated for the reconstruction from the individual residuals, R_i, for each PMT

$$\chi^2 = \sum_{i=1}^{NPTS} \frac{R_i^2}{(NPTS - 4)} ,$$

where the number 4 stems from the number of parameters being sought.

We note that the residual function, R, is not positive-definite. The implication is that only a few "bad" PMT hits can throw off the fitting routine. In the ideal case, the PMTs used to fit the event are only those with activity resulting from direct Čerenkov photons. PMTs with activities from scattered photons (i.e., photons arriving late) or PMTs that are completely unrelated with the event (i.e., PMT noise) can cause a reconstruction problem.

Corrected PMT Time Distribution

To minimize the effects of "bad" PMT hits, we remove them from the fit by using the corrected time distribution of PMT activities. Ideally, the difference between the time of occurrence of an event, t_o, and the time for the PMT activity, t_i, corrected for the time of flight for the photon, $r_i n/c$, is zero. Due to the time jitter of the PMTs, however, this time difference normally has a finite, non-vanishing value, δT_i:

$$\delta T_i = \Delta T_i - r_i \frac{n}{c} .$$

If this distribution is calculated using only the Čerenkov photon starting points and if only PMTs that are hit by direct Čerenkov photons are included, then this should reproduce the time jitter distribution of the PMT. Therefore, this distribution is a measure of the quality of the event data set and enables the use of further constraints on the selection of PMTs for event reconstruction.

Point Fitter Procedure

The following iterations are used in order to reconstruct an event. Because the reconstruction involves four parameters to be determined, we require a minimum of eight PMTs for a trigger before attempting a fit.

STEP 1

Reduce the number of PMTs that generated the trigger in the 200ns window by removing the last 20%. This number is adjustable and is intended to remove "late" PMTs. Start the first determination of (x_o, y_o, z_o, t_o) by setting (x_o, y_o, z_o) equal to the average of the hit PMT positions, (x_i, y_i, z_i). Given that, in the ideal case, the residual function, R, is zero, t_o is given by:

$$t_o = \frac{1}{NPTS} \sum_{i=1}^{NPTS} (t_i - r_i \frac{n}{c}) \ .$$

The point fitter is then called using this initial assumption for (x_o, y_o, z_o, t_o) as input.

STEP 2

The point fitter routine returns a new location, (x_o, y_o, z_o, t_o), which is used to fix a reduced coincidence time window of 50ns around the δt_i's corrected time distribution. Only data from PMTs within this window are selected for the next iteration and the point fitter is called.

STEP 3

Again the point fitter routine returns a new location, (x_o, y_o, z_o, t_o), which is used to fix a reduced coincidence time window of 28ns around the δt_i's corrected time distribution for the total set of hit PMTs in the event. Then the point fitter is called.

STEP 4

Again the point fitting routine returns a new location, (x_o, y_o, z_o, t_o). Of the four iterations, the fit result with the minimum reduced χ^2 is selected as the best

fit. If the reduced χ^2 is less than about 70, the event is defined to have a "good" fit, otherwise the event is rejected.

If a "good" point-fit is obtained, a set of direction cosines, (u_o, v_o, w_o), is determined for the event by calculating the weighted average of the unit vectors from the reconstructed starting point, (x_o, y_o, z_o, t_o), to the hit PMTs used in the reconstruction. The weight factor used for each PMT is the number of detected photoelectrons.

All further analysis is based on the successful event reconstruction and the information derived from it:

- (x_o, y_o, z_o, t_o), *the reconstructed starting point.*
- (u_o, v_o, w_o), the reconstructed starting direction cosines.
- the total number of PMTs used in the best fit.
- the total number of photoelectrons derived from the final fit.

12.2 Geometry Optimization

The detector geometry is discussed in section 3.1. This geometry was arrived at after an optimization technique that is described here. In the simple configuration that the neutrino source is a point and no shielding is required, the optimum shape of the detecting surface is a sphere. The counting rate is proportional to the radius of the sphere, and the area to be covered by photocathodes depends on the square of this radius. In the real world, the neutrino source needs to be shielded and construction costs are minimized by making the detector geometry cylindrical. In addition, the forward direction is more difficult to shield and decay-in-flight neutrinos are more uncertain. These are the reasons that the asymmetric cylindrical geometry shown in Fig. 12.3 is proposed, avoiding the region within about 71° of the forward beam direction.

The cylindrical annulus is bounded on the inside by the neutron shield; the radius of this shield is determined by background considerations described in chapter 7. It is expected that this radius is now very close to the final value, but before a final determination is made some calibrating measurements will be necessary. Outside the shield surface is space for the phototubes, and then a sensitive volume the radius of which is a parameter that is used in the optimization. Outside the sensitive volume is a veto region of 1.5m thickness. This veto region is also at the top of the tank so that the height of the sensitive volume allows for space for phototubes at the bottom of the tank and a veto region at the top. The sensitive volume is a cylindrical annulus subject to these constraints. The radius of the annulus and the height are variables that must be optimized for maximal counting rate for a given area of photocathode coverage.

The geometry factor is defined by the integral

$$G = \int dV/4\pi r^2 \ ,$$

where r is the distance from the target. The geometry factor is numerically equal to the radius of the sphere described in the first paragraph of this section. The goal of the experiment is to achieve a geometry factor of 2.9m to ensure adequate counting rate. In Fig. 12.4 is shown the relation between the radius of the annulus and the geometry factor for a fixed area of photocathode coverage. About 2870m^2 sensitive area gives a geometry factor of 2.91m for a fiducial radius of 6m and a fiducial height of 12.0m.

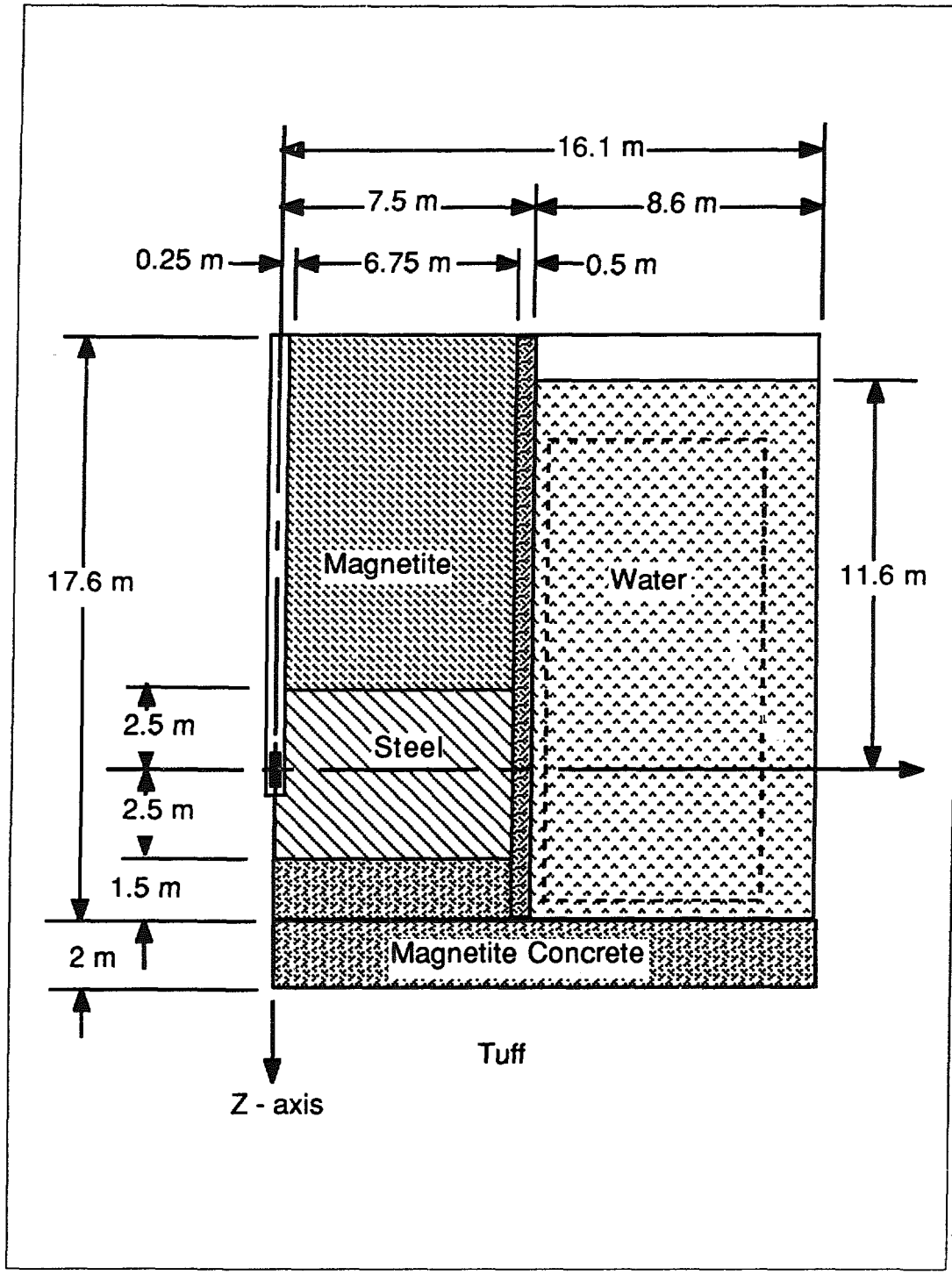

Fig. 12.3. The asymmetric cylindrical geometry. The sensitive volume is inside the dashed line, while the veto region is outside.

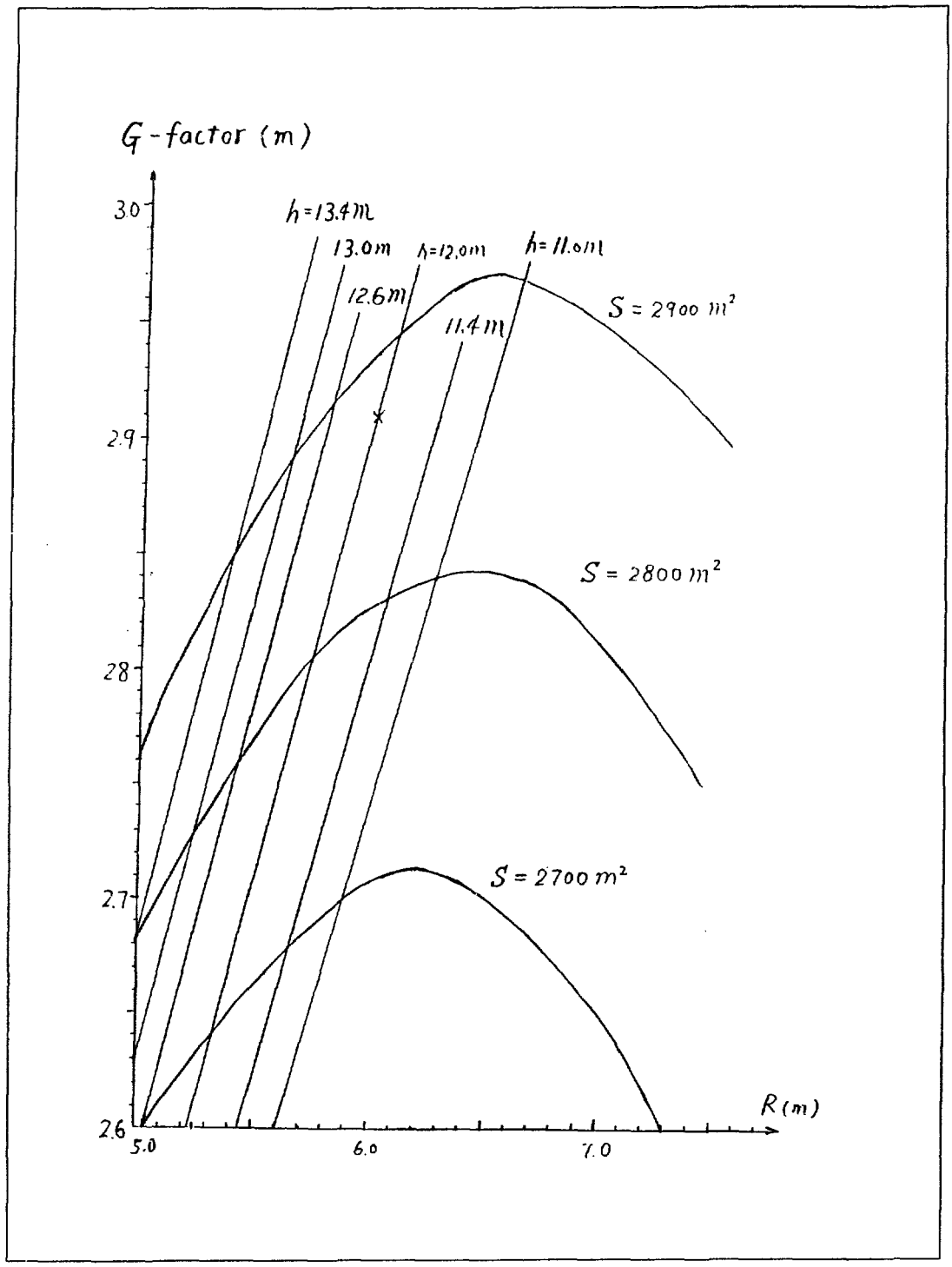

Fig. 12.4. The relation between the radius of the annulus and the geometry factor for a fixed area of photocathode coverage. S, h, and R are the fiducial area, height, and radius, respectively.

12.3 Detector Efficiency

The resolution and performance of the detector has been studied by the Monte Carlo simulation of the apparatus with 14,000 phototubes. Almost 50,000 neutrino-electron-elastic scattering events and 150,000 neutrino-oxygen events, corresponding to the number and composition we expect to observe, have been generated and reconstructed in the sensitive region of the detector. The sensitive region of the detector is the volume of water defined by the phototube surfaces. The Monte Carlo simulation of the neutrino-electron-elastic scattering has the electron-energy spectra of Figures 6.4–6.6. There is also a fiducial region that has 75% of the volume of the sensitive region and is 80cm inside the sensitive region except along the inner cylinder. An active veto region is outside and optically isolated from the sensitive region. Figures 12.5, 12.6 show the number of hit phototubes and photoelectrons after event reconstruction. The present event fitter[2] requires at least eight hit phototubes, and approximately 82% of the neutrino-electron-elastic events have more than eight hits and are successfully fit. Figures 12.7, 12.8 give the reconstruction efficiency as a function of electron energy and radius from the beam axis. After reconstruction, events are required to have at least 20-hit phototubes, a reconstructed energy of at least 10 MeV (or at least 27 photoelectrons), and a reconstructed position within the fiducial volume of the apparatus. Figures 12.9, 12.10 show the number of hit phototubes and photoelectrons after these cuts. The average number of phototubes and photoelectrons are 54 and 65, respectively. About 50% of all events thrown in the sensitive volume have successful fits inside the fiducial region and survive the cuts. Figures 12.11, 12.12 give the total event efficiency as a function of electron energy and radius from the beam axis. Note that the total efficiency is 80% above energies of 20 MeV (due mostly to the fiducial volume cut), and the efficiency is roughly flat with radius except near the inner radius of the detector on account of the fiducial volume cut, and at the outer radius because of the requirement of eight hit tubes.

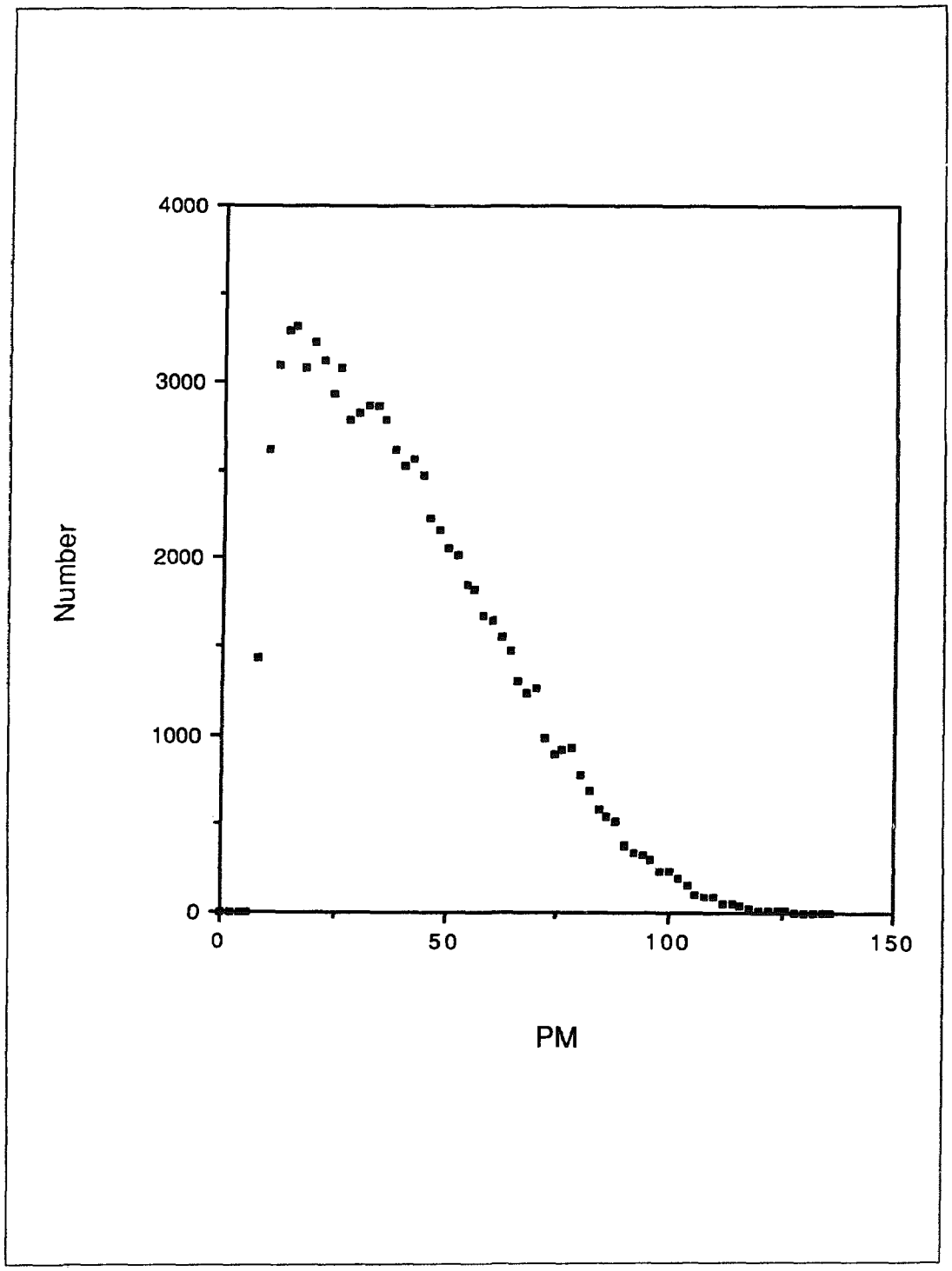

Fig. 12.5. Raw number of hit phototubes after event reconstruction. The fitter requires a minimum of eight hit tubes.

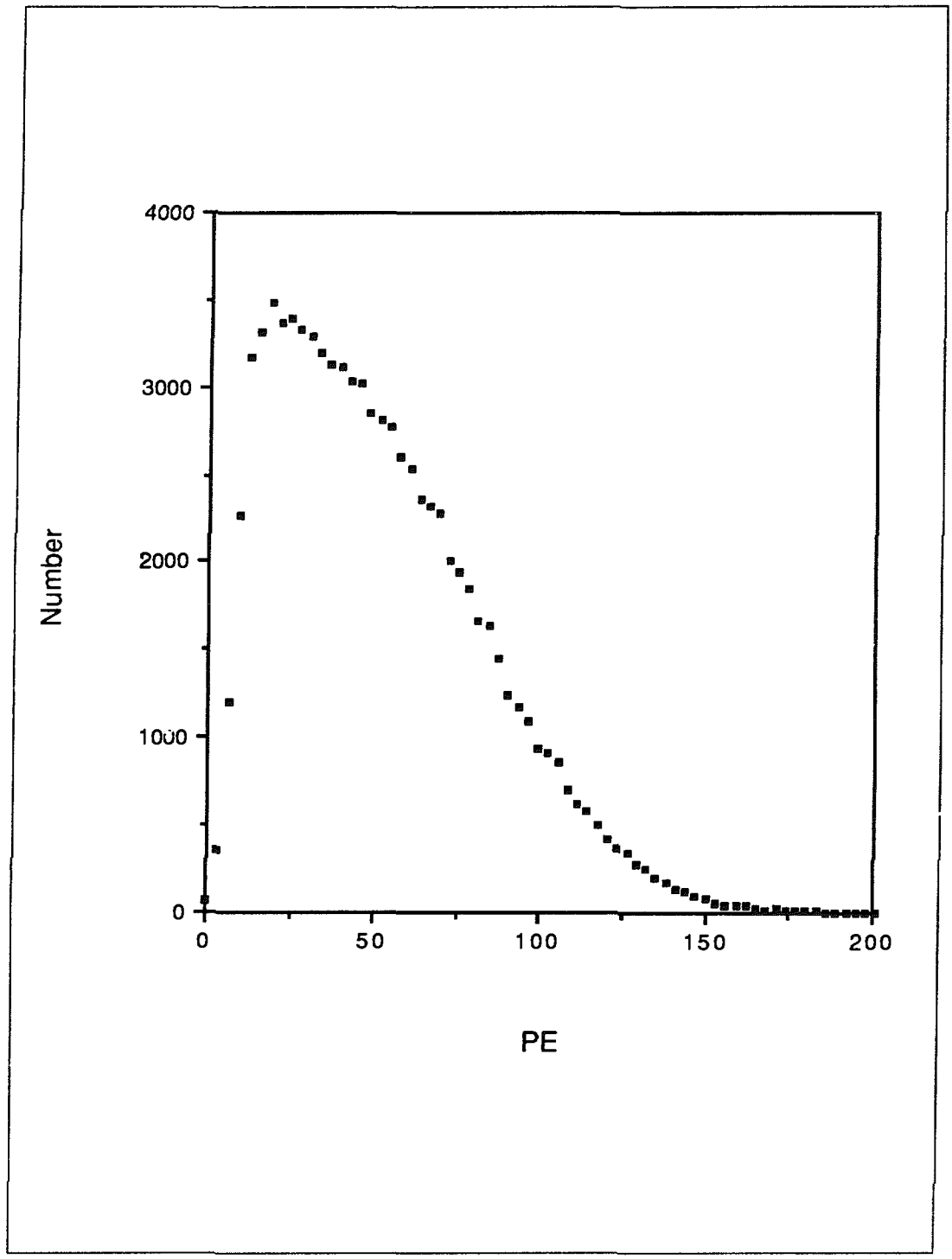

Fig. 12.6. Raw number of photoelectrons in the fit after event reconstruction.

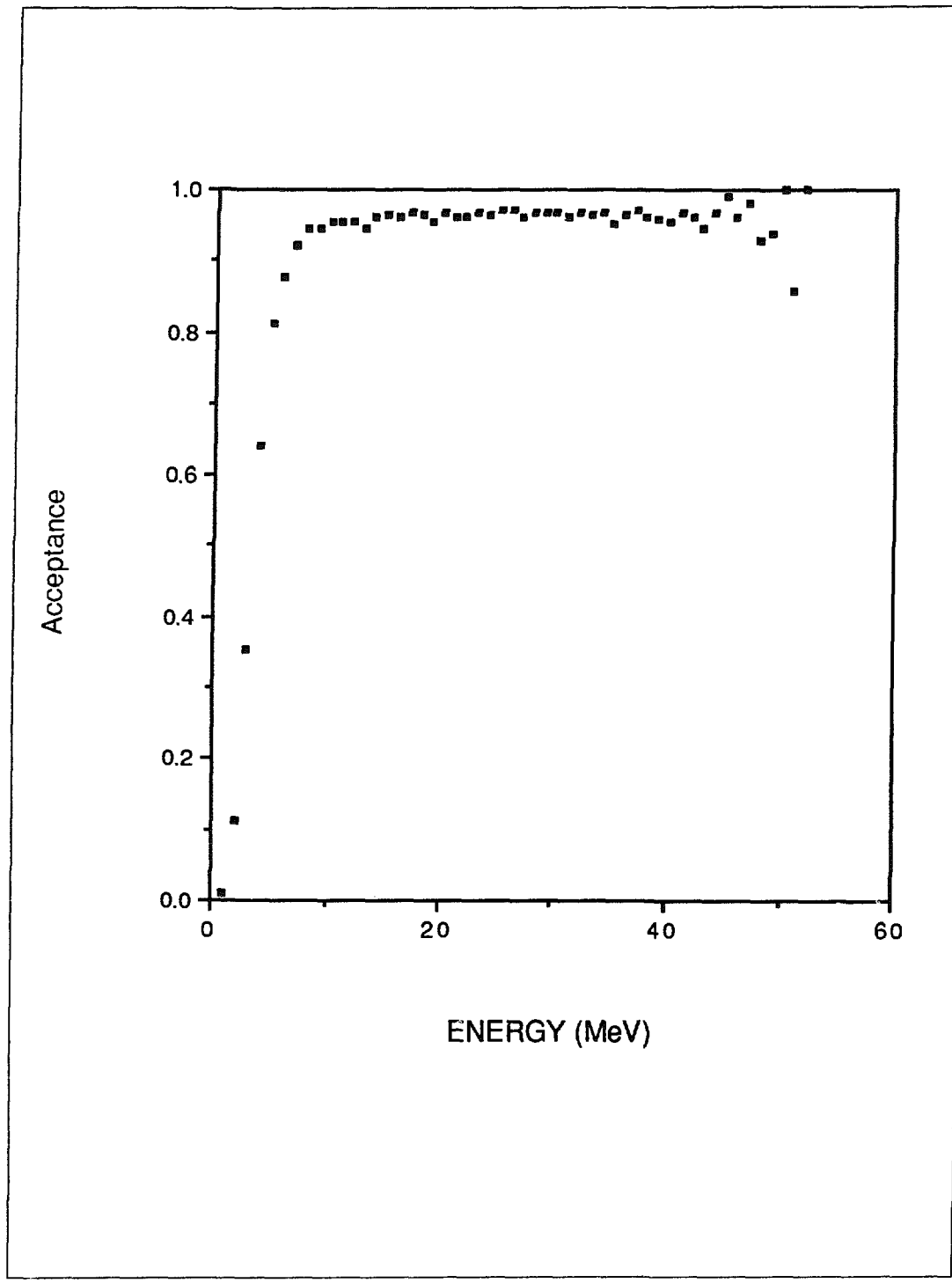

Fig. 12.7. Reconstruction efficiency as a function of electron energy.

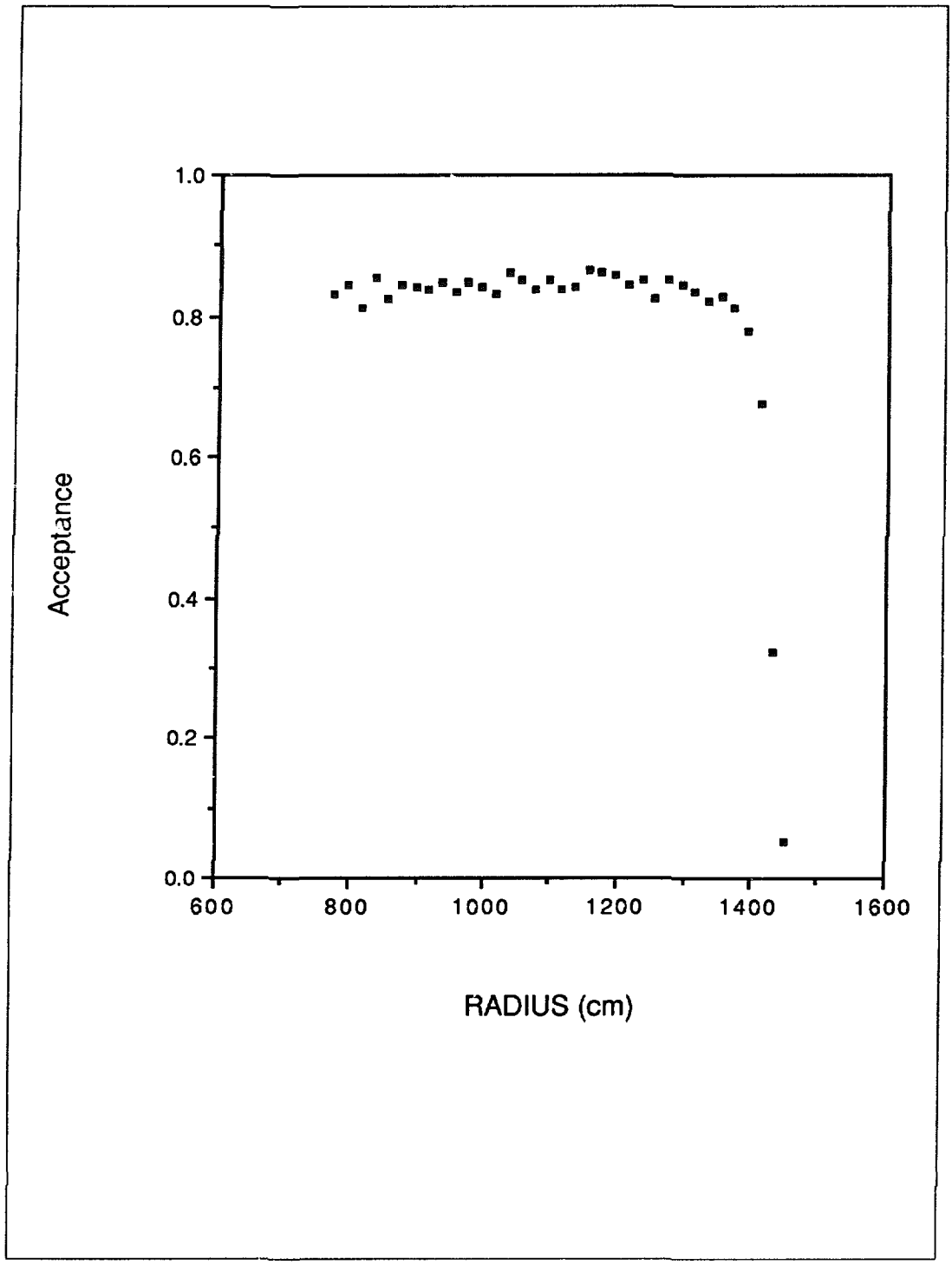

Fig. 12.8. Reconstruction efficiency as a function of event radius.

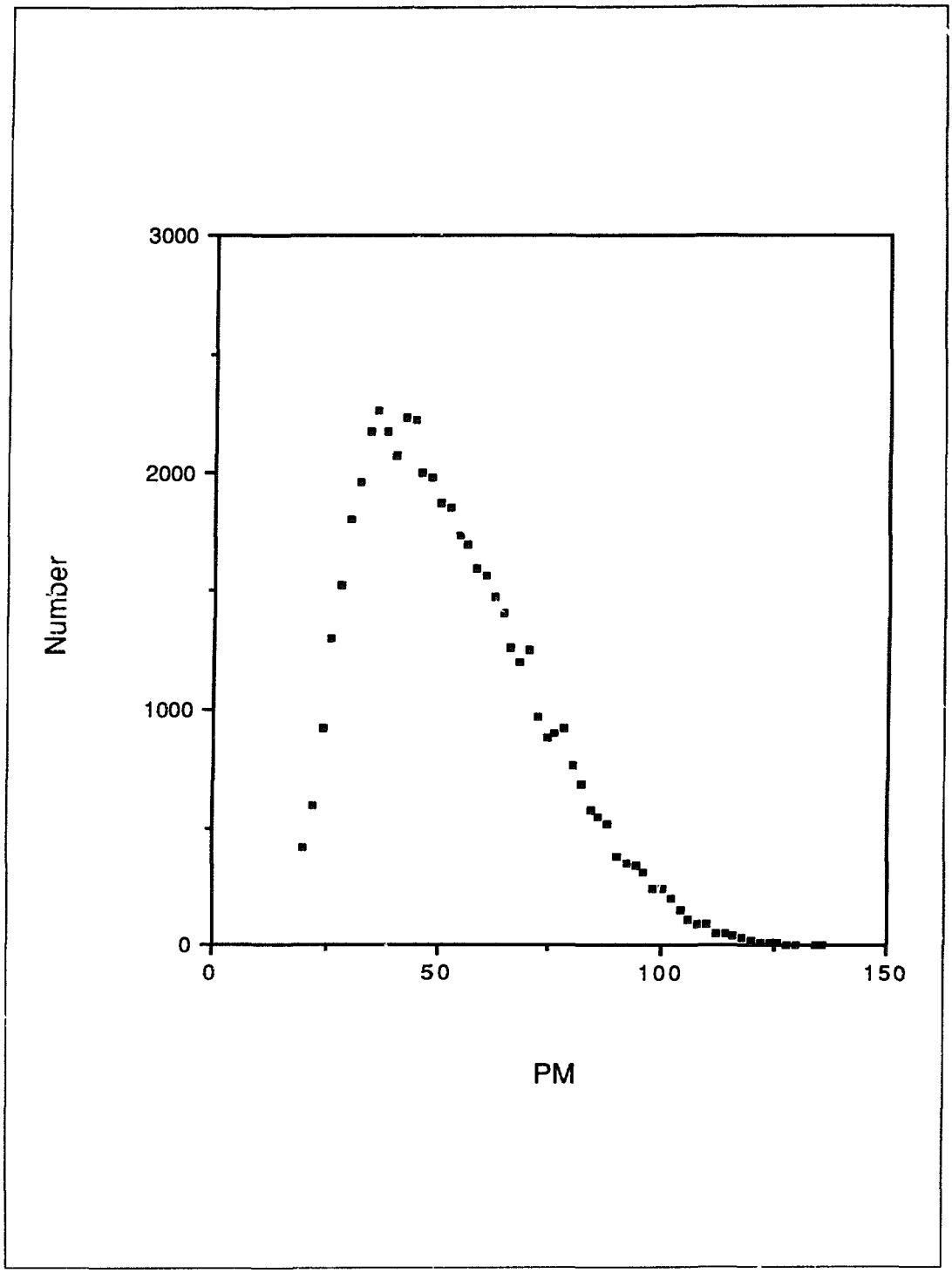

Fig. 12.9. Raw number of hit phototubes after all applied cuts.

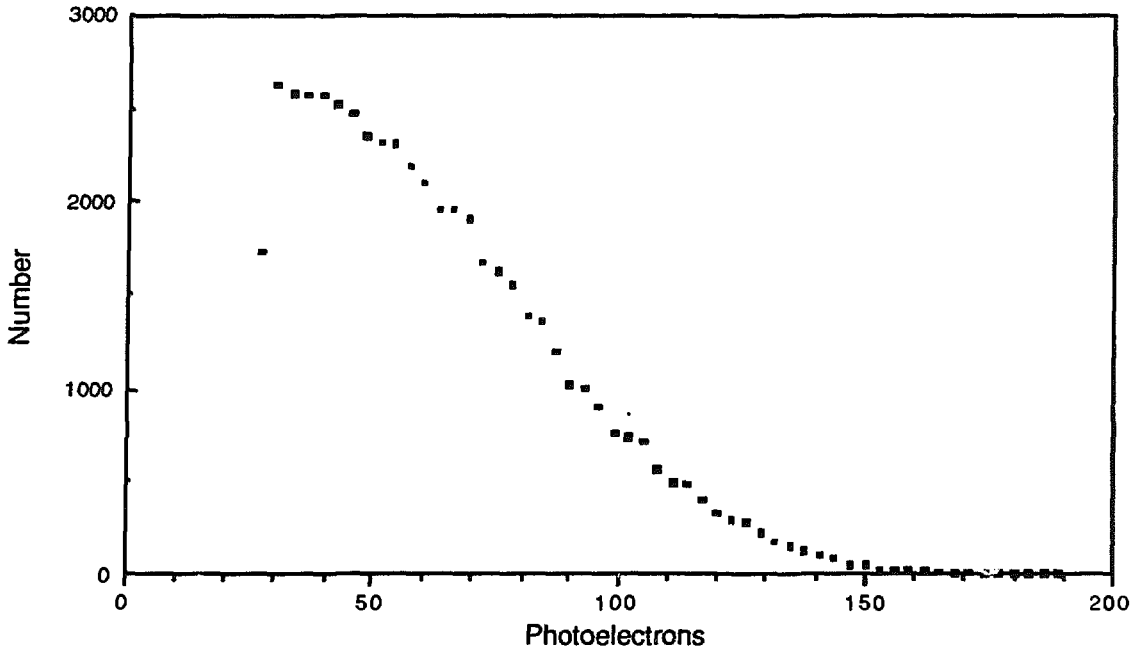

Fig. 12.10. Number of photoelectrons after all applied cuts.

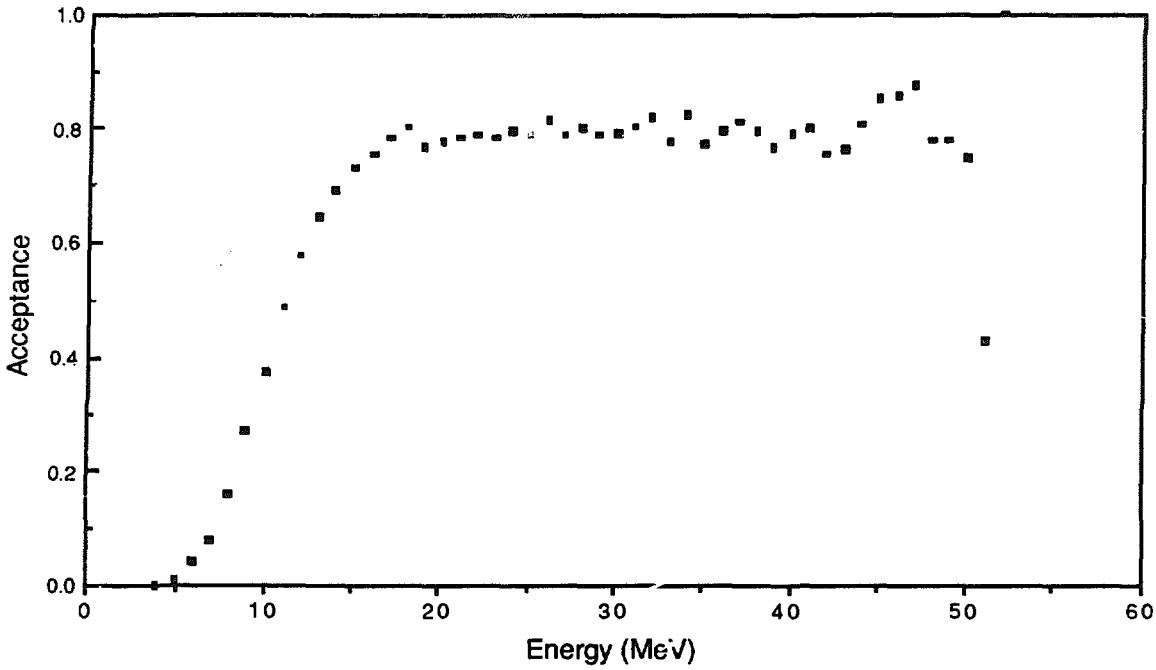

Fig. 12.11. Total efficiency as a function of electron energy.

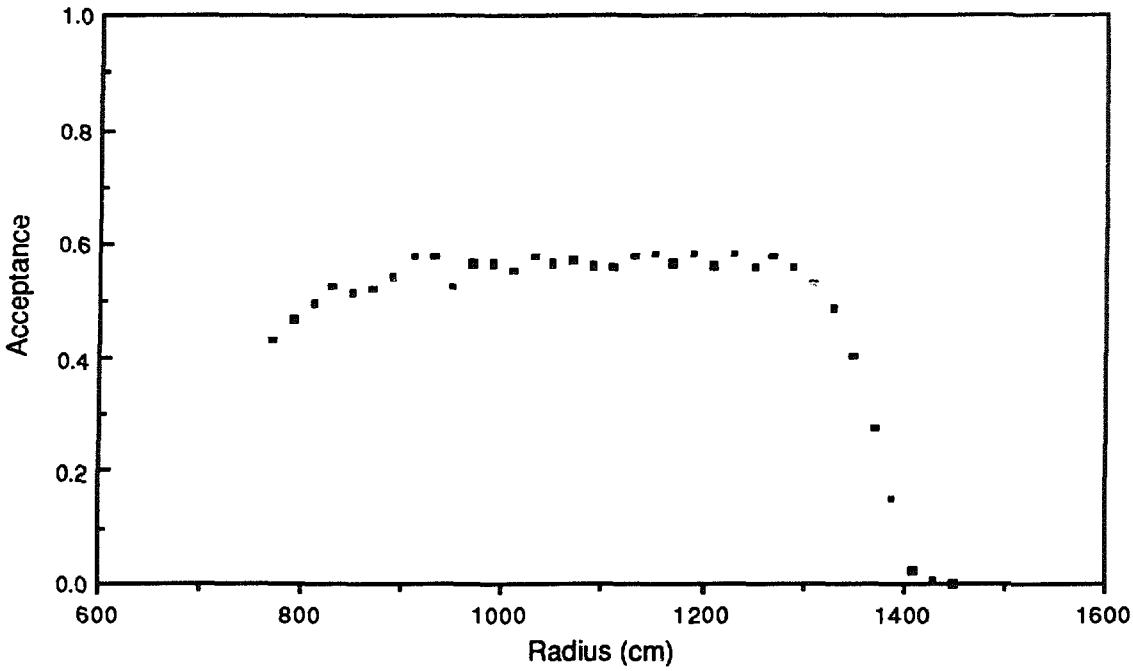

Fig. 12.12. Total efficiency as a function of event radius.

12.4 Detector Resolution

The time and energy resolutions for νe scatters are shown in Figs. 12.13 and 12.14, and the angle and position average errors are shown in Figs. 12.15 and 12.16. Each figure is a histogram of the difference between the reconstructed and generated quantity. Figures 12.15b,c also show the generated and reconstructed angular distributions for neutrino-electron scattering. Note that the average reconstructed angle is approximately the sum of the average generated angle and the average angular error. The time resolution (at the target) is about 0.5ns, which is due primarily to the 2.5-ns time jitter (FWHM) of each phototube and the fitting procedure. The average energy resolution of approximately 20% has contributions from both photon statistics and the reconstruction process because during fitting it is not always clear which phototubes are associated with the event and which phototubes are extraneous. Note that the average number of phototubes and photoelectrons discussed above impose a 0.15ns limit on the time resolution and a 12.4% limit on the energy resolution from statistical considerations. The angular and position average errors are 13^o and 40cm, respectively, and the average reconstructed angle of 19^o is close to the limit imposed by multiple scattering of about 10^o. The present event fitter[2] uses only time information; we expect to improve the resolutions by making use also of pulse height and constraining the electron Čerenkov cone to 41^o. It is interesting to observe that the time resolution is so much better than one would expect from the position resolution; this is because of the closeness of the velocity of the neutrino to the velocity of light in water, a radial position error is largely compensated by the neutrino travel time.

12.5 Response to Oxygen Background

The resolutions for neutrino-oxygen interactions are somewhat worse than for neutrino-electron-elastic scattering. This is due in part to the flat angular distribution of electrons from neutrino-oxygen interactions and also to the slightly lower electron energy. From a study of more than 50,000 neutrino-oxygen events, the time resolution is 2.0ns, substantially worse than for neutrino-elastic scatters, while the position average error, angular average error, and energy resolution are 42cm, 15^o, and 22%, respectively. The reconstruction efficiency for oxygen events is 98%, while the total efficiency is 69%. These efficiencies are higher than for neutrino-electron events because there are few oxygen events with energies below 10 MeV. Figures 12.17 and 12.18 show the reconstruction and total efficiencies as functions of angle.

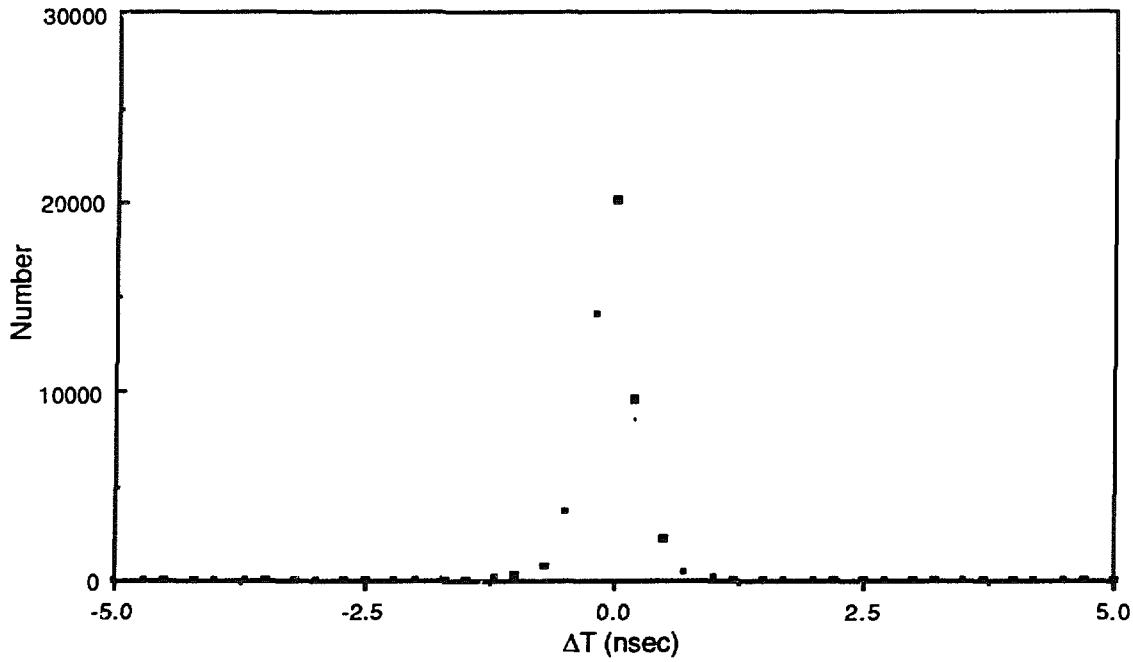

Fig. 12.13. Time resolution of the detector.

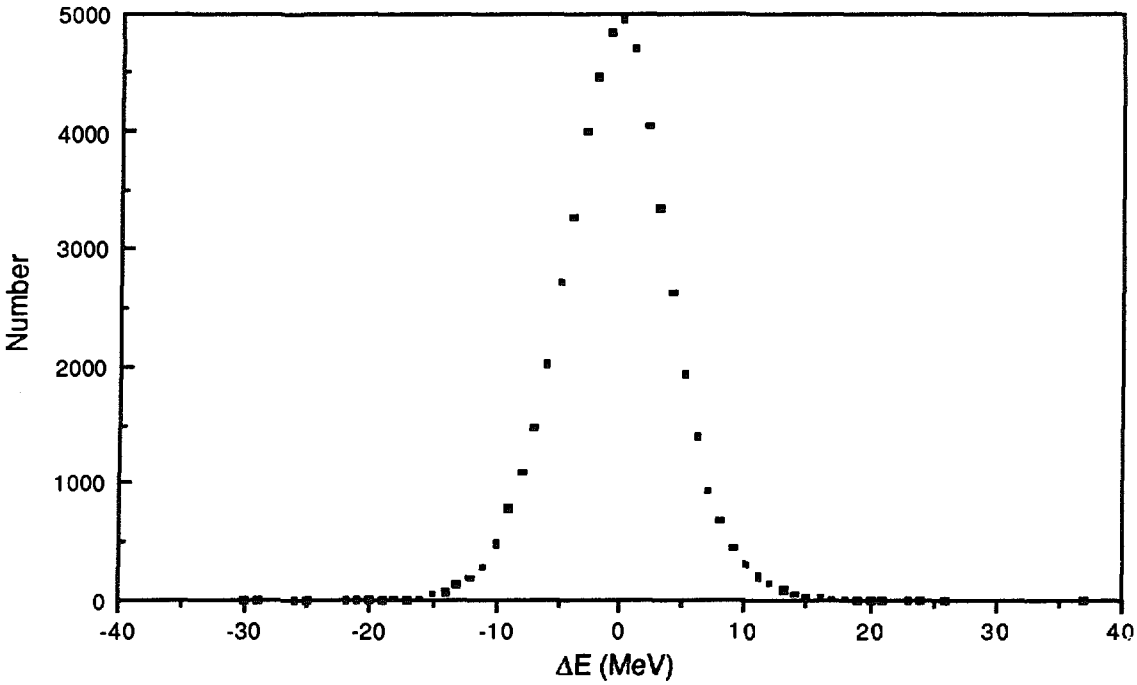

Fig. 12.14. Energy resolution of the detector.

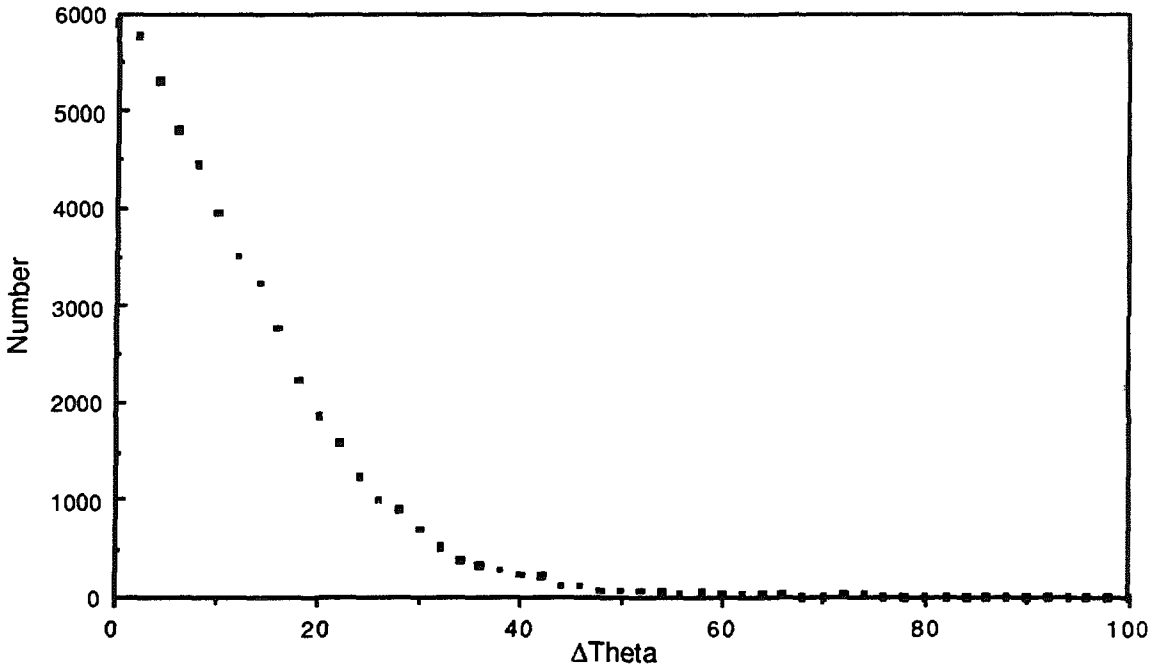

Fig. 12.15 (a). Angular resolution of the detector.

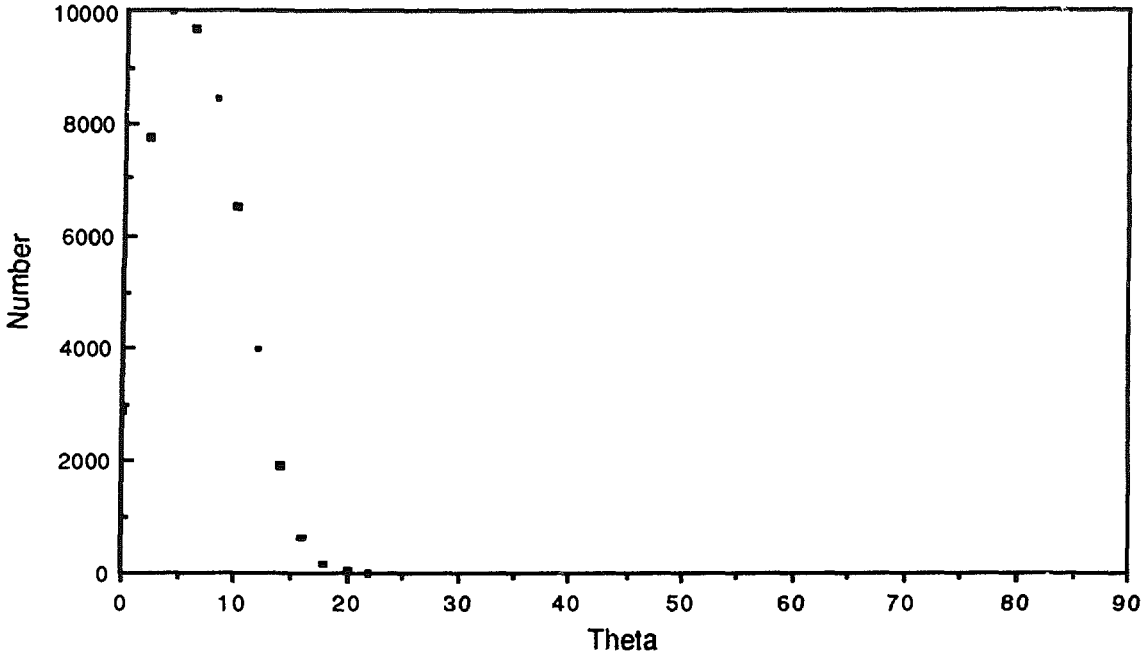

Fig. 12.15 (b). The generated angular distribution for neutrino-electron scattering.

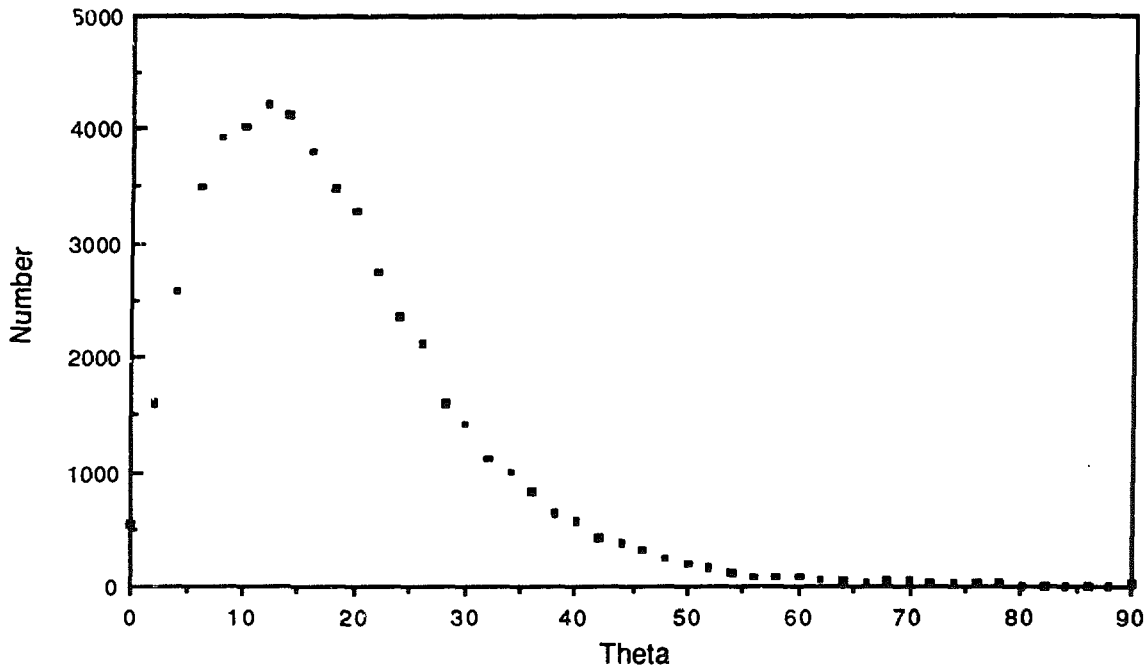

Fig. 12.15 (c). The reconstructed angular distribution for neutrino-electron scattering.

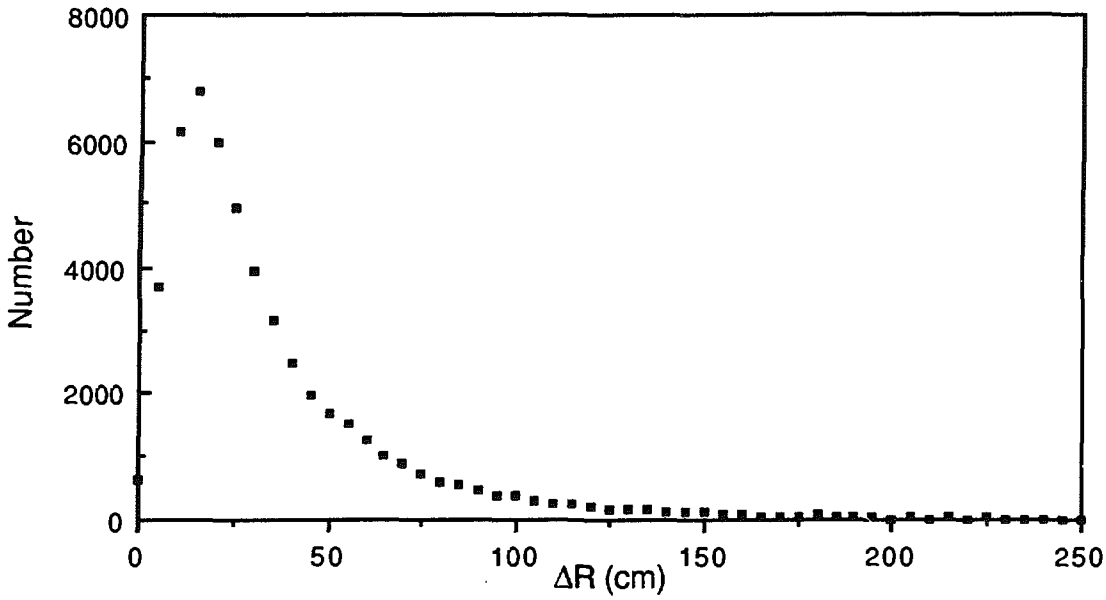

Fig. 12.16. Position resolution of the detector.

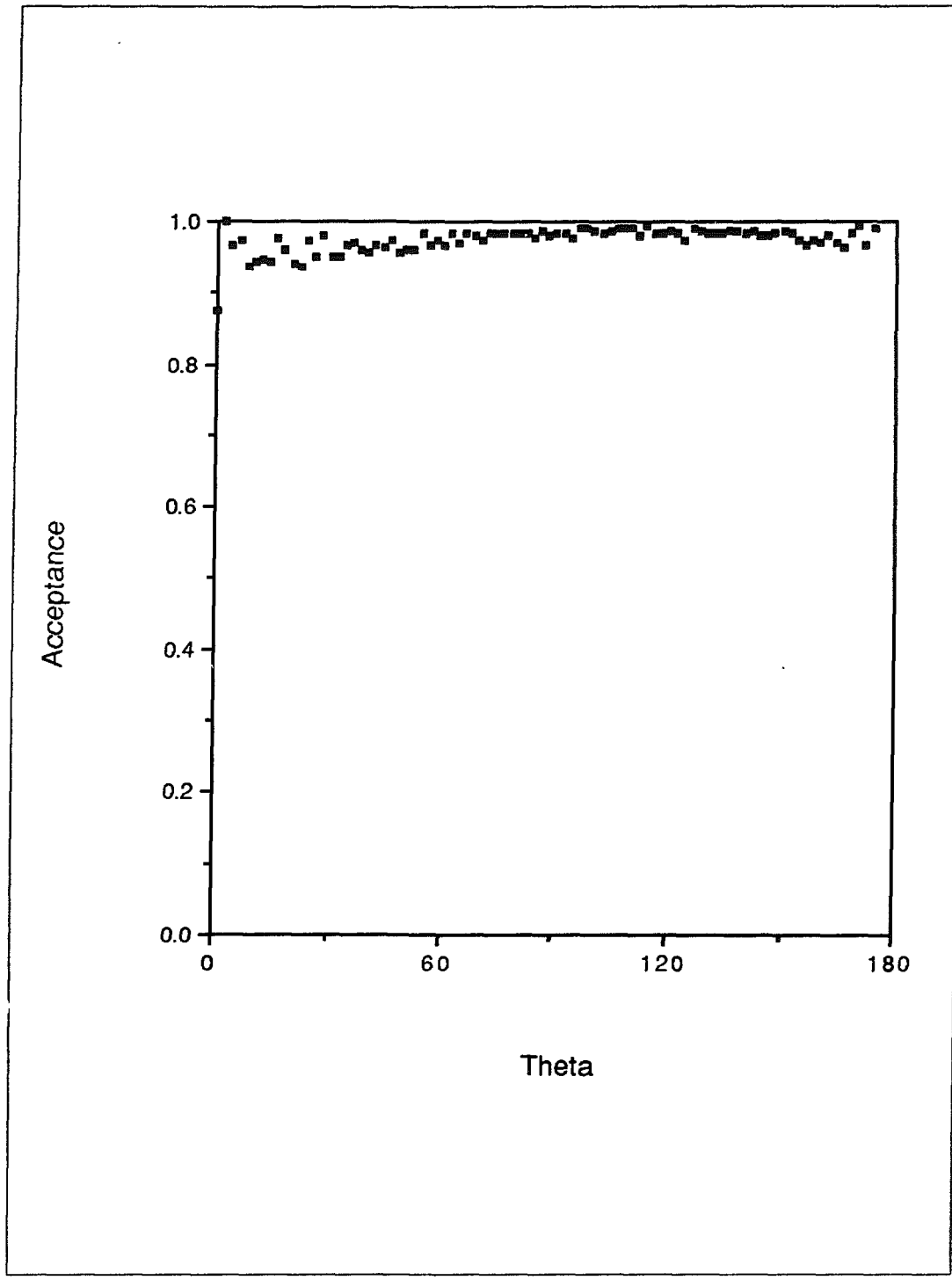

Fig. 12.17. Reconstruction efficiency as a function of angle.

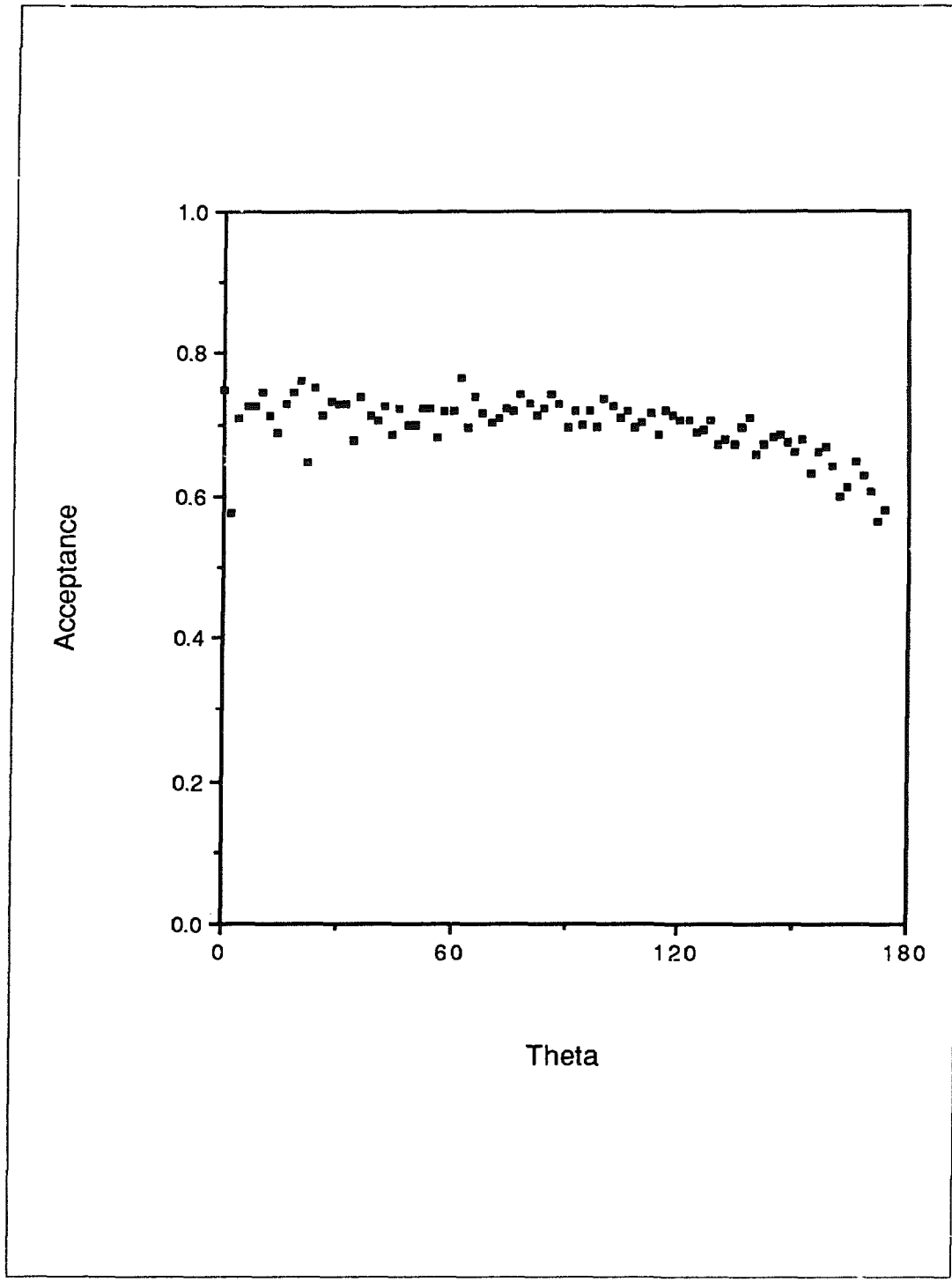

Fig. 12.18. Total efficiency as a function of angle.

12.c Resolution vs Energy and Radius

As shown in Table 12.1, the position average error, angular average error, and energy resolution all improve with energy for neutrino-electron-elastic scatters. Near 10 MeV the position average error is 39cm, the angular average error is about 13°, and the energy resolution is approximately 21%. At 50 MeV, however, the resolutions improve to 38cm, 12°, and 15%, respectively. There is also variation of the resolutions with position, as seen in Table 12.1. The angular average error improves from 15° near the inside radius to 11° near the outside radius. The position average error also improves from 46cm to 32cm, going from the inner to outer radius of the detector. There is only a slight variation of the energy resolution with radius: 20% near the inner radius and 21% near the outer radius.

Table 12.1 Variation of the resolutions with radius and energy.

R (m)	*dθ (degrees)*	*dr (cm)*	*dE/E (%)*
7.0-8.1	14.8	45.8	19.5
8.1-9.2	13.9	46.0	19.8
9.2-10.3	13.0	41.3	20.2
10.3-11.3	12.0	35.2	20.4
11.3-12.4	10.9	32.2	20.5
12.4-13.5	10.8	32.3	21.3
E (MeV)			
10-17	13.4	40.1	21.3
17-24	12.4	38.1	20.5
24-31	12.3	37.1	18.5
31-38	11.5	39.0	16.7
38-45	11.7	38.9	16.1
45-52	11.7	38.4	15.2

12.7 Counting Rate and Statistical Error

12.7.1 Expected Number of Events

The event rate of neutrino-electron-elastic scattering can be estimated by a numerical integration over the proposed geometry

$$\text{Rate} = \int dE_e \int dE_\nu \int dV \cdot N_e \cdot \frac{N_\nu \phi(E_\nu)}{4\pi r^2} \cdot \frac{d\sigma}{dE_e} \ ,$$

where N_e is the number of the target electrons per unit volume, N_ν is the rate of neutrinos produced in the beam stop, $\phi(E_\nu)$ is the normalized energy spectrum of neutrinos from the beam stop, and $d\sigma/dE_e$ is the cross section for monoenergetic neutrinos. Explicitly, we have

$$N_e = 3.33 \times 10^{29} \ \text{m}^{-3}$$

$$\begin{aligned} N_\nu &= (p \text{ rate on beam stop}) \times (^{\#}\pi \text{ produced per } p) \\ &= 2.25 \times 10^{22} \times (^{\#}\pi \text{ produced per } p)(\text{A} \cdot \text{h})^{-1}. \end{aligned}$$

For convenience, the above equation can be rewritten in a series of independent terms,

$$\text{Rate} = C \cdot (^{\#}\pi \text{ produced per } p) \cdot (\nu\text{-factor}) \cdot (\text{Geom-factor}) \ (\text{A} \cdot \text{h})^{-1} \ ,$$

where $C = 3.23 \times 10^3$ is a constant, the number of pions produced per proton is estimated to be 0.088, and

$$\text{Geom-factor} = \int \frac{dV}{4\pi r^2} \ (\text{meter})$$

$$\nu\text{-factor} = \int \int \frac{4m_e}{\sigma_0} \cdot \phi \cdot \frac{d\sigma}{dE_e} \cdot dE_\nu dE_e \ ,$$

where m_e is the mass of the electron and $\sigma_0 = 8.8 \times 10^{-45}$ cm^2. The Geom-factor is 3.58 m in the sensitive region and 2.91 in the fiducial region. The ν-factor, a product of the ν-e scattering cross section and the neutrino energy spectrum integrated over all available energy, is determined solely by the value of $\sin^2\theta_W$. In Table 12.2 below, we list the numbers of expected events based on an assumption of $\sin^2\theta_W = 0.23$ and a total beam exposure of 1.5 $A \cdot hr$. The stopped and prompt muon veto efficiency in the table was estimated in chapter 9. The acceptances due to various cuts are based on the Monte Carlo simulation. The photoelectron

threshold of 27 corresponds to an energy threshold of 10 MeV. (The percentage of events reconstructed in the fiducial volume is different for each neutrino species because a successful reconstruction requires at least 8 hit phototubes and therefore a minimum energy.)

Table 12.2 Expected number of events.

Events	$\nu_\mu e$	$\nu_e e$	$\bar{\nu}_\mu e$	*Total*
ν-factor	10.70	69.10	11.43	91.23
Generated in sensitive region	16 332	105 476	17 447	139 255
Reconstructed in fiducial region	10 450 (64.0%)	71 265 (67.6%)	11 441 (65.6%)	93 156
Stopped & prompt anti-efficiency	10 168 (97.3%)	69 341 (97.3%)	11 132 (97.3%)	90 641
$P.E. \geq 27$	7 524 (74.0%)	54 571 (78.7%)	8 505 (76.4%)	70 600
$\cos\theta > 0.76$	7 035 (93.5%)	51 570 (94.5%)	7 986 (93.9%)	66 591

As shown in the table, the total number of expected events above a 10-MeV threshold is 70 928. When the proton beam current is 100μA, 625 days of data taking are needed to obtain 1.5A-h. We therefore expect 113 total events per day and 12.0$\nu_\mu e$ events per day.

In the following section, we will estimate the statistical error of the ratio

$$R = \frac{\nu_\mu e \text{ events}}{(\nu_e e + \bar{\nu}_\mu e) \text{ events}}$$

based on these numbers of events. These numbers and the value of the ratio R are directly related to the value of $\sin^2\theta_W$. A 2.08% measurement uncertainty in R will cause a 1% uncertainty in $\sin^2\theta_W$ for $\sin^2\theta_W \sim 0.23$.

12.7.2 Statistical Error

The difference in decay rates of pions and muons, and the short beam spill in the PSR make it possible to determine the ratio R based on the time distribution of the

observed ν-e events. The total neutrino time distribution from a triangular 270-ns beam spill is shown in Fig. 6.1. We can determine R by fitting the distribution using the least-χ^2 method.* To determine the statistical error, we assume that the shape of the beam spill and the distribution of events are well determined. Therefore, statistical error is the only source of error in this fitting. Using events with more than 27 photoelectrons, we found that the statistical error on R is $\pm 1.50\%$.

This statistical error is bigger than one might guess. In fact, a substantial contribution to this error comes from the overlapping of ν_μ and $\nu_e + \bar{\nu}_\mu$ events in the first 270ns. For a better understanding, we also studied the statistical error by separating the time distribution into two parts ($>$ 270ns and $<$ 270ns), and then determining R by solving an equation based on the observed events and proportions of ν_μ and ν_e ($\bar{\nu}_\mu$) in each part. The statistical error of R is found by error propagation of the square root of the observed events. It turns out that if we have accurate knowledge on proportions of different events in two time regions this method gives closely similar results as the χ^2 fit.

Because electron-energy spectra from different νe events vary, the energy distributions are helpful in separating events. Figs. 6.4-6.6 show the electron energy distributions of ν_μ-e, ν_e-e and $\bar{\nu}_\mu$-e events. The angular distribution is also useful, especially in background subtraction, as we shall discuss in the next section. Using a three-dimensional fit to time, energy, and angle, the statistical error is reduced to 1.44% ($\Delta R/R$).

12.7.3 Effect of the Background Subtraction

There are several different backgrounds in the ν-e scattering data sample. They can be categorized into three sources: background caused by cosmic rays, neutrinos and neutrons. By knowing their distributions in time (and/or energy, angle, position), we can subtract these backgrounds. Generally, this procedure induces a systematic error and increases the statistical error. The systematic error has been discussed elsewhere. In this section we shall estimate the increased statistical error due to this subtraction. This is done by assuming that within the resolution of the measurement a perfect knowledge of these distributions is known.

The background rate from cosmic rays was estimated to be about 1 event per day for $\cos\theta > 0.76$ and energy $E > 10$ MeV. This source is independent of the beam spill, and we assume that this background has a uniform distribution in time. We can verify that assumption experimentally by looking at the data taken before the beam spill. Using a time window of 10μs for analysis, the statistical error is determined by fitting. In Table 12.3 we list results with various background levels in units of events per day. We can see that the subtraction causes only a very minor increase, compared to the results in the last section. It is also useful to point

* A CERN Library routine MINUIT is used.

out that the systematic error induced by this subtraction is about 0.01% since we plan to subtract the background to about 1%.

Table 12.3

Cosmic background (per day)	$\frac{\Delta R}{R}$ (%)
1.0	1.50
3.7	1.51
10	1.52
30	1.55

The background from neutrino sources (nuclear interaction with O^{16}, O^{17}, O^{18}) was estimated to be 3.8 times the number of $\nu_e e$ events for $E > 10$ MeV and without a forward-angle cut. With the angle cut ($\cos\theta > 0.76$), the background is about 27% of the $\nu_e e$ events (24 per day).

The angular distribution of this background, in contrast to the neutrino scattering events, is peaked in the backward direction, which makes it separable from the signal. By fitting in three dimensions (time, energy and angle), we find the statistical error shown in the table below. The event numbers shown below are those with $\cos\theta > 0.76$. However, the fitting is performed for $0 \leq \cos\theta \leq 1$.

Table 12.4

Neutrino background (per day)	$\frac{\Delta R}{R}$ (%)
14	1.52
18	1.54
24	1.57

The background from neutrons includes two parts: a prompt component with a similar time distribution to $\nu_\mu e$ events (< 1 event per day in the forward direction) and a delayed component with a similar time distribution to $\nu_e e$ events (< 1 event

per day). The statistical error is estimated for different background levels. The number of events are for $E > 10$ MeV and $\cos\theta > 0.76$.

Table 12.5 Neutron background.

Prompt (per day)	*Delayed (per day)*	$\frac{\Delta R}{R}$ (%)
0.5	0.5	1.51
1	1	1.53
5	5	1.67
10	10	1.80
20	20	2.03
50	50	2.61

In the above fitting only the time distributions are used. If other information (energy, angle, position) is available, the error will be reduced. The increase in the statistical error is minor due to cosmic rays and neutrino background, and is also minor due to high-energy neutrons because the rates are less than about 1 per day. An overall background subtraction shows that the total statistical error will be about 1.60% in terms of $\Delta R/R$.

12.8 Systematic Errors

The energy and fiducial volume cuts discussed above can potentially lead to systematic errors in R and $\sin^2\theta_W$; due to uncertainty in the fiducial volume or the energy, the cuts may effect the numerator (ν_μ) differently from the denominator ($\nu_e + \bar{\nu}_\mu$). Fortunately, all of the $\nu - e$ interactions have the same position resolution and, therefore, the same fiducial volume acceptance of 80%. Thus, the fiducial volume cut should not introduce a systematic bias. However, the average energies and energy acceptances of the three different neutrino interactions are somewhat different. The numerator has an average energy (after cuts) of 20 MeV and an energy acceptance of 52%, while the denominator has an average energy of 24 MeV and an energy acceptance of 59%. Due to the differences in the electron-energy spectra, we must consider two types of systematic errors that are discussed below.

The first systematic error is due to the uncertainty in the energy calibration. We plan to calibrate the threshold to ± 1 photoelectron, which is an uncertainty of about 4% for a threshold of 10 MeV or 27 photoelectrons. The resulting systematic error in R is 0.4%.

The second systematic error is due to the non-uniformity of the total efficiency as a function of electron energy (see Fig. 12.11). We believe that we can correct this non-uniformity to 1%. Because the difference in acceptances between the numerator and denominator is approximately 10%, this leads to an additional systematic error of 0.1%.

12.9 Detector with Fewer Phototubes

Studies have also been done, as seen in Table 12.6, for a detector with a smaller coverage of 8 inch and 5 inch phototubes. For a detector with only 10000 phototubes in the sensitive region, a significant reduction in the number used in the above analysis, the resolutions and efficiencies are slightly worse than before. For neutrino-electron elastic scattering, the total acceptance decreases from 50% to 47%, largely due to the 20-hit phototube requirement, which we have maintained. The position and angular resolutions increase from 39cm to 41cm and from 12.6° to 13.3°, while the energy resolution worsens from 20% to 22%. The time resolution remains at approximately 0.5ns. The experiment, therefore, can still be done with this smaller number of tubes, although the systematic and statistical errors would be somewhat larger.

Table 12.6 Detector Performance with Fewer Phototubes.

Tubes	14K 8"	14K 8"	10K 8"	25K 5"	10K 5"
Coverage	16%	16%	12%	12%	5%
Timing	2.5 ns	5.0 ns	2.5 ns	5.0 ns	5.0 ns
Accep.	49.8%	49.4%	46.9%	43.4%	35.9%
$< PE >$	64.5	64.9	49.0	47.9	21.2
$< PM >$	53.6	53.5	41.0	43.2	19.5
$< DR >$	38.9cm	55.7cm	41.3cm	66.5cm	91.5cm
$< D\Theta >$	12.6°	13.5°	13.3°	16.1°	19.5°
DE/E	19.9%	19.9%	21.9%	25.9%	31.2%
DT	0.4ns	0.6ns	0.4ns	1.0ns	1.2ns

References

1. W. C. Haxton, *Neutrino Reactions on Oxygen and the Proposed LAMPF Measurement of the Weinberg Angle*, (1987).
2. R. C. Allen et al., " Monte Carlo Simulation of the Sudbury Neutrino Observatory Heavy Water Čerenkov Detector," UCI-Neutrino NO. 87-35, (September 1987).

13 PHOTOMULTIPLIER SELECTION AND TESTING

The technical requirements and testing procedures for 8-in.-diameter photomultipliers suitable for this experiment are described. Preliminary tests of Amperex, Burle, EMI, and Hamamatsu photomultipliers with different size photocathodes and electron multiplier structures indicate than an 8-in.-diameter design with excellent efficiency, charge resolution, and timing resolution at the single photoelectron level can be achieved at an attractive cost.

13.1 Photomultiplier Development and Testing

The photomultiplier tubes that detect the Čerenkov light are perhaps the most critical electronic devices in this experiment. They must have good time and charge resolution at the single-photoelectron level.

In the present design there are approximately 13 000 PMTs viewing the sensitive volume and lining the outside cylindrical wall, the central pillar, and the top and bottom surfaces. They must operate reliably underwater and have large photocathode areas and high quantum and photoelectron collection efficiencies. They must have excellent timing characteristics, good single-photoelectron response, low dark pulse rates, and they must be relatively inexpensive. (Quantitative values for these specifications are listed below.) The feasibility of using PMTs underwater for Čerenkov light detection has been well demonstrated by the IMB collaboration (using 5-in.-diameter EMI 9870 PMT and newer 8-in. designs) and the Kamioka collaboration (using a 20-in.-diameter Hamamatsu R1440).

The scale of the proposed experiment dictates that we consider several different PMT vendors. In our tests, described below, we have used PMTs from Amperex, Burle (formerly RCA), EMI, and Hamamatsu.

The last version of this proposal was based on the Kamioka proton-decay detector design using 20-in. Hamamatsu R1440 PMTs. The successful operation of that detector gave a proof in practice of the water-Čerenkov technique for the detection of low-energy electrons. It was from this detector that we extracted the photocathode design parameter of 20% coverage by area.

Subsequent events persuaded us that the option of using a smaller-diameter PMT would have advantages offsetting the increase in number of channels. These advantages are better timing resolution, more uniform distribution of photocathode area, and a larger choice of vendors, with the consequent reduction in price per tube.

It was also recognized that a relevant quantity for comparison was not just the photocathode area but the product of collection efficiency, quantum efficiency, and area, that is, the number of photoelectrons in an event. The experiment's Monte Carlo simulations have shown that improved timing resolution leads to a significant improvement in signal-to-noise and in the ability to identify and reject backgrounds.

Inquiries were made to the previously listed vendors. Interest was shown by Amperex, Burle, EMI, and Hamamatsu in producing a competitive 8-in.-diameter tube. Amperex had designed a 15-in.-diameter spherical tube that used a hybrid design of a 30-kV photodiode, a scintillator target, and a small-diameter PMT. Our concern for reliable operation underwater, without service, the high after-pulse probability, and the relatively high price of $4000 per tube removed it from further consideration. They have a design study underway for an 8-in. to 10-in. diameter tube. EMI is in the process of redesigning their 8-in. hemispherical tube, but they did not have prototypes available yet for testing. Their older designs are well understood, and so we did not need to include them in our tests.

A design study was undertaken for us by Burle. Their design is based on a scaleup to an 8-in.-diameter design of the RCA8854, a 5-in.-diameter, flat-faced, 14-stage PMT with a cesiated gallium phosphide first dynode (a quantacon).

Three designs are presented in their report based on the number of changes that would need to be made to the 8854 manufacturing techniques. These are

1. the simple enclosing of the 8854 electrode structure in an 8-in.-diameter cylinder,
2. a direct scaleup of the 8854 including the Einzel electrostatic lens, and
3. design of an 8-in. model with conical electrodes.

The electron trajectory simulations for the last design give transit time variations from the photocathode to the first dynode of 1.9-ns (FWHM), which was very encouraging.

The electron multiplier structure of this tube would be similar to the 8854, with its excellent single-photoelectron response (see ADC spectra below). This design of the electron multiplier contributes little to the timing variation, and the extremely high secondary-emission ratio of its first dynode provides a significant reduction in the noise pulse rate. (The first dynode surface is cesiated gallium phosphide; the other 13 dynode surfaces are conventional beryllium oxide.) The photocathode will be potassium-cesium-antimony (bialkali) on a Pyrex glass window (low-expansion borosilicate glass). The Pyrex window is the material of choice for resistance to optical damage by water, and with the bialkali photocathode a reasonable match to

the Čerenkov spectrum in water can be made. The Čerenkov spectrum is described in Sec. 13.2 below.

The 8854 and the 8-in. derivative are "flat-face" designs manufactured with a metal cylinder forming the body of the tube. Burle prefers this design over a hemispherical bulb because they feel that a "flat-face" design has broader utility and a larger market. To achieve isochronous photoelectron paths from the photocathode to the first dynode, they use a series of electrostatic lenses to shape the electric field. The result is a somewhat reduced collection efficiency near the edge of the photocathode, but this can be partially corrected for by adjusting the voltages on the focusing electrodes.

The metal cylinder provides a rigid support for the relatively heavy-lens electrodes and maintains alignment of the lens and multiplier assembly. In manufacture the lens-multiplier assembly is fabricated as one unit; the photocathode-glass faceplate, as a second unit. The two are then welded together and the tube is pumped down through a glass stem in the lead pin-out. This type of construction allows for greater control in the fabrication of the glass-metal seals and offers a simple way of mounting the large electrode structure inside.

The ends of the cylinders that make up the faceplate-photocathode and the lens-electrode structures can be flared out at a location along the tube body corresponding to a plane through the center of buoyancy. The weld then becomes a flange for supporting the tube. A cross-sectional diagram illustrating the fabrication is shown in Fig. 13.1. Although much work remains to be done, Burle thought that a tube could be designed and manufactured at a price we could afford.

The other PMTs under consideration have hemispherical photocathodes and relatively compact electrode structures. Their electron multiplier dynodes are typically made from copper beryllium with beryllium oxide surfaces. The different tubes have different multiplier configurations, resulting in rather different single-electron responses, charge resolutions, and timing resolutions. In particular, the Hamamatsu R1408 (an 8-in. tube) that we tested showed very high gain but poor timing and poor charge resolution at the single-photoelectron level (see test results below).

Tests were made on the Burle 8854, Hamamatsu R1440 (a 20-in.-diameter tube), Hamamatsu R1408, and an Amperex XP2232B. The XP2232B is a 2-in.-diameter tube that we used to verify our testing procedure, it is not a candidate for the water-Čerenkov detector.

The PMT under test was placed in a dark enclosure, put on high voltage (typically 2000V), and left in the dark for 24 hours. A green Hewlett-Packard light-emitting diode (peak intensity at approximately 500nm) driven by an avalanche-transistor pulse generator was coupled to the PMT through an optical fiber.

The green LED was selected to better match the photocathode spectral response, although at the expense of somewhat worse timing in the LED. (A new pulser system to drive the LED in the reversed-bias mode with subnanosecond pulses is under development and will be tested with the green LED and with a blue silicon carbide LED. This system should allow a much finer evaluation of the transit time variation. The present pulser-green LED has an intrinsic jitter of approximately 2ns, which must be subtracted in quadrature from the measured widths. We expect to reduce this to a negligible subnanosecond value with the reverse-bias pulser system.) Wratten filters (neutral density) were inserted between the fiber and the PMT to attenuate the light intensity. The LED drive pulse was not varied. The test setups are shown in Figs. 13.2 and 13.3.

The ratio of the number of times the LED is fired to the number of times the PMT triggers is defined as the occupancy factor and is a rough measure of photocathode efficiency times collection efficiency. We use it to set the intensity of the light at the PMT's photocathode to produce single photoelectrons. Typically, tests were run with an occupancy of from 1 to 7%. The test procedure was as follows:

1. Record single-photoelectron anode waveforms, measured with a Tektronix 7912AD digitizer, PMT voltage of 2000V. From this measurement, we determined the single-photoelectron (p.e.) pulse height and charge.

2. Dark pulse rate versus tube voltage (from 1500 to 2500V) at a 1/4 p.e. threshold or 5mV, whichever is greater. This is a simple scaling of the anode pulse rate as a function of voltage across the PMT.

3. Dark pulse ADC spectra at a 1/10 p.e. threshold or 5mV, whichever is greater.

4. Plateau rate measurement with LED pulser at the same threshold as in item 3. The plateau rate is a measurement of the occupation fraction, defined by requiring a coincidence between the LED and the PMT, so it is relatively immune to the noise rate. Tube voltage was varied from 1500 to 2500V. At end of this test, we reset the tube voltage to the setting determined in item 2.

5. ADC and TDC histograms for full photocathode illumination.

6. ADC and TDC histograms for 1-cm-diameter spot photocathode illumination (centered on tube axis).

7. ADC and TDC histograms for spot photocathode illumination across the tube face, that is, at 1- and 2-in. from tube center.

8. After-pulse rate (or probability) in a 5-μs interval. (We used a gated TDC to search for single-photoelectron pulses after an initial drive pulse. This test will be improved in sensitivity with the reverse-bias pulser system.)

Examples of items 1 through 7 for the Burle 8854 are shown in Figs. 13.4–13.8. An anode-pulse waveform from single-photoelectron events is shown in Fig. 13.4. A dark pulse rate as a function of voltage and the occupancy plateau is shown in Fig. 13.5(a) and (b), respectively. The presence of the single-photoelectron shoulder is easily seen in both these curves.

Operation of the PMT at 2000V (corresponding to a gain of 4×10^7) gives a noise pulse rate less than 1kHz. Figure 13.6 shows the ADC spectrum and a clean single-photoelectron peak. A TDC spectrum is shown in Fig. 13.7, which is, unfortunately, dominated by the width of the LED. The contribution by the LED to the width can be estimated from Fig. 13.8, a TDC spectrum from an XP2232B, which is a fast 2-in.-diameter PMT that contributes little to the timing variance.

The after-pulse-rate tests gave results at the fraction of a percent level and were dominated by pulser noise. They will be repeated with improved instrumentation and a larger dynamic range of initial light pulses, but this level is consistent with other measurements at the gains we are using.

Also being examined is the possibility of increasing the voltage between the photocathode and the first dynode to further reduce the transit-time variation. However, this increase in voltage also increases the probability of afterpulsing and changes the collection efficiency. The optimal operating voltage and taper will need to be determined after the PMT design is better established.

In addition to these tests, we have measured the recovery times to 1000 photoelectron pulses and find that, electrically, the tail of the pulse is dominated by a single exponential, which can be compensated for by either a cable clip or a pole-zero filter to cancel the dominant pole. This latter method is preferred in the pulse-shaping electronics. A more difficult problem is the fluorescence in the glass and photocathode. The low afterpulsing indicates that this is not a problem.

In conclusion, we think that it is possible to secure a photomultiplier that meets or exceeds the following specifications:

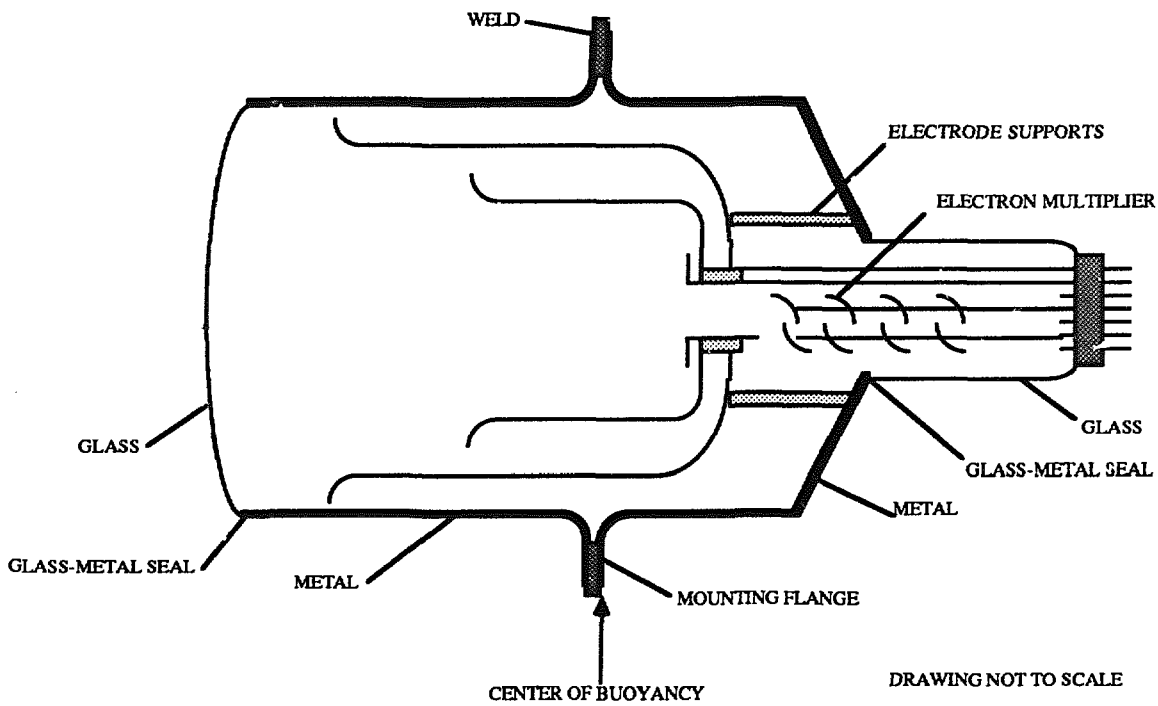

Fig. 13.1. Mechanical assembly of the proposed 8 in., flat-face photomultiplier.

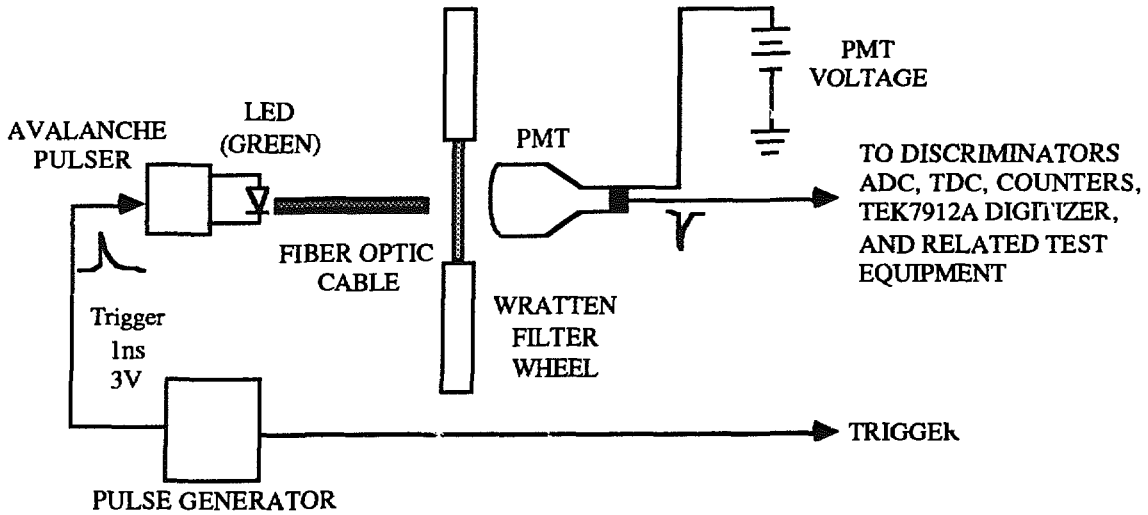

Fig. 13.2. Electro-optical set-up for photomultiplier tests. The LED is driven by a fixed pulse height pulse generator and the intensity at the photocathode is controlled by neutral density filters.

PMT "Plateau" Test Setup

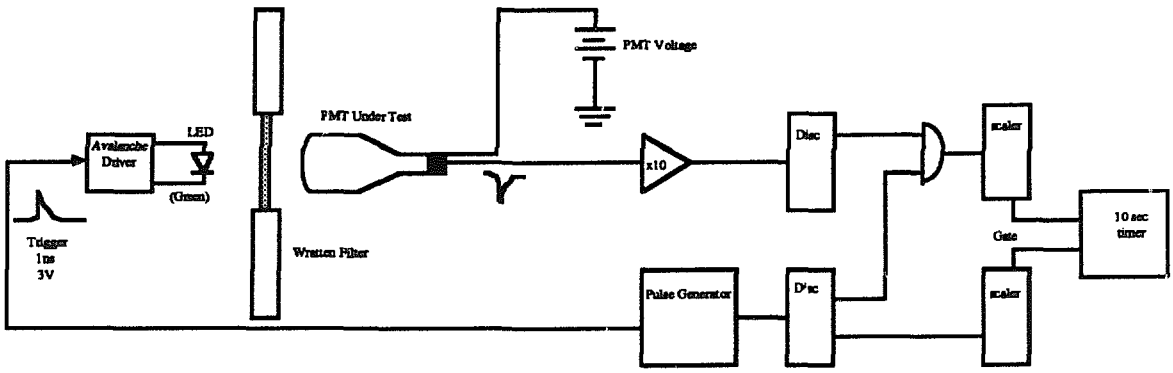

Fig. 13.3 (a). Test set up for "plateau" and dark count measurements.

PMT Timing and ADC Test Setup

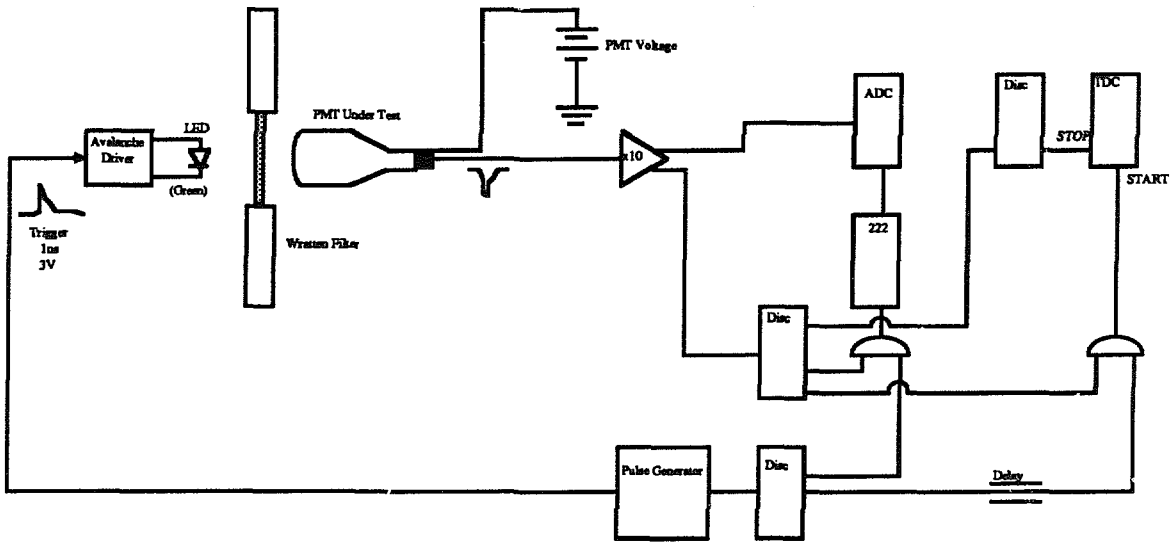

Fig. 13.3 (b). Test set up for timing and charge resolution measurements.

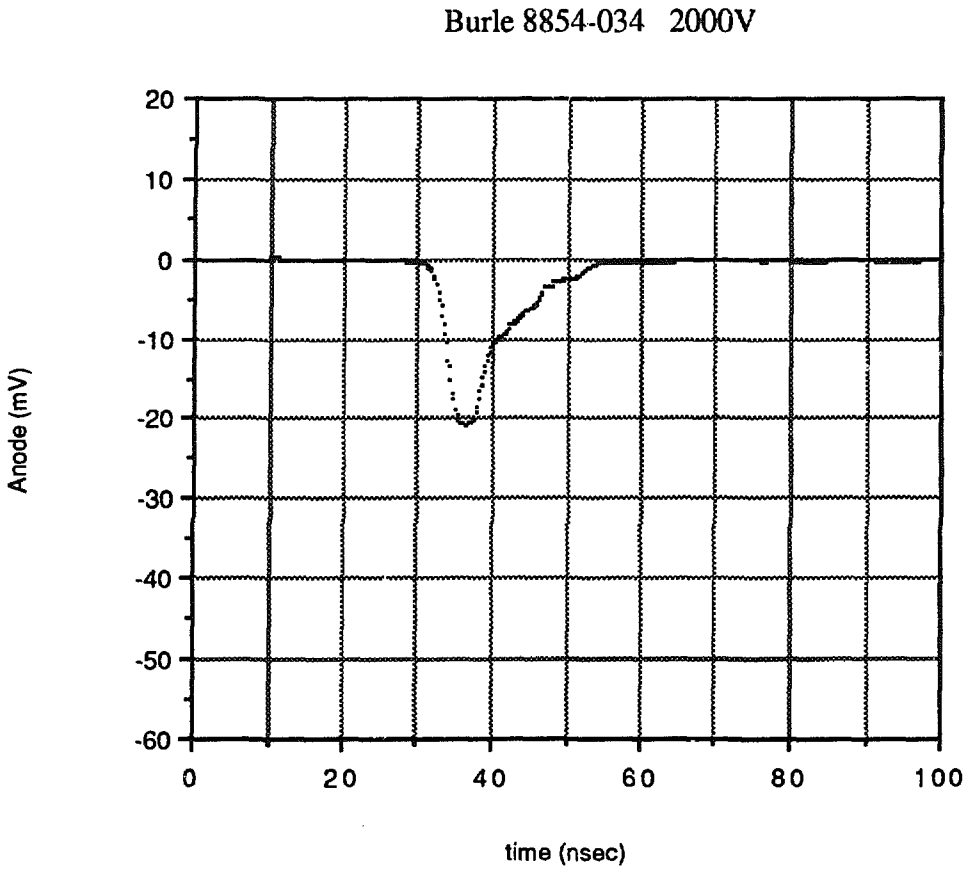

Fig. 13.4. Burle 8854 anode waveform for a single photoelectron from the photocathode. The cathode-anode voltage was 2000V. There is 3.77 pC of charge in this pulse.

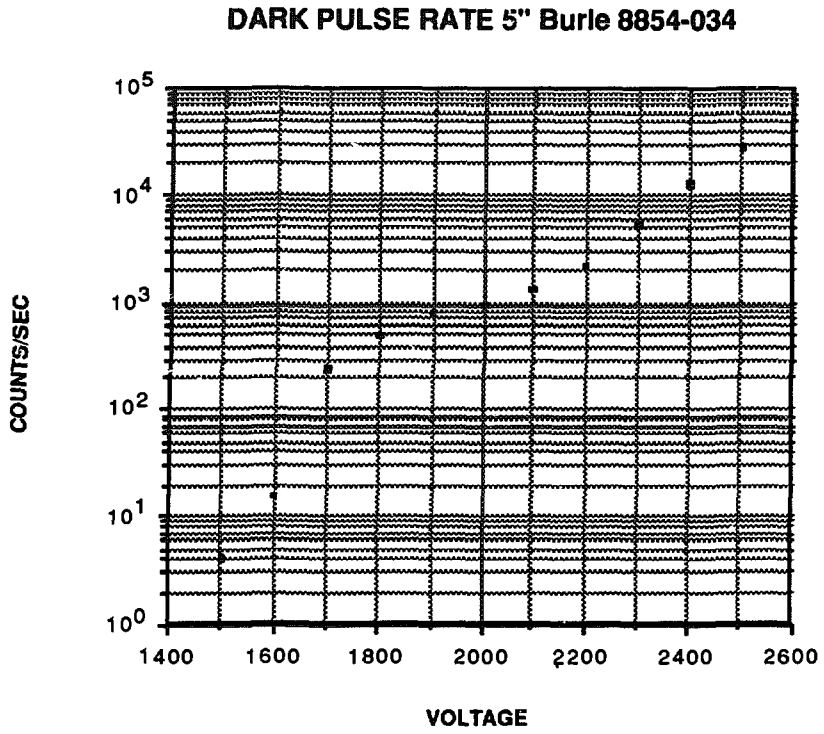

Fig. 13.5 (a). Dark pulse rate as a function of tube voltage.

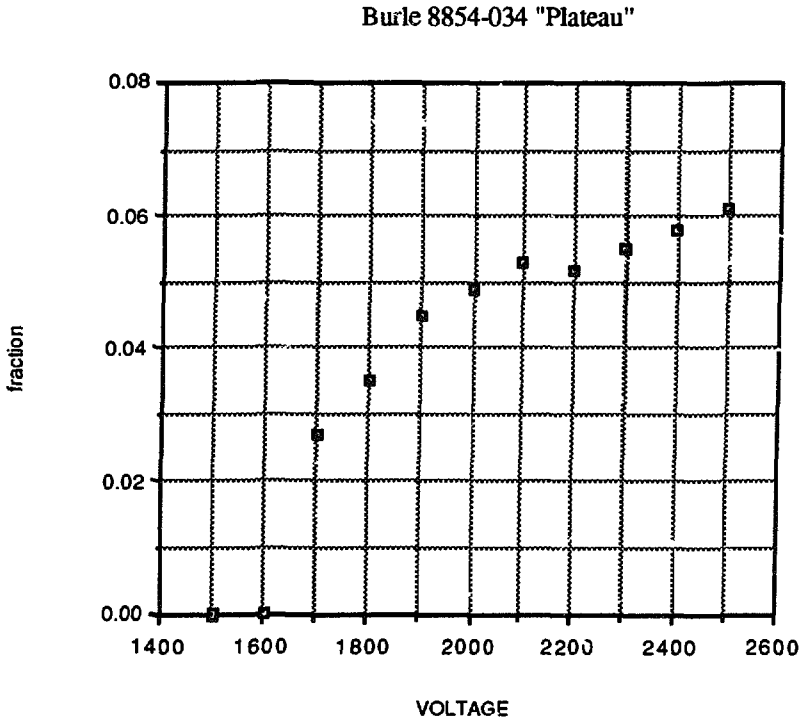

Fig. 13.5 (b). Occupancy plateau as a function of tube voltage.

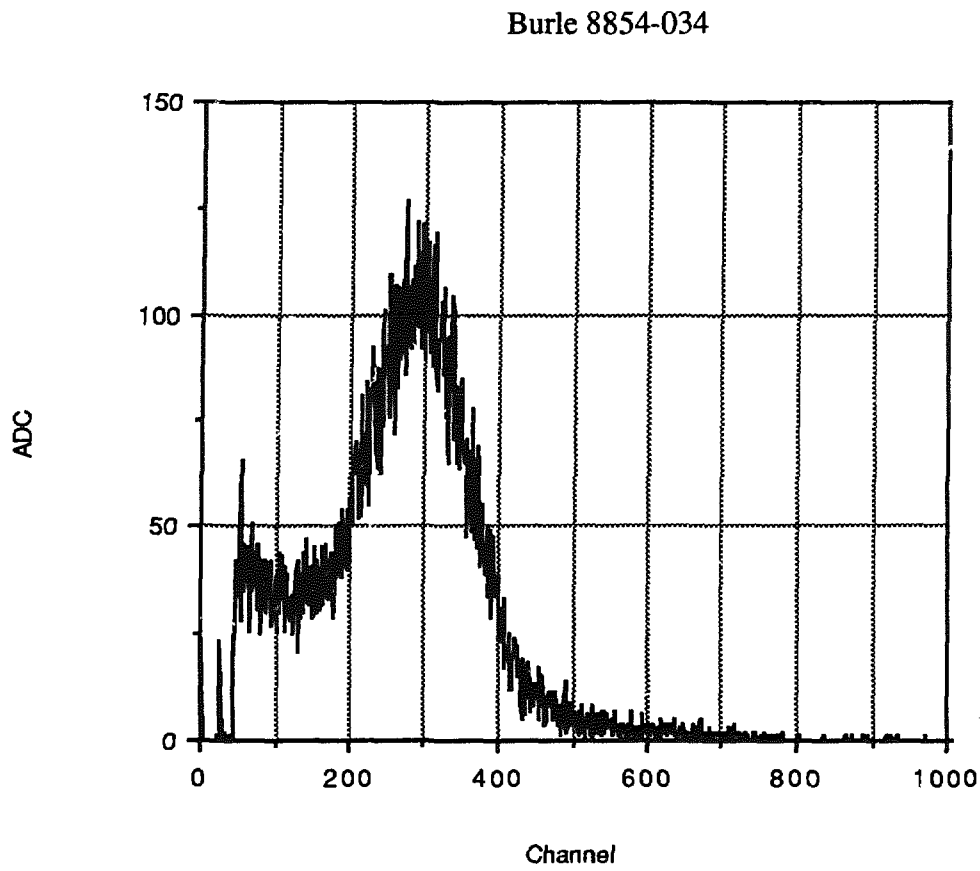

Fig. 13.6. A typical ADC spectrum at the single photoelectron level. The calibration factor is .25 pC / Channel.

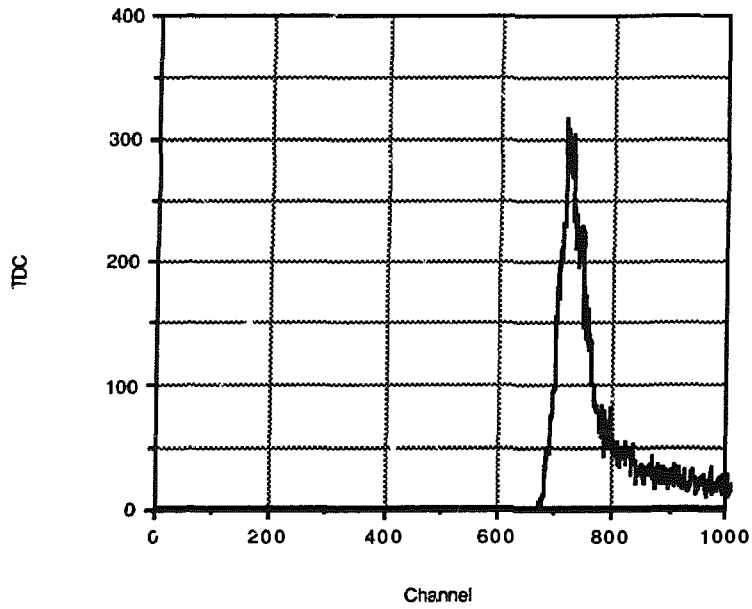

Fig. 13.7. A TDC spectrum. The width is dominated by the green LED light source and is not representative of the quality of the photomultiplier. The calibration is 100 psec / Channel.

XP 2232, 2200V, 5mV threshold

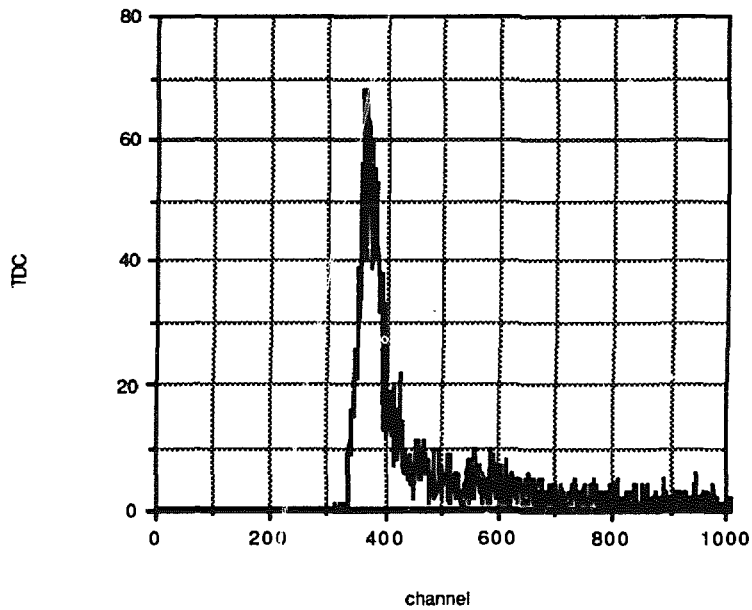

Fig. 13.8. A TDC spectrum for a fast, 2 in. diameter XP2232B photomultiplier. This histogram clearly illustrates the domination of the resolution by the green LED light source. The calibration is 100 psec / Channel.

1. Large photocathode area.
2. Time resolution of 2–3-ns (FWHM).
3. Good single-photoelectron resolution, for example, a single-photoelectron ADC spectrum with a peak-to-valley ratio of approximately 3, a single-photoelectron resolution of approximately 20%, and reasonable linearity to 2, 3, ... photoelectrons. The tube must also recover quickly after a large pulse and be sensitive at the single-photoelectron level within 100ns.
4. Dark pulse rates less than 1000 pulses per second at thresholds of 5mV and gains of 10^7.
5. Afterpulsing at the single-photoelectron level of less than 0.1% in a 1-μs-wide interval.
6. Quantum efficiencies of 27% at 400nm, and uniform collection efficiencies across the photocathode of nearly 100%.
7. The PMT must be as low in cost as possible.

The companies mentioned above have been very responsive, and we expect to work with all of them to bring a PMT with the above characteristics into existence.

13.2 Transmission of Čerenkov Spectrum in Pure Water

The measurements of the attenuation length of light in water have produced inconsistent results over the past several decades, especially at short wavelengths (300 - 400nm). Without making a critical evaluation of the various experiments, we have taken the results of the two most recent experiments[1,2] on the transmission of light in chemically pure water, assumed a path length of 10m, and folded this with the Čerenkov spectrum (for $v/c = 1$) to yield the expected number of photons transmitted per cm of particle path length per 20nm interval of wavelength.[2] This is shown in Fig. 13.9.

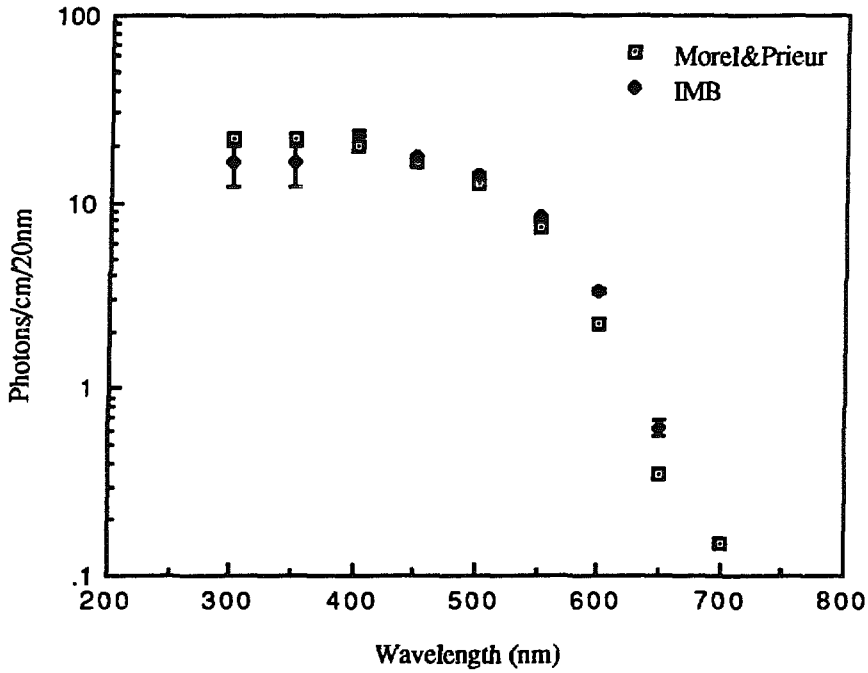

Fig. 13.9. Transmission of a Cherenkov spectrum through 10m of chemically pure water.

13.3 Methods of Extending Photocathode Area

There are two possible methods of extending the effective photocathode area: light-collecting funnels, or wavelength-shifting plates, as used by IMB.

Light-Collecting Funnels

Funnels have not been used in water detectors, because of the isotropy of light emitted by the sought-for events. In LCD, the recoil electrons are forward-peaked, and light is at the Čerenkov angle to the electron path, so that it is possible to consider enhancement of the collection efficiency for the forward-scattered electrons. Multiple scattering of the electron smears some of the correlation between the initial neutrino direction and the direction of the light, but significant correlation will remain, perhaps enough to make funnels useful.

The important parameter for light collection by an optical system is r sin(A), where r is the width in one dimension of a bundle of light rays, and A is the half-angle between the extreme rays. Strictly, this is to be calculated at a place where the angle of a ray is uncorrelated with its position. Another way of measuring the same quantity is the area occupied by the bundle on a plot of the sine of the angle of the rays to the optic axis versus the transverse position. This parameter cannot be decreased by optical devices, although it can be held constant or increased.

If the light falling on a phototube goes out to 90°, sin(A) is 1, so it is not possible to increase the effective radius. In LCD, if we assume for the moment that the recoil electrons are in the same direction as the neutrinos, and there is no multiple scattering, and we point the phototubes directly at the target, the maximum angle of incidence is the Čerenkov angle in water, or about 41°, with sin(A) = 0.669. An increase in radius of a factor of 1.5, and in area, a factor of two, is thus possible with these overly-simple assumptions.

In the real case, the angle between the electron and the radius vector to the interaction point is not zero; this angle is as large as 41°, implying an angle of incidence of up to 83° (the sine of 83° is 0.99), so apparently nothing would be gained by using a cone, and something may be lost if a funnel shadows the PMT face. However, while in this case the solid angle subtended by the PMT face is very small for light collected at this extreme angle, on the opposite side of the Čerenkov cone the angle of incidence is nearly normal, so a light-funnel would increase the light collected overall.

Practically, funnels could be made of molded plastic or of Alzac. For a complex shape, molded plastic would be necessary, with an aluminum coating; costs are expected to be small – on the order of $10 per funnel – but no detailed estimates have been made. Also, the phototube mountings must allow the tube axis to be

aligned with the target, which would complicate the mechanical structure. Studies of the effect of long-term immersion in water would need to be done.

There are other disadvantages to the use of funnels: reconstruction of the event will be more difficult if hits are not recorded over the full 'circle' of impact of the Čerenkov cone, and the reflective surface will return photons to the detector, where they might produce spurious triggers. These questions can only be resolved by putting funnels into the full Monte Carlo, and including the effect of the reflections. It's almost certainly true that funnels in the veto region will enhance collection efficiency.

Waveshifter Plates

Waveshifter plates are made of plastic (acrylic or polystyrene) with an organic phosphor, which absorbs in the short-wavelength region of the spectrum and emits at a longer wavelength. By using total internal reflection, fluorescent light can be piped to the PMT. The efficiency of internal reflection is about 50%; the fraction of light collected depends on the detailed geometry, but could be as high as 25% for photons striking close to the PMT. Thus a plate with the PMT centered in it could extend the effective area of the PMT. In IMB, a factor of 2 was obtained for plates on the order of two feet square, matched to a hemispherical PMT.[3] This shape of PMT is ideal, because little photocathode is obscured that would otherwise be useful. The factor of 2 is low partly because the spectrum of the fluorescent light is at longer wavelengths than the peak of the photocathode efficiency.

In LCD, this technique would not be as helpful as in IMB. We expect to use flat-face PMT's, so the plate would have to cover an appreciable area of photocathode that faces the detector volume, thus absorbing photons that would otherwise hit the photocathode directly. The fluorescence decay time would degrade our timing resolution significantly – typical decay times are 10ns. While the method is not promising, we will investigate whether there is a short-decay-time phosphor with good fluorescent properties; this could produce a modest increase in effective area.

References

1. A Morel and L. Prieur, *Linnology and Oceanography 22*, 709 (1971).
2. Proposal for a Nucleon Decay Detector; IMB Collaboration.
3. R. Claus et al., *Nuclear Instruments and Methods* **A261**, 540 (1987).

14 ELECTRONICS AND DATA READ OUT

The front-end electronics records the charge and time of occurrence of the phototube pulses and provides the detector triggers for various classes of events. The charge and time data are stored in analog form in an array of switched capacitors to buffer each input channel and achieve "deadtimeless" operation. The analog data are then converted to digital form and transferred to a node of an ACP-like microprocessor farm. The designs are realized in CMOS and bipolar application specific integrated circuits (ASICs) with a cost of less than $100 per channel.

14.1 Introduction

This detector, with over ten thousand identical elements, requires electronics exhibiting not only nearly deadtimeless behavior (to avoid misidentification) and excellent time resolution (to minimize fitting errors and thus maximize the fiducial volume and event rate), but also costs low enough to be manageable. The electronics design, in addition, must be matched to the design of the photomultiplier tubes (PMTs). This design assumes the use of an 8-in. PMT with the properties of the Burle Industries PMT.*

Thus the electronics/data-acquisition design goals are:

1. zero deadtime;
2. time resolution (and stability) somewhat better than the photomultiplier tubes—about 1ns, so that reconstruction accuracy is not limited by the electronics;
3. charge resolution of 0.1 photoelectron for small charges, going to 1 photoelectron for large pulse heights, i.e., 10^6 electrons per count at the bottom end rising to 10^7 electrons per count after about 50 counts (8 bits bilinear);
4. a trigger system sensitive to 10-MeV electrons; and
5. a cost for the entire electronics and data-acquisition system, from PMT pins to the input to the final computer, to be of the order of 20% of the cost of the photomultiplier tubes to balance properly costs versus photocathode coverage for the detector.

---

* NOTE: As measured on the prototype 8854 style tube:

1. Rise time less than 5ns;
2. Electron gain around 10^7;
3. Quantum efficiency around 25%; and
4. Time jitter/difference around 3-ns sigma.

From a technical point of view the design requirements for LCD electronics are very similar to the requirements for the KII detector, and a comparison is useful. The 1000-PMT KII detector electronics was based in large part on the experience gained in the design and construction of the Brookhaven Exp. 734 4000-PMT and 13 000-PDT systems.

The time resolution in KII was 1ns, but the charge resolution was a much more demanding 10 counts per photoelectron, 13-bit linear system. Thus, in terms of resolution the KII electronics would directly satisfy LCD. However, the cosmic-ray background rate for LCD is about 50 000 times as great as the trigger rate at KII so that it is more difficult to maintain a deadtimeless operation. More attention must be paid to pileup rejection and the resultant baseline shifts in LCD. Fortunately, the analog multiplicity trigger used in KII can carry over to LCD with almost no changes.

Finally the overall cost for the KII electronics (even without including bases, cables, and high-voltage supplies) was appreciably greater than the cost goal per channel for LCD.

In summary, we can use much of the design philosophy of the KII electronics, but we must reduce the sensitivity to high-rate effects by careful signal handling, and we must also improve the ratio of cost of electronics to cost of PMTs. Fortunately, there is a serendipitous interaction with DOE-funded research at the University of Pennsylvania on Superconducting Super Collider (SSC) detector design.

It has become clear in the last six months that the best method of attacking costs is to use the newly available tools for creating fast-analog-integrated circuits to produce denser, less-power-hungry and more-capable circuitry. We expect to include more-precise signal shaping at a parts cost per channel slightly less than the discrete KII version. We expect, however, by using monolithic technologies, to reduce the cost of power, cooling, printed circuit board real estate, and pc assembly by more than an order of magnitude relative to the KII budget.

14.2 Front-End Signal Processing

Figure 14.1 is a block diagram of the LCD signal processing. The individual PMT is fed high voltage over a separate wire. The signal cable is of necessity quite long (60m), and pulse dispersion in the cable means that for a simple discriminator some software correction for slewing must be made at low-pulse heights (thus the 0.1pe least count). In addition, it must be remembered that the PMT anode will be ac coupled to the cable (a photocathode at a large negative potential relative to the surrounding water would generate leakage currents), and thus there will be an overshoot tail (or ballistic deficit) that must either be canceled or made negligible.

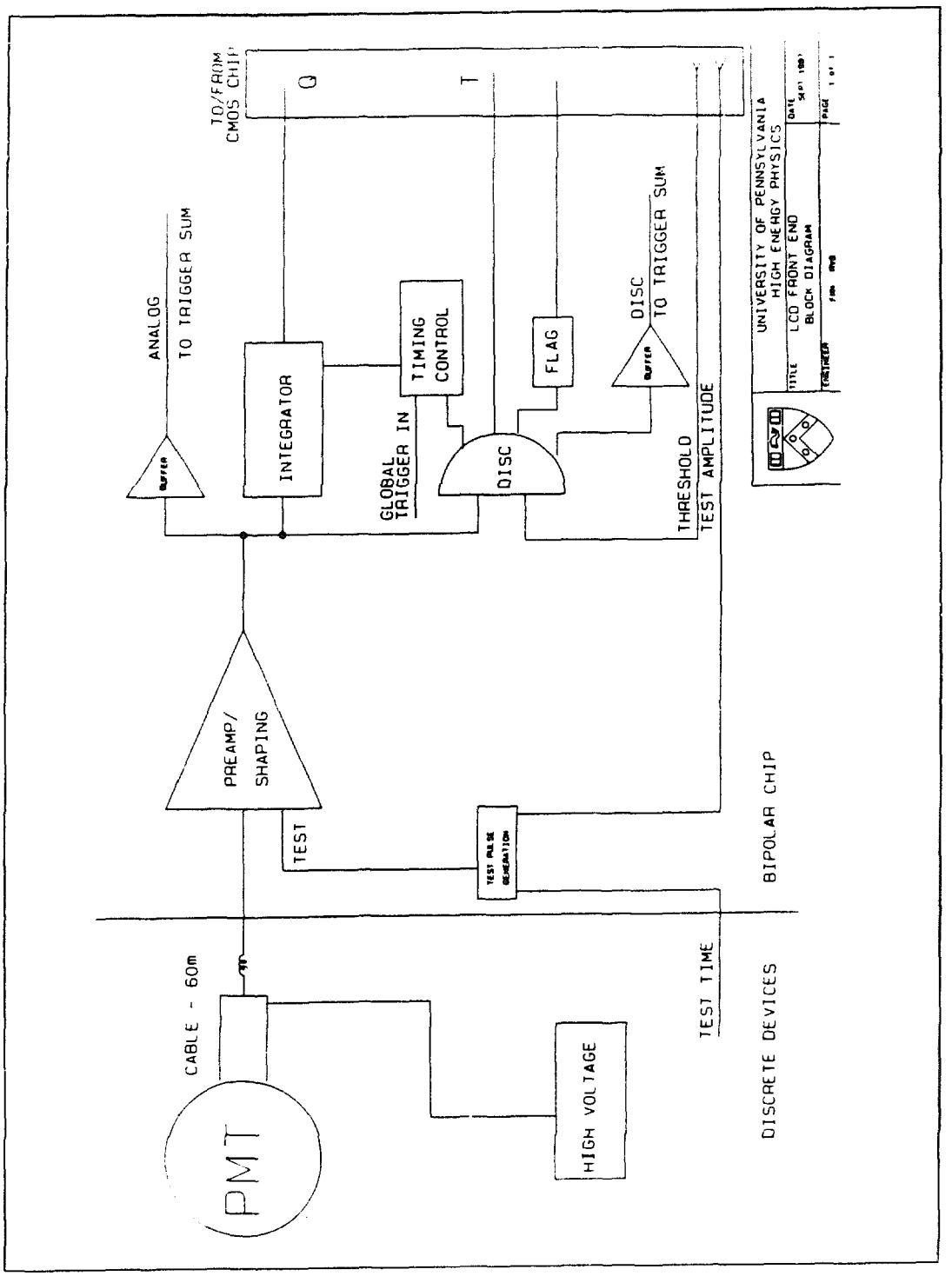

Fig. 14.1. Front-end block diagram.

The preamp block is intended to remind us that the signal must be properly terminated, but the signal from the proposed PMTs will already be sizable, and amplifier gain and noise are not a concern. The shaping amplifier compensates for the ballistic deficit. The output of the shaping amplifier is then sent to the discriminator and the integrator.

The discriminator provides a reference time for the beginning of charge integration, starts ramping a fine-time capacitor in the time-to-voltage converter, loads a 1-bit register, and starts a timeout process so that the PMT channel resets itself if no global trigger is received within 300ns (see Fig. 14.2 for system timing). Because the PMT response to small or moderate light levels recovers in less than 100ns, the individual phototube is "dead" to a second pulse only during this 300-ns period, and the detector as a whole is capable of refiring every 300ns and thus is "deadtimeless." (The size of the time window is determined, in part, by the transit time of light through the LCD tank.)

Both the output of the shaping amplifier and a discriminator output are driven to the trigger system (see TRIGGER). Figure 14.3 is a schematic and simulation of a preamplifier/shaper being developed for SSC R&D that exhibits both lower noise and higher bandwidth than necessary for the LCD detector. A prototype of this circuit or a variation of it fabricated in a high-speed bipolar analog array should be available in March 1988. For the somewhat simpler LCD case, the present bipolar technology is more than sufficient (6-GHz gain bandwidths), and the density, even in analog arrays, should be high enough (4 channels per chip) to satisfy all of the design requirements. Figure 14.4 is a preliminary design for both the preamp (a) and discriminator sections (b).

14.3 Storage

If there were only one event of interest for each PSR spill, we would only have to add some analog multiplexing and digitization and be done. However, in the real world there is a steady flux of cosmic-ray muons, electrons from stopping muons, and low-energy, radioactivity-induced events occurring throughout the time of interest. It is necessary that the electronics/data-acquisition system be capable of recording not only neutrino events but also all of the various backgrounds occurring in a window of roughly 30μs before and 10μs after the PSR spill.

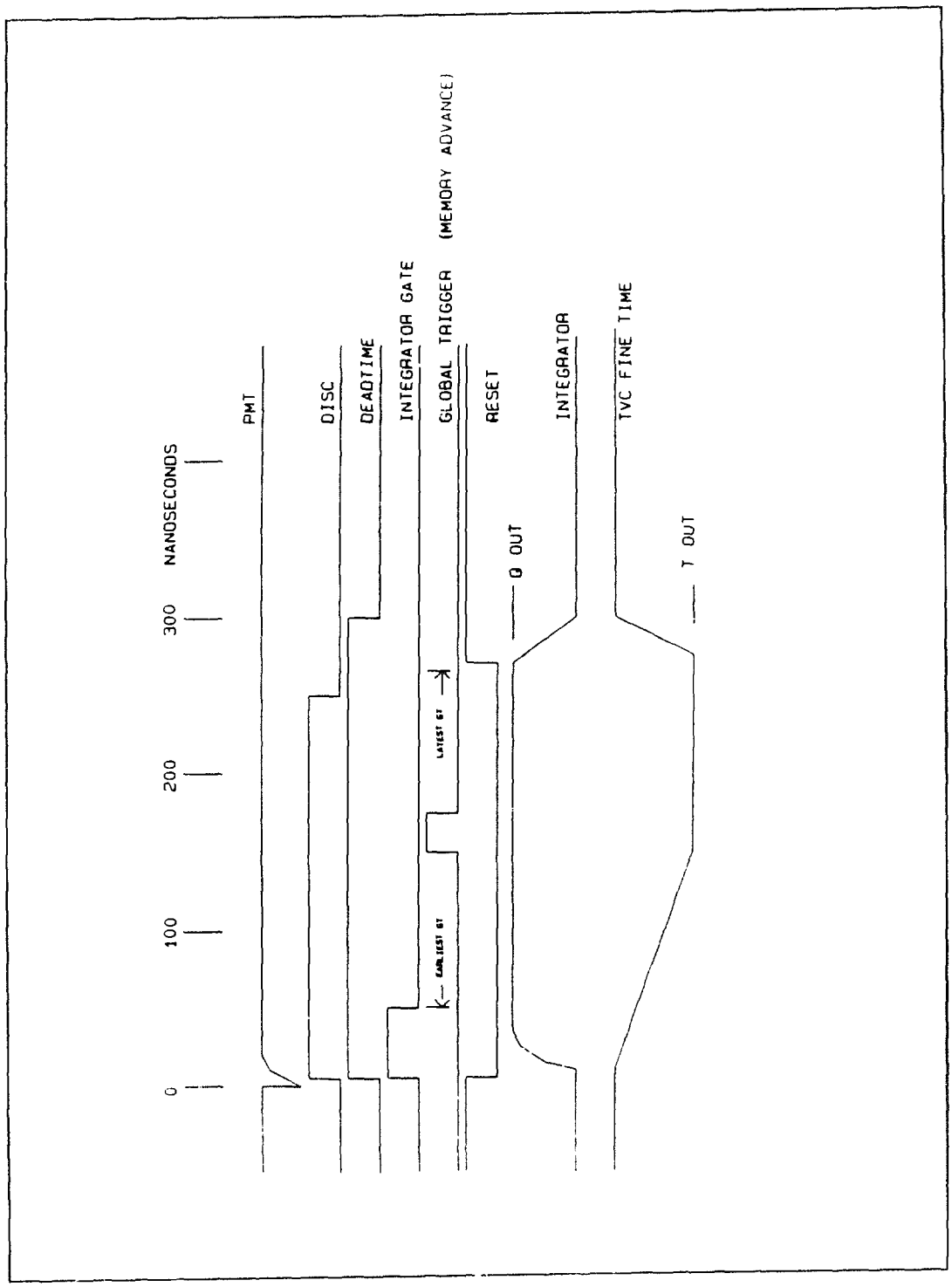

Fig. 14.2. Front-end timing.

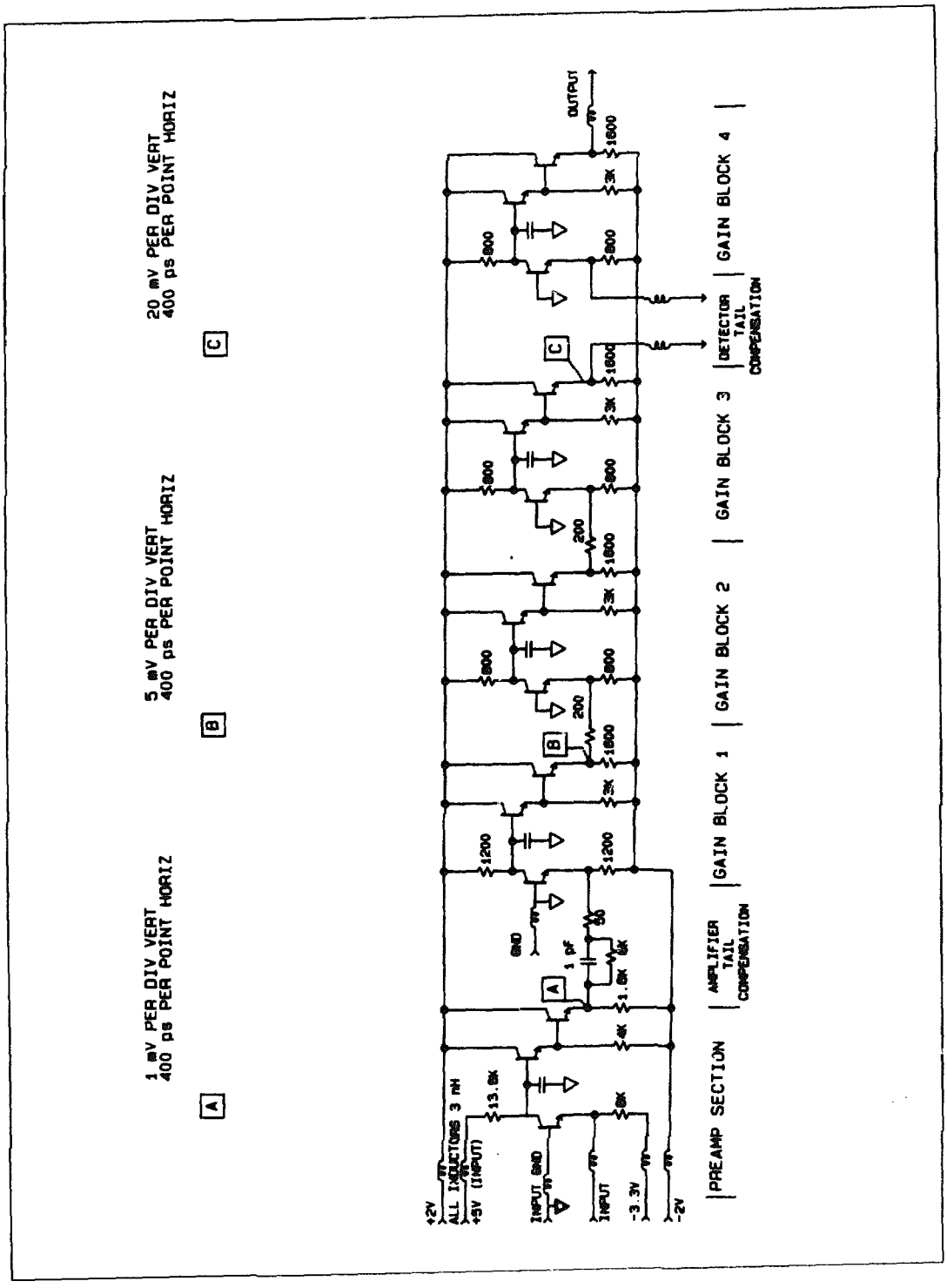

Fig. 14.3. SSC preamp/shaper schematic and simulation.

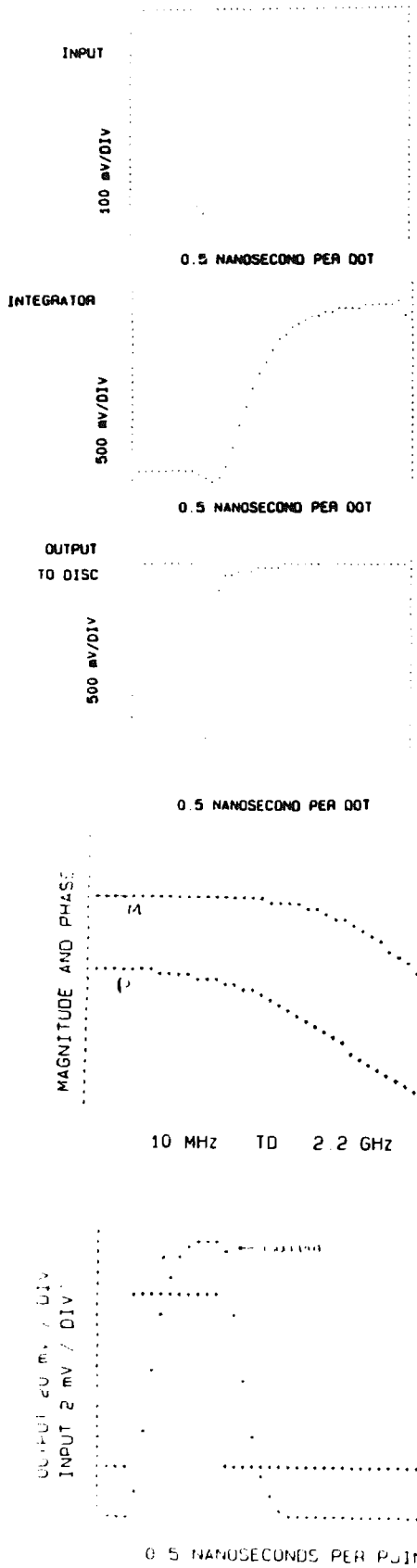

(a)

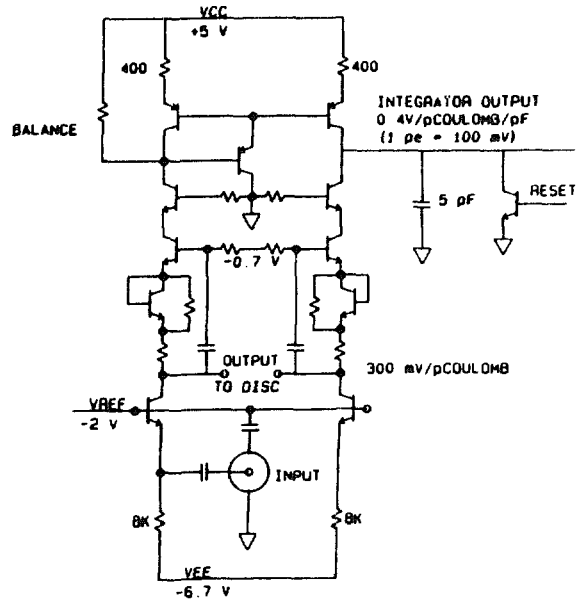

12 mWATT TOTAL POWER DISIPATION

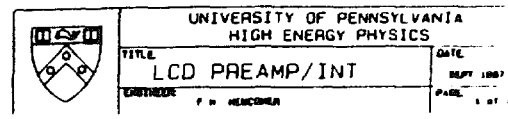

GAIN BANDWIDTH = 2.2 GHz

(b)

TOTAL POWER CONSUMPTION ~3 mW

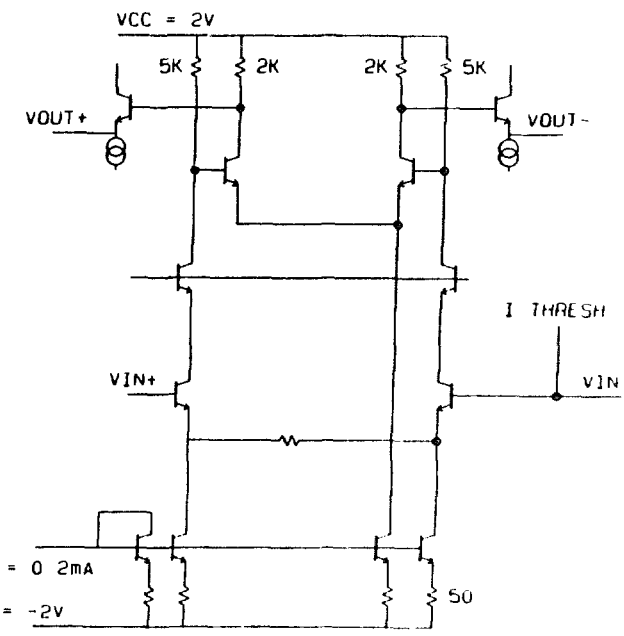

Fig. 14.4. LCD bipolar design for (a) preamp and integrator and (b) discriminator.

Assuming a 18.7-kHz cosmic-ray rate, with about 41% stopping muons, the average density of cosmic-ray-induced background will be $\leq$ 2 events per 40-μs gate. At a PSR repetition rate of 24Hz, we would then have 50 events per second or, conversely, we would have about 40ms to deal with two cosmic-ray events and any radioactivity-induced backgrounds (the real signal rate is sufficiently small that it may be ignored for the data-rate calculations).

Because of the geometry of the detector, an individual phototube will have an average of one or more events per spill, and a tube with four or five events will not be unusual. To digitize charge and time and recover within the 300-ns deadtime would require 3-megasample-per-second flash ADC on Q and T. Such fast ADCs are available, but by themselves (even without the necessary high-output current amplifiers and reference supplies) they would represent several percent of the cost of a PMT—simply too expensive

We propose that the data for a given PMT be stored in an analog buffer for all the events within a beam gate and then be cycled and multiplexed with the stored information from other PMTs into a relatively small number of relatively slow (microseconds) ADCs during the 40-ms interval between PSR pulses. This is, in fact, exactly the KII scheme, except that for KII the analog buffer is only four events deep per PMT, and clearly LCD will require a somewhat deeper buffer given the much higher event rate (50Hz or more versus 0.5Hz). (Note that a Poisson distribution with a mean of 1.3 has a 1.8% chance of having a fifth event within the 60-μs gate).

At KII the analog storage elements were individual mica capacitors buffered by operational amplifiers with JFET analog multiplexers switching inputs and outputs. It is now possible, however, to design and produce CMOS monolithic structures of fine enough dimensions (1 to 2μm) to allow the fabrication of very fast (2–5ns), very low-leakage (10^{15} Ω), and very high-density capacitors and multiplexers that should exhibit the required stability and accuracy (better than 8 bits).

For instance, Fig. 14.5 is the floor plan of a CMOS design done at the University of Pennsylvania as a part of SSC detector R&D. This chip was fabricated at Hewlett-Packard (HP) and is now being tested. Preliminary test results are quite encouraging. This design is a time-to-voltage converter (TVC) with multiple-switched (eight) ramping capacitors, as shown in the schematic of Fig. 14.6. This TVC is designed for SSC rates and times, about 200ps least count and 50ns full scale, so that by simply reducing the reference current source by a factor of five one would get an appropriate scale for LCD. A similar but less complex system could serve as the charge-storage system for LCD. Charge storage requires only input and output switches, a reset switch around each capacitor, and an output buffer.

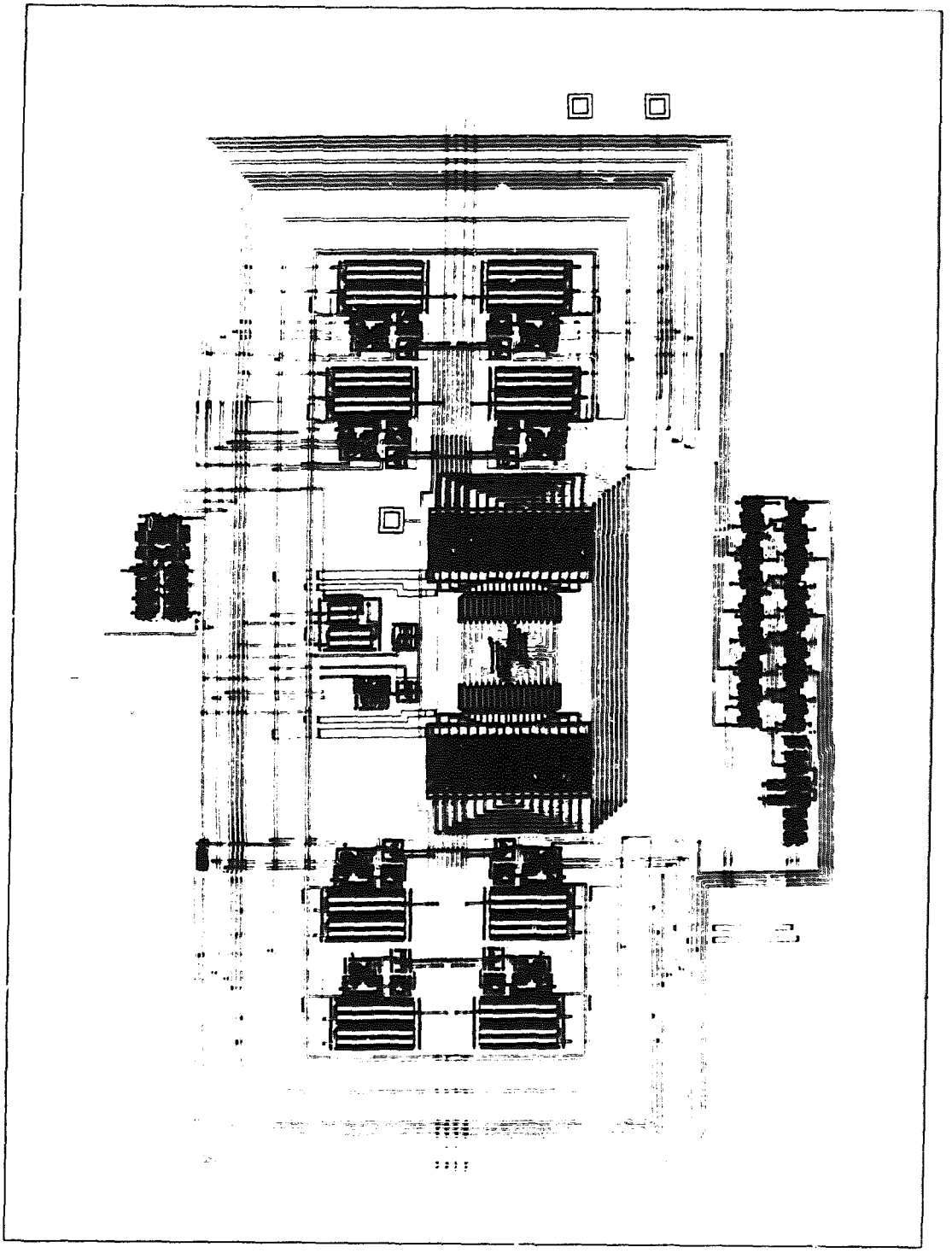

Fig. 14.5. SSC TVC floor plan.

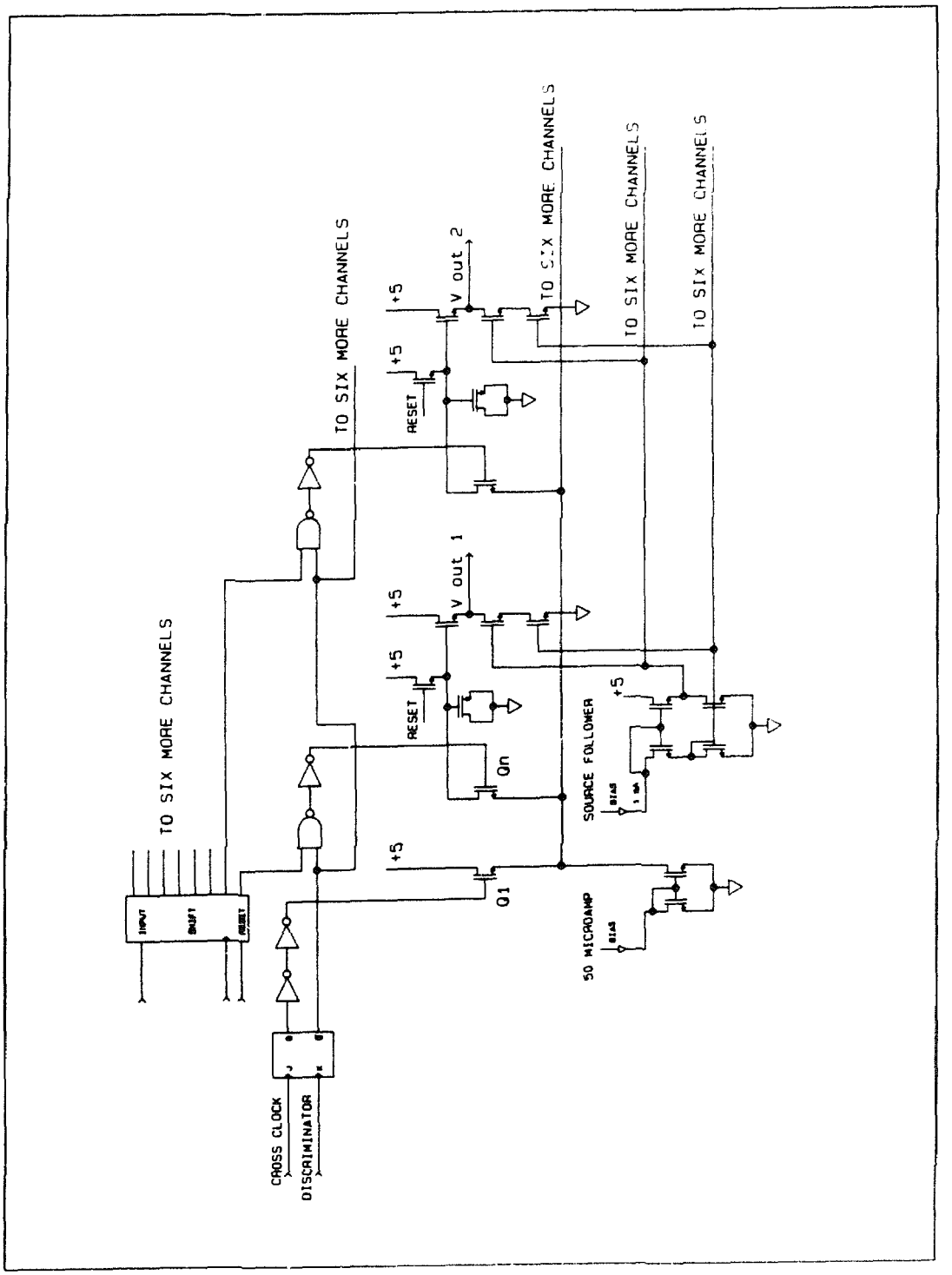

Fig. 14.6. SSC TVC schematic.

The floor plan of Fig. 14.5 occupies less than one-tenth of the available chip area. In the test chip the additional area is used for two slightly modified replications of the TVC plus many test structures plus a great deal of blank space. Thus even without sharing some of the logic functions between charge and TVC storage systems it is easy to imagine a single CMOS chip (Fig. 14.7) with four TVCs, four charge storage arrays, each with eight samples, an 8-bit shift register for the discriminator flag, eight low-resolution D/A converters to control discriminator thresholds, and test pulse amplitudes, and some control logic.

14.4 Read out

In parallel with KII we plan a read-out scheme (Fig. 14.8) that has slow (order of 10μs) ADCs for both charge and time located at each crate of the front-end system—for example, every 256 PMTs. The crate ADCs would be read out into a FIFO memory, which would record charge and time values coupled with the event identification and the PMT address. The output of the local (or crate) FIFOs would feed onto a single parallel data bus with one crate at a time acting as the bus driver. Unlike the KII system, however, LCD has a relatively high average data rate (50 events per second at 25 000 bytes per event gives 1.25 Mbytes per second) that is not reasonable to send directly to permanent storage. Therefore, the read-out data bus feeds into memory buffers in a farm of microprocessors, one spill per processor (for example, see the D0 data-acquisition system). Muon events are then fitted, and only overall charge, trajectory, and stopping vertex (if any) are passed on to the output stream. If all low-energy events are passed on without change, then the average, data rate becomes much more manageable (10 kbytes per second, or 1 Gbyte per day). Using KII as a model, we estimate that a muon-fitting algorithm will require about one million instructions to complete, so that for 50 events per second we would require about twenty of the present ACP node processors, or ten 68030 class processors. This is a relatively modest processor farm by present standards.

14.5 Trigger

At KII the trigger is a simple multiplicity coincidence—all 1000-PMT discriminator outputs enter into an analog sum (with an adjustable resolving time) and a set of discriminators looks at the output of the sum allowing multiple thresholds.

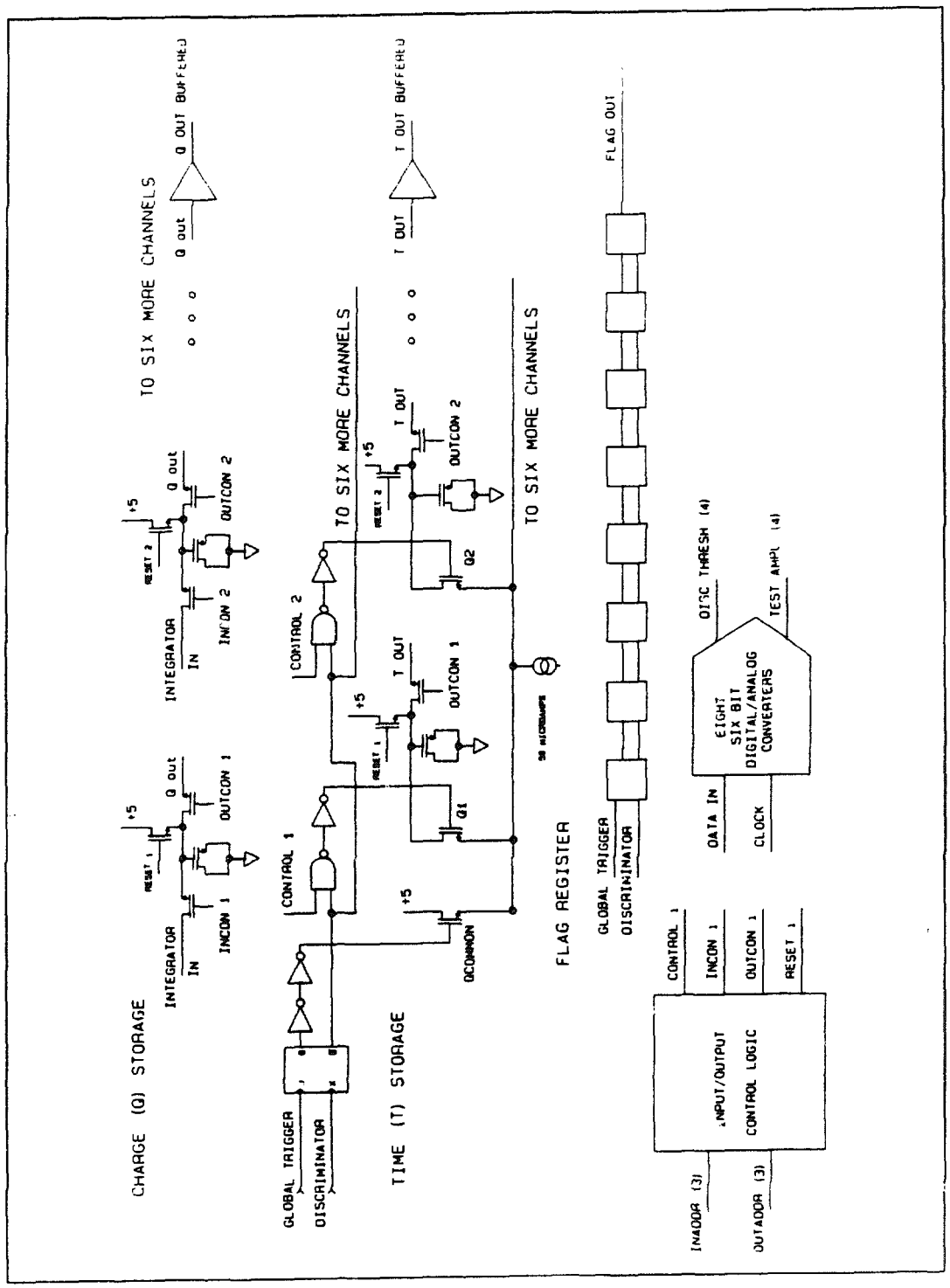

Fig. 14.7. LCD CMOS block diagram.

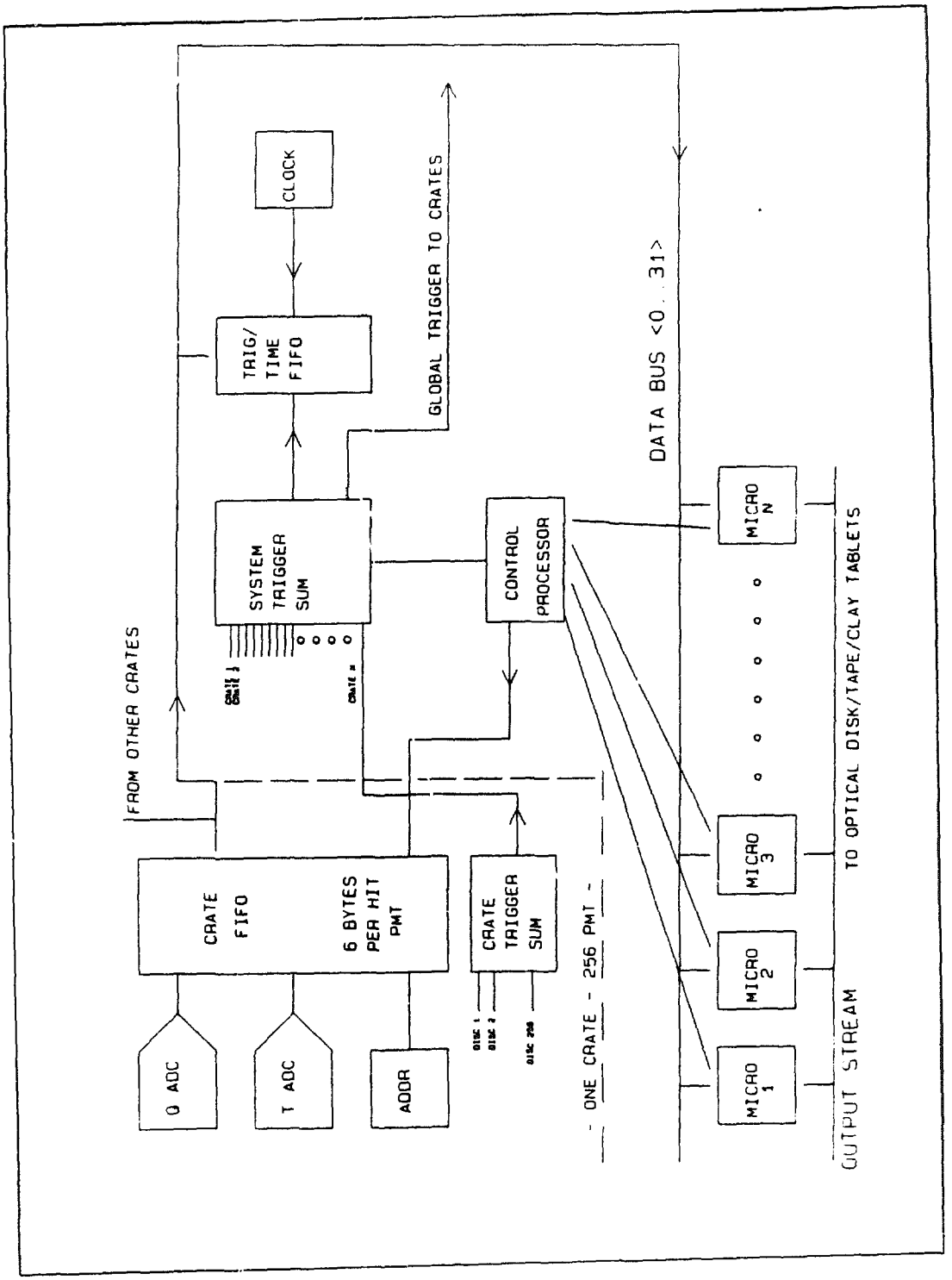

Fig. 14.8. LCD read out.

At the moment the KII thresholds are set at 17-PMT hits (raw NHIT) for the normal trigger and 13 hits for the spallation trigger, which is enabled for a brief time after each large pulse-height event (as defined by an overall analog charge sum). This trigger is simple to implement, needing only one card per crate to do preliminary summing and one card for the final sums. The discriminator sum is arranged so that there is a clear plateau for each NHIT (from 1 to about 50), at which point saturation begins to limit the resolution of the system. LCD is also a low-energy signal experiment, and a similar trigger (Fig. 14.9) will serve, not only for the data-acquisition system, but also to do preliminary tagging of low-energy events, through-going muons, and stopping muons. A separate multiplicity trigger on the anticoincidence counter will serve to tag most corner clipping muons.

14.6 Timing and Event Numbering

Each system trigger will be associated with an absolute time of day, derived from a precision clock in the trigger/timing system. This time of day need only be entered once per event buffer, all other times are the individual PMT's fine time offset from the system trigger time (plus the fixed transit-time offsets).

The entire detector is triggered at each event time. If a given PMT discriminator has fired within the last 300ns, then a tag bit in the CMOS storage system is set (see Fig. 14.7) and the Q and T voltages will be recognized as valid data that must be digitized and loaded into the FIFO.

The FIFO also records the PMT address and an event number (the lowest three bits corresponding to the CMOS storage system address). The crate read-out control system will thus advance the output of the storage chip one location, scan the PMTs in a crate for hits, digitize and store the data, and then advance to the next storage chip location. The data bus output control empties the FIFO of data for a given event number, advances to the next FIFO, and at the end of data in the last FIFO, in the chain, the ACP microprocessor is changed and the read-out for the next spill proceeds.

In such a scheme it is possible to imagine steering different event types to different farm processors, ignoring and flushing given events or other more complex operations with only the addition of one more programmable device watching ove the data path. This could be very useful if one wished to keep the detector operating in a continuous mode, or for various calibrations and tests.

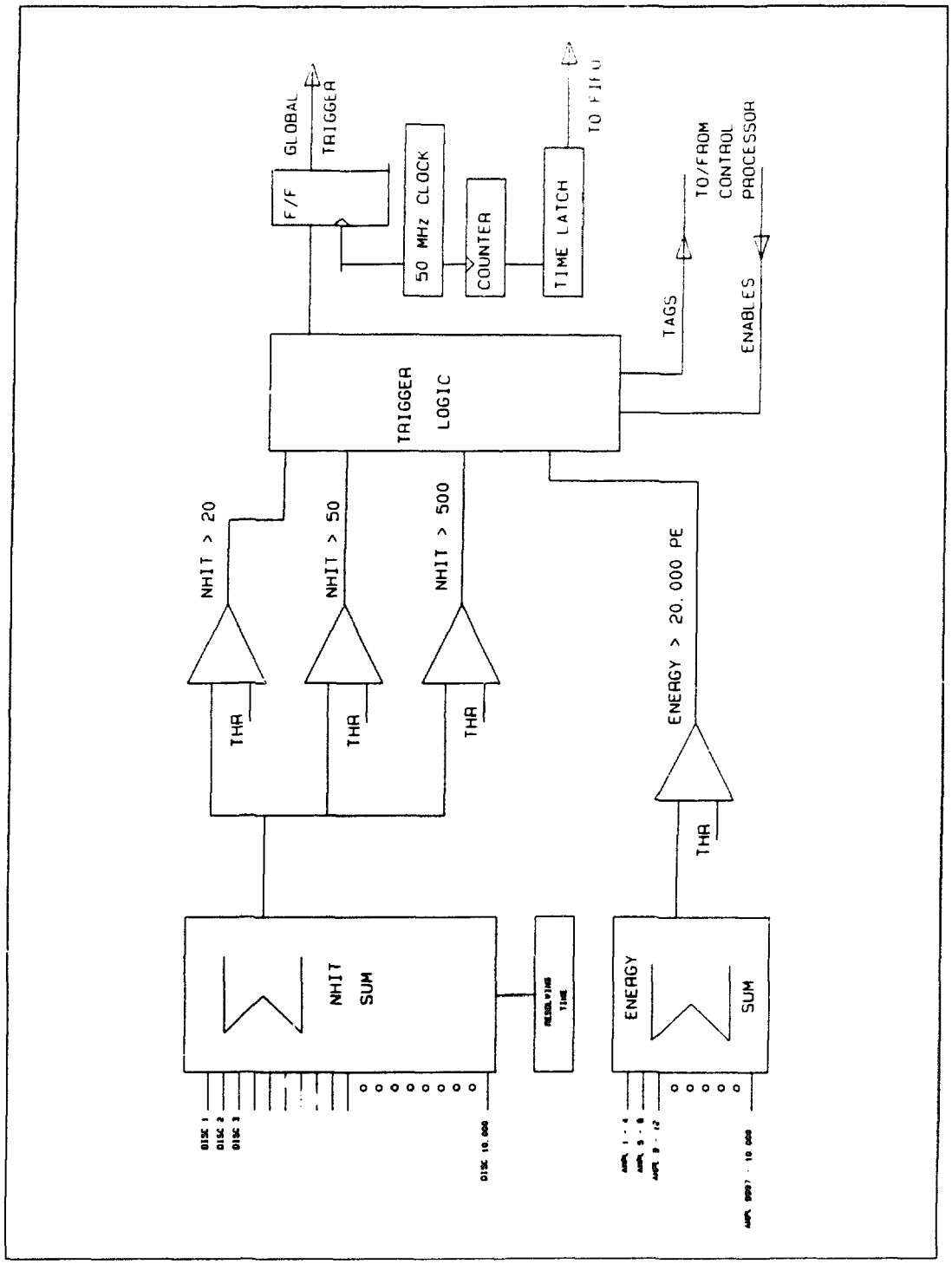

Fig. 14.9. LCD trigger.

14.7 Base and High Voltage

The base for the PMT has a passive voltage divider, is back-terminated in the cable impedance, and has suitable high-voltage decoupling.

The high-voltage distribution for the detector will allow individual, computer-controlled measurement of set voltage and current, and will also provide a PMT disable so that individual tubes may be turned off, both for diagnostic purposes and to allow the shutdown of a misbehaving base or tube. The remote-controlled shutdown would not have to be complete; simply greatly limiting the current or dropping the applied voltage by a third will allow time for human intervention to complete the shutdown. Similarly, the high-voltage adjust can be a manual resistor change in order to avoid unnecessary complexity or cost. Additional measures to control costs will entail the use of much less expensive connectors and cable than, for instance, SHV and RG-59/U. High-voltage power will be provided by commercial bulk supplies.

14.8 Summary

The electronics/data-acquisition system will be made up from a 4-channel application-specific bipolar integrated amplifier and discriminator, followed by a 4-channel application-specific CMOS-integrated storage element with both chips buffered from and interfaced to the rest of the system by standard integrated circuits and discrete components. The channels will be packaged 16 channels to a card (6U by 280-mm eurocard), 16 cards to a crate. Each crate has one digitizing and control card and one trigger card. The outputs of the 40 to 50 digitizing and control cards drive a 32-bit data cable into a small microprocessor farm that fits muon tracks and compresses the data by a factor of about 100. The estimated cost for the system is approximately $100 per PMT.

15 OTHER PHYSICS

The detector will be sensitive to additional physics topics, such as neutrino oscillations, neutrino charge radius and magnetic moment limits, and supernova neutrino bursts. $\nu_\mu - \nu_e$ oscillations will be probed in the region $sin^2 2\alpha > 0.0002$ and $\Delta m^2_{21} > 0.06$ eV^2, limits on the neutrino charge radius and magnetic moment will reach $10^{-33} cm^2$ and $10^{-10}\mu_B$, respectively, and from 10 to 16,000 neutrino electron scatters will be observed in 10 seconds from the next supernova burst.

15.1 Neutrino Oscillations

In this section we discuss the sensitivity of LCD to neutrino oscillations. Neutrino oscillations have been discussed extensively in the literature. Here it is assumed initially that a two-component model of transitions between lepton families is adequate to establish approximate sensitivity of LCD. The probability of observing ν_2 beam in an initially pure ν_1 beam is given by

$$P(\nu_1 \to \nu_2) \;=\; \sin^2 2\alpha \;\; \sin^2(1.27\Delta m^2 \ell / E_\nu) \;\; ,$$

where E_ν is in MeV, ℓ is in m, and Δm^2 is in eV^2. For $\nu_\mu \to \nu_e$ oscillations, for example, the peak of the sensitivity of the experiment comes when the argument of $sin^2(1.27\Delta m^2 \ell / E_\nu)$ is $\pi/2$. For a ν_μ monoenergetic spectrum at 30 MeV and a mean detector radius of 10m, the peak of sensitivity in Δm^2 is at 3.7 eV^2. In LCD, both neutral-current scattering on electrons, and charged-current scattering of ν_e on oxygen and $\bar{\nu}_e$ on free protons may be detected.

To lowest order in the Standard Model, the cross sections for neutrino-electron scattering are given by

$$\sigma(\nu_\ell e) \;=\; \frac{2G_F^2 m_e}{\pi} \;\; E_\nu \;\; \left[\left(\frac{1}{2} - S^2\right)^2 + \frac{1}{3} \;\; S^4\right]$$

$$\sigma(\bar{\nu}_\ell e) \;=\; \frac{2G_F^2 m_e}{\pi} \;\; E_\nu \;\; \left[\frac{1}{3} \;\; \left(\frac{1}{2} - S^2\right)^2 + S^4\right]$$

$$\ell = \mu, \tau$$

$$\sigma(\nu_e e) \;=\; \frac{2G_F^2 m_e}{\pi} \;\; E_\nu \;\; \left[\left(-\frac{1}{2} - S^2\right)^2 + \frac{1}{3} \;\; S^4\right]$$

$$\sigma(\bar{\nu}_e e) \;=\; \frac{2G_F^2 m_e}{\pi} \;\; E_\nu \;\; \left[S^4 + \frac{1}{3}\left(-\frac{1}{2} - S^2\right)^2\right]$$

where

$$S^2 \equiv \sin^2\theta_W \quad .$$

The cross sections for ν_μ - e scattering and ν_τ - e are equal apart from small radiative corrections, so that neutrino-electron scattering is insensitive to $\nu_\mu \rightarrow \nu_\tau$ oscillations. However, the cross section for $\nu_e - e$ scattering is about a factor of seven larger than the other two so that $\nu_e \rightarrow \nu_\mu, \nu_\tau$ can be readily observed in the neutral-current channel.

Neutrino oscillations would manifest themselves in a number of ways in LCD:

1) $\nu_e \rightarrow \nu_\mu$: The flux of ν_e, ν_μ, and $\bar{\nu}_\mu$ are changed. The effect of these oscillations on the ratio R is discussed analytically by Marciano[1] and Lim.[2] Limits on oscillation strength have been calculated for our geometry by Monte Carlo, assuming that the value of the ratio R from the experiment will be in agreement with the Standard Model after one-loop corrections are made. The oscillation limit shown in Fig. 15.1 is then set at 90% confidence from a 1.7 standard deviation change on the ratio. It is important to note that only an increase in the observed value of R can be ascribed to neutrino oscillations.
2) $\nu_e \rightarrow \nu_\tau$: The effect from oscillations on the ratio is shown in Fig. 15.2. This limit is somewhat less stringent than 1) above because only the ν_e part of the ratio is affected, and the incident neutrino-energy spectrum is broad, diluting the effect somewhat.
3) Disappearance effects are also apparent in the ratio when the second neutrino becomes sterile. For example, when $\nu_\mu \rightarrow \bar{\nu}_\mu$ in a $\Delta\ell = 2$ transition (ℓ is lepton number) without a helicity flip, then the left-handed $\bar{\nu}_\mu$ does not interact and disappears from the beam. In Fig. 15.3 is shown the limits for disappearance for both ν_μ and ν_e.
4) When the physical wavelength of the oscillation is comparable to LCD dimensions, then it is possible to learn more from the radial dependence of the events. Oscillations involving ν_μ are particularly apparent in the distribution of events at short times (numerator) alone because of the monoenergetic nature of the incoming neutrinos.
5) The cross section for ν_e scattering on oxygen has been discussed extensively in section 7.6. Although the absolute value of this cross section is not known well enough to constrain the oscillation possibilities, the radial dependence of the neutrino flux is very well known. A comparison of the radial dependence of the wide-angle (ν_e - O) events with the uniform distribution that is expected, will yield the limit given in Fig. 15.4. Because this process proceeds by charged current only, this experiment tests for

disappearance of ν_e and is comparable to the reactor experiments. The electron-energy spectrum from oxygen as seen in the detector is shown again in Fig. 15.5.

6) In the case that $\bar{\nu}_e$ appears from $\bar{\nu}_\mu$ then the reaction $\bar{\nu}_e + p \rightarrow e^+ + n$ proceeds at a rate far in excess of the cross section for $\nu_e + O \rightarrow e^- + F$ for full mixing. This observation is identical to that presently being made in experiment E645 at LAMPF. A radial dependence of the signal will allow separation of the effects of mixing ($\sin^2 2\alpha$) and Δm^2 as indicated above. There are relatively few events above 30 MeV, so that the same measurement as is presently being made in E645 can be made in LCD with considerably improved statistics. In fact there are some effects that will enhance the sensitivity of LCD: the endpoint of the oxygen energy spectrum is lower than for carbon, which is the target in E645; the oxygen cross section is a factor-of-four lower than carbon; and of, course, in LCD it is expected that there are many more events contributing to the limit. The probable limiting background will be the charged current reaction from ^{18}O, which has a Q value of 4.5 MeV, close to 2.7 MeV in the free proton reaction

$$\bar{\nu}_e + p \rightarrow e^+ + n \ .$$

If we assume the mixing limit in $\bar{\nu}_\mu \rightarrow \bar{\nu}_e$ oscillation is given by knowledge of the ^{18}O contribution, then the limit will be the product of the ratio of cross sections

$$(\nu_e + {}^{18}O \rightarrow e^- + {}^{18}F)/(\bar{\nu}_e + p \rightarrow e^+ + n) \sim 1 \ ,$$

the systematic limit on the knowledge of the ^{18}O contribution (10%), and the fraction of oxygen that is ^{18}O (0.2%), which gives 2×10^{-4}. The resulting oscillation limit as a function of Δm^2 is shown in Fig. 15.6. This estimate clearly indicates the potential sensitivity from measuring the ratio of fluxes $\bar{\nu}_e$ to $\bar{\nu}_\mu$ in a water detector with excellent statistical precision and largely background free, so that the systematic limit pertains.

7) LCD also will be sensitive to $\nu_\mu \rightarrow \nu_e$ oscillations in yet another way; if these oscillations occur, then there will exist prompt $\nu_e O$ events which are monoenergetic. A rough estimate indicates a maximum sensitivity of $sin^2 2\alpha < 10^{-3}$.

Recently, interest has grown in the possibility of oscillations with all three generations involved. To proceed with an estimate of the sensitivity of LCD, we first repeat the phenomenology expressed in Marciano[1] and Lim.[2] The mixing

matrix between the three flavors is expressed in the same form as the KM matrix as

$$\begin{matrix}\nu_e \\ \nu_\mu \\ \nu_\tau\end{matrix} = \begin{pmatrix} C_1C_3 & S_1C_3 & S_3e^{-i\delta} \\ -S_1C_2 - C_1S_2S_3e^{i\delta} & C_1C_2 - S_1S_2S_3e^{i\delta} & S_2C_3 \\ S_1S_2 - C_1C_2S_3e^{i\delta} & -C_1S_2 - S_1C_2S_3e^{i\delta} & C_2C_3 \end{pmatrix} \begin{pmatrix}\nu_1 \\ \nu_2 \\ \nu_3\end{pmatrix}$$

$$S_1 = sin\theta_1$$

$$C_1 = cos\theta_1 \ .$$

A particularly interesting scenario is when the masses of both the electron and muon neutrino are very small and the τ neutrino mass is about 1eV. This corresponds to a possible solution of the solar-neutrino problem through the M.S.W. effect. In this scenario no vacuum oscillations between ν_e and ν_μ are observable, but a second-order effect induces apparent oscillations between ν_e and ν_μ with an effective mass-difference squared of $1eV^2$. The transition probabilities in this scenario are shown below.

$$m_{\nu_e} \sim m_{\nu_\mu} = 0 \quad m_{\nu_\tau} \sim 1eV^2 \ .$$

$$P(\nu_e \rightarrow \nu_\mu) = 4 \ \sin^2\theta_2 \ \sin^2\theta_3 \ \cos^2\theta_3 \ \sin^2 \ (1.27\Delta m^2 \ell \ / E_\nu)$$

$$P(\nu_e \rightarrow \nu_\tau) = 4 \ \sin^2\theta_3 \ \cos^2\theta_2 \ \cos^2\theta_3 \ \sin^2 \ (1.27\Delta m^2 \ell / E_\nu)$$

$$P(\nu_\mu \rightarrow \nu_\tau) = 4 \ \sin^2\theta_2 \ \cos^2\theta_3 \ \cos^2\theta_2 \ \cos^2\theta_3 \ \sin^2 \ (1.27\Delta m^2 \ell / E_\nu) \ .$$

The $\nu_e \rightarrow \nu_\tau$ transition is first-order, and this is reflected in the probability. The $\nu_e \rightarrow \nu_\mu$ transition cannot be observed in first-order, but appears in second order and so has two $\sin^2 2\theta$ terms. An experiment sensitive to $\nu_\mu \rightarrow \nu_\tau$ oscillations at the $1eV^2$ mass level would observe oscillations directly, but such an experiment does not exist as yet. Using the sensitivity shown in Fig. 15.6 at $1eV^2$, and a value of θ_2 equal to the Cabibbo angle, a limit of 0.01 for $\sin^2 2\theta_3$ is attainable.

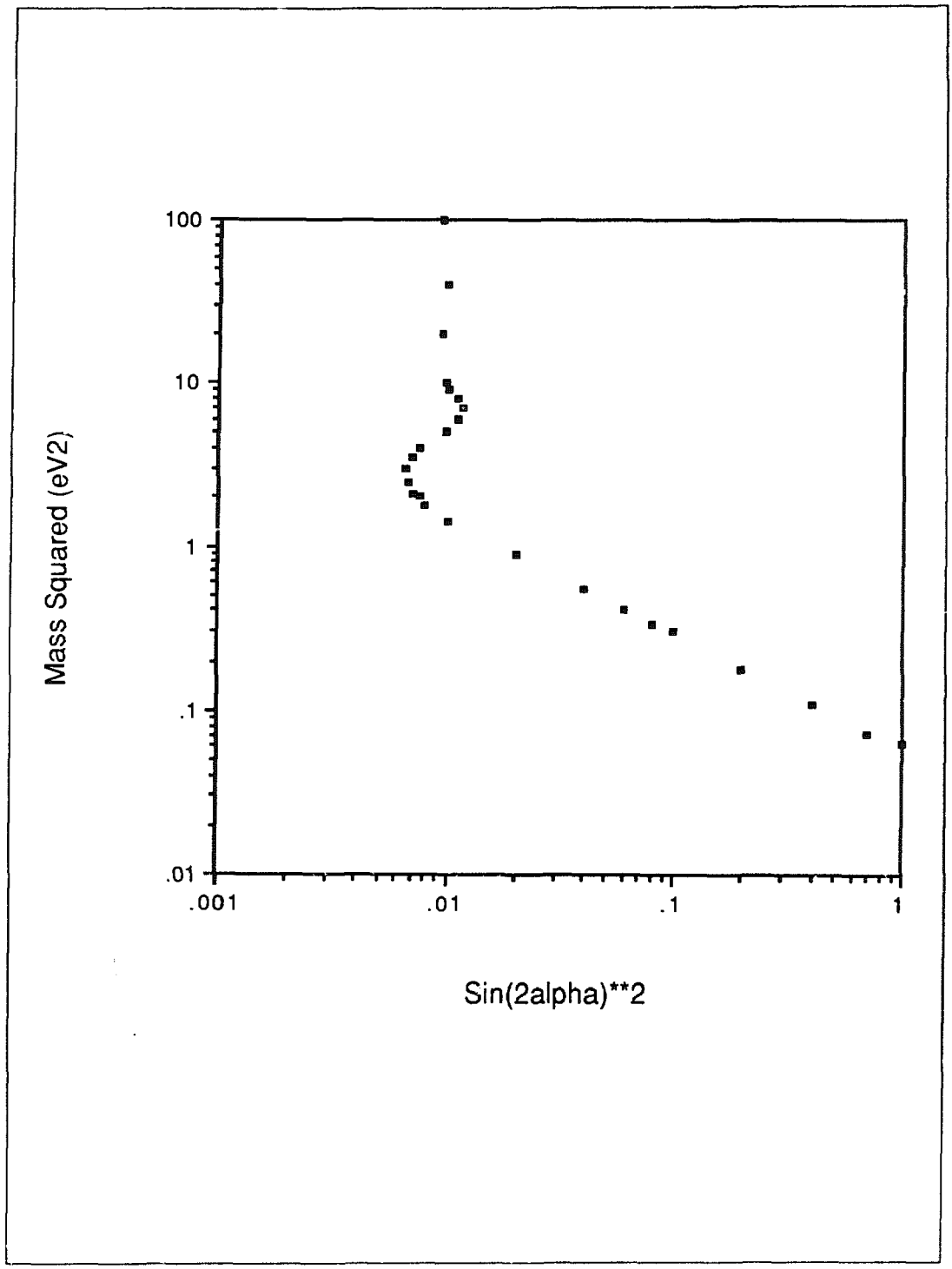

Fig. 15.1. Oscillation limits for $\nu_\mu \longleftrightarrow \nu_e$.

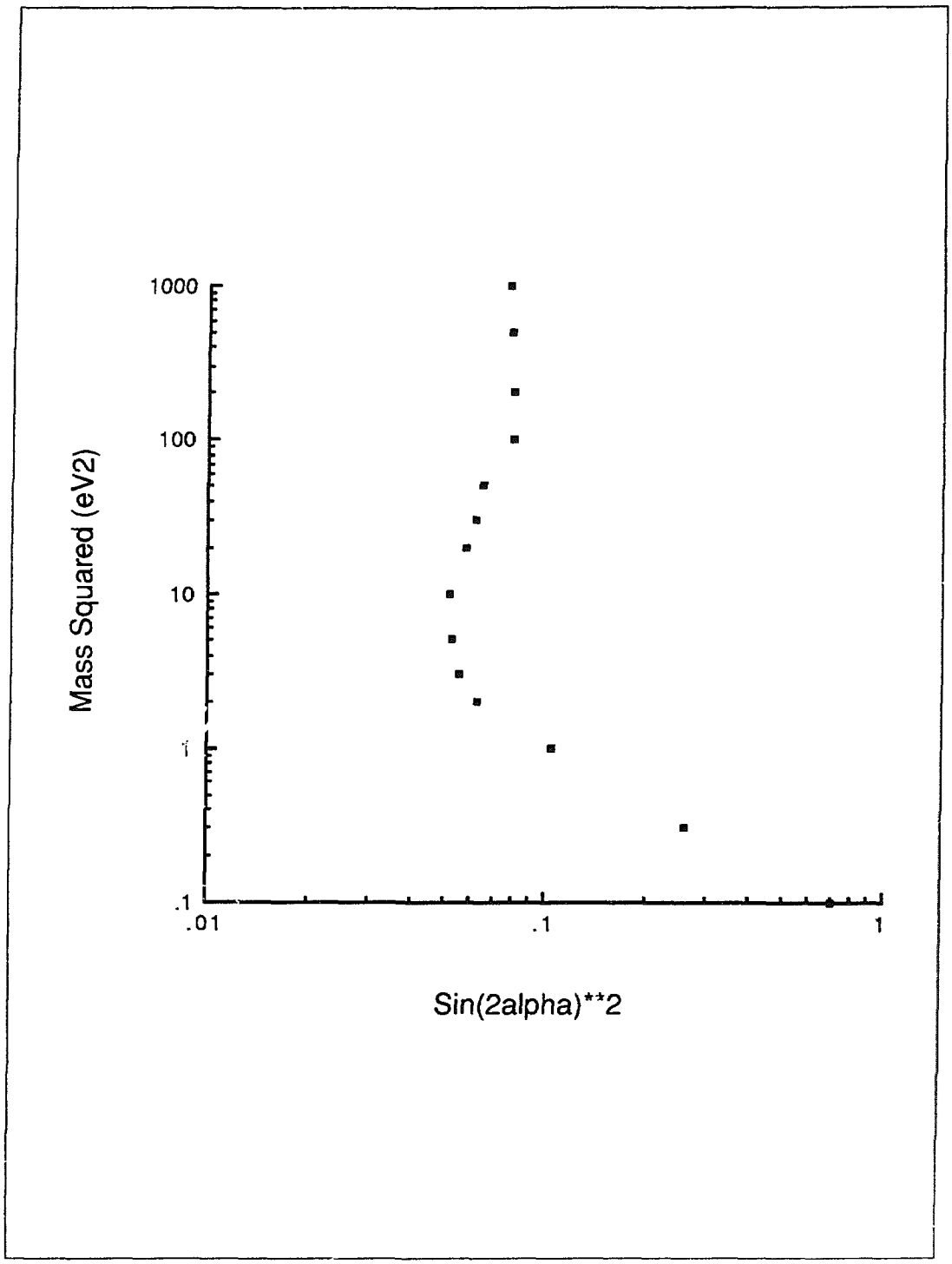

Fig. 15.2. Oscillation limits for $\nu_e \longleftrightarrow \nu_\tau$.

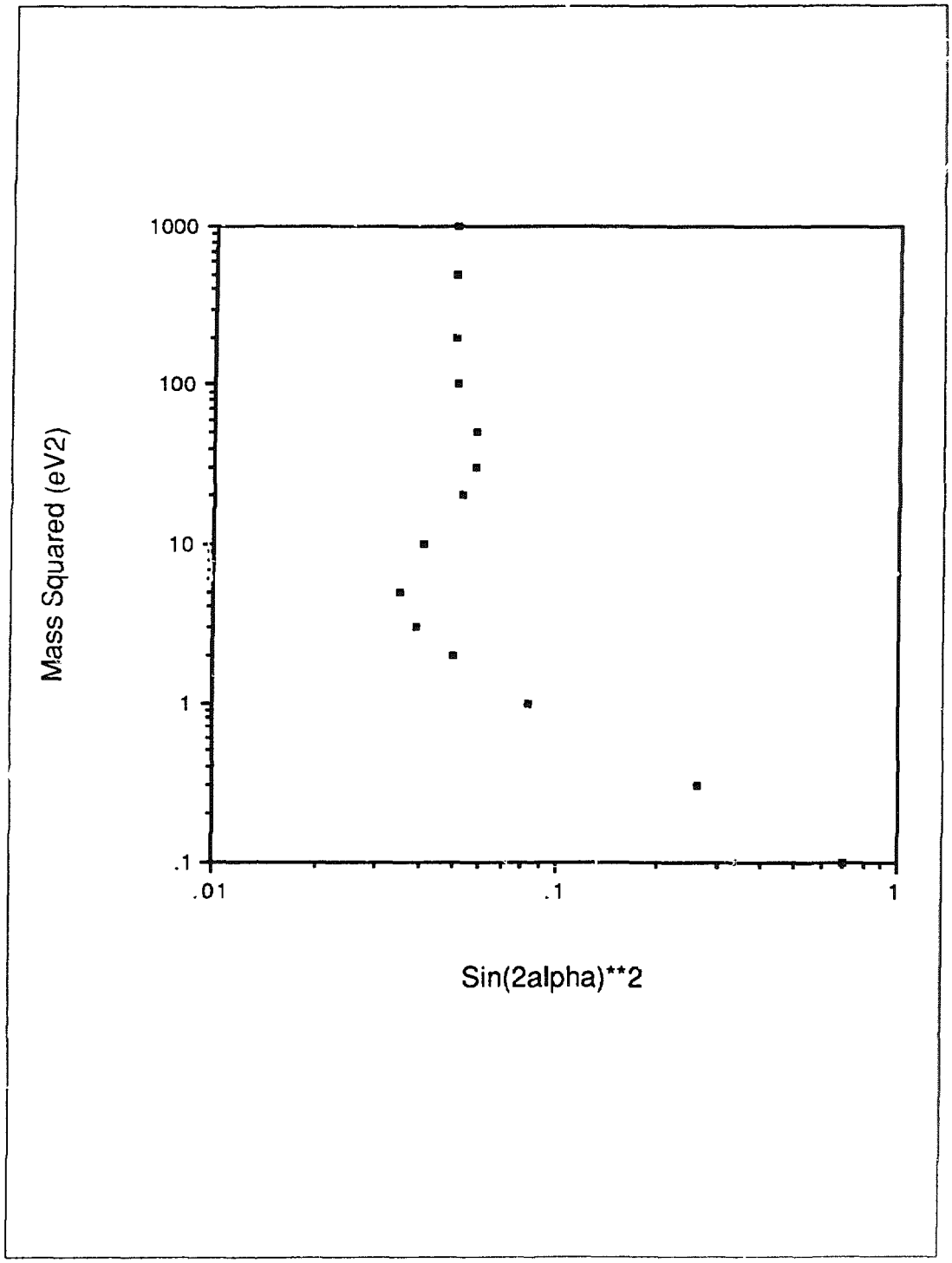

Fig. 15.3. Disappearance limits for ν_μ *and* ν_e.

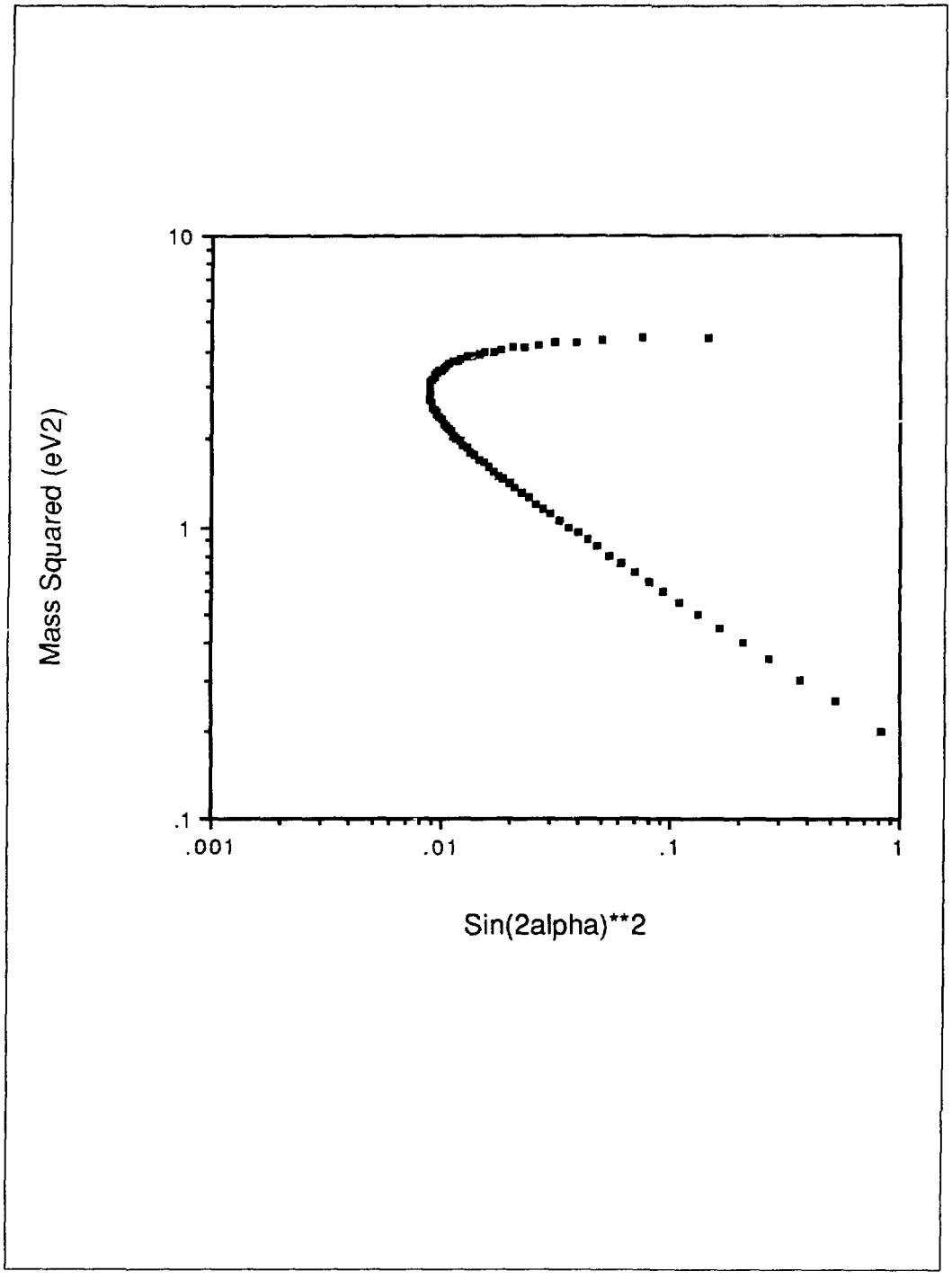

Fig. 15.4. Oscillation limits from the radial distribution of ν_eO events.

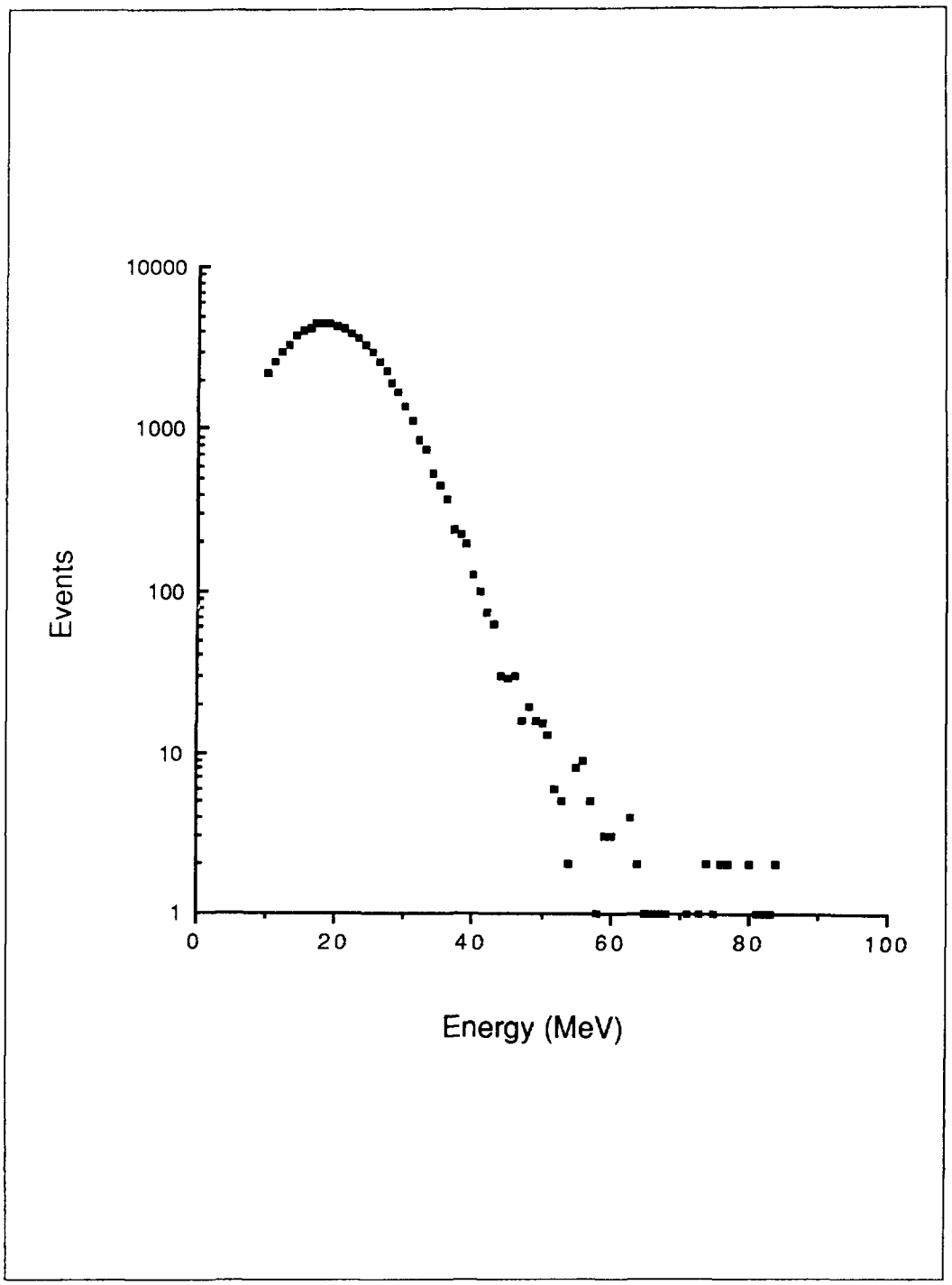

Fig. 15.5. Electron-energy spectrum from ν_eO interactions.

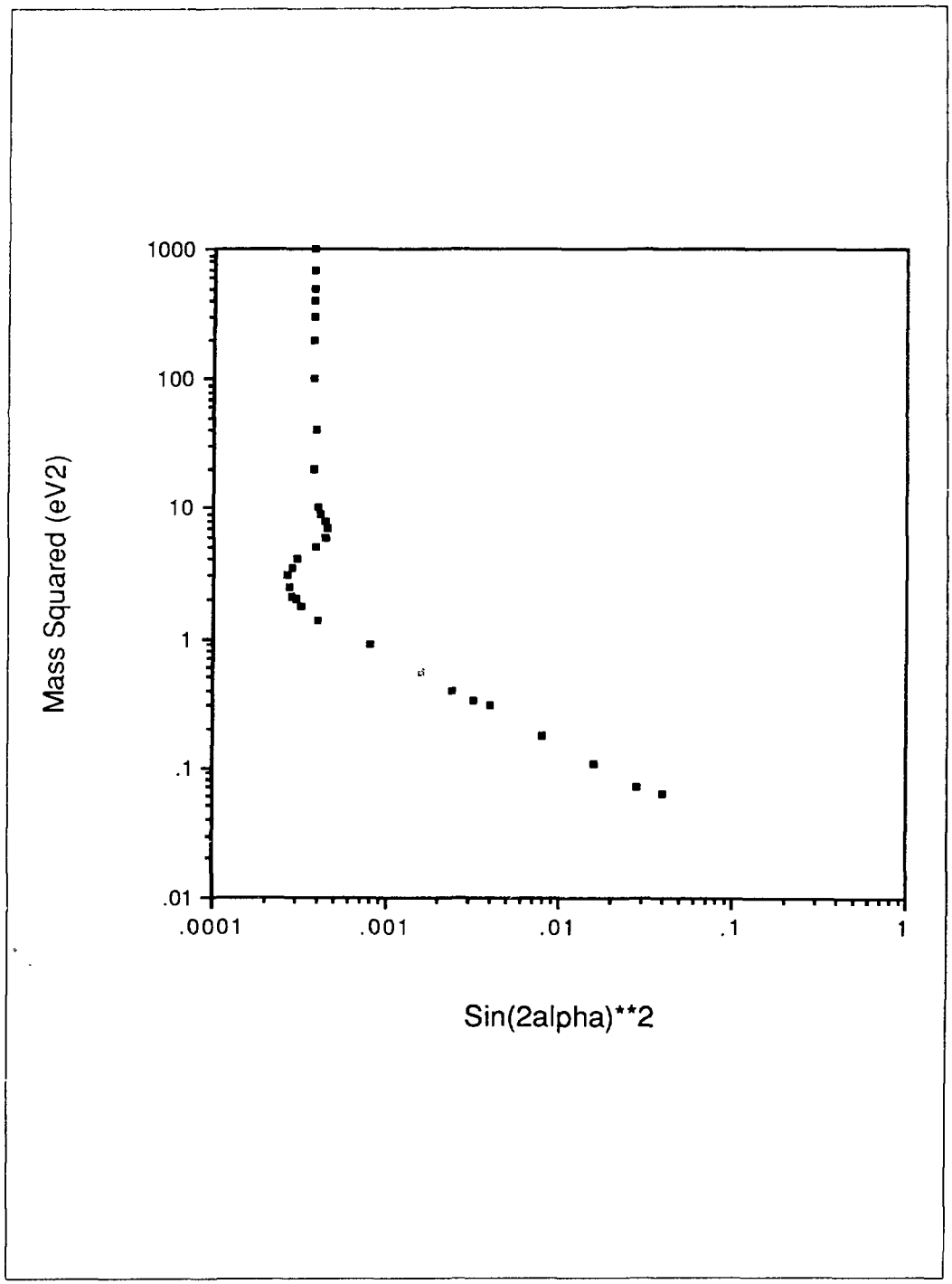

Fig. 15.6. Oscillation limits for $\bar{\nu}_\mu \longleftrightarrow \bar{\nu}_e$.

15.2 Neutrino Magnetic Moment and Charge Radius

If the electron or muon neutrino has a sufficiently large magnetic moment or charge radius, then LCD will observe an anomalous value of R and an anomalous y distribution ($y=E_e/E_\nu$). A non-zero magnetic moment (or electric moment) increases the neutrino-electron cross section and makes the y distribution peaked toward y=0. A non-zero charge radius can increase or decrease the cross section and has the effect of flattening the y distribution. If no such anomalies are observed, then stringent limits can be placed on the magnetic moment and charge radius.

Neutrino Magnetic Moment

If a muon or electron neutrino has a magnetic moment equal to $Ke/2m_e$, then the neutrino-electron cross section is increased by the additional term[3,4] $\Delta\sigma = K^2\pi\alpha^2/m_e^2[ln(E_\nu/E_e) - 1 + E_e/E_\nu]$, where E_ν is the neutrino energy, E_e is the minimum electron energy detected by the apparatus, and we have assumed that $m_e << E_e$. Note that this term is not proportional to the neutrino energy and becomes relatively more important at lower neutrino energies. Furthermore, this term is independent of neutrino flavor and is always positive due to the absence of interference effects. By taking the derivative of the above term, we see that the y distribution is augmented by $\Delta d\sigma/dy = K^2\pi\alpha^2(1/y\text{-}1)$. A large magnetic moment, therefore, has the effect of increasing the cross section at lower y values.

For LCD E_e=10 MeV, E_ν ~30 MeV, and from the increase in cross section alone we shall set limits at 90% C.L. of $K<1.2\times10^{-10}$ for the muon neutrino and $K<2.6\times10^{-10}$ for the electron neutrino. Present limits from terrestrial measurements are $K<4\times10^{-10}$ and $K<1\times10^{-9}$ for the electron[5] and muon[6] neutrinos, respectively. Astrophysical arguments[7] constrain $K < 10^{-10}$ for all neutrinos with masses less than 10 keV, although these limits depend on models for the evolution of Red Giant and White Dwarf stars and, therefore, require more assumptions than the terrestrial limits. The Standard Model predicts[8] for Dirac neutrinos that $K=3\times10^{-19}m_\nu$, where m_ν, the neutrino mass, is measured in eV; however, there are other models that predict much larger K values. One model[9], for example, uses a very large electron-neutrino magnetic moment to solve the solar neutrino problem and predicts that $K=(0.3\text{-}1.0)\times10^{-10}$. In the case of Majorana neutrinos, K=0, although non-zero transition magnetic moments may also lead to larger neutrino-electron cross sections.

Neutrino Charge Radius

If a neutrino has a non-zero charge radius, $< r^2 >$, then the neutrino-electron cross section is modified by an amount $\Delta\sigma$. Note that for charge radius we don't

include the radiative corrections, which have been discussed earlier and which are predicted by the Standard Model; rather, we consider unexpected compositeness, which is not part of the Standard Model. The modification of the cross section is dependent on the type of neutrino. For muon neutrino-electron scattering,

$$\Delta\sigma = \sqrt{2}m_e E_\nu/3[\pi\alpha G_F < r^2 > (8\sin^2\theta_W/3 - 1) + 2\sqrt{2}\pi^2\alpha^2 < r^2 >^2] \ .$$

For antimuon neutrino-electron scattering, the -1 in the above expression is replaced by -1/3. Therefore, depending on the type of neutrino, $\sin^2\theta_W$, and the value of $< r^2 >$, $\Delta\sigma$ can be positive or negative. (Note that due to interference effects, $< r^2 >$ can be positive or negative.) The y distribution is similarly affected. For muon neutrino-electron scattering, there is an additional term in the differential cross section proportional to $1+4y\sin^2\theta_W-2y^2\sin^2\theta_W$. Thus, charge radius contributions appear at large values of y. The current best limit on the muon neutrino-charge radius is[3] $0.81\times10^{-32}cm^2 > < r^2 > > -7.3 \times 10^{-32}cm^2$. LCD will set limits approximately an order of magnitude better: $| < r^2 > | < 10^{-33}\text{cm}^2$, for both muon and electron neutrinos.

15.3 Extraterrestrial Neutrinos from Supernovae

LCD is similar to IMB and KII in its ability to detect neutrinos, muons, and electrons but has significantly higher cosmic-ray related backgrounds. In spite of this it is possible to detect supernovae electron neutrinos from the prompt collapse phase and delayed high-energy muon neutrinos. Atmospheric neutrinos from cosmic rays in the atmosphere can also be seen, although solar neutrinos will be masked by low-energy background.

It is hardly necessary to emphasize the physics involved: neutrino masses, neutrino production, discovery of supernovae and their location and type, tests of supernovae models of collapse, possible identification of the type of remnant (black hole, pulsar), and the identification of antimatter supernovae. The effort needed to make the detector capable of these tasks appears reasonable. The quality of the data will be competitive with the rest of the world for intense neutrino bursts, with coincidence information over a long base line, when linked with similar detectors.

The hardware needed to collect external neutrino events is mostly an integral part of the proposed data acquisition. An interesting event would be signaled by an abnormal number of electrons unaccompanied by parent cosmic-ray muons in the detector. The background that has to be dealt with consists of electrons from the decay of muons stopped in the detector. The rate of these stopped muons was described in chapter 11, it is expected to be about 8 KHz.

15.3.1 Supernovae Rates and Physics

We calculate rates using an area of $400m^2$ and 5000 metric tons of water in the fiducial region, assuming directional cuts of 40° ($\sim$ 10:1 reduction in solid angle) and the efficiencies of KII.

Neutrinos (and Antineutrinos) from Supernovae

Type I Supernovae may be thermonuclear explosions caused by accretion of matter on to a white dwarf from a binary partner. This model does not emit many energetic neutrinos above a few MeV, so the observation of neutrinos from them would deal a blow to this explanation, according to Wheeler and Wheeler.[10]

Type II Supernovae have a more widely accepted mechanism[10] — a core that burns to iron, followed by gravitational collapse and electron – proton annihilation into neutrons and neutrinos. However, there is uncertainty beyond this. The 1-10ms shock wave may damp out or bounce again after 0.1-10s. It is generally agreed that heating makes gammas and then electron pairs, which annihilate into neutrino-antineutrino pairs of all flavors that come out with about 10ms rise times and die out on time scales of seconds with energies of about 10 MeV [compared to 20 MeV for the millisecond burst]. Fig. 15.7 is a prediction[10] of the rate of emission of neutrinos during the gravitational collapse. This slow burst would be truncated if the star is massive enough to collapse into a black hole instead of a neutron star (10-20 $\times$ the sun mass), as the gammas would not get out. Only a fast initial burst would be seen, dying after about 10ms. A less massive star might form a rotating neutron pulsar, which would emit both light and neutrinos at the time of collapse, followed by high-energy neutrinos weeks later, and high-energy gammas if a rotating neutron pulsar were formed.

The properties of these supernovae can be studied by the time and energy spectra of neutrinos and compared to the sub-classes of type I and II supernovae.[11] The next supernova that occurs is likely to occur at less than 10kPc, in a region of our galaxy that is obscured by gas. A recent publication by Bruenn[12] makes calculations of fluxes from SN1987a and finds that SN1987a is one of the optically weaker types of supernovae. There is also considerable leeway in the determination of the temperature (3-7 MeV) of the system.[13] We use these features to estimate what the detectable flux might be when the next supernova occurs in our galaxy – the estimated frequency is one per 7 - 50 years. Our motivation in making this estimate is not to enter into prediction of future events but to estimate the potential load on a data-acquisition system. If an event is identical to SN1987a, the response in LCD would be 25 (solid angle) $\times$ 2.5 (mass ratio of LCD to KII) $\times$ 12 (events in KII) = 750 events. The fluctuations in this number could be a factor of three for

star size and a factor of seven for star temperature, mostly due to the rising detector efficiency with neutrino energy. LCD should be prepared to collect as many as 750 $\times$ 3 $\times$ 7=16000 events in 10s. Table 15.1 gives rate estimates for LCD.

Table 15.1

Rate estimates were made using Ref. 10, 12, and 13, and the following formula for event rates in a water detector:

$$N_{ev} = 0.28 N_{56} (10/R)^2 M(kT) \times \sigma_{42}$$

where σ_{42} = detection cross section times efficiency in units of 10^{42}cm^2 for each water molecule, and N_{56} is the number of neutrinos emitted in units of 10^{56}, and R in kPc.

Table 15.1a Cross sections per water molecule from Ref. 13.

Reaction	*3 MeV*	*5 MeV*	*7 MeV*
ν_e – e elastic	0.29	0.78	1.34
$\bar{\nu}_e$ + O → e + N	0.023	0.61	3.34
ν_e + O → e + F	0.04	0.83	5.63
$\bar{\nu}_e$ – e elastic	0.12	0.31	0.54
all other ν_e – e elastic	0.05	0.14	0.24
$\bar{\nu}_e$ p → e + n	16.1	52.9	105

Table 15.1b Supernova neutrino flux estimates.

N_{56}	*W&W(10)*	*Bruenn(12)*	*Typical*
ν_e 1st 10ms	1	1 – 2.8	2
ν_e & $\bar{\nu}_e$ > 10ms	100	20–50	50
other ν	50	10–25	25

Table 15.1c Typical supernova (5-MeV) event totals in LCD.

Reaction	*Nevents*	
ν_e - e (< 10ms)	2	(small angle)
ν_e + O (< 10ms)	2 (0.1–30 for star temp. 3–7 MeV)	(large angle)
ν_e – e (> 10ms)	55	(small angle)
$\bar{\nu}_e$ – e (> 10ms)	22	(small angle)
other ν - e (> 10ms)	20	(small angle)
ν_e + O (> 10ms)	58	(large angle)
$\bar{\nu}_e$ + p (> 10ms)	3704	(large angle)
$\bar{\nu}_e$ + O (> 10ms)	43	(large angle)

For a 5kT LCD we expect $N_{e\nu} = 1.4\ \sigma_{42}\ N_{56}$, and this is reflected in Table 15.1c, which shows events for a "typical" supernova. This object is taken to have neutrino fluxes intermediate to Wheeler and Bruenn, while the detector has a detection efficiency determined by Haxton for a star of temperature kT=5 MeV. In the first 10ms there are two events of ν_e - e type and two of ν_e + O type. This last type can go up and down a factor of 10 (each way) due to the varying dependence on energy of the cross section $\nu_e + O \rightarrow e + F$. In 3700 $\bar{\nu}_e$ events on from 10ms to 10s there are 100 $\bar{\nu}_e$ or ν_e - e events, protons, and about 100 $\bar{\nu}_e$ or ν_e events on oxygen. Several important measurements are listed below:

a) It is of importance to determine the source of the neutrinos and that may be accomplished in two ways. A local supernova may have as many as $100\nu_e$ - e events in the early period, and the average direction will be calculable to a degree or two. Time resolution to a millisecond on the initial electrons in conjunction with other similar detectors (KII and IMB for example) allows the direction to be determined to about 3^o about the baseline direction.

b) The frequency of collapse in our galaxy is predicted to be one per 7 - 50 years for type II supernovae from observations of distant galaxies, but only one local supernova per 250 years has been seen. These predictions are based on pulsar formation rates and observations of other galaxies, but there is conflicting evidence, such as the unexpected lack of pulsars in supernova remnants where one would expect to find them.[10] Most of these distant supernovae have actually been type I, which occur in less gaseous (more visible) regions. The neutrino detectors can be expected to shed some light on the validity of the predictions and clear up the apparent discrepancy.

c) Neutrino arrival times with a 1-ms rise time would give a limit of 0.1ev on the ν_e mass if the event occurred at 10kPc. Unfortunately, the other leptonic flavors are not easily separable, so one cannot expect to get such a good limit on the ν_μ or ν_τ mass.

d) Antimatter/matter determination can be made by the electron (or positron) angular distribution observed in LCD. Antineutrinos produce wide-angle positrons, while neutrinos make electrons with about 50% of them in a narrow forward cone from elastic-electron scattering, and the rest are mostly backward peaked from $\nu_e + O \rightarrow e + F$. An anti-supernova would have a copious early antineutrino burst instead of a neutrino burst. This would give many more early events, or about 200 events instead of four as estimated above.

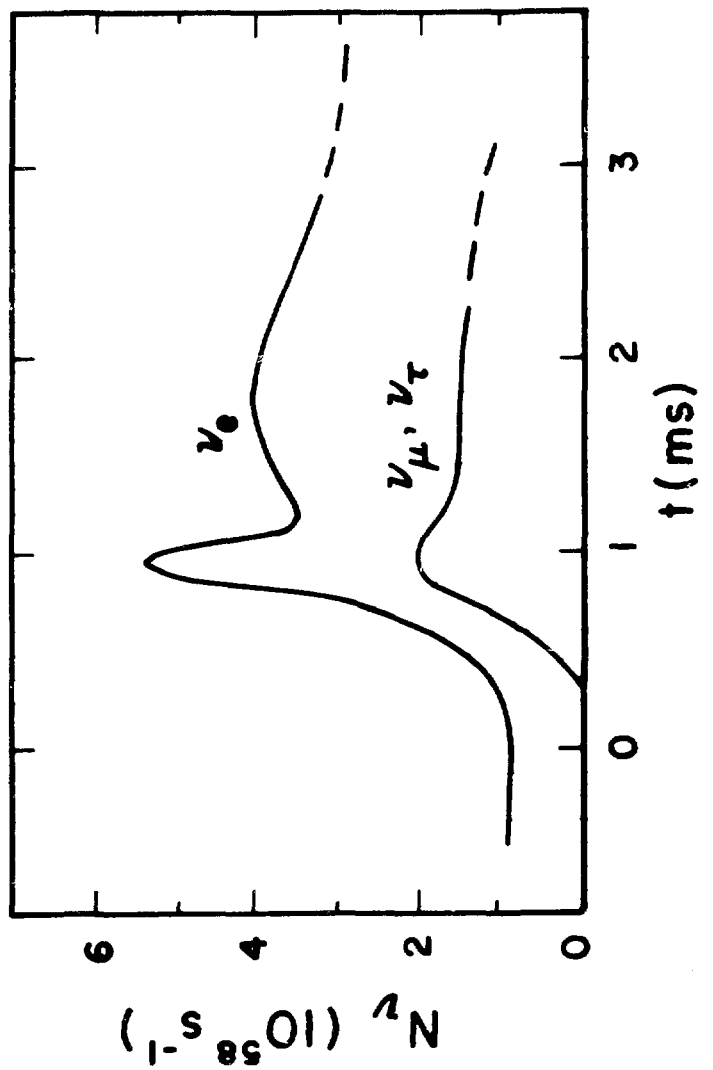

Fig. 15.7. The rate of emission of neutrinos during the gravitational collapse of a stellar core (from Ref. 10).

15.3.2 Upward-going Muons in the GeV Range

The directional sensitivity of LCD will allow effective selection of these events, which must come from neutrino interactions in rock below the detector and the detector itself. There are two weak sources of high-energy neutrinos that can be detected — atmospheric neutrinos from pion and muon decay and galactic supernovae. All other known sources are weaker. Our galactic center[14] emits about 10^{38} ergs/s in gammas and perhaps 10^{40} ergs/s in primary cosmic rays, varying on time scales of months (so the sources are compact). They are simply too weak and require DUMAND size detectors for reasonable rates. Atmospheric neutrino energy spectra have been calculated by Gaisser[15] and the sensitivity of these spectra to oscillations for path lengths through the Earth are sufficient to give ν_e mass-squared differences of $10^{-4}(\mathrm{eV})^2$. Actual event rates have been estimated by Koshiba[16] to be about 180/yr. for LCD. KII presently has 75 of these events and IMB 300 events. The small numbers here are a blessing in a sense, because this is a dc background to muons from the other source — high-energy neutrinos coming from supernovae.

Upward muons produced from high-energy neutrinos from SN1987A, see Fig. 15.8, have been estimated recently by Gaisser.[17] For two quite different models of proton acceleration mechanisms, he finds that GeV neutrinos will have different time and energy spectra. In one case the shell becomes transparent within days and 20 upward neutrinos are produced in 20 days for a $100\mathrm{m}^2$ detector, assuming a power-law proton energy spectrum. In the other case, the transparency time is about two months and most of the 40 events are produced in the following 200 days, assuming a uniform energy proton beam from a newly formed neutron pulsar.

For our detector this scales up to 80 events in 20 days or 160 events in 200 days. The signal would already be here if the first model is correct. This possibility has apparently been excluded by KII. (The second model is possibly also excluded by the KII and IMB data; however, this does not lessen the importance of looking for upward-going muons from supernova bursts.) Directional information should also be present. Opening angles of 36^o and 18^o for 1 and 10-Gev interactions, respectively, are expected. Contained events will allow ν_μ to ν_e ratios to be determined for antimatter tests.[15] As stated earlier, the next supernova is likely to produce many more neutrino events. This makes it very much easier to study the details of the supernova; perhaps gaining insight into cosmic-ray acceleration mechanisms. If a pulsar is formed after collapse, one can also expect to see high-energy gammas from the same region in the sky.

15.3.3 Backgrounds

LCD is 25mwe below the surface and has a 1.5-m thick water Čerenkov veto. Hadronic and electronic cosmic-ray components are effectively removed by the overburden, and the muon component by the veto system. The signature for a neutrino event is a contained relativistic track with the Čerenkov cone pointing to the expected source. For supernovae and other discrete cosmic sources, one has a directional constraint that can be used to reduce background by 90%. The signal from each source also has a characteristic energy spectrum, and cuts can be applied that enhance the signal-to-noise ratio.

The backgrounds in LCD are all related to the muon cosmic-ray rate of $38m^{-2}s^{-1}$, which gives 15kHz of singles rate in the fiducial volume, 8kHz of stopping muons, and a total muon rate of 19kHz. The predicted backgrounds are listed below with an angle cut included:

a. Near-miss muons that make gammas and neutrons not detected by the veto. The rate is estimated by scaling E225 to be $.05s^{-1}$ from 10-50 MeV.

b. Long-lived beta decay (16ms, 20 MeV as seen in KII) of ^{12}N spallation nuclei. The KII rate has been scaled to give $.05s^{-1}$ for LCD from 10-20 MeV.

c. Negative muon capture on ^{16}O giving ^{16}N (7s, 11-MeV beta decay) has been measured by Guichon[18] and results in about $.012s^{-1}$ above 10 MeV.

d. $\mu \rightarrow$ e decay will result in fake events if delayed by more than the veto length, which we take to be $10\mu s$ for the sake of discussion. This gives a detector dead time of 19% (later we show this can be reduced to about 5%), but reduces the 8-kHz background to 80Hz for 10-60 MeV. Subsequent reconstruction to reject events with nearby (within 1m) muons should lower this background far below the others. But one must store all PM data for the preceding $30\mu s$, and one must be able to select and read out the $80s^{-1}$ events that pass the hardware veto and energy cuts.

The beta spallation rates above could be reduced if events with big energy deposits and/or prompt trailing μ decays were to be saved. These are signatures for hadronic cascades that coincide with the formation of long-lived nuclei. There are few enough of these in 16ms to not create dead-time problems (4% by the technique described in the cosmic-ray chapter). Ignoring this possibility, the background is 0.1Hz for 10-50 MeV, .08Hz for 7-15 MeV , and .05Hz for 10-15 MeV. This is considerably higher than the solar-neutrino signal (.0003Hz) and much less than the supernovae burst rates of 1Hz for SN1987A and 0.37kHz for the "typical" SN event. Hard estimates of background for the high-energy upward events are difficult

to calculate, but KII has been able to select events cleanly if the azimuthal angle exceeds 90^o.

Table 15.2 Signal to noise summary.

Event Type	*Signal(ev)*	*Noise(ev)*	*Comments*
Supernova II	10–16000	1	10s, 10–20 MeV
Upward Muon	80–100000	1–10	1–6 mo., 1–10 GeV

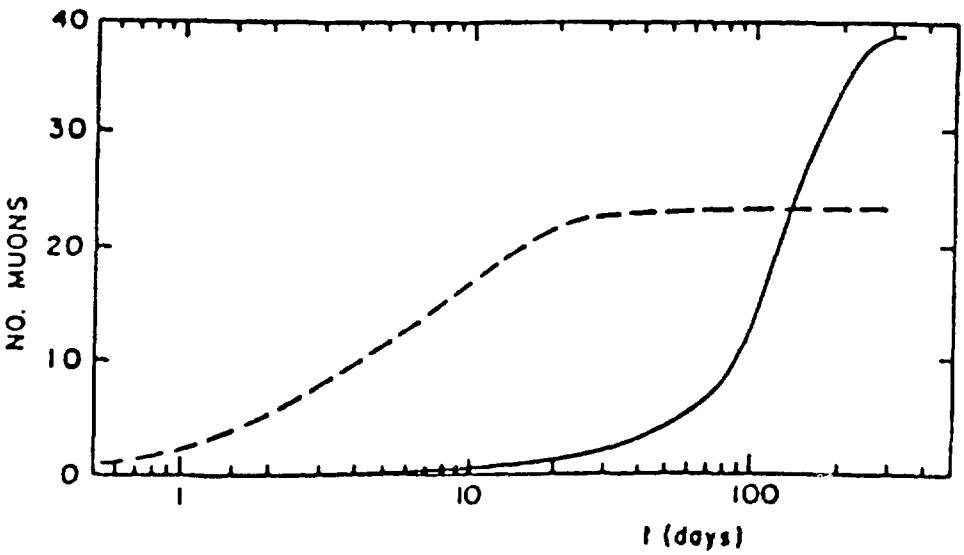

Fig. 15.8. Accumulated signal of neutrino-induced muons per $100m^2$ as a function of time for two quite different models of proton acceleration mechanisms (from Ref. 17).

15.3.4 Trigger Requirements and Characteristics

The detector must be able to handle bursts of 20,000 events in 10s, as well as keeping up with a steady rate of about 12/s background triggers. A scenario for triggering and data flow is presented here, which is consistent with the electronics for the main experiment with a few additions.

For example, the possibility of reducing the beta spallation background by reading out all candidate muon hadronic interactions may require hardware generation of flags so that these events are not simply vetoed, but read-out. The raw rate, scaled from KII is about 25Hz. These could be read-out and saved or eliminated if no event trigger occurs within 16ms. This would remove spallation events with about 75% efficiency. Running LCD in a DC mode to search for supernovae or other cosmic events, implies handling many more events. Through-going muons can be filtered with a hardware veto, leaving many stopping $\mu \rightarrow$ e decays still to contend with. We present here a simple means of dealing with this background without introducing a large deadtime. Our method is to generate a hardware trigger that reduces the triggers to about 100/s, followed by a crude filter to throw out events with the wrong space-time topology. Simple sums and times from different banks of PM tubes should give us the tools to reduce event collection to a few per second. These remaining events will be fully analyzed.

The discussion here focuses on two event types with different properties, each of which requires a different trigger: 10-50 MeV prompt supernova neutrinos, and 1-10 GeV upward-going muons from high-energy neutrino interactions in and below the LCD. Different triggers will be required for each of these event types and others could be added later.

Supernova Neutrino Trigger

These events have characteristics that are identical to those from the beam dump experiment, except that they have 100% duty factor. A simple trigger would have a fast veto to remove through-going μ's and a slow veto to remove 99% of the $\mu \rightarrow$ e decays (see Fig. 15.9). The dead time is less than 3% for the signal, and the trigger rate is reduced to the order of 100/s. The trigger has no segmentation and is formed from simple sums of pulses in the central region and the veto region. The events that remain are mainly $\mu \rightarrow$ e decays with times greater than 10μs, or small pulse-height muons that fake an electron. These can be reduced dramatically by simple sums in segments of the detector to get crude localization, and searching for pulses in the 20μs following the main trigger. It appears that we can filter this way for the small number of PMs involved in less than 500μs — the time between events for the biggest SN that we considered. We also can weed out the triggers effectively

enough (to about a few/s) to allow a particle fitter to keep up with the analysis. In summary, this trigger has the capability of keeping up with background filtering and the burst rates of a likely supernova.

Upward Muon Trigger

This event class does not have the problem of coping with $\mu \rightarrow$ e decays because the energy deposit is much larger. Basically, we are trying to identify long tracks pointing upward. The key to recognizing them without a complete fit is to segment the veto and central regions and use the spatial and timing information for each segment to generate triggers that accept the most common event topologies. These topologies are shown in Fig. 15.10. In the current version of the electronics, the PMTs will be grouped in banks of 256 with sum discriminator, charge, and time available. The bank sum pulses can be used to generate good timing signals for use in the trigger logic. One needs to have timing resolution of about 20ns between lower and upper banks to separate upward from downward muons of class three topology. Class three can then be separated by the following logic:

$$TR_3=(V_l).(V_u.C_u) \text{ delayed, where}$$

V_l is any lower bank veto sum, and V_u is any upper bank veto sum, and C_u is any upper bank detector sum.

Trigger class two events can be selected (with less rejection of background, perhaps) by requiring that there be big pulse heights in the central detector bank next to an upper veto bank. A downward-going muon track would not give a big pulse in the upper detector bank, but would radiate Čerenkov light into lower banks. We define class two event triggers as:

$$TR_2 = (V_u.C_n), \text{ where}$$

V_u is as above, and C_n is the bank in the central detector next to the veto bank.

Trigger class one events are selected by the logic:

$$TR_1 = C.V, \text{ where}$$

V is the sum of all veto banks, and C is the sum of all detector banks.

The above section is meant only to outline possibilities. For example one could get better topology selection if a lower bank and an upper bank were not allowed to be on the same wall, when constructing TR_3. A Monte Carlo code will be used to determine if any extra complexity is needed to generate clean triggers.

Accidentals in these triggers might be expected to be about 10,000/s $\times$ 10,000/s $\times$ 2 $\times$ 10^{-8} s = $2s^{-1}$ for 20ns time resolution coincidences, which is quite manageable. The total trigger rate will be about $100s^{-1}$ before the filtering is done by the microprocessor farm.

The Effects of Singles Rates on the Trigger

Single photoelectrons from noise create a 14 MHz rate(14,000 tubes $\times$ 1 KHz) in the central detector, and about 1/10 as much in the veto. This could cause accidental triggers or vetoes that are unwanted. These can be lowered to a reasonable level with a crude sum trigger and a threshold energy of 10 MeV, or a lower level if the trigger is made more complicated.

Assuming 3pe/MeV and 300-ns pulse widths, we shall get an average of 5pe in each 300-ns gate if all the central detector tubes are summed. There are no more than 1.4 $\times$ 10^7 such gates per second. If the threshold energy is set to 7 MeV or 20pe (10 MeV or 30pe) then a 4 (6) std. dev. fluctuation is required to create an accidental pulse. The chance of this happening is 6 $\times$ 10^{-3} (3 $\times$ 10^{-7}), giving a rate of 10^4s^{-1} ($5s^{-1}$). This indicates that 7-MeV threshold will cause too many triggers, while 10 MeV is OK. However, requiring that all pe's be within eight banks, or about 2000 PMs, reduces the average pe/gate to about 0.5. There is no chance of an accidental trigger even at 7 MeV because a 14 st. dev. fluctuation is required to reach threshold. The veto has only about 2000 PMs and thus falls into this latter category of having a negligible accidental rate. Thus the veto efficiency is preserved and reasonable accidental trigger rates can be achieved for 7- to 10-MeV thresholds.

Summary

Events that are not beam related can be handled by generating hardware triggers to reduce the number of events processed by the microprocessor farm to the order of a few hundred per second. An initial filter on the farm that uses spatial resolutions of the order of the area of 256 PMTs should reduce the number of full fits to a few per second. The track fitting should then reduce this sample to candidate events that will be sent to permanent storage. The system can handle both the average trigger rate of hundreds per second and the instantaneous rate of thousands per second from a supernova without serious loss of data. Fig. 15.11 shows a schematic of the data flow that is essentially the same as that used for the beam associated triggers.

SIGNALS	AVERAGE RATE
C1 = DETECTOR SUM > 200 TUBES	25 kHz
C2 = ν - e SIGNAL 10 TUBES < DETECTOR SUM < 200 TUBES	8 kHz
V1 = THRU - μ VETO	25 kHz
V2 = μ - e DECAY VETO	8 kHz

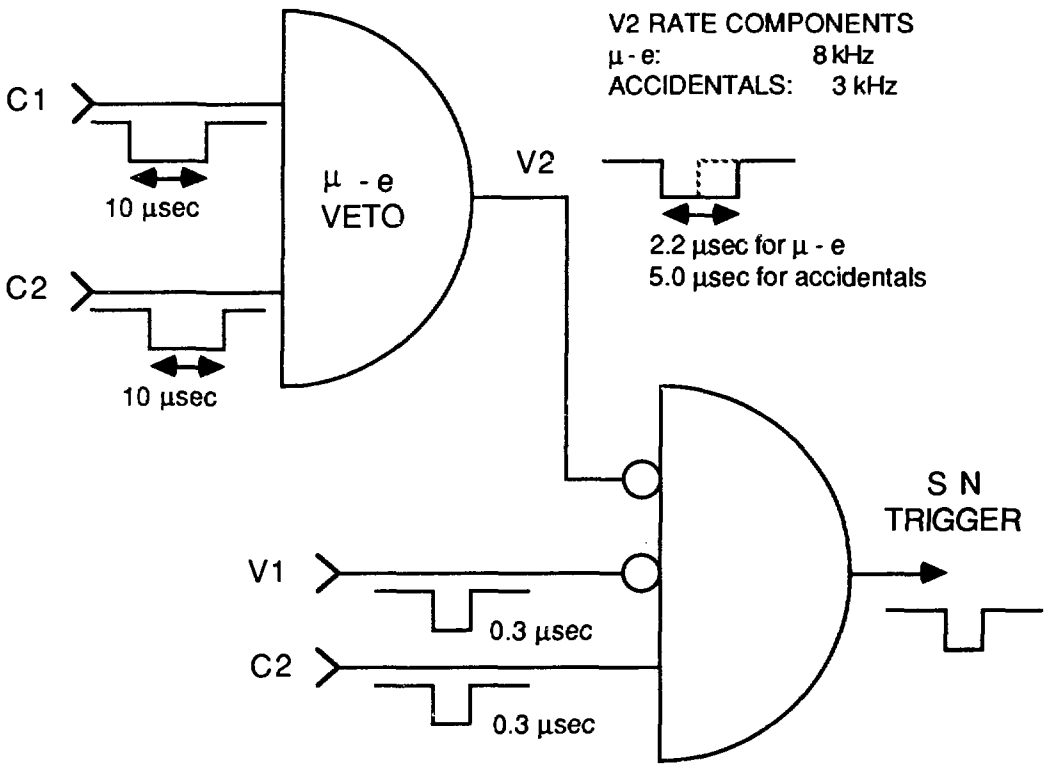

TRIGGER RATE	
μ - e longer than 10 μsec:	80 /sec
low energy μ:	40 /sec
TOTAL S N TRIGGER RATE	120 /sec

DEADTIMES IN TRIGGER	
V2 ACCIDENTALS:	1.5 %
V2 μ-e:	1.8 %
V1 ACCIDENTALS:	0.6 %
SUM =	3.9 %

Fig. 15.9. Simple version of a supernova neutrino trigger. The trigger is formed from the sum of pulses in the central region and the veto region. The candidate events are primarily μ - e decays with times greater than 10 μsec or small pulse height muons from low energy muons that are missed by the veto and trigger the central region phototubes.

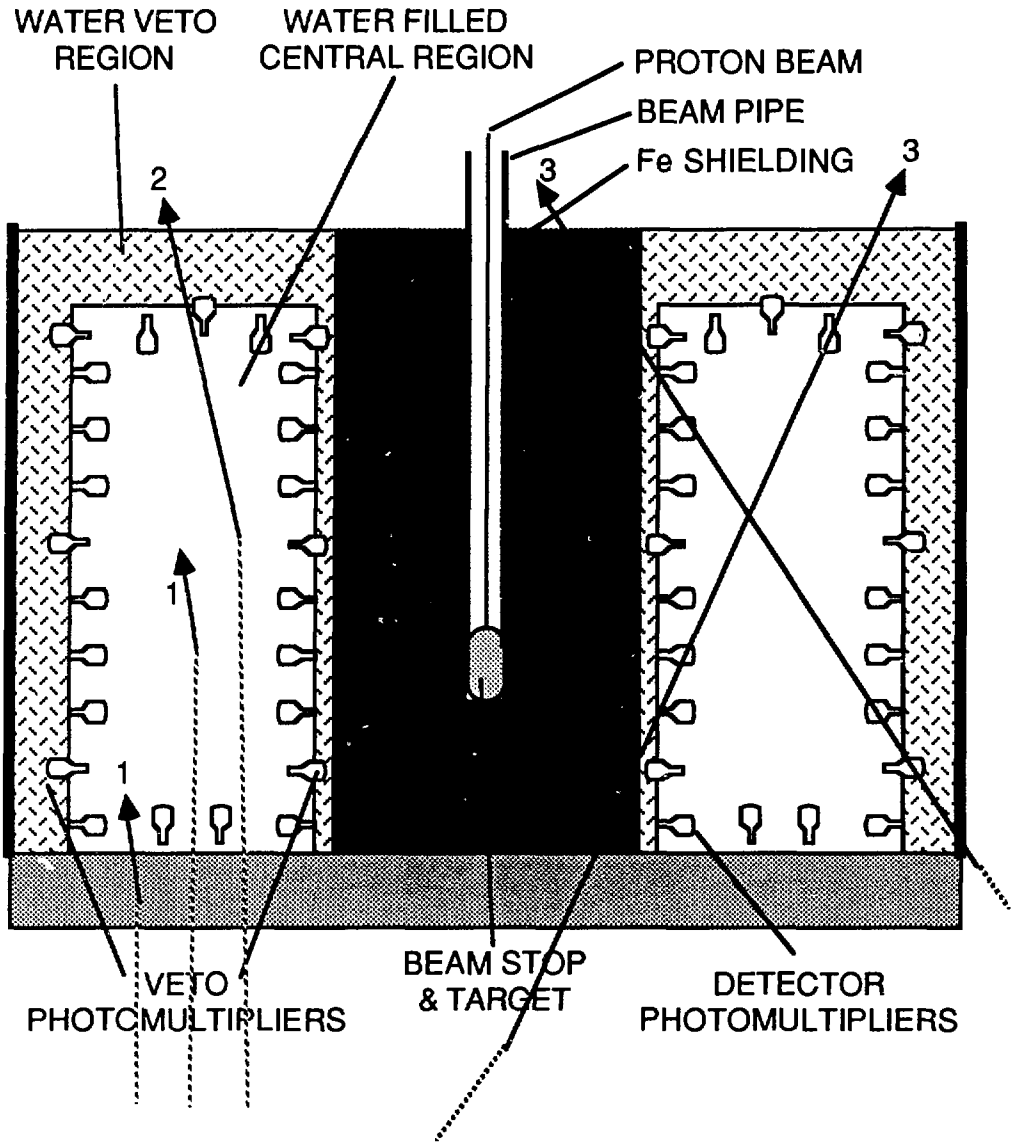

Fig. 15.10. Trajectories and regions triggered by neutrino induced upward going muons: class 1 events require only a gross veto, class 2 and class 3 events require spatial and timing information.

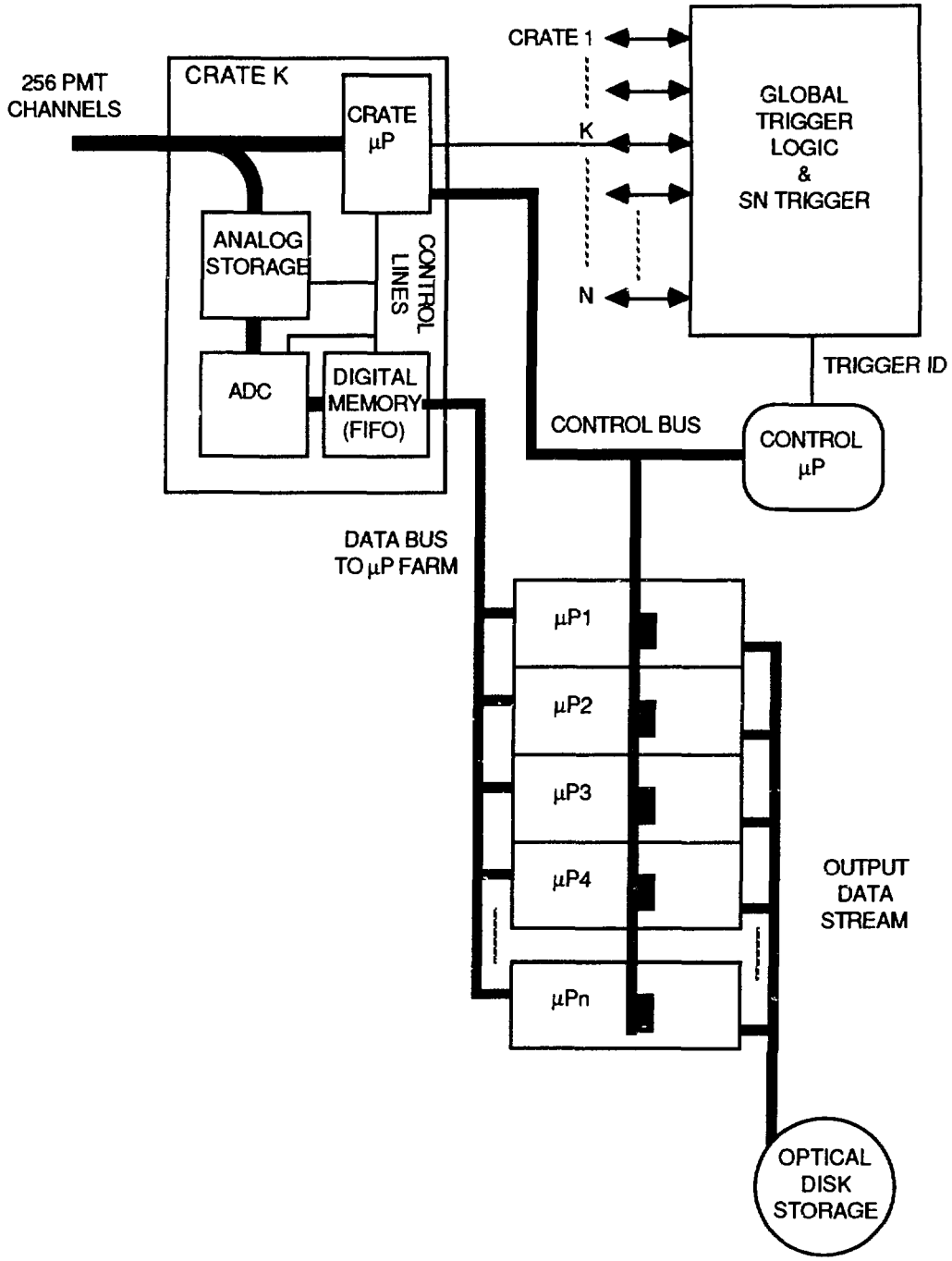

Fig. 15.11. Simplified illustration of the LCD data flow as is relevant for the upward going muon and supernovae triggers.

15.3.5 Conclusion

A modest effort is all that is needed to make a variety of interesting measurements possible:

1. Star collapse dynamics.
2. Neutrino mass.
3. Matter/antimatter tests of neutrino sources.
4. Supernova detection and location.

15.4 Lepton Number Violation and Weakly Interacting Particles

If muons violate lepton number by decaying according to $\mu^+ \rightarrow e^+\bar{\nu}_e\nu_\mu$, then $\bar{\nu}_e p \rightarrow e^+ n$ interactions occur with a large cross section and a large average positron energy. The main background to observing these events is $\nu_e^{18}O \rightarrow e^-\ ^{18}F$ interactions, as discussed in section 15.1. We estimate that our sensitivity for these decays is $B.R.(\mu^+ \rightarrow e^+\bar{\nu}_e\nu_\mu) \geq 2 \times 10^{-4}$. The present best limit[19] for this decay is $\sim 8 \times 10^{-3}$ from experiment 225 at LAMPF.

The LCD experiment also will be sensitive to weakly interacting particles, such as heavy neutrinos or axions, which decay in the fiducial volume of the detector. A heavy neutrino, ν_H, could be produced, for example, in the decay $\pi^+ \rightarrow e^+\nu_H$ and then in turn decay by $\nu_H \rightarrow e^+e^-\gamma$. Similarly, an axion, A, could be produced by $\pi^+ \rightarrow e^+\nu_e A$ and then decay according to $A \rightarrow \gamma\gamma$. The weakly interacting particle would produce in both cases a distinctive multi-track shower which could be distinguished statistically from the normal νe scatters.

In summary, LCD is in some sense the ultimate beam dump experiment because of its large mass and high incident proton intensity. The detector is therefore very sensitive to rare phenomena of many kinds.

References

1. W. Marciano, Proceedings of Brookhaven National Laboratory Neutrino Workshop, BNL 52079 (1987).
2. C. Lim, Proceedings of Brookhaven National Laboratory Neutrino Workshop, BNL 52079 (1987).
3. Ushida et al., *Physical Review Letters* **57**, 2898 (1986).
4. W. Marciano and Z. Parsa, *Annual Review of Nuclear and Particle Science* **36**, 171 (1986). A. Kyuldjiev, *Nuclear Physics* **B243**, 387 (1984).
5. R. C. Allen et al., *Physical Review Letters* **22**, 2401 (1985).
6. K. Abe et al., *Physical Review Letters* **58**, 636 (1987).
7. F. Sutherland et al., *Physical Review* **D13**, 2700 (1976).

8. M. A. B. Beg, W. Marciano, and M. Ruderman, *Physical Review* **D17,** 1395 (1978).
9. L. B. Okun, M. B. Voloshin, and M. I. Vysotsky, ITEP Report No. 86-82, 1986 (to be published); M. Fukugita and T. Yanagida, *Physical Review Letters* **58,** 1807 (1987).
10. J. C. and J. A. Wheeler, Science Underground (Los Alamos, 1982), AIP Conference Proceedings **96,** (1982), p. 214.
11. D. Helfand, "BANG; Supernova of 1987," *Physics Today*, (August 1987) p. 25.
12. S. Bruenn, *Physical Review Letters* **59,** 938 (1987).
13. W. Haxton, "The Nuclear Response of Water Čerenkov Detectors to Supernova and Solar Neutrinos," preprint (1987).
14. D. Eichler, *Neutrino (81)* V. I., Department of Physics, Univ. of Hawaii (1981) p. 314.
15. T. Gaisser, "Neutrino Mass and Low Energy Weak Interactions," in *Telemark, 1984*, Barger and Cline, eds., (World Scientific 1985), p. 204.
16. Private Communication to D. Hywel White, Los Alamos National Laboratory, MP-4, Los Alamos, New Mexico.
17. T. Gaisser, *Physical Review Letters* **58,** 1695 (1987).
18. Guichon et al., *Physical Review* **C19,** 987 (1979).
19. Private Communication to R. Burman, Los Alamos National Laboratory, MP-4, Los Alamos, New Mexico.

*U.S. GOVERNMENT PRINTING OFFICE: 1988-0-573-034/80042